Old Dominion University

ODU Digital Commons

Electrical & Computer Engineering Theses & Dissertations

Electrical & Computer Engineering

Summer 8-2022

Fabrication of Nb_3Sn by Magnetron Sputtering for Superconducting Radiofrequency Application

Md Nizam Sayeed
Old Dominion University, md.nizamsayeed@gmail.com

Follow this and additional works at: https://digitalcommons.odu.edu/ece_etds

 Part of the Electrical and Computer Engineering Commons, and the Materials Science and Engineering Commons

Recommended Citation

Sayeed, Md N.. "Fabrication of Nb_3Sn by Magnetron Sputtering for Superconducting Radiofrequency Application" (2022). Doctor of Philosophy (PhD), Dissertation, Electrical & Computer Engineering, Old Dominion University, DOI: 10.25777/993y-fg12
https://digitalcommons.odu.edu/ece_etds/241

This Dissertation is brought to you for free and open access by the Electrical & Computer Engineering at ODU Digital Commons. It has been accepted for inclusion in Electrical & Computer Engineering Theses & Dissertations by an authorized administrator of ODU Digital Commons. For more information, please contact digitalcommons@odu.edu.

FABRICATION OF NB_3SN BY MAGNETRON SPUTTERING FOR SUPERCONDUCTING RADIOFREQUENCY APPLICATION

by

Md Nizam Sayeed
B.S. December 2012, University of Dhaka

A Dissertation Submitted to the Faculty of
Old Dominion University in Partial Fulfillment of the
Requirements for the Degree of

DOCTOR OF PHILOSOPHY

ELECTRICAL AND COMPUTER ENGINEERING

OLD DOMINION UNIVERSITY
August 2022

Approved by:

Hani E. Elsayed-Ali (Director)

Helmut Baumgart (Member)

Gon Namkoong (Member)

Grigory V. Eremeev (Member)

ABSTRACT

FABRICATION OF NB_3SN BY MAGNETRON SPUTTERING
FOR SUPERCONDUCTING RADIOFREQUENCY APPLICATION

Md Nizam Sayeed
Old Dominion University, 2022
Director: Dr. Hani E. Elsayed-Ali

Particle accelerators are considered as an important device that has wide applications in cancer treatment, sterilizing waste, preserving foods, ion implantation in semiconductor industry, and in production of isotopes for medical applications. Superconducting radiofrequency (SRF) cavities are the building blocks of a linear particle accelerator. Current particle accelerators use niobium (Nb) superconductors as the sheet material to fabricate a single SRF cavity for particle acceleration. With better superconducting properties (critical temperature T_c ~ 18.3 K, superheating field H_{sh}~ 400 mT), Nb_3Sn is considered a potential candidate in SRF technology. Magnetron sputtering is a promising deposition method to fabricate Nb_3Sn thin films inside SRF cavities.

Superconducting Nb_3Sn films were fabricated on Nb and sapphire substrates by magnetron sputtering from a single stoichiometric Nb_3Sn target, by multilayer sputtering of Nb and Sn followed by annealing, and by co-sputtering of Nb and Sn followed by annealing. The variation of morphological and superconducting properties was investigated for different substrate temperatures, annealing temperatures, annealing durations, and thicknesses. The film properties were characterized by X-ray diffraction (XRD), scanning electron microscopy (SEM), atomic force microscopy (AFM), and energy dispersive X-ray spectroscopy (EDS). The films had crystalline Nb_3Sn structure without any presence of poor superconducting Nb_6Sn_5 and $NbSn_2$

phases. The highest T_c of the films fabricated from the stoichiometric target, multilayer sputtering and co-sputtering were 17.44, 17.93, and 17.66 K respectively.

Finally, a cylindrical sputter coater with two identical magnetrons was designed and commissioned to fabricate Nb_3Sn films inside a 2.6 GHz SRF cavity. The magnetrons were installed facing opposite to each other in a custom designed vacuum chamber and multilayers of Nb and Sn films on 1 cm^2 Nb substrates replicating the beam tubes and equator locations of the cavity and the coated multilayered films were annealed at 950 °C for 3 h. The XRD of the as-deposited and annealed films confirmed the formation of Nb_3Sn after the annealing.

The dissertation discusses the fabrication process, characterized results of the fabricated films, the design of the cylindrical sputter coater and the preliminary data obtained from the sputter coater.

Copyright, 2022, by Md Nizam Sayeed, All Rights Reserved.

This dissertation is dedicated to my parents Md Abdul Hye and Ms Nilufa Yesmin, my sister Tanjery Sultana, and my wife Sadiya Tahsin.

ACKNOWLEDGMENTS

First, I would like to thank my Ph.D. advisor Dr. Hani E. Elsayed-Ali for his continuous support and valuable suggestions throughout my doctoral study. I am thankful to him for offering me an opportunity to conduct research at his lab. I have learned a lot about materials science and properties of thin films from our discussions during the weekly meetings. I also got the opportunity to get trained on different thin film fabrication and characterization tools in his well-equipped labs during the dissertation research.

I would also like to thank my Ph.D. supervisor Dr. Grigory V. Eremeev for his continuous mentoring to complete the dissertation work. I would like to express my gratitude to him for providing me an excellent research opportunity at Jefferson Lab. He guided me from the first day of my research work at Jefferson Lab, trained me to adapt at the research environment of Jefferson Lab, and monitored my work progress and advised to complete the research work.

I also thank Dr. Helmut Baumgart and Dr. Gon Namkoong for their valuable comments on my work, and for participating as members of my thesis committee, despite their busy schedules.

My sincere thanks to Dr. Charles E. Reece and Dr. Michael Kelley for their insightful comments during the weekly team meetings. I would also like to thank Dr. Anne-Marie Valente-Feliciano for her comments and suggestions on designing the cylindrical magnetron sputter coater. I would also acknowledge Dr. Gianluigi Ciovati, Dr. Pashupati Dhakal, Dr. Mathhew Burton, Josh Spradlin, David Beverstock, Pete Kushnick, Peter Owen, Harshani Senevirathne, Olga Trofimova, and the Jefferson Lab technical staff for their help throughout my Ph.D. research work.

A special thanks to Dr. Uttar Pudasaini for his continuous help throughout the research work. He assisted me throughout the whole research works by performing the annealing part of the Nb_3Sn film fabrication, running some characterization of the films, and providing his insights on improving the reports.

I would like to extend my thanks to Drs. Md Haider Shaim, Md Mahmudur Rahman, Abdullah Al Mamun, and Tanzila Tasnim Ava who motivated me throughout the Ph.D. research work. I also gratefully acknowledge Dr. Wei Cao who trained me on operating multiple thin film deposition and characterization tools and troubleshooting the tool issues.

A special thanks to Dr. Andranik Sarkissian and his team of *Plasmionique Inc.* for designing and building the cylindrical magnetrons. I would like to acknowledge the hard work of Dr. Wei Cao, Dr. Grigory V. Eremeev, and Md Sharifuzzaman Shakel on assembling and commissioning the cylindrical sputter coater. Thanks to Shakel for sharing data from his initial experiments on multilayer sputtering from the cylindrical magnetron sputter coater. Without this help, this dissertation could not be completed.

I wish to extend a heartfelt thanks to my mother, father, sister, and friends for their everlasting support and encouragement. Finally, I would like to mention the most inspirational person in my life, my wife “Sadiya Tahsin”. Thank you for your unconditional support in my personal and professional life.

NOMENCLATURE

α	Lattice Parameter, nm
B	Full Width Half Maximum of XRD Peaks, radian
d	Lattice Spacing, nm
D	Crystallite Size, nm
E_{acc}	Accelerating Gradient, MV/m
H_c	Critical Magnetic Field, T
H_{c1}	Lower Critical Magnetic Field, T
H_{c2}	Upper Critical Magnetic Field, T
H_{sh}	Superheating Field, T
P	Pressure, Torr
Q_0	Quality Factor, (No Units)
RRR	Residual Resistivity Ratio, (No Units)
T_c	Critical Temperature, K
TC	Texture coefficient, (No Units)
α	Thermal Expansion Coefficient, K^{-1}
Δ	Superconducting Energy Gap, meV
ΔT_c	Superconducting Transition Width, K
λ	London Penetration Depth, nm
ζ	Coherence Length, nm

TABLE OF CONTENTS

Page

Page

LIST OF TABLES

Page

LIST OF FIGURES

Figure Page

Page

Page

Page

Page

Page

Page

Page

CHAPTER 1

INTRODUCTION

Particle accelerators are used in high energy physics research to probe the inner structure of atoms, semiconductor industries for ion implantation, environmental research for wastewater treatment, medical research to sterilizing medical equipment, food irradiation, and in isotope production for medical imaging and cancer treatment, and for many other applications in medicine, sciences, and engineering [1-5]. An efficient way to accelerate a charged particle is using superconducting radiofrequency (SRF) cavities which are metallic structures typically made of a niobium superconductor that uses electromagnetic waves at a frequency range of 50 MHz to 4 GHz to set up an accelerating field [6]. Some SRF-based accelerators that are currently established or under construction include Large Hadron Collider (LHC) at European Organization for Nuclear Research (CERN) in Switzerland [7], Continuous Electron Beam Accelerator Facility (CEBAF) at Thomas Jefferson National Accelerator Facility (Jefferson Lab) in U.S.A. [8], European X-Ray Free-Electron Laser Facility (European XFEL) at Deutsches Elektronen-Synchrotron (DESY) in Germany [9], Facility for Rare Isotope Beams (FRIB) at Michigan State University in U.S.A. [10], and Linac Coherent Light Source (LCLS) II at Stanford Linear Accelerator Center (SLAC) in U.S.A [11], and Proton Improvement Plan II (PIP-II) at Fermilab [12].

Because of its high critical temperature (T_c = 9.3 K) and superheating field (H_{sh} = 200 mT) among pure metals, niobium has been considered as the material for the SRF cavities for many years [13, 14]. The chemically inert nature, suitable mechanical properties for machining and deep drawing and sufficient availability in nature made Nb a suitable candidate for SRF cavity fabrication. The two important parameters that determine the performance of a SRF cavity

is the quality factor Q_0 and the accelerating gradient E_{acc}. Since the quality factor is the ratio of the energy stored to power dissipated in the cavity per RF cycle, it is required to obtain a high Q_0 value. The power dissipation in a cavity is dependent on the surface resistance of the inside surface of the cavity. Due to the low surface resistance of Nb, high Q_0 of ~10^{11} can be achieved in Nb cavities [15]. However, to obtain this Q_0, Nb cavities need to be cooled down to ~2 K. Creating such an environment is complex and expensive. Also, due to the rigorous research on Nb SRF technology over the last five decades, the bulk Nb cavities are approaching their theoretical limit [16-18]. To overcome this, some alternative approaches are currently under consideration. The proposed alternative approaches to improve the SRF cavity performance include N_2 doping and N_2 infusion into Nb cavities [19,20], Nb deposition on Cu cavities [21], thin film superconductor-insulator-superconductor multilayers [22], and thin films of alternative materials (NbTiN, Nb_3Sn, MgB_2, V_3Si) on Nb/Cu cavities [23].

1.1. Nb_3Sn Properties

Nb_3Sn is an intermetallic compound with an A15 crystal structure. The A15 crystal structure has a chemical structure of A_3B where A is a transition metal and B is any element in the periodic table. Some noticeable compounds of this crystal family are Nb_3Ge, Nb_3Al, Nb_3Sn, V_3Si etc. Apart from the A15 Nb_3Sn, Nb and Sn form two other compounds; Nb_6Sn_5 with a critical temperature T_c < 2.8 K and $NbSn_2$ with a critical temperature T_c < 2.68 K [24]. It is important to understand optimum conditions for fabrication of Nb_3Sn without the presence of Nb_6Sn_5/$NbSn_2$ compounds to avoid the degraded superconducting T_c. The binary phase diagram of Nb and Sn is shown in Fig. 1.1. The A15 crystal structure of Nb_3Sn is shown inset of Fig. 1.1. The crystal is formed by a body center cubic (BCC) lattice of Sn atoms which is orthogonally

bisected by Nb-Nb atom chains in all sides. The lattice parameter of Nb_3Sn crystal is 5.29 Å. Based on the phase diagram, at thermal equilibrium, only Nb_3Sn films can be fabricated when the two elements are combined in a ratio so that the atomic Sn composition on the film remains in the range of 17-26%. Also, the phase diagram suggests a threshold temperature of 930 °C below which other compounds of Nb and Sn may exist. Table 1.1 shows some characteristic parameters of Nb and Nb_3Sn. Nb_3Sn has superconducting T_c and H_{sh} that is almost double that of Nb. Such properties of the compound make the material a potential candidate for SRF cavity application. Due to the close thermal expansion coefficient of Nb_3Sn and Nb, the thermal stress on the Nb_3Sn films fabricated on Nb substrates is expected to be low.

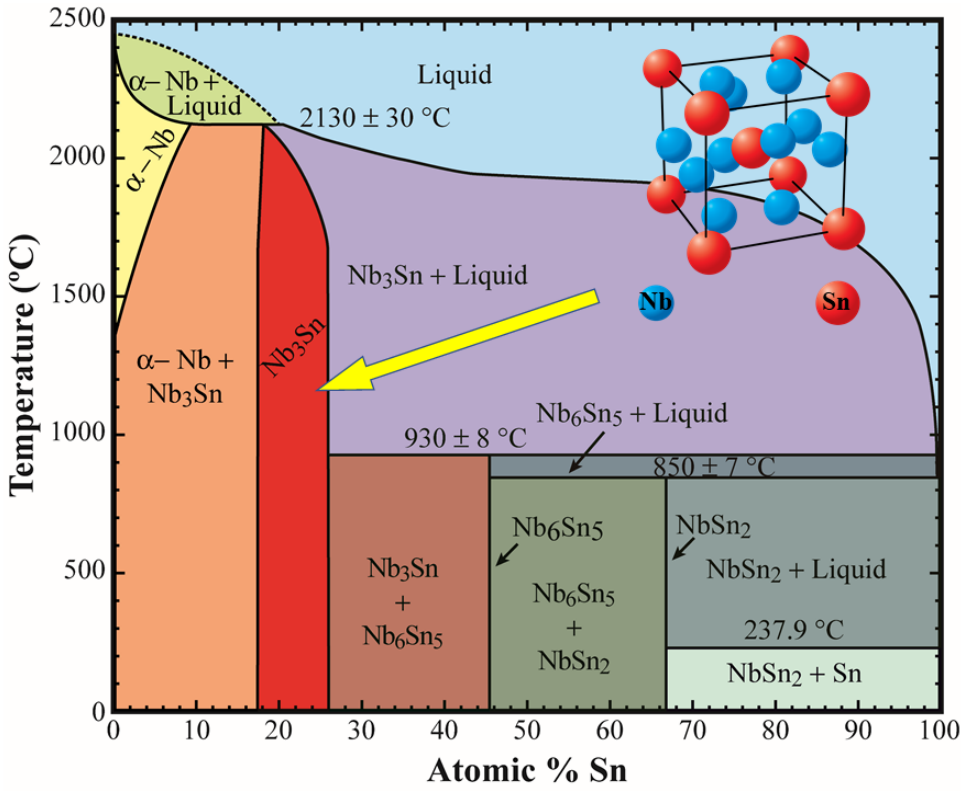

Fig. 1.1. Binary phase diagram of Nb and Sn reproduced from [25]. The crystal structure of A15 Nb_3Sn is shown inset.

Table 1.1. Characteristic parameters of Nb and Nb_3Sn [23, 24, 26, 27]. T_c, H_{sh}, Δ, λ, ζ, H_c, H_{c1}, H_{c2}, and α represent the critical temperature, superheating field, superconducting energy gap, London penetration depth, coherence length, critical magnetic field, lower critical magnetic field, upper critical magnetic field, and thermal expansion coefficient, respectively.

Material	T_c **(K)**	H_{sh} **(mT)**	Δ **(meV)**	λ **(nm)**	ζ **(nm)**	$H_c(0)$ **(T)**	$H_{c1}(0)$ **(T)**	$H_{c2}(0)$ **(T)**	α **(20 °C)** **(K^{-1})**
Nb	9.23	200	1.5	40	35	0.20	0.18	0.28	7.6×10^{-6}
Nb_3Sn	18.3	400	3.1	80-200	4	0.54	0.05	28	9.8×10^{-6}

1.2. Literature Review of Fabrication Process

1.2.1. Nb_3Sn for SRF Application

One of the widely considered methods to fabricate Nb_3Sn on Nb substrates is the Sn vapor diffusion method introduced by Saur and Wurm [28]. In this method, Nb is annealed at high temperature (~1200 °C) with Sn environment. The method was adapted to fabricate Nb_3Sn inside the SRF cavities in 1970s by Siemens AG [29]. Several research groups including Kernforschungszentrum Karlsruhe, University of Wuppertal, Jefferson Lab, CERN, SLAC, and Cornell University conducted research on Nb_3Sn SRF cavities fabricated by vapor diffusion method during the 1990s [30-33]. The method is currently adapted at Cornell University, Jefferson Lab and Fermilab to coat single cell and multicell SRF cavities [34-36]. Nb_3Sn/Nb cavities fabricated by the Sn vapor diffusion technique at Jefferson Lab have shown a $Q_0 \geq 2 \times 10^{10}$ at 4 K before quenching at ≥ 15 MV/m for 1.3 GHz single cell cavities [37] and low field Q_0 of $\sim 3 \times 10^{10}$ [38] and maximum accelerating gradient up to 5 MV/m at 4 K for CEBAF 5-cell cavities [39]. Till now, the highest reported accelerating gradient of 24 MV/m at 4 K has been achieved for 1.3 GHz single cell cavities at Fermilab [40]. Several high frequency cavities (2.6 GHz and 3.9 GHz) coated by Nb_3Sn at Cornell University have shown some promising results [41]. Besides the cavity fabrication, the Sn vapor diffusion method was used to fabricate Nb_3Sn

film on small Nb substrates at Jefferson Lab, Fermilab and Cornell to study the growth properties and atomic level properties during the film nucleation and growth [42-46].

1.2.2. Thin Film Fabrication of Nb_3Sn on Small Substrates

Apart from the conventional Sn vapor diffusion method, several fabrication techniques have been applied to fabricate Nb_3Sn films on flat substrates. Nb_3Sn film was fabrication by codeposition of Nb and Sn in General Electric Research Laboratory, New York in 1964 [47] where Nb was deposited by evaporation from the molten tip of a Nb rod by electron bombardment and Sn was evaporated by resistance heating. The fabricated films had a superconducting critical temperature T_c up to 16.9 K. At Brookhaven National Laboratory in 1970s [48,49], Nb_3Sn on Nb was deposited by depositing thin film of Sn on Nb substrate by thermal evaporation then the Nb_3Sn film was formed by thermal diffusion. Perpeet et al. also fabricated Nb_3Sn on sapphire substrate by the Sn vapor diffusion method which is usually considered for Nb substrate [50]. A thick Nb film of ~2 μm thickness was sputtered on the sapphire substrate to provide enough Nb surface for the Sn diffusion. Then the film was transferred to a separate reaction chamber where the samples were annealed at 1100 °C for 5 h with background of Sn and $SnCl_2$. The films showed a critical temperature T_c = 18.0 K and a critical current density J_c of 5-6.5 MA/cm^2 at 4.2 K. Another approach was used at the National Institute for Nuclear Physics- Legnaro National Lab (INFN-LNL), Italy [51], where Nb was introduced into 99.99% molten liquid Sn for a short duration and further annealed outside a Sn bath. The process was also applied to fabricate a 6 GHz Nb_3Sn cavity. Other approaches to fabricate Nb_3Sn films are electrochemical deposition [52-56], bronze method [57], electroplating of Sn on Nb substrate followed by annealing [58], and magnetron sputtering [59-72].

An early report on the fabrication of Nb_3Sn films by magnetron sputtering from a stoichiometric target was published by Argonne National Lab in 1976 [59, 60]. Nb_3Sn thin films were fabricated by magnetron sputtering from a compressed powder stoichiometric target with a varying Ar pressure of 5 to 50 mTorr on polished sapphire substrates at a substrate temperature of 800 °C. The Sn composition of the films increased with the increased sputtering pressure. Though a maximum T_c of 18.3 K was achieved on the fabricated film, the sputtering process became more challenging than other processes to fabricate Nb_3Sn thin films because of leaching of Sn due to the heat generated in the plasma interface. The problem was overcome by replacing the compressed powder targets with a target made from Nb sheets which was overcoated with Sn and reacted to form ~40 μm thick Nb_3Sn target surface. The films deposited at constant substrate temperature of 800 °C and varied sputtering pressure from 5 to 50 mTorr revealed that the Sn composition varied with varying deposition pressure. The films deposited at the lower pressures had a broad transition width with multiple superconducting transitions. The multiple transition disappeared, and the transition width became narrower with increased sputtering pressure. The film's highest T_c was 18.3 K for a sputtering pressure of 40 mTorr and the superconducting properties degraded above this pressure. The residual resistivity ratio (RRR), measured from the ratio of the resistivity at 300 K to the resistivity at 20 K increased with increasing deposition pressure and reached about 5 for the films deposited at 40 and 50 mTorr. The powder mixture approach was also used at Pacific Northwestern National Lab to prepare the Nb-Sn and Nb-Sn-SnO_2 target to deposit Nb_3Sn and $Nb_3(SnO)$ [61]. The films deposited on stainless steel and Nb-Ti alloy substrate at room temperature had a fine-grained BCC phase of Nb with grain sizes from 10 to 100 nm. An A15 phase was formed after annealing at 750 °C for 24 h. Depositing Nb-Sn films from the single target at high substrate temperature above 700 °C also resulted in an A15

Nb_3Sn phase with a larger grain size. However, the T_c of the films deposited at higher temperature were 1 to 2 K lower than the films deposited at room temperature and annealed afterwards. Another approach to sputter Nb_3Sn films was taken by the Electrochemical Laboratory at Ibaraki, Japan in 1996 [62]. The sputtering targets were made by mixing Nb and Sn in a 3:1 ratio and then reacted by thermal diffusion at 950 °C under Ar environment to form single phase Nb_3Sn target. Thin films deposited by RF sputtering from the target showed amorphous structure which started crystallization after annealing at a temperature above 600 °C and showed mixed phases of Nb_3Sn, Nb_6Sn_5, and $NbSn_2$ with a surface of equiaxed grains. A T_c of 15.3 K was reported on the film annealed at 900 °C for 1 h. An approach of depositing at heated substrate was attempted instead of annealing after the coating. Though the films coated at a substrate temperature above 600 °C showed crystalline films of columnar grains, the superconducting T_c of the films were less than the T_c of the annealed films. The formation of Nb_3Sn by the reactive diffusion of sputtered Nb/Sn multilayers at high temperature was investigated by AT&T Bell Laboratories [63]. The experiments of Nb/Sn multilayers on oxidized Si and sapphire showed that, above 600 °C, the A15 Nb_3Sn structure starts to grow with Nb_6Sn_5 phase. The Nb_6Sn_5 phase disappeared above 800 °C and highest superconducting T_c of 17.45 K was observed on the film annealed at 850 °C. The method of multilayer sputtering was later adapted at INFN-LNL and Padua University in Italy to fabricate thin films on sapphire substrates [64,65]. The thickness of Nb films were kept 4.5 times the thickness of Sn films to obtain the desired stoichiometry of an A15 structure. To get this thickness, Nb films were deposited with a direct DC power of 880 W and Sn films were deposited with 126 W. The multilayered films were annealed further at 930 °C for forming Nb_3Sn through thermal diffusion. The X-ray

diffraction (XRD) patterns of the resulted films showed no evidence of the other phases of Nb-Sn and the films had a maximum T_c of 17.88 K with a ΔT_c of 0.02 K and *RRR* of 3.58.

Recently, Nb_3Sn films were fabricated by DC magnetron sputtering at CERN [66]. Nb_3Sn films of 1.5-2 μm thickness sputtered from a Nb-Sn stoichiometric target on oxygen-free electronic grade copper substrates to study the films properties to apply on copper cavities. Ar gas at a sputtering pressure range of 1×10^{-3} to 5×10^{-2} mbar and Kr gas at a sputtering pressure range of 3×10^{-4} to 3×10^{-2} mbar was used for the film growth to adjust the films composition. The effect of temperature during the film growth was studied in two ways. For the first process, the films sputtered at room temperature were annealed from 600 to 830 °C for a duration from 24 to 72 h to study the effect of annealing temperature. The annealing temperature in the experiment was limited to 800 °C to maintain the temperature below the melting temperature of copper. The films coated with this process had an atomic Sn composition of 21 to 27% depending on the sputtering gas pressure. The Sn composition of the coated films increased with the increase of Ar gas pressure whereas the Sn composition decreased with increasing Kr gas pressure. Annealing the film resulted in Sn reduction due to evaporation and the amount of the Sn loss strongly depended on the deposition parameters of the films. While the films deposited at up to 1×10^{-3} mbar had a very small amount of Sn loss due to evaporation, the films deposited above 5×10^{-2} mbar had lost most of the Sn from the film after annealing. Therefore, the superconducting A15 phase disappeared from the film. The XRD patterns of the as-deposited film at room temperature and a sputtering pressure of 1×10^{-3} mbar showed amorphous structure. The same film showed crystalline Nb_3Sn diffraction peaks after annealing under vacuum at 700 °C for 24 h. The annealing process also affects the surface morphology of the films; while the as-deposited films had irregular structure, the annealed films had surface with well-structured grains. Different

sputtering gases also played an important role on the surface morphology of the deposited film. While the films sputtered by Ar suffered multiple cracking after annealing, the films sputtered by Kr had a crack-free surface. For the second process, the films were deposited on a hot substrate to form Nb_3Sn during the deposition. The temperature range used for this experiment was 600 to 735 °C. The films deposited from these conditions had an atomic Sn composition of 19-25% depending on the Ar gas pressure. The XRD peaks revealed the Nb_3Sn diffraction peaks with crystallite size above 400 nm. The surface of the deposited films showed grain structure that is similar for both Ar and Kr sputtering gas. However, the morphology of the films varied with the varying gas pressure and the deposition temperature. The films deposited at higher temperature exhibited large grains due to the high adatom mobility. The films had a superconducting T_c up to 16 K with a transition width ranging between 0.4 to 5 K. Tan et al. fabricated Nb_3Sn thin films on copper substrates by co-sputtering method to study the feasibility of the process for fabricating Nb_3Sn thin film inside the copper cavity surface [67]. Since both the Nb and Sn are deposited simultaneously, the important parameter in the process is identifying the optimum deposition condition to reach the stoichiometric 24-26% Sn. To do that, the current applied at the Nb target was varied keeping the current at the Sn target constant to 0.1 A. The deposition took place at substrate temperature of 500 °C and the films were annealed later in a separate furnace at 650 and 750 °C for two different annealing durations of 2 and 30 h. While Nb_3Sn phases were identified from the X-ray diffraction pattern of some of the as-deposited films at 500 °C, all annealed films had the A15 phase. The surface of the fabricated films showed some random Sn rich islands throughout the films which became smaller in size with increased Nb deposition. The films showed superconducting transition due to Nb_3Sn with a maximum T_c of 12 and 15 K for the films annealed at 650 and 750 °C respectively. Nb_3Sn films were also fabricated by co-

sputtering at the Institute of Materials Science, Advanced Thin Film Technology of TU Darmstadt, Germany [68]. The deposition power of Nb and Sn targets were adjusted in several ratios at room temperature to obtain the stoichiometry required for the A15 phase. Then the suitable power ratios P_{Nb}:P_{Sn} of 5.25:1 was utilized to deposit thin films at different substrate temperatures from 260 to 435 °C. The deposited film stoichiometry was constant for different substrate temperatures. The XRD patterns of these films showed diffraction peaks due to Nb_3Sn for all films deposited at the temperature range. All films except the one deposited at 260 °C showed superconducting transition due to Nb_3Sn with a highest reported T_c of 15.06 K for the film fabricated at a substrate temperature of 410 °C. Since the increased power to the target material can transfer additional kinetic energy to the system, and can increase the species mobility, the effect of powers applied to the Nb and Sn targets was also studied at a constant power ratio of 5.25:1 and substrate temperature of 435 °C. The resulted films had a crystalline Nb_3Sn phase only with the largest crystallite size obtained on the films deposited at higher power (P_{Sn}:P_{Nb}~ 30 W:158 W). The measured T_c also reached the highest value of 16.31 K for this condition. This low processing temperature to fabricate Nb_3Sn thin films enables the possibility to apply this method on copper substrates without deforming the substrate. Beside the mentioned studies, recent Nb_3Sn research has been conducted on copper and sapphire substrates by magnetron sputtering at ASTeC, STFC Daresbury Laboratory, Warrington, UK [69], the Institute of Heavy Ion Physics, Peking University, Beijing 100871, China [70], ULVAC Inc. and KEK at Japan [71], and the Department of Materials Science and Engineering, University of Wisconsin-Madison, Madison, WI 53706, USA [72].

1.2.3. Magnetron Sputtering in SRF Cavity Fabrication

Magnetron sputtering has been successfully used to coat Nb films inside a copper cavity. CERN conducted DC magnetron sputtering of Nb onto Cu cavities in the large electron-positron collider (LEP) in 1980 [73]. The coated cavities at time showed a higher Q_0 (~3.5×10^9) than the bulk Nb cavities (~2.5×10^9) at low field [74]. DC magnetron sputtering was also used to deposit a few microns thick Nb inside 400 MHZ RF cavities used in the LHC at CERN [75]. The method was also applied to quarter wave resonators (QWR) used in the High Energy and Intensity-Isotope mass Separator On-Line facility (HIE-ISOLDE) at CERN [76]. The Acceleratore Lineare Per Ioni (ALPI) facility at INFN-LNL, Italy also applied sputtered Nb onto 160 MHz QWR resonators [77, 78]. Other facilities that used sputtered Nb on Cu cavities include Synchronous Light Source SOLEIL at Saclay Nuclear Research Centre, France [79], third harmonics superconducting passive cavities in ELETTRA and Swiss Light Source (SLS) at Saclay [80], and at the Institute of High Energy Physics (IHEP) and Institute of Modern Physics (IMP) in China [81, 82]. More recently, an emerging technology named high power impulse magnetron sputtering (HiPIMS) has been considered to improve the performance of Nb coated Cu cavities at Lawrence Berkeley National Laboratory, CERN, and Jefferson Lab [83-86].

Deambrosis et al. reported on a cylindrical magnetron sputtering system with Nb-Sn cathode for depositing Nb_3Sn films inside 6 GHz SRF cavities [8]. The reported system consists of a target made of both Nb and Sn and the cavity is connected to a substrate holder that can move up and down to deposit multilayer inside the cavity. The films deposited from had T_c of 17.3 K and ΔT_c of 0.13 K. Rossi et al. later reported RF results of the coated 6 GHz cavity [65]. The cavity was coated by moving it up and down for 5 h for each deposition and then the coated

cavity was annealed at 960 °C for 3 h inside a vacuum furnace maintain a base pressure of 1.5 × 10^{-9} mbar. The measured Q_L of the cavity at 4.2 K was 3 × 10^7.

1.3. Organization of the Dissertation

Magnetron sputtering is applied successfully in three possible ways: sputtering Nb_3Sn film from a single stoichiometric Nb_3Sn target, multilayer sputtering of Nb and Sn films followed by annealing at high temperature to form Nb_3Sn, and co-sputtering of Nb and Sn on heated substrate. Previously reported studies discussed the effect of deposition parameters (sputtering gas, sputtering pressure, substrate temperature, multilayer thickness, deposition ratio) and post-deposition processing parameters (annealing temperature, annealing time) on the structural and superconducting properties of the fabricated films. Though all three magnetron sputtering processes were studied at different research organizations, the properties of the fabricated films are difficult to compare with each other because of different substrate materials, coating parameters (deposition gas/pressure, substrate temperature, annealing temperature) as well as the differences in the deposition systems. This dissertation deals with a comparative study on the properties of films fabricated by all three processes from same deposition chamber on to substrates of identical properties. The main goal of the dissertation is to study the fabrication processes and characterize the properties of the films to understand the best condition that can be applied inside a Nb cavity. Therefore, Nb substrates were prepared from Nb sheets used in the SRF cavities and processed by following all the processing steps applied during the Nb cavity fabrication. The dissertation also reports the RF surface resistance of some of the fabricated films to understand the feasibility of applying magnetron sputtering for Nb_3Sn SRF cavity fabrication. Finally, it also discusses the recently designed and commissioned cylindrical magnetron sputtering system to fabricate Nb_3Sn thin film inside a 2.6 GHz SRF cavity.

Chapter 2 focuses on the experimental procedures of the thin film deposition and characterization of the fabricated films. Nb_3Sn films were fabricated in three different ways: from a single target, by multilayer sputtering of Nb and Sn, and by co-sputtering of Nb and Sn. The effects of different growth parameters on the structural, morphological, and superconducting properties of the fabricated films from the three processes are discussed in Chapters 3, 4, and 5, respectively. Chapter 6 gives the design of a cylindrical magnetron sputtering system to deposit Nb_3Sn films inside a 2.6 GHz RF cavity. Finally, Chapter 7 concludes the dissertation with a summary and prospects of the research.

CHAPTER 2

EXPERIMENTAL TECHNIQUES

2.1. Introduction

Thin film deposition methods can be categorized into two different methods, i.e., Physical Vapor Deposition (PVD) and Chemical Vapor Deposition (CVD). Films are formed by atoms directly transported from source (target material) to substrate through the gas phase in the first method, whereas the latter involves chemical reaction on the surface of the substrate materials. In PVD reactions the background gas is sometimes used to grow compounds, such as oxides and nitrides. Magnetron sputtering is one of the PVD methods that is widely used to deposit metallic and insulating thin films. This chapter discusses the basic sputtering phenomenon, the sputtering system used for the experiments and the characterization techniques used to study the deposited film properties.

2.2. Sputtering Phenomenon

Sputtering is conducted in a chamber containing ionized gas (a plasma) that generates ions, which bombard a target causing its sputtering. When a DC voltage is applied between two electrodes in an inert gas, a small current will initially flow due to the small number of charged carriers present in the gas. As the electrons are accelerated in the electric field, they gain enough energy to cause secondary ionization collisions, creating more electron-ion pairs. The resulted positive ions are accelerated towards the cathode. When the ion energy is high enough to cause secondary emission, secondary electrons are ejected from cathode and enter the surrounding plasma. The ejected electron can repeat the ionization process causing more positive ions to

strike the cathode surface. When the applied voltage is high enough, the ions generated by the secondary electrons also gain energy to generate other secondary electrons and charge multiplication takes place. At this point, breakdown occurs, and the discharge becomes self-sustaining. A simple schematic of the sputtering process is shown in Fig. 2.1. Energetic ions generated in a glow discharge plasma bombard the target material (cathode). Typically, an inert gas (e.g., Ar, Xe) is used to generate the plasma. The atoms from the target material are removed by the bombardment process, reach the substrate, and then condense on the substrate as a thin film. A thin film of the target atoms can be deposited by varying the deposition time.

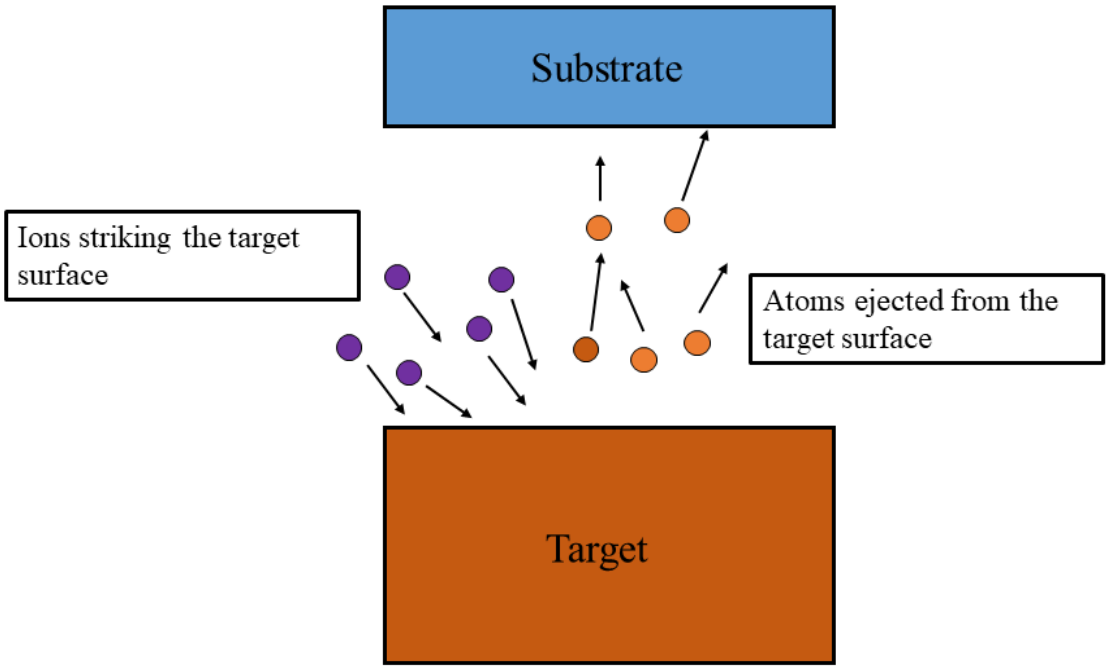

Fig. 2.1. Basic sputtering process.

Sputter yield S is the average number of atoms sputtered per incoming ion on target is expressed as [87]:

$$S = \frac{3\alpha}{4\pi^2} \frac{4M_{ion}M_{target}}{(M_{ion}+M_{target})^2} \frac{E_{ion}}{U_{sub}} \qquad (2.1)$$

Here, α is target-to-ion mass ratio, M_{ion} is the mass of incident ions, M_{target} is the mass of target atoms, U_{sub} is heat of sublimation of target material. Equation 2.1 is valid when the energy of incident ion energy $E_{ion} < 1$ keV. The sputter yield is proportional to ion energy and inversely proportional to sublimation energy of target material.

2.3. DC/RF Sputtering

DC sputtering is the most commonly used sputtering technique for metal targets. The basic configuration of a DC sputter system is shown in Fig. 2.2. The target and substrate are placed parallel to each other inside a vacuum chamber. The chamber is evacuated to a base pressure low to ~10^{-7} Torr to remove impurities from the chamber and then backfilled by sputtering gas (usually argon). The pressure of the chamber is controlled by a gate valve to ignite plasma. Typically, 0.5 mTorr to 100 mTorr sputter pressure is used in the sputtering process. A negative DC voltage is applied to the target from the DC power supply connected to the target. The Ar^+ ions accelerate to the cathode and sputter atoms from the target surface. The sputtered atoms reach the substrate to form a thin film of the target material.

DC sputtering is a cost-effective way to deposit conductive metal targets. In the DC sputtering process when plasma ions strike the target, the electrical charge in target is neutralized by positive charge. In dielectric targets (silicon oxide, aluminum oxide etc.), the neutralization process results in a positive charge on the surface of the target. At one point, the bombarding

ions are repelled due to this excessive positive charge and the deposition stops. To avoid this situation, RF sputtering is used where the polarity of the target is reversed by using a radiofrequency (RF)/AC voltage to attract enough electrons from plasma. During the negative electric field, the energetic positive ions accelerate to the cathode and sputter atoms from the targets. During the positive electric field, the positive ions accumulated to the top surface of the target are repelled back to the chamber and the sputtering process continues without any hindrance.

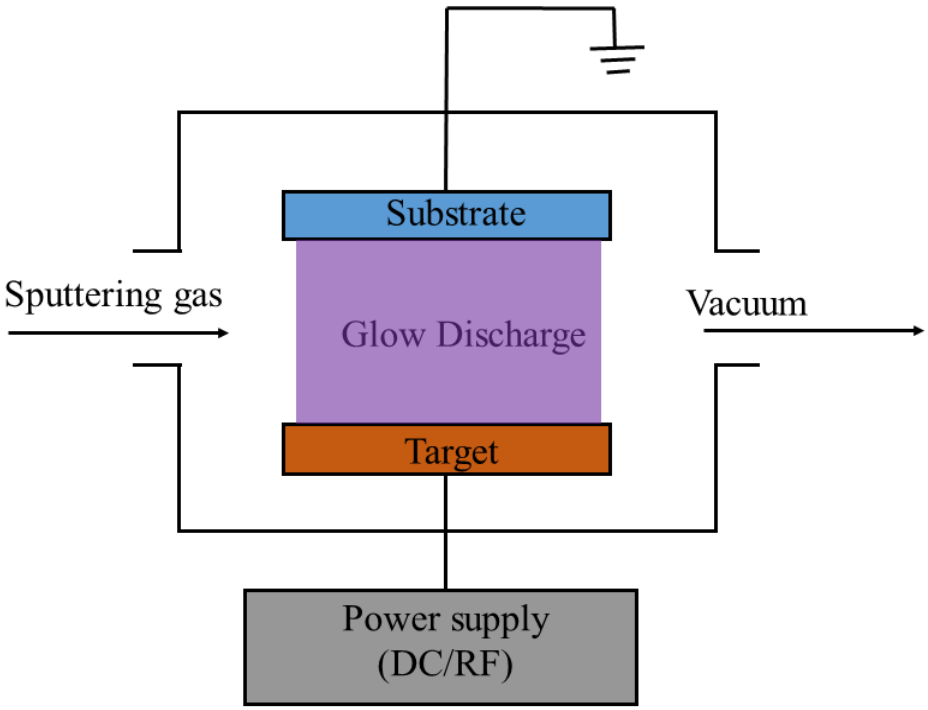

Fig. 2.2. Schematic diagram of DC/RF sputtering.

2.4. Magnetron Sputtering

Magnets are used behind the target to trap electrons by the magnetic field parallel to target surface, which significantly increases the plasma density near the target forming more ions and, therefore, enhancing the sputter rate. A basic arrangement of magnets is shown in Fig. 2.3. One pole is positioned at the central axis of the target whereas the magnets with other pole form a ring around the edge. Electrons are trapped in the magnetic field produced by the magnets with different polarities, which increase the probability of ionizing electron-atom collision. In this magnetron discharge, the deposition can be performed at lower sputtering pressure and lower operating voltages.

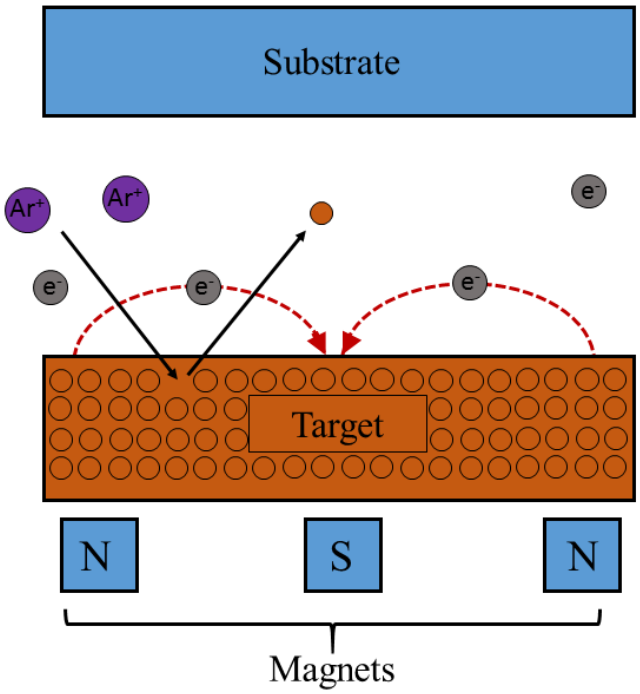

Fig. 2.3. Basic operation in magnetron sputtering process.

2.5. Experimental: Film Fabrication

2.5.1. Deposition Chamber

The sputtering system used is ATC Orion-5 sputter coater from AJA International. Fig. 2.4 shows the schematic of the deposition chamber. The chamber is equipped with three 2" magnetron sputter guns where the sputter targets are covered with shutters that are mechanically controlled by pressurized air. The chamber is equipped with a turbomolecular pump that can pump the chamber to ~10^{-8} Torr. A gate-valve is connected to the turbomolecular pump and is used to control the pressure inside the chamber during deposition. The substrate holder is placed from the top of the chamber and the distance between the substrate holder and the targets is ~100 mm. The sample holder can be rotated (0-40 rpm) to ensure uniform coating. Argon gas is used for sputtering and the gas flow rate is controlled by a mass flow controller (MFC). The sputtering chamber is equipped with one 750 W DC and two 300 W RF sputter guns.

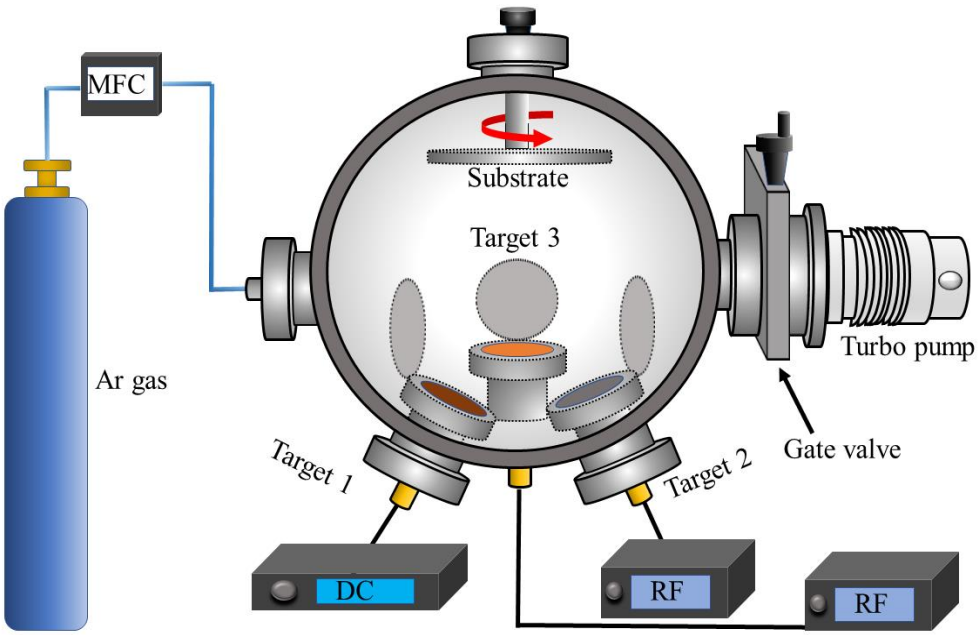

Fig. 2.4. Schematic of the sputtering chamber used for the experiments.

2.5.2. Sputtering Targets

The sputter targets were purchased from Kurt J. Lesker. The Nb targets were 99.95% pure and manufactured by electron beam melting, rolling, and annealing. The Sn targets were 99.999% pure. The stoichiometric Nb_3Sn target (99.9% purity) was made by co-evaporation from 2 sources. All these targets had a diameter of 2 inch and thickness of 0.25" to fit it in the magnetron guns.

2.5.3. Substrates

Sapphire substrates were used to grow films to measure the T_c and RRR of the films in addition to microstructural properties, and Nb substrates were used to study the film microstructural properties and surface resistance. The sapphire substrates were 430 μm thick and had double-side polished surface and C-M orientation (University Wafers Inc. part # 1251). The substrates were cleaned with ethanol and isopropanol and dried with N_2 gas flow before loading in the deposition chamber. The Nb substrates were 1 cm × 1 cm Nb cut from an Nb slice (Tokyo Denkai Co., Japan, *RRR* ~250) by wire electro-discharge machining and then buffered chemical polished (BCP 1:1:1) to remove 100 μm. The Nb substrates were baked at 800 °C for 2 h in a vacuum furnace operating at or below 10^{-5} Torr. A second BCP was applied to etch an additional 25 μm from the surface. Nb disks of 2-inch diameter were coated with Nb_3Sn following the same procedure and used for RF surface resistance measurement below and above T_c.

2.5.4. Furnace

The annealing is performed in a vacuum furnace that is separate from the sputtering system. The furnace is located at the Jefferson Lab and used for fabricating Nb_3Sn inside single cell and multicell SRF cavities by Sn vapor diffusion method. Details about the furnace chamber

were reported by Eremeev et al. [39]. The furnace temperature was raised from room temperature at a rate of 12 °C/min until the desired annealing temperature was reached. The films were annealed by maintaining the desired annealing temperature. After annealing for the desired duration, the heater was turned off and the samples were kept in vacuum to allow them to cool down gradually. The sample holder used in the furnace is made from Nb sheets and Nb foils to avoid contamination.

2.6. Experimental: Film Characterization

2.6.1. Structural and Morphological Properties

The crystal structures of the films were studied by X-ray diffraction (XRD, Miniflex II, Rigaku, Japan) using a CuKα radiation (λ =1.54056 Å). The XRD patterns of the films obtained before and after the annealing process and the diffraction peaks of the as-deposited and annealed films were compared to understand Nb_3Sn formation after annealing. The average crystallite size of different diffraction orders was calculated from the peak broadening by using Scherrer's equation [88]:

$$D = \frac{K\lambda}{B\cos\theta} \qquad (2.2)$$

Where K is shape factor, λ is the wavelength of the incident X-ray wavelength, B is full width at half maximum (FWHM) of the diffraction peak in radian, Θ is the diffraction angle.

The lattice parameter was calculated from [88]:

$$\frac{1}{d^2} = \frac{h^2+k^2+l^2}{a^2} \qquad (2.3)$$

where *d* is the lattice spacing, *a* is lattice parameter, and *h,k,l* are Miller indices representing the crystal plane.

The optical image of the film surface was observed by a HIROX RH-2000 high resolution digital video microscope. The film morphology was observed by field-emission scanning electron microscopic images (FESEM S-4700, Hitachi, Japan). After each experiment, SEM images were collected on the films at multiple magnifications (×5, ×10, ×25, ×50, ×75, ×100) to examine the film morphology closely. A Noran 6 energy dispersive X-ray spectroscopy (EDS) detector connected to a Jeol JSM 6060 LV scanning electron microscope was used to measure the surface composition. EDS was performed using 15 kV accelerating voltage on a surface covering ~1.2 mm^2 area at five randomly selected regions of each sample. The X-ray transmission fraction for Nb-Lα, and Sn-Lα lines estimated from the Anderson-Hasler equation is 0.68 μm and 0.76 μm respectively for 15 keV electrons [89]. The high-resolution transmission electron microscopy (HRTEM) images of the film cross-sections were obtained by a ThermoFisher Titan 80-300 probe aberration corrected scanning transmission electron microscope (STEM). The cross-sectional films for TEM were prepared by focused ion beam (FIB) sectioning using Thermofisher Quanta 3D FEG.

Raman spectra of the films were obtained using a Renishaw inVia Raman microscope and spectrometer. The excitation source was an Ar laser at 514 nm wavelength. The laser spot has 2.5 μm diameter at its focal point. The Raman spectra was recorded at three different spots of each sample and compared with the Raman spectra of Nb, Nb_3Sn, and oxides of Nb found in literature.

The surface roughness of the samples was measured by a Dimension 3100 Atomic Force Microscope (AFM) from Veeco. The tip used for AFM is made of monolithic silicon and have a tip radius <10 nm, force constant of 40 N/m, and resonant frequency of 300 ± 100 kHz. AFM was collected on the selected samples using tapping mode at different scan sizes (2 μm ×2 μm, 5 μm ×5 μm, 10 μm ×10 μm, 20 μm ×20 μm) depending on the grain sizes of the fabricated films. The root mean squared (RMS) roughness and the peak-to-valley height differences throughout the films were calculated by processing the AFM images using Nanoscope Analysis version 2.0 image processing software.

2.6.2. Superconducting Properties

2.6.2.1. DC Superconducting Properties

The superconducting critical temperature T_c and the transition width ΔT_c of the films were measured by the four-point probe method down to ~2 K. The measurement system maintained an isothermal environment using calibrated Cernox thermometers with temperature resolution less than 50 mK [90]. The T_c and ΔT_c of the films were calculated from [91]:

$$T_c = \frac{T^{90} + T^{10}}{2} \qquad (2.4)$$

$$\Delta T_c = T^{90} - T^{10} \qquad (2.5)$$

where T^{90} and T^{10} represent the temperature where the resistivity of the film is 90% and 10% of the resistivity during transition. The residual resistivity ratio *RRR* of the films was calculated from [60]:

$$RRR = \frac{\rho_{300}}{\rho_{20}} \quad (2.6)$$

where ρ_{300} and ρ_{20} are the film resistivity at 300 and 20 K, respectively.

2.6.2.2. RF Superconducting Properties

The RF surface resistance of the Nb_3Sn films coated on 2-inch Nb disks were measured inside the surface impedance characterization (SIC) system at Jefferson Lab which is a 7.4 GHz sapphire-loaded Nb cavity described in [92]. The sample-loaded cavity was placed inside a dewar supplying liquid He at a pressure of 23 Torr to maintain a temperature of 2 K at the cavity surface. The sample placed inside the cavity was thermally isolated from the cavity and connected to a calorimeter. Therefore, the temperature on the sample can be varied by conducting heat via the calorimeter, while the cavity still is at 2 K. The sample temperature was varied from 2 to 22 K, which is a sufficient range to measure the transition due to both Nb (T_c = 9.23 K) and Nb_3Sn (T_c = 18.3 K). Cernox thermometers with a sensitivity of 50 mK were connected at the back of the substrates to measure the temperature.

The transition temperature of the sample was measured from the loaded quality factor Q_L of the cavity as a function of sample temperature using Agilent's FieldFox N9915A network analyzer. The loaded quality factor was estimated by 3 dB technique using the following formula [93]:

$$Q_L = \frac{f_0}{|f^{+(-3dB)} - f^{-(-3dB)}|} \quad (2.7)$$

where, f_0 and $f^{(-3dB)}$ are the resonant frequency of the cavity and the half-transmitted power frequency, respectively.

The SIC system implements power compensation technique to measure the RF surface resistance of the film. The temperature of the sample under investigation was controlled by a heater which is placed underneath the sample holder, while the whole cavity remained typically at 2 K. The heater keeps the sample temperature constant when an RF field is applied. Power dissipated into the film surface due to the RF field can be calculated from the difference of the heater power needed to keep the sample at constant temperature with or without the RF field [94]:

$$P_{RF}\left(H_{peak}T_{sample}\right) = P_{heater}^{H=0;T=T_{sample}} - P_{heater}^{H=H_{peak};\ T=T_{sample}} \quad (2.8)$$

Finally, RF surface resistance R_{RF} of the film was measured from the dissipated power by [94]:

$$R_{RF}\left(H_{peak}T_{sample}\right) = \frac{P_{RF}\left(H_{peak}T_{sample}\right)}{k \cdot H_{peak}^2} \quad (2.9)$$

where, K is a geometry dependent constant found with numerical simulations [93,94] and H_{peak} is the peak magnetic field on the film surface.

CHAPTER 3

NB_3SN FABRICATION BY SPUTTERING FROM A SINGLE TARGET

3.1. Introduction

Nb_3Sn films were fabricated by sputtering from a single stoichiometric Nb_3Sn target. Early successful fabrication of Nb_3Sn films by magnetron sputtering from a stoichiometric target was performed at Argonne National Lab [59, 60]. In these studies, Nb_3Sn films were grown on sapphire and the superconducting properties of the films were examined for films grown at various sputter argon background pressures of 5 to 50 mTorr and substrate temperatures of 600 to 800 °C. The reported T_c and critical current density of the grown films were up to 18.3 K and 15×10^6 A/cm^2, respectively [60]. Nb_3Sn films sputtered from a single phase Nb_3Sn target on MgO substrates had a T_c of 15.3 K after annealing at 900 °C for 1 h [62]. Recently, Nb_3Sn sputtered on Cu substrates were studied for its application in SRF cavities at CERN, Peking University, and STFC [66,67,69]. The highest T_c of 15.5 K was reported by Ilyina et al. for a film deposited at an Ar pressure of 5×10^{-2} mbar and annealing at 750 °C for 24 h [66].

I report on the properties of Nb_3Sn film grown on Nb and sapphire by magnetron sputtering from a single stoichiometric Nb_3Sn target. The main goals of this experiment are to investigate the film structural, morphology, chemical composition, and correlate these material properties with superconducting DC and RF properties of the Nb_3Sn films. I report on the properties of Nb_3Sn films grown on sapphire and determine the deposition conditions leading to films with highest T_c. Then, these conditions were followed in depositing Nb_3Sn on Nb substrates.

3.2. Design of Experiment

Fig. 3.1 shows the schematic of the sputtering process used. The Nb_3Sn target was purchased from Kurt J. Lesker. The sample chamber was evacuated by a turbomolecular pump to low 10^{-7} Torr before deposition. Deposition was done at 3 mTorr Ar background pressure at a flow rate of 20 SCCM using at a constant magnetron current of 150 mA. The substrate holder was rotated at 30 rpm during the deposition to ensure uniform coating. During the deposition, the substrates were heated at ~800 °C using a quartz heater.

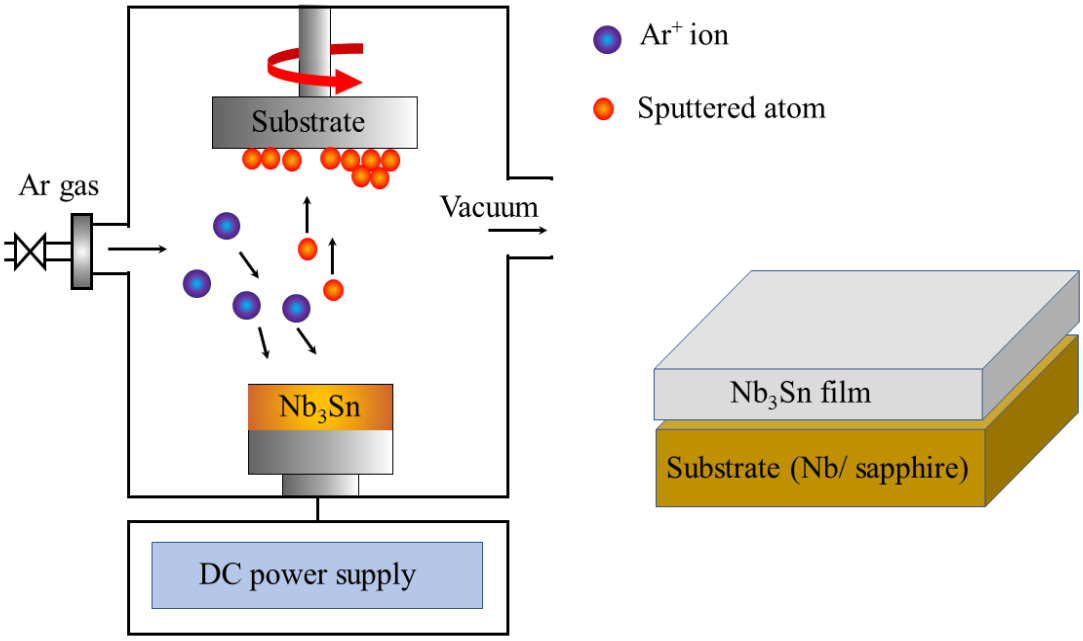

Fig. 3.1. Schematic diagram of the sputtering from a single Nb_3Sn target and the deposited film.

Samples sputtered on sapphire were deposited for 6 h, while samples sputtered on Nb were deposited for 14 h, all under the same magmetron operating current, the same Ar

background pressure, and fixed target-to-substrate disctance of 10 cm. The coated samples were removed from the sputter coater and then annealed at different temperatures and different annealing durations in a separate vacuum furnace. The pressure during the annealing was ~10^{-6} Torr and an annealing ramp rate of 5 °C/min was used.

3.3. Results

3.3.1. Nb_3Sn Deposited on Sapphire

3.3.1.1. Film Structure, Morphology, and Composition

Fig. 3.2 shows the XRD patterns of the as-deposited film and films annealed at different temperatures for 24 h. As-deposited films show both Nb and Nb_3Sn diffraction peaks. The Nb peaks disappeared when the film is annealed at 800 and 900 °C. However, a few Nb peaks reappeared when the film was annealed at 1000 °C for 24 h. For films annealed at 800 and 900 °C, the Nb_3Sn peak intensity became stronger, indicating better crystallinity. At an annealing temperature of 1000 °C, Sn evaporation resulted in weak Nb_3Sn diffraction peaks indicating the decomposition of the Nb_3Sn, which is accompanied by the appearance of intense Nb peaks.

An expanded view of the diffraction patterns taken for 2θ of 45-75° are shown in the inset of Fig. 3.2. The Nb_3Sn (222), (320), (321), (400) diffraction peaks are observed. The peak intensity increased with the annealing temperature for annealing at 800 and 900 °C, then decreased for annealing at 1000 °C. The XRD pattern of the film annealed at 1000 °C for 24 showed diffraction peaks corresponding to Nb (110), (200), (211) and (220). All annealed films showed two diffraction peaks near 2θ of 37° and 78° that are either due to the presence of the Nb_6Sn_5 or $NbSn_2$.

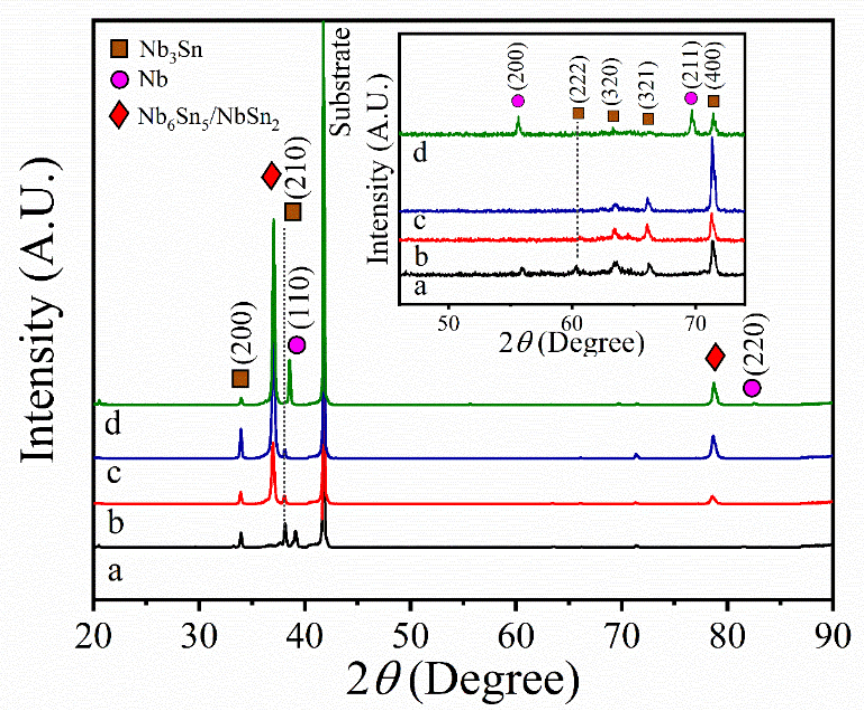

Fig. 3.2. XRD patterns of as-deposited and annealed films on sapphire substrate [95]. Condition a, b, c, and d represent as-deposited film, and annealed films at 800, 900, and 1000 °C for 24 h, respectively.

The Raman spectra of the as-deposited films and films annealed for 24 h are shown in Fig. 3.3. The peaks were compared to previously reported Raman spectra of Nb_3Sn, Nb, Nb_2O_5, and NbO_2 [96-101]. The as-deposited film shows a wide Raman peak with its maximum at 189 cm^{-1}. This wide peak can be deconvolved into peaks at 134, 159, and 189 cm^{-1}. The peaks at 134 and 189 cm^{-1} are close to the Raman lines assigned to the F_{2g} and E_g phonon modes of Nb_3Sn, respectively, as reported by Schicktanz et al. [97]. The E_g optical phonon mode occurs in *A*15 compounds due to transition metal atoms that are lined up in chains, moving against each other along the chain. The wavelength of this mode was shown to shift with temperature [97]. In this dissertation's results, the peak at 189 cm^{-1} became stronger and shifts to 186 cm^{-1} with annealing at 800 °C for 24 h. The peak shift from 189 to 186 cm^{-1} is too small to make any conclusion

about it but the relief of residual stress in the film is known to cause Raman peak wavelength shift.

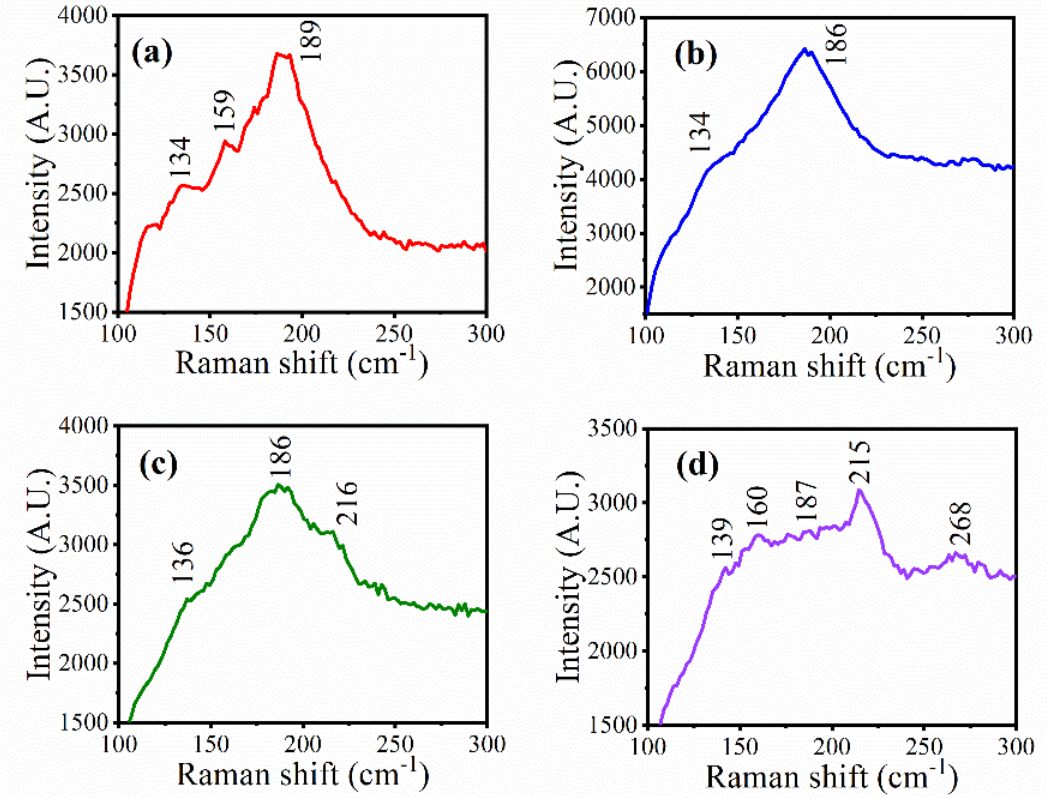

Fig. 3.3. Raman spectra of Nb_3Sn films on sapphire: (a) as-deposited, (b) annealed at 800 °C for 24 h, (c) annealed at 900 °C for 24 h, (d) annealed at 1000 °C for 24 h [95].

The F_{2g} peak at 134 cm^{-1} was suggested to be either due to an allowed mode in the *A*15 structure or due to defect-induced scattering [97]. The peak at 159 cm^{-1} was previously observed in a near stoichiometric Nb_3Sn and was proposed to be possibly due to tetragonal micro-domains that are too small in size to be observable in the obtained XRD patterns of Nb_3Sn, suggesting that Raman could be more sensitive than XRD in detecting micro-domain structures [97]. As the

film is annealed to 900 °C, the peak at 186 cm^{-1} is reduced in intensity and an additional peak at ~216 nm appears. The peak at 216 cm^{-1} is close to the reported peak position of NbO_2 [98] and could be a result of the decomposition of some grains of Nb_3Sn exposing Nb to the surface which is oxidized as the sample is exposed to air. This hypothetic is consistent with the reduction in Nb_3Sn XRD peak intensity as the film is annealed at 900 °C compared to that annealed at 800 °C, as shown in Fig. 3.2. For films annealed at 1000 °C for 24 h, the Nb_3Sn peak at 186 cm^{-1} (observed in Fig. 3.3 (d)) at 187 cm^{-1}) becomes small, due to decomposition of the Nb_3Sn and the of NbO_2 peak at 215 cm^{-1} becomes the strongest peak. Two more peaks at 160 and 268 cm^{-1} appeared as the film is annealed at 1000 °C for 24 h. These two peaks correspond to Nb_3Sn [30] and Nb [99] respectively. The result is in agreement with the XRD data as both Nb and Nb_3Sn diffraction peaks are seen for films annealed at 1000 °C for 24 h. These results, while preliminary, point out that Raman is a powerful tool to study microstructural properties of Nb_3Sn films.

The SEM micrograph of the surface of as-deposited and annealed films are shown in Fig. 3.4. The thickness of the as-deposited films after 6 h coating was ~ 350 nm, as estimated from the cross-sectional SEM image (inset of Fig. 3.4 (a)). The surface of the as-deposited films consists of uniformly distributed 50-150 nm grains with some randomly distributed ~200-300 nm agglomerated clusters. The regular grains had ~27 At. % of Sn, whereas the clusters showed ~30 At. % of Sn, as detected by EDS. These values show that the clusters are Sn-rich, but the reported values are affected by the penetration of the EDS electron beam to deeper layers. As the films were annealed at 800, 900 and 1000 °C for 24 h, the grain size increased. Meanwhile, voids appeared on the surface (black regions in Fig. 3.4 (b)), which appear to be formed during Sn evaporation from the clusters on the surface. EDS analysis of the clusters showed ~19% Sn after

annealing at 800 °C for 24 h, whereas regular grain area of the annealed film had ~21% Sn. The films had randomly distributed Sn rich particles on top of the grains. These particles are formed after Sn evaporation from the Sn rich clusters.

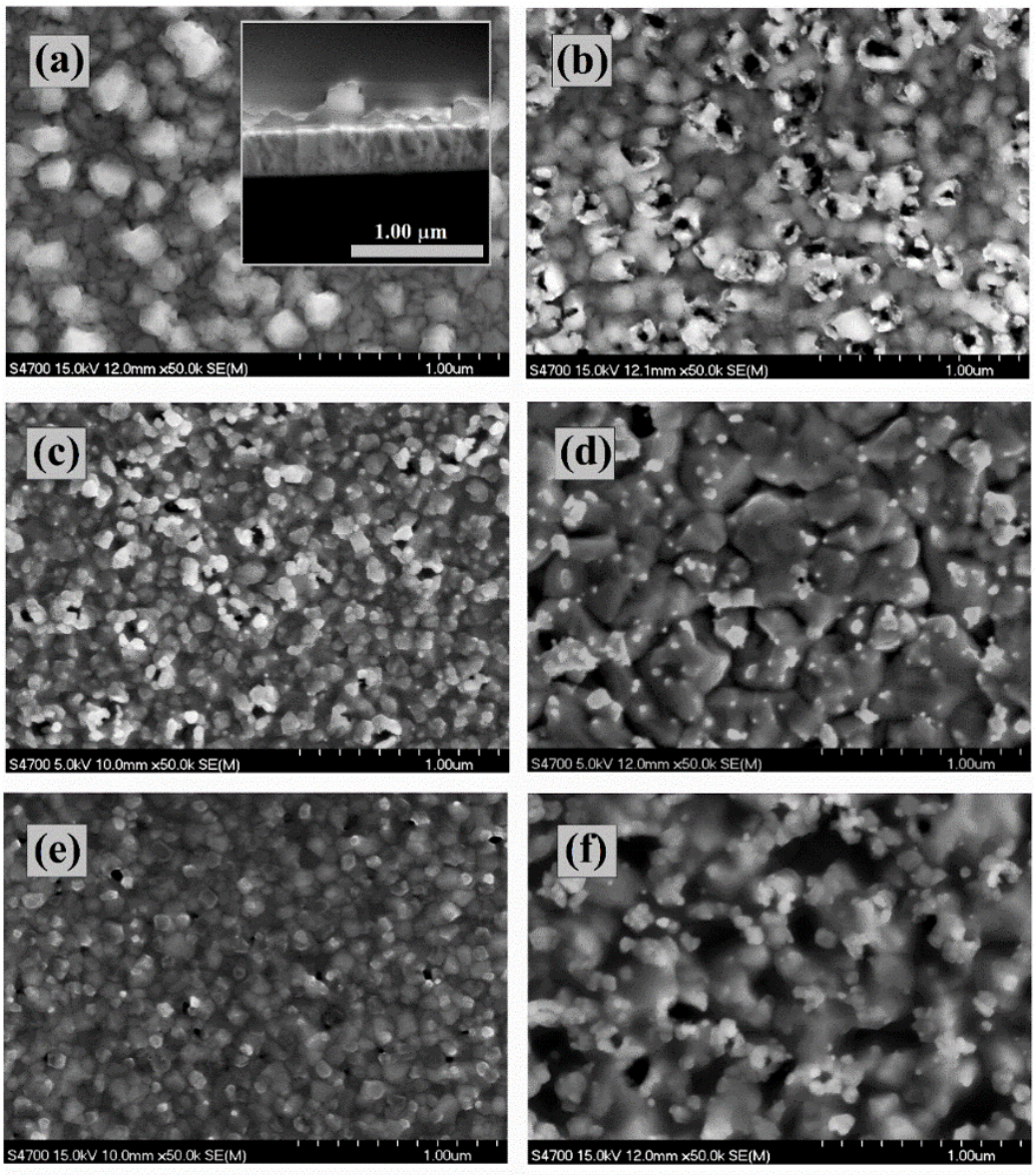

Fig. 3.4. SEM images of the surface of Nb_3Sn films deposited on sapphire: (a) as-deposited, (b) annealed at 800 °C for 24 h, (c) annealed at 900 °C for 24 h, (d) annealed at 1000 °C for 1 h, (e) annealed at 1000 °C for 12 h, and (f) annealed at 1000 °C for 24 h. The inset of (a) shows the cross-section of the as-deposited film [95].

The development of Sn particles from Sn-rich clusters after annealing at 800-1000 °C for 24 h can be observed from Fig. 3.4 (a)-3.4 (d). Fig. 3.4 (e) and 3.4 (f) show the surface of films annealed at 1000 °C for 1, and 12 h, respectively. The film annealed for 1 h had grains of ~100-150 nm diameter with some Sn particles. As the annealing time was increased to 12 h, the grain size as well as the Sn particle distribution increased (Fig. 3.4 (f)).

The film composition plays an important role on the superconducting property of Nb_3Sn. Fig. 3.5 shows the Sn composition of ~350 nm thick films with annealing temperature and time, as measured by EDS. The as-deposited films had atomic Sn composition of ~26.1 ± 0.5%, which is consistent with the target composition of ~27% measured prior to target placement in the sputter coater. For the annealing temperature of 1000 ^{o}C, the Nb_3Sn decomposes, and Sn evaporates from the surface.

I have observed large Sn loss when the film was annealed at 1000 °C for 24 h, with the Sn atomic composition reduced to ~4.1 ± 0.4%. Sn loss during annealing was also observed on Nb_3Sn films grown by multilayer sequential sputtering [102]. The amount of Sn loss depends on both annealing temperature and annealing time. For the annealing temperature of 1000 °C, the Sn composition of the film was 11.3 ± 0.3 % for 12 h annealing time, and ~21.0 ± 0.6% when the film was annealed for just 1 h.

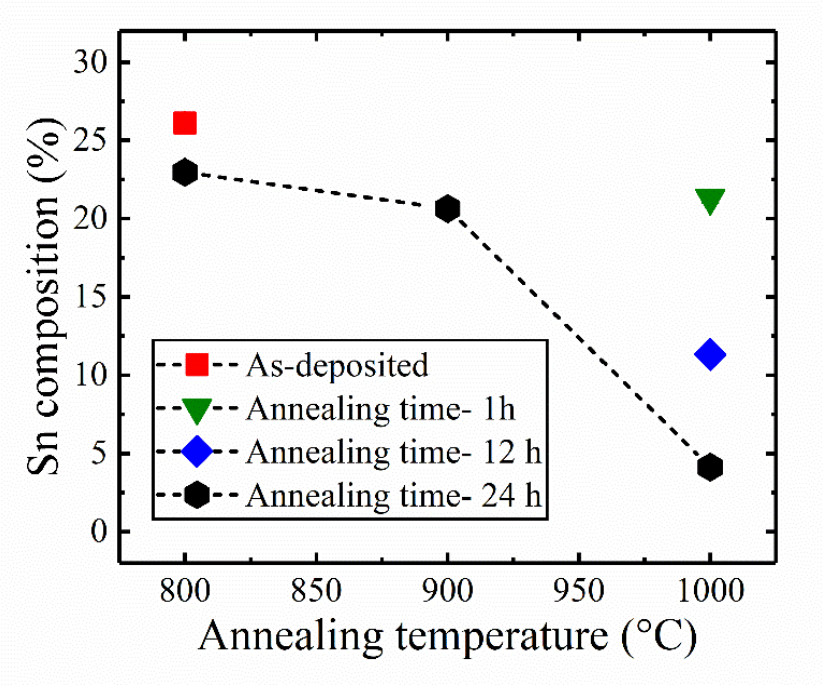

Fig. 3.5. Sn atomic composition of the Nb_3Sn films deposited on sapphire [95]. The red square is for the sample deposited at 800 °C. The substrate heater was turned off right after deposition. The black hexagons are for films deposited at 800 °C then annealed for 24 h. The blue diamond and green triangle are for films annealed at 1000 °C for different times.

The AFM images of the films are shown in Fig. 3.6. The clusters observed in the SEM image of as-deposited films are more clearly observed in the AFM images. The lateral sizes of the clusters were ~300 nm, which is an agreement with that observed in the SEM images. The heights of the clusters were ~80-120 nm. The size and height of the regular grains increased after annealing whereas the clusters height did not change. As the films were annealed, the atoms gained enough activation energy to occupy the lower energy sites of crystal lattice to form large grains [103, 104].

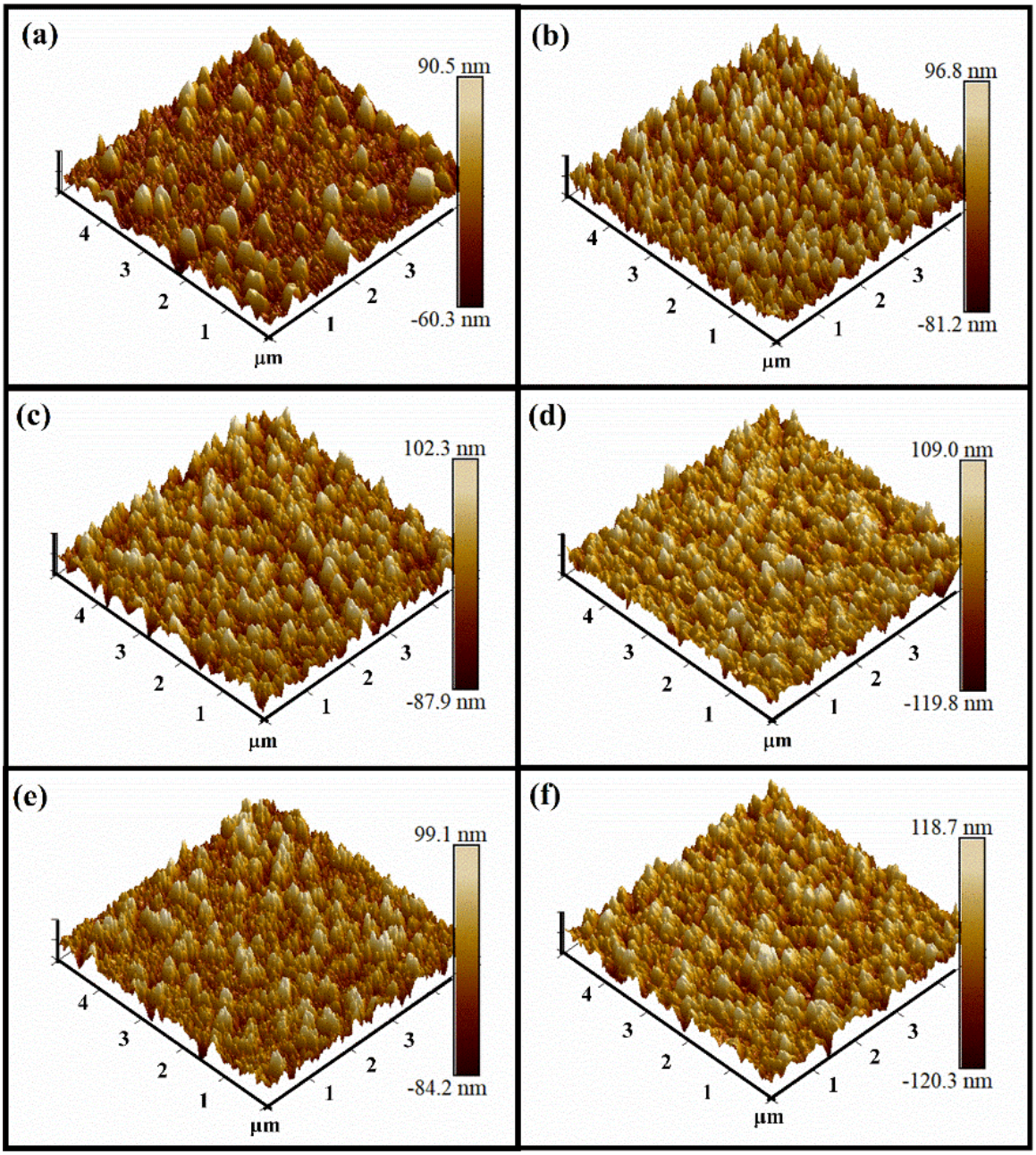

Fig. 3.6. AFM images of (5µm × 5 µm) scan size of Nb_3Sn films on sapphire: (a) as-deposited, (b) annealed at 800 °C for 24 h, (c) annealed at 900 °C for 24 h, (d) annealed at 1000 °C for 24 h, (e) annealed at 1000 °C for 1 h, and (f) annealed at 1000 °C for 12 h [95].

Fig. 3.7 shows RMS roughness obtained by averaging three different areas with error bars representing the standard deviation of measurements. The RMS roughness of the as-deposited films is ~20.2 ± 0.8 nm. The roughness of the films increased to ~ 29.7 ± 1.2 nm when the film was annealed at 800 °C for 24 h. Annealing at 900, and 1000 °C for 24 h increased roughness to 30.0 ± 0.4 and 32.2 ± 0.7 nm respectively. Films annealed at 1000 °C for 1, 12, and 24 h show increased roughness with annealing time with most increase in roughness occurring after 1 h of annealing.

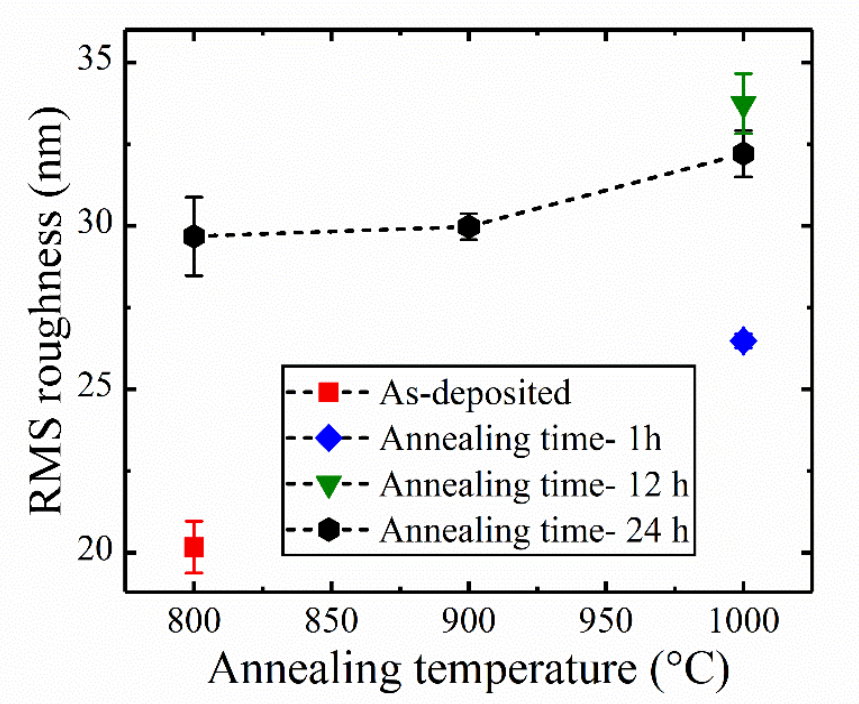

Fig. 3.7. RMS surface roughness of Nb_3Sn films on sapphire [95]. The error bars represent the standard deviation of different measurements.

3.3.1.2. DC Superconducting Properties

Fig. 3.8(a) shows the film resistance with temperature for as-deposited films and films annealed at 800, 900, and 1000 °C for 24 h, while Fig. 3.8(b) shows the resistance with temperature for films annealed at 1000 °C for 1, 12, and 24 h. All films except the one annealed at 1000 °C for 24 h showed the superconducting transition of Nb_3Sn. The measured T_c, ΔT_c, and *RRR* of the films are given in Table 3.1 along with the EDS measurement of Sn atomic % and AFM measurement of surface RMS roughness. The critical temperature T_c of the as-deposited film was 17.21 K. T_c increased with annealing at 800 °C for 24 h reaching 17.83 K. Increasing the annealing temperature to 900 °C while keeping the annealing time 24 h resulted in a film with T_c = 17.66 K. For films annealed at 1000 °C, the Sn composition decreased with increased annealing time, consequently degrading the films's superconducting properties. For the film annealed at 1000 °C for 24 h, the resistance starts to drop near 17.7 K (position A in the inset of Fig. 3.8(a)) and a sharp drop of resistance is observed near 9 K (position B in the inset of Fig. 3.8(a)). This behavior is due to the superconding transitions of Nb (T_c ~9.23 K) and Nb_3Sn (T_c ~18.3 K) present in the film. The transition width increased with increased annealing temperature and time. Based on the measured data, high quality superconducting films can be obtained with annealing at 800-900 °C for 24 h or annealing at 1000 °C for 1 h.

The residual resivity ratio *RRR* calculated from the resistance at 300 and at 18 K is given in Table 3.1. The as-deposited film had a *RRR* value of 2.53. The highest *RRR* value of 5.41 was observed on the film annealed at 800 °C for 24 h. Further increase in annealing temperature reduced the *RRR* of the film. For the annealing temperature of 1000 °C, the *RRR* was reduced from 3.01 to 2.07 when the annealing temperature was increased from 1 to 24 h.

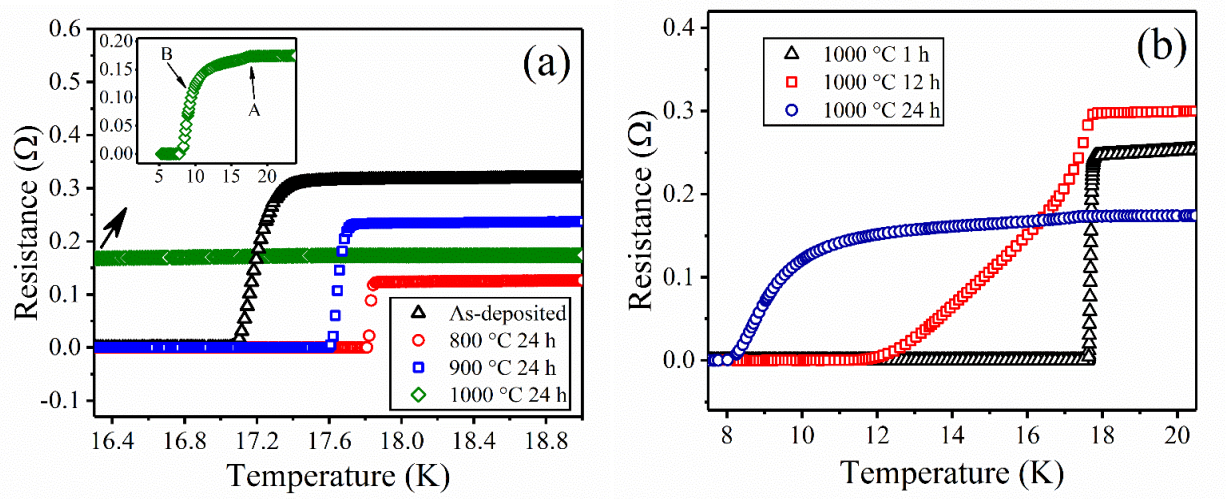

Fig. 3.8. (a) Nb_3Sn film resistance with temperature of as-deposited film and films annealed at three different temperatures for 24 h, the inset of shows the transition region of film annealed at 1000 °C for 24 h, (b) resistance versus temperature of films annealed at 1000 °C for 1, 12, and 24 h [95].

Table 3.1. Film properties of as-deposited and annealed films on sapphire substrate. The films were coated at 800 °C coating temperature for 6 h.

Annealing temperature (°C)	Annealing time (h)	Sn composition (%)	RMS roughness (nm)	T_c (K)	ΔT_c (K)	*RRR*
---	---	26.1 ± 0.5	20.2 ± 0.8	17.21	0.18	2.53
800	24	23.0 ± 0.3	29.7 ± 1.2	17.83	0.03	5.41
900	24	20.6 ± 0.4	30.0 ± 0.4	17.66	0.06	4.36
1000	1	21.0 ± 0.6	26.5 ± 0.2	17.68	0.06	3.01
1000	12	11.3 ± 0.3	33.7 ± 0.9	15.74	3.61	2.13
1000	24	4.1 ± 0.4	32.2 ± 0.7	10.95	4.69	2.07

3.3.2. Nb_3Sn Deposited Nb

3.3.2.1. Film Structure, Morphology, and Composition

The X-ray diffraction patterns of the Nb_3Sn films grown on Nb substrates are shown in Fig. 3.9. The XRD peaks due to the Nb substrate is shown in Fig. 3.9 (a). All films showed diffraction patterns for Nb_3Sn with no diffraction peaks corresponding to Nb_6Sn_5 or $NbSn_2$ detected. The peak intensity of the (210) and (211) diffraction order increased relative to the (200) diffraction order after annealing. A few intense Nb diffraction peaks are observed due to the Nb substrate. The crystallite size of (200), (210), and (211) diffraction order estimated from the Scherrer equation are shown in Fig. 3.9(e). The crystallites increased in a narrow range from 32 to 41 nm after annealing.

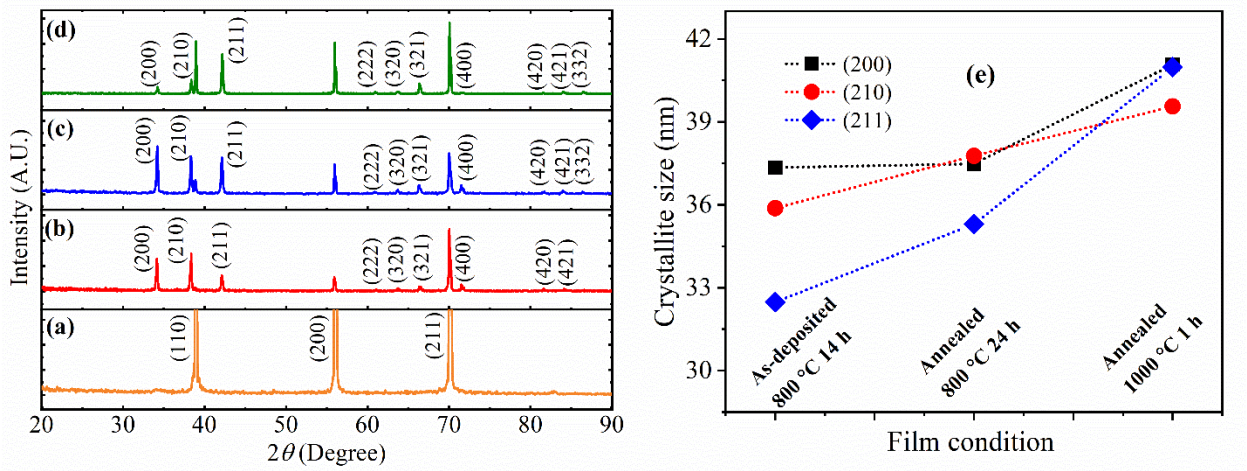

Fig. 3.9. (a-d): XRD patterns of (a) Nb substrate, (b) as-deposited film, (c) film annealed at 800 °C for 24 h, and (d) film annealed at 1000 °C for 1 h, (e) crystallite size of different crystal planes of the as-deposited and annealed films [95].

Fig. 3.10 shows the optical microscope and SEM images of Nb_3Sn films on Nb. Similar to the Nb_3Sn films deposited on sapphire, the films on Nb substrates also have scattered clusters

on the surface. The distributions of these clusters depend on the grain orientation of the Nb substrate. As seen in Fig 3.10(a) and 3.10(d), the cluster concentration has a strong grain orientation preference. The clustered density was reduced after annealing as observed in the optical and SEM images in Fig. 3.10(a-f). The grain size and shape of the as-deposited films differed from that of the annealed films. As seen from Fig. 3.10(g-i), as-deposited films had faceted small grains, whereas the annealed films showed rounded grains with increased grain size.

To estimate the Sn composition on the regular and clustered grains, EDS spot analysis was performed on the films. Fig. 3.11 shows the spot analysis of as-deposited film. Both regular and clustered grains had similar Sn composition of ~ 23-24.5 %. For films annealed at 800 °C for 24 h, the Sn atomic % on the clustered grain was ~23.6 %, whereas for regular grain area was ~22.7 %. For the films annealed at 1000 °C for 1 h, Sn composition on clustered and regular grains were ~21.2 % and ~21.6 %, respectively. The overall Sn atomic % on the 1.2 mm^2 surface area were ~22.3 ± 0.3 % for the as-deposited film, 22.9 ± 0.7 % for the film annealed at 800 °C for 24 h, and 22.4 ± 0.2 % for the film annealed at 1000 °C for 1 h. However, the spatial resolution of SEM EDS is limited and cannot give the accurate Sn composition throughout the whole cross-section. The TEM EDS obtained from the cross-section of the film confirmed that, the clusters have ~40% Sn whereas the regular grains have ~22% Sn.

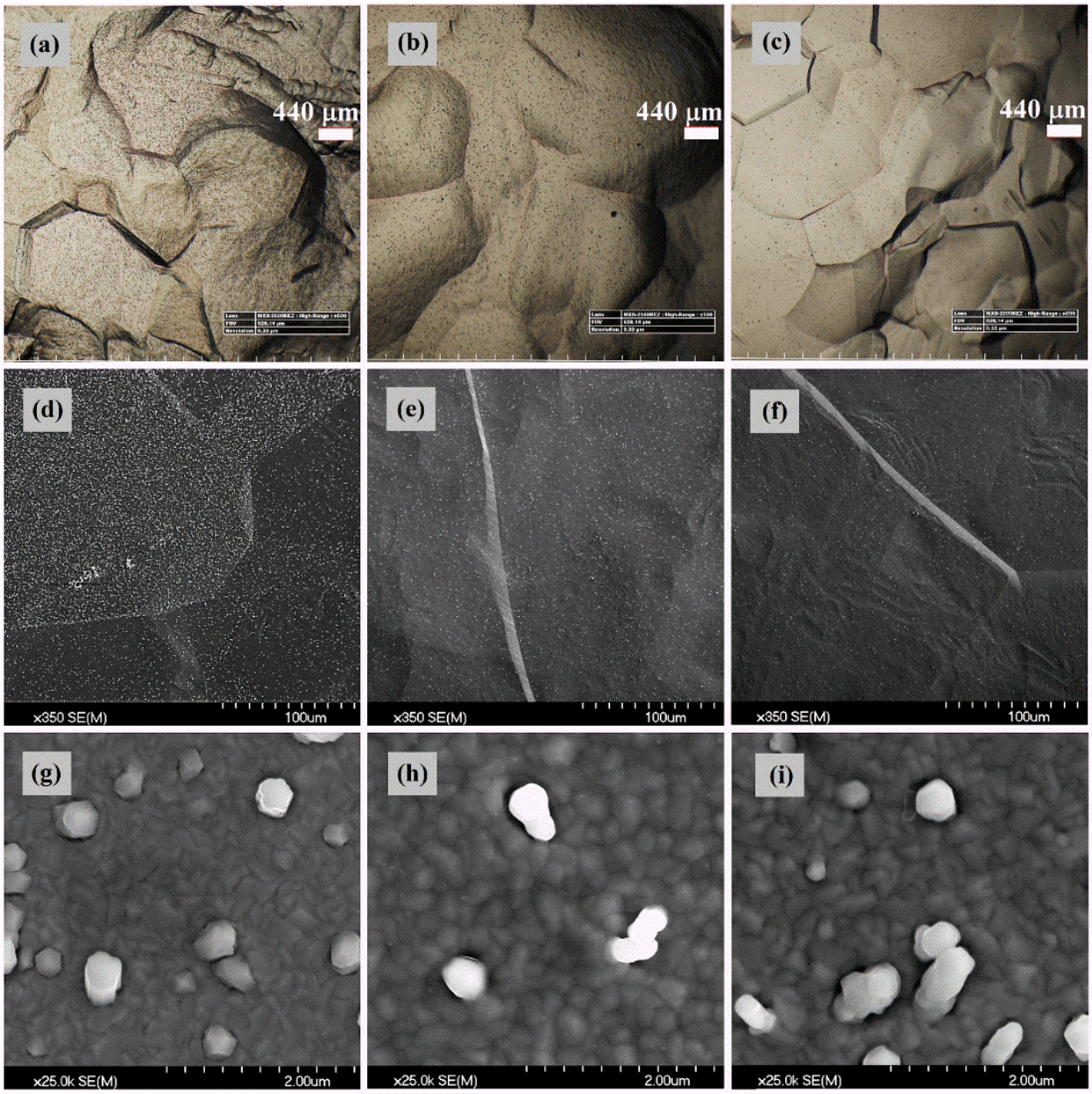

Fig. 3.10. (a-c): Surface micrograph under optical microscope (a) as-deposited film, (b) film annealed at 800 °C for 24 h, (c) film annealed at 1000 °C for 1 h, (d-f): SEM micrograph of the surface with ×350 magnification (d) as-deposited film, (e) film annealed at 800 °C for 24 h, (f) film annealed at 1000 °C for 1 h, (h-i): SEM micrograph of the surface with ×25.0k magnification (h) as-deposited film, (j) film annealed at 800 °C for 24 h, (i) film annealed at 1000 °C for 1 h [95].

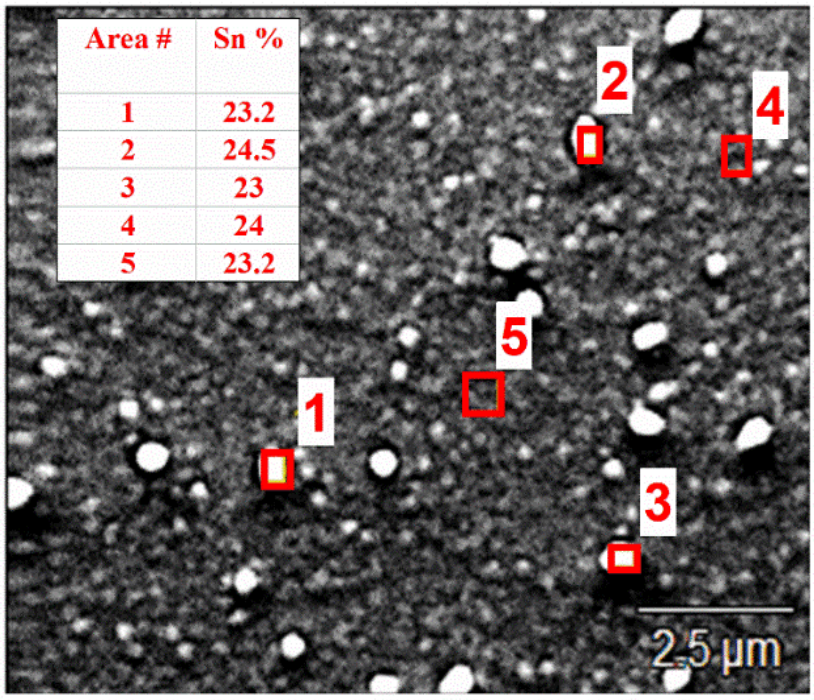

Fig. 3.11. EDS spot analysis of five different regions of as-deposited Nb_3Sn film surface [95]. The Sn atomic % of the spots are given in the inset.

Fig. 3.12 shows the 2D and 3D AFM images and line scans taken along the lines shown on the 2D images of the films. The random distribution of the clustered grains of different heights gave rise to film surface roughness. The height of these irregular clustered grains in as-deposited films were in the range of ~50-300 nm whereas the regular grains of the films had height below 40 nm as seen in Fig. 3.12(a). The average height of 10 different clusters of the film annealed at 800 °C for 24 h were 132 ± 41 nm, whereas the film annealed at 1000 °C for 1 h had an average height of 190 ± 88 nm.

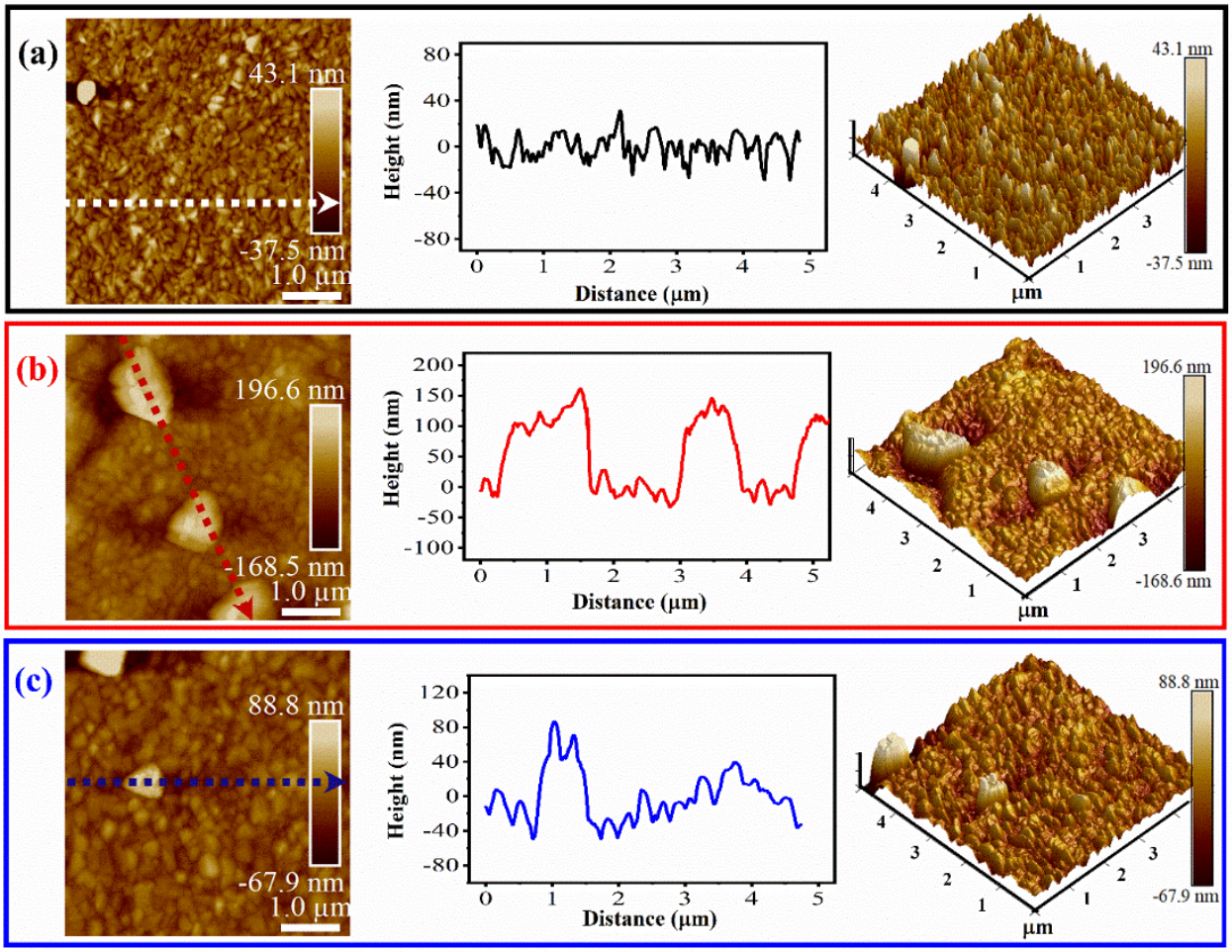

Fig. 3.12. 2D and 3D AFM images of Nb_3Sn films on Nb substrate: (a) as-deposited, (b) annealed at 800 °C for 24 h, and (c) annealed at 1000 °C for 1 h [95]. The line analysis of the surface corresponds to the broken arrows on 2D images are shown in the middle.

3.3.2.2. RF Superconducting Properties

From Fig. 3.13, both as-deposited and annealed films had a superconducting transition due to the Nb_3Sn films. The resistance of as-deposited films dropped sharply below 16.02 K. The error bars were estimated from different parameters (fluctuations in ambient temperature and pressure, noise in the electronics, calibration errors) during the measurement [105]. The T_c obtained from the as-deposited film was 16.02 K, which increased to 17.44 K after annealing at 800 °C for 24 h. The RF superconducting properties of the film degraded when annealed at 1000 °C for 1 h.

For this condition, T_c was 14.22 K. For all samples, no transition was observed near 9.3 K which confirmed that the RF field did not penetrate to the Nb substrate. The RF surface resistance at ~18.5 K in the normal conducting state increased from 22.2 ± 5.5 to 29.7 ± 3 mΩ when the as-deposited film was annealed at 800 °C for 24 h. The measured surface resistance of the film annealed at 1000 °C for 1 h was 29.9 ± 2 mΩ at 18.5 K.

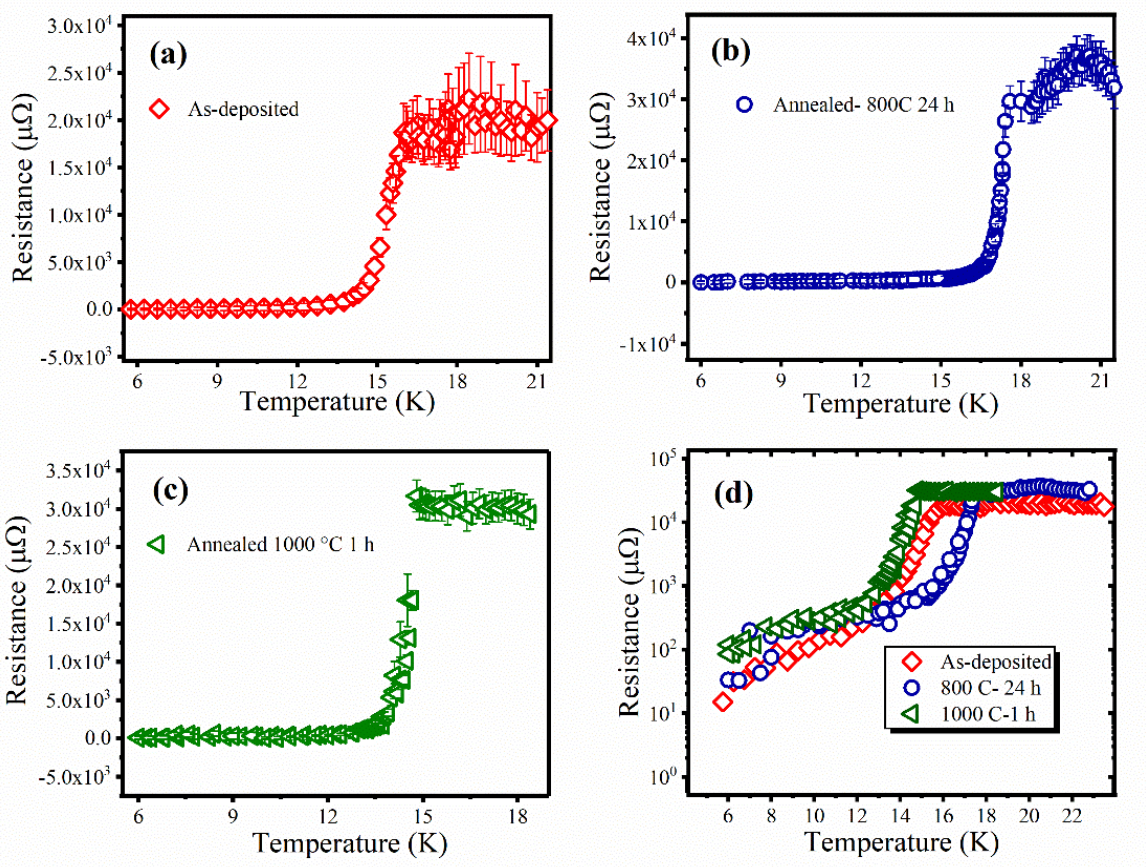

Fig. 3.13. RF surface resistance of the Nb_3Sn films with temperature: (a) as-deposited film, (b) film annealed at 800 °C for 24 h, (c) film annealed at 1000 °C for 1 h, (d) comparison of all three conditions.

The T_c obtained from the as-deposited film was 16.02 K, which increased to 17.44 K after annealing at 800 °C for 24 h. The RF superconducting properties of the film degraded when annealed at 1000 °C for 1 h. For this condition, T_c was 14.22 K. The RF surface resistance at ~18.5 K in the normal conducting state increased from 22.2 ± 5.5 to 29.7 ± 3 mΩ when the as-deposited film was annealed at 800 °C for 24 h. The measured surface resistance of the film annealed at 1000 °C for 1 h was 29.9 ± 2 mΩ at 18.5 K.

3.4. Summary

I fabricated Nb_3Sn films on sapphire and Nb substrates by DC magnetron sputtering from a stoichiometric target. The films were post-annealed at different temperatures and for different durations. The films had polycrystalline Nb_3Sn and developed improved crystallinity when annealed at 800 °C for 24 h. The film quality degraded when annealed at 1000 °C for 12 and 24 h due to Sn evaporation from the surface. The highest T_c =17.83 K was for the film annealed at 800 °C for 24 h. The RF properties of films deposited on Nb substrates were measured. Both as-deposited and annealed films had superconducting transition due to Nb_3Sn. The T_c of the as-deposited film increased from 16.02 K to 17.44 K when annealed at 800 °C for 24 h, and decreased to 14.22 K when annealed at 1000 °C for 1 h. Based on the RF results, magnetron sputtering from a stoichiometric Nb_3Sn target can be used to coat large cavities and the performance of the coated cavities can be improved by heat treatment with best conditions from the those investigated is annealing at 800 °C for 24 h. Annealing at 1000 °C reduced Sn content due to its decomposition and evaporation adversely affecting the superconducting properties of the film. Raman study of the films show high sensitivity to the surface composition and show that the strength of the Nb_3Sn E_g phonon modes and absence of NbO_2 and Nb modes correlates well with obtaining the highest T_c for the film.

CHAPTER 4

Nb_3Sn FABRICATION BY MULTILAYER SPUTTERING

4.1. Introduction

Multilayer sputtering allows independent control over the deposition of multiple layers to adjust film stoichiometry. The method was successfully applied to fabricate A15 Nb_3Ge [106,107], Nb_3Al [108,1098], V_3Si [110], and Nb_3Sn [63,64,111]. Vandenberg et al reported the formation of Nb_3Sn by the reactive interdiffusion of Nb/Sn multilayers on oxidized Si and on sapphire [63]. The experiments showed that, at substrate temperatures above 600 °C, the A15 structure of Nb_3Sn was present along with the orthorhombic $NbSn_2$ phase. The Nb_6Sn_5 phase disappeared above 800 °C. In this study, the highest T_c of 17.45 K was observed for films annealed at 850 °C. Deambrosis et al. fabricated Nb_3Sn films by annealing multilayered Nb-Sn films at 600-930 °C [64]. The stoichiometry of the films was adjusted by keeping the Nb-to-Sn thickness ratio of 4.5:1. The highest T_c of 17.9 K, ΔT_c of 0.02 K, and *RRR* of 3.6 were achieved for the film that was fabricated by annealing multilayers at 930 °C for 1.5 h. Ito et el. successfully fabricated Nb_3Sn by depositing Nb and Sn films alternately on silicon substrates and annealing the multilayers at 600 °C for 1 h. The XRD of the resulted films had Nb_3Sn diffraction orders. Better crystallinity was found for the films with higher Nb concentration. The highest T_c of 12.66 K was achieved on the film that had 27.5% Sn before annealing whereas the films with 33.8% Sn had a T_c of 8.25 K. Nb_3Sn films were fabricated by HiPIMS using multilayers [112]. Results obtained on copper substrates suggest that multilayer HiPIMS is feasible for fabricating Nb_3Sn films inside copper cavities.

This chapter discusses the properties of the Nb_3Sn films fabricated on Nb and sapphire substrates by multilayer sputtering. The effects of the multilayer thickness, substrate temperature, and annealing temperature and time were studied.

4.2. Design of Experiments

Fig. 4.1 shows the schematic diagram of the deposition process and fabricated films. The Nb and Sn films were sputtered from 99.95% pure Nb and 99.999% pure Sn targets with 2″ diameter. Before deposition, the chamber was evacuated to ~10^{-7} Torr and the deposition was carried out at an Ar background pressure of 3×10^{-3} Torr. The flow rate of the Ar gas (20 SCCM) was controlled by a mass flow controller.

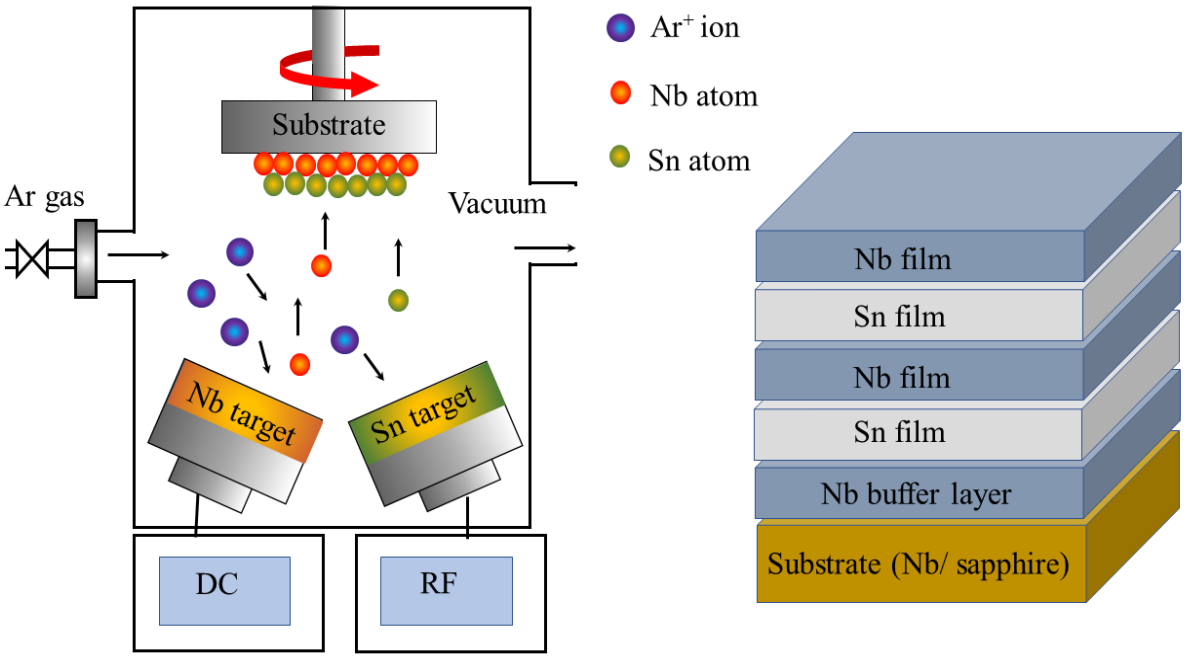

Fig.4.1. Schematic diagram of the multilayer sputtering and the deposited film.

Initially, a 200 nm thick Nb buffer layer was deposited on the substrate. Then, multilayers of Nb and Sn were deposited on top of the buffer layer. The thickness of the Nb and the Sn layers were 20 and 10 nm, respectively. The final layer deposited from Nb target so that it can block Sn evaporation from the surface during the annealing. All multilayer films were annealed in a separate vacuum furnace to form Nb_3Sn.

4.3. Results

To understand the Nb_3Sn formation, I compared the XRD patterns of the as-deposited and annealed films. The films were deposited on Nb substrate and had multiple layers of 20 nm thick Nb and 10 nm thick Sn films. The total thickness of the as-deposited film was ~1 μm. Fig. 4.2 shows the X-ray diffraction patterns of the Nb-Sn multilayered film before and after annealing.

The as-deposited film had the X-ray diffraction peaks correspond to Nb (110), (200), (211), (310) and Sn (200), (101), (220), (211), (112), (400). The annealed film had diffraction peaks corresponding to Nb_3Sn (110), (200), (210), (211), (222), (320), (321), (400), (420), (421), and (332) diffraction orders. Two diffraction peaks of Nb (200) and Nb (310) are from the substrate. The absence of any diffraction peak due to Sn confirmed the intermetallic compound formation after annealing. Since Nb and Sn form two more intermetallic compounds (Nb_6Sn_5, $NbSn_2$) of low transition temperature, the diffraction data were checked for those compounds also. The film did not exhibit any diffraction peak due to Nb_6Sn_5 and $NbSn_2$.

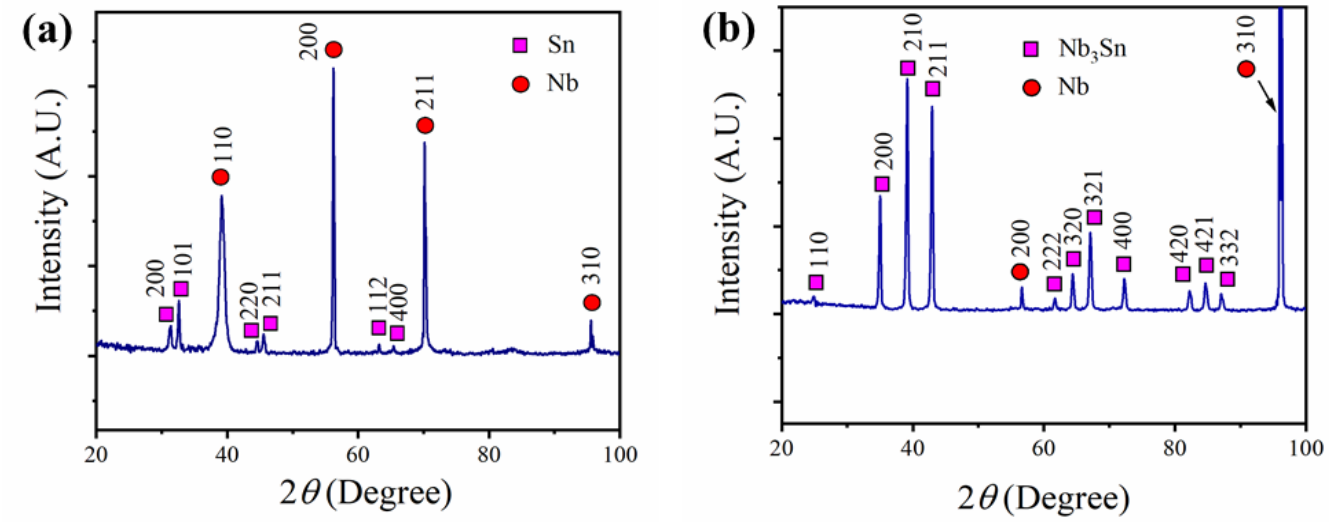

Fig. 4.2. XRD patterns of the films: (a) as-deposited Nb-Sn multilayered films, (b) multilayered Nb-Sn films after annealing at 950 °C for 3 h.

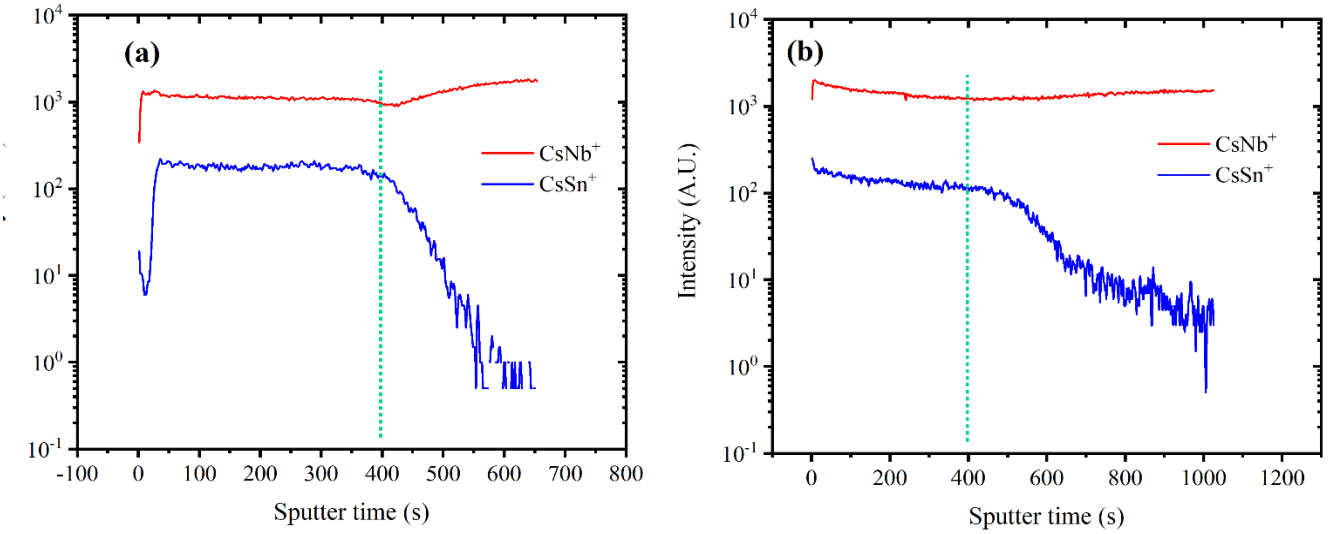

Fig. 4.3. ToF-SIMS depth profile of the films: (a) as-deposited Nb-Sn multilayered films, (b) multilayered Nb-Sn films after annealing at 950 °C for 3 h. The dotted green line shows the substrate-film interface [113].

The Time of Flight Secondary Ion Mass Spectrometry (ToF-SIMS) depth profile was performed on the films on Nb substrates to observe Sn diffusion after annealing. Depth profile was performed on both as-deposited and annealed films to observe variation. Fig. 4.3 shows the depth profiles of the films. Due to the rough surface of the films, the individual layers on the as-deposited film were hard to distinguish. In case of as-deposited film, a sharp fall of Sn signal is observed at the interface whereas annealed samples showed a tail after the interface region that indicates Sn diffusion through Nb.

4.3.1. Effect of Multilayer Thickness

The purpose of this study was to identify the appropriate thickness of Nb and Sn films to achieve the correct stoichiometry. The detail about the multilayer thickness is shown in Table 4.1.

Table 4.1. Deposition conditions of the films of different thicknesses.

	Condition	Nb layer thickness (nm)	Sn layer thickness (nm)	Nb:Sn	Total thickness (nm)
Films with different stoichiometry	1	10	10	1	900
	2	20	10	2	900
	3	30	10	3	900
	4	40	10	4	900
Films with fixed stoichiometry	5	10	5	2	1200
	6	20	10	2	1200
	7	50	25	2	1200
	8	200	100	2	1200

In the study of film stoichiometry, I chose a constant thickness of 10 nm of Sn and four thicknesses (10, 20, 30 and 40 nm) of Nb layers. These four conditions will be referred as Conditions 1–4 in these results. The total thickness of all four conditions was kept constant to 900 nm by varying the number of layers. In the other set of films, I kept the Nb-to-Sn thickness ratio 2:1. For all films on these conditions, the total thickness was 1.2 μm. These four conditions will be referred as Conditions 5–8 in the results. All films were annealed in a separate vacuum furnace at 950 °C for 3 h with a temperature ramp rate of 12 °C/min.

4.3.1.1. Results: Film with different stoichiometry

4.3.1.1.1. Structural and morphological properties

The Sn composition of as-deposited and annealed films are shown in Table 4.2. The Sn composition was reduced with increasing Nb layer thickness on as-deposited films. About 43.6% Sn was observed on films with Condition 1, where both Nb and Sn layer thickness was maintained at 10 nm. All annealed films showed Sn loss after annealing. Large amount of Sn loss was observed on films with Condition 1. The Sn composition changed from about 43.6% to about 23.8%. This large amount of Sn loss occurred due to sublimation of Sn during annealing. All annealed films showed Sn composition ~20-23%. The composition of the as-deposited films was ~16% in Condition 4, however, the annealed film had ~20% Sn. Annealed film showed more Sn due to the uniform distribution of Sn throughout the film after annealing.

Table 4.2. Summary of structural, morphological, and superconducting data.

Condition	At. % Sn as-deposited	At. % Sn annealed	RMS Roughness (nm)	T_c (K)	ΔT_c (K)	*RRR*
1	43.6	23.8	66.2 ± 24.3	17.93	0.02	5.1
2	28.4	23.0	31.8 ± 3.2	17.84	0.03	4.4
3	20.3	21.4	31.6 ± 0.9	17.56	0.09	3.29
4	16.0	20.2	26.8 ± 1.2	17.54	0.11	2.68
5	29.5	23.1	28.2 ± 2.9	17.82	0.02	4.96
6	28.9	21.7	31.5 ± 1.2	17.83	0.01	4.69
7	27.2	22.4	41.0 ± 5.5	17.83	0.02	4.88
8	20.0	21.4	64.7 ± 3.2	17.84	0.03	4.72

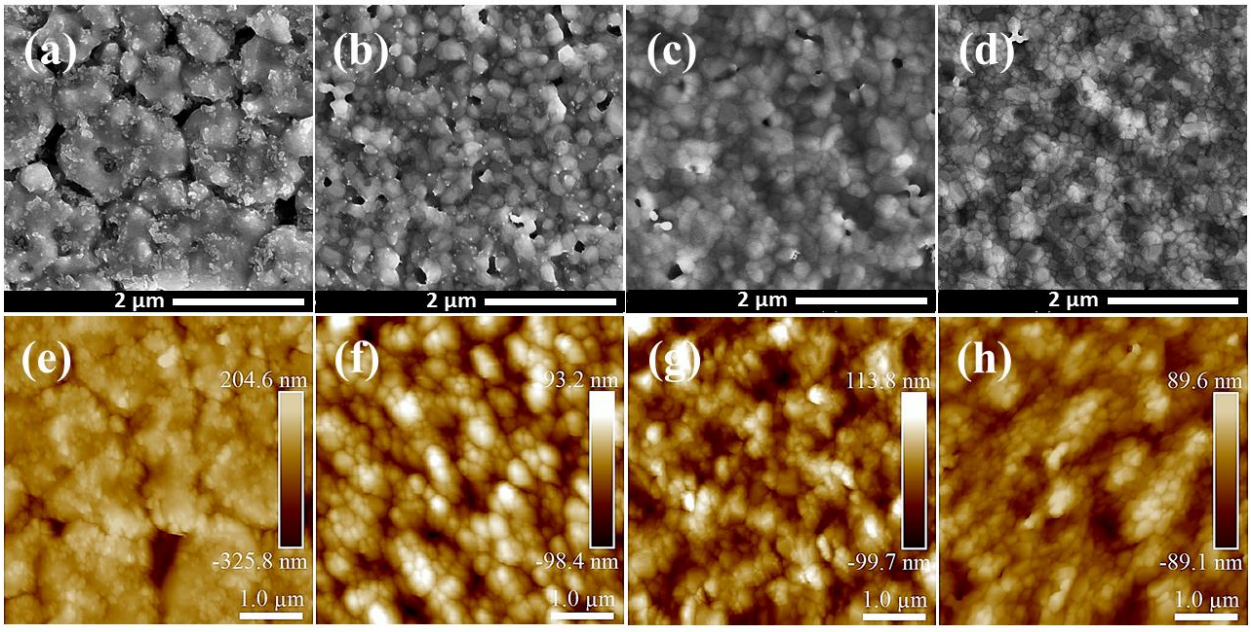

Fig. 4.4. SEM and AFM images of the films: (a) and (e) Condition 1, (b) and (f) Condition 2, (c) and (g) Condition 3, (d) and (h) Condition 4 [89].

Fig. 4.4 shows the SEM and AFM images of the films. For Condition 1, where the Nb and Sn layer thicknesses were 10 nm, several clusters separated by large voids were observed. The grains were not visible on the surface of this film. However, for the other three conditions, the films had surface with uniformly distributed grains showing some voids. The film with Condition 4, where the Nb:Sn was 4:1, showed smaller grains than that for other conditions. The surface roughness for Condition 1 was higher due to the film having clusters of larger heights and deeper voids. The RMS roughness for this condition is 66.2 ± 24.3 nm. The large standard deviation originated from the irregular distribution of the clusters and voids. Films with the other three conditions had smoother surfaces. The average roughness was measured to be 31.8 ± 3.2, 31.6 ± 0.9, and 26.8 ± 1.2 nm for Conditions 2, 3, and 4, respectively.

The XRD patterns of the films with different Nb thicknesses (10, 20, 30, 40 nm) and constant Sn thickness of 10 nm after annealing at 950 °C for 3 h are compared in Fig. 4.5(a). All annealed films were polycrystalline Nb_3Sn films showing (200), (210), (222), (320), (321), (400), (420), (421) diffraction orders. The crystallite size and lattice parameter corresponding to Nb_3Sn (210) diffraction peak of the films as a function of Nb:Sn thickness ratio are shown in Fig. 4.5(b). The crystallite size decreased with increasing Nb layer thickness, which is in agreement with the grain size observed in SEM and AFM. Lattice parameters calculated from the *d* value of XRD peak are less than lattice parameter of bulk Nb_3Sn (5.290 Å). This is because the Sn composition in the film is less than ideal condition of 25%.

4.3.1.1.2. Superconducting properties

The resistivity versus temperature is shown in Fig. 4.5(c). The calculated T_c, and ΔT_c from the graph are shown in Table 4.2 and Fig. 4.5(d). All films exhibited good superconducting properties. The highest critical temperature is observed on the film fabricated with Condition 1,

where the Nb and Sn thicknesses were the same. Better T_c at this condition was obtained due to higher Sn composition on the annealed films. It has been reported that T_c of Nb_3Sn is dependent on the Sn composition of the films [24]. The transition width also became wider with increasing Nb:Sn.

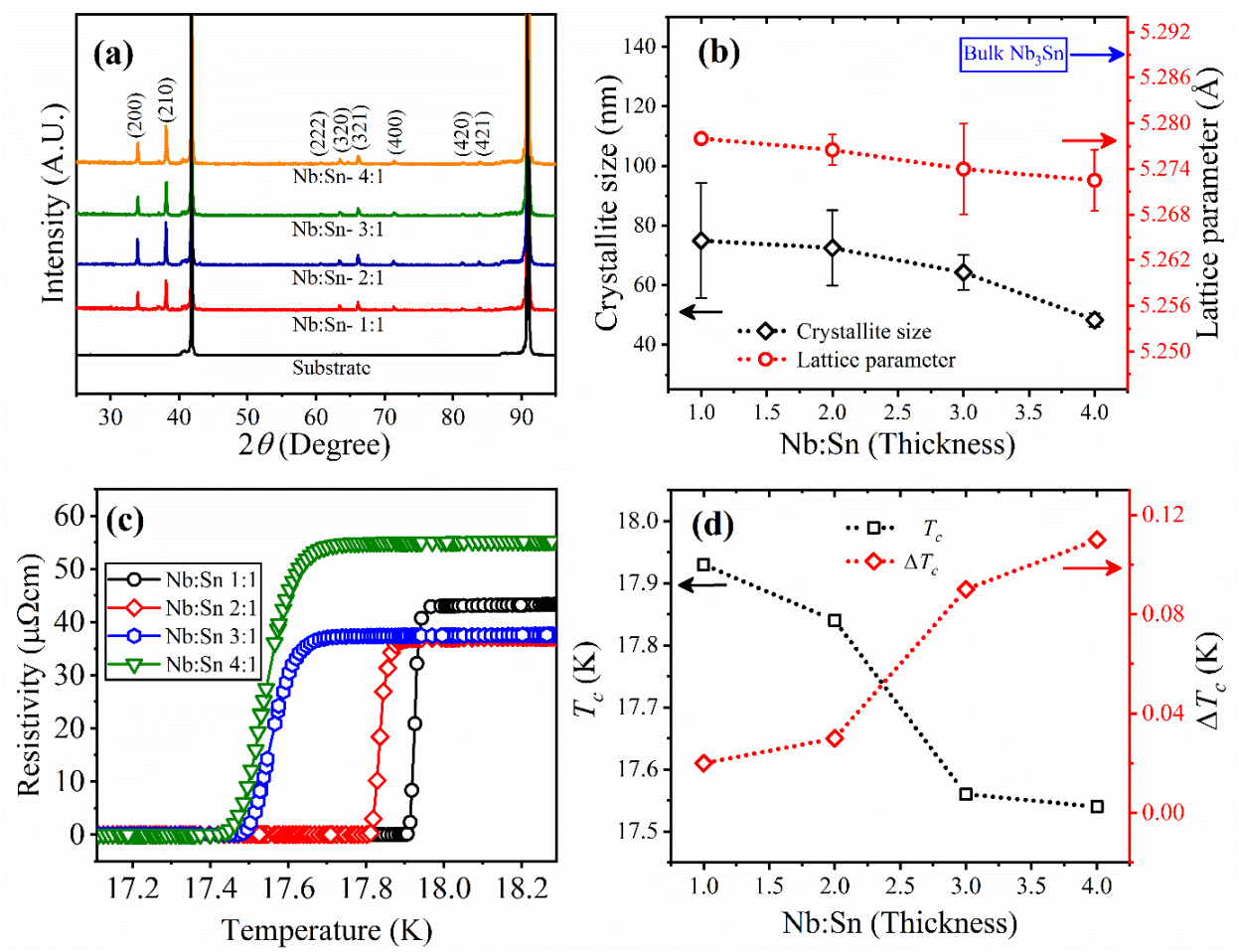

Fig. 4.5. (a) X-ray diffraction patterns of the films with Conditions 1–4, (b) crystallite size and lattice parameters of the films as a function of Nb:Sn film thickness, (c) resistivity versus temperature of the films, (d) corresponding T_c and ΔT_c for different Nb:Sn layer thicknesses [89].

4.3.1.2. Results: Films with Similar Stoichiometry

4.3.1.2.1. Structural and Morphological Properties

All annealed films (Conditions 4-8) had Sn composition in the range of 21-23%. Fig. 4.6 shows the SEM and AFM images of annealed films of different thicknesses. These films showed uniformly distributed grains with some voids similar to those fabricated under Conditions 1–4. However, for films fabricated under Condition 8 (Fig. 4.6(d) and 4.6(h)), the presence of deep voids was not observed. Surface of the film of this condition shows small grains aggregating into clusters. The color pattern on the AFM image of the surface in Fig. 4.6(h) confirmed that the clusters have different heights, which caused a relatively rough surface. RMS roughness of the films are shown in Table 4.2. The surface became increasingly rough with increased layer thickness. The lowest roughness of 28.2 ± 2.9 nm was observed for films of Condition 5 (Sn layer thickness 5 nm), whereas films of Condition 8 (Sn layer thickness 100 nm) had the highest surface roughness of 64.7 ± 3.2 nm.

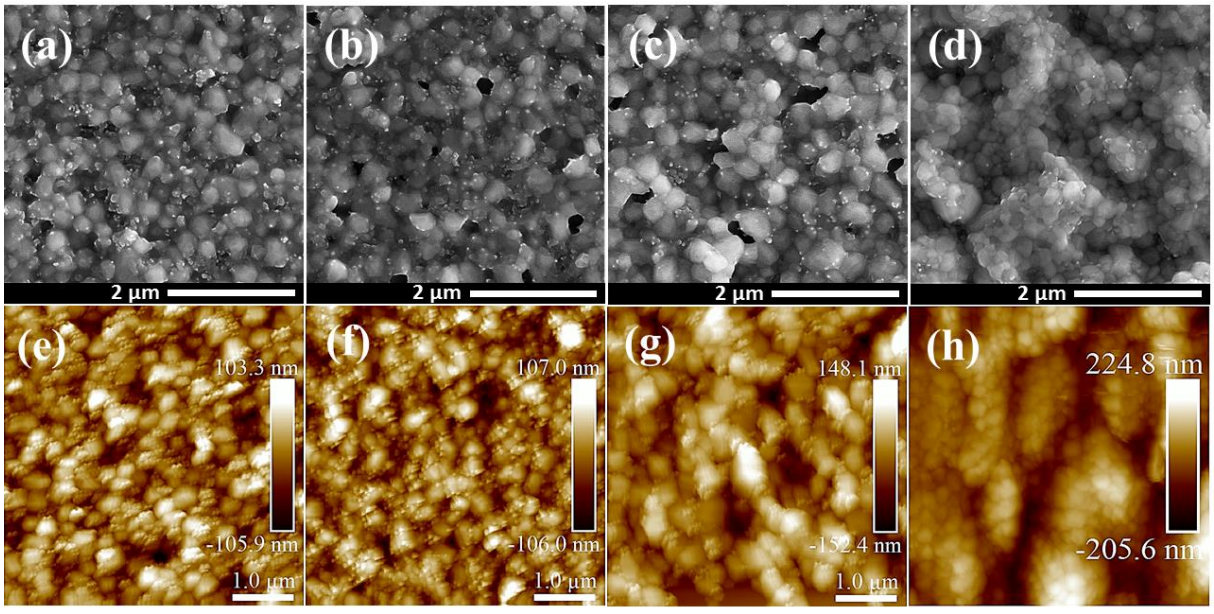

Fig. 4.6. SEM and AFM images of the films: (a) and (e) condition 5, (b) and (f) condition 6, (c) and (g) condition 7, (d) and (h) condition 8 [89].

Fig. 4.7(a) shows the XRD patterns of annealed films with Condition 5–8. Similar to the films for Condition 1-4, these films also exhibit diffraction peaks corresponding to Nb_3Sn (200), (210), (222), (320), (321), (400), (420), (421) diffraction orders. The lattice parameter and crystallite size of (210) reflection is shown in Fig. 4.7(b). The lattice parameter and crystallite size correspond to the film of Condition 2 is also plotted to compare it with similar condition 6. The lattice parameter of the films showed little variation due to the almost similar Sn composition of the films. The crystallite size of the films also did not vary significantly with increased layer thickness. Films with Condition 5 had crystallites with an average size of 72.1 ± 5.2 nm, whereas the films with Condition 8 had crystallites with an average size of 68.5 ± 2.5 nm.

4.3.1.2.2. Superconducting Properties

The surface resistivity of the films for different Sn layer thicknesses is shown in Fig. 4.7(c) and the corresponding T_c and ΔT_c data are shown in Table 4.2 and Fig. 4.7(d), respectively. The T_c and ΔT_c of film of Condition 2 is also included to compare with Condition 6. The T_c and ΔT_c of all films are close. Slight increased T_c is observed on the film with Condition 8, however, the ΔT_c also increased.

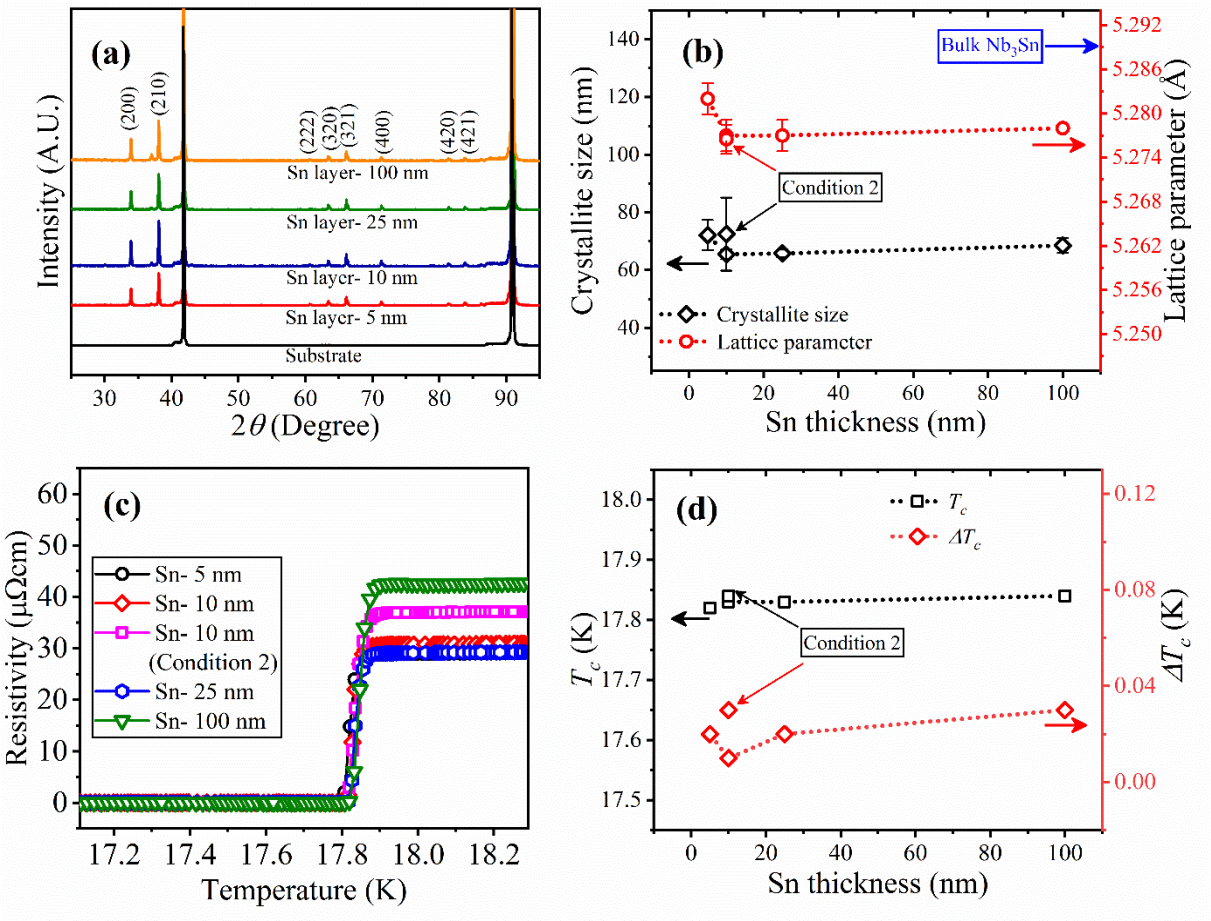

Fig. 4.7. (a) X-ray diffraction patterns of the films with Condition 5–8, (b) crystallite size and lattice parameters of the films as a function of Sn film thickness, (c) resistivity vs temperature curve of the films, (d) corresponding T_c and ΔT_c as a function of Sn layer thickness with Conditions 5–8 [89].

4.3.2. Effect of Annealing Temperatures

Though some of the Nb_3Sn films deposited at room temperature reached a T_c of 17.93 K [89], the surface of the film had a large distribution of voids, which can affect RF superconducting performance. Here, I examined the properties of the Nb_3Sn film with varied deposition substrate temperatures. Nb-Sn multilayers were deposited at different substrate temperatures starting from room temperature (RT) up to 250 °C. The deposition of the

multilayers was conducted at substrate temperatures of RT, 100, 150, and 250 °C. All multilayers were post-annealed inside a separate vacuum furnace at 950 °C for 3 h.

4.3.2.1. Results

4.3.2.1.1. Structural and Morphological Properties

Fig. 4.8(a) and 4.8(b) show the XRD patterns of films annealed at different temperatures and annealing time, respectively. All annealed films showed diffraction orders of Nb_3Sn. As the annealing temperature increased, the Nb_3Sn diffraction patterns changed. For films annealed at 1100 °C, the characteristic diffraction peaks for Nb (110), (200), (211) (220) and (310) appeared along with the Nb_3Sn (200), (210), (222), (320), (321), (400), (420) and (421) diffraction peaks. Diffraction peaks between 37.6 and 39.2° are shown in the inset of Fig. 4.8(a) and 4.8(b). In the inset of Fig. 4.8(a), the diffraction peak of Nb_3Sn (210) at 38.18° appeared for films annealed at 850, 950 and 1000 °C. The film annealed at 1100 °C showed two peaks at 38.2 and 38.54° corresponding to the diffraction order of Nb_3Sn (210) and the Nb (110), respectively. Upon annealing at 1200 °C, the Nb_3Sn (210) peak completely disappeared while the Nb (110) peak at 38.62° appeared. For films annealed at 950 °C with different periods of 1, 3, and 12 h, similar diffraction peaks were observed for all three annealing periods with these diffraction peaks corresponding to Nb_3Sn (200), (210), (222), (320), (321), (400), (420) and (421) diffraction peaks. The inset of Fig. 4.8(b) shows the absence of the Nb (110) diffraction peak.

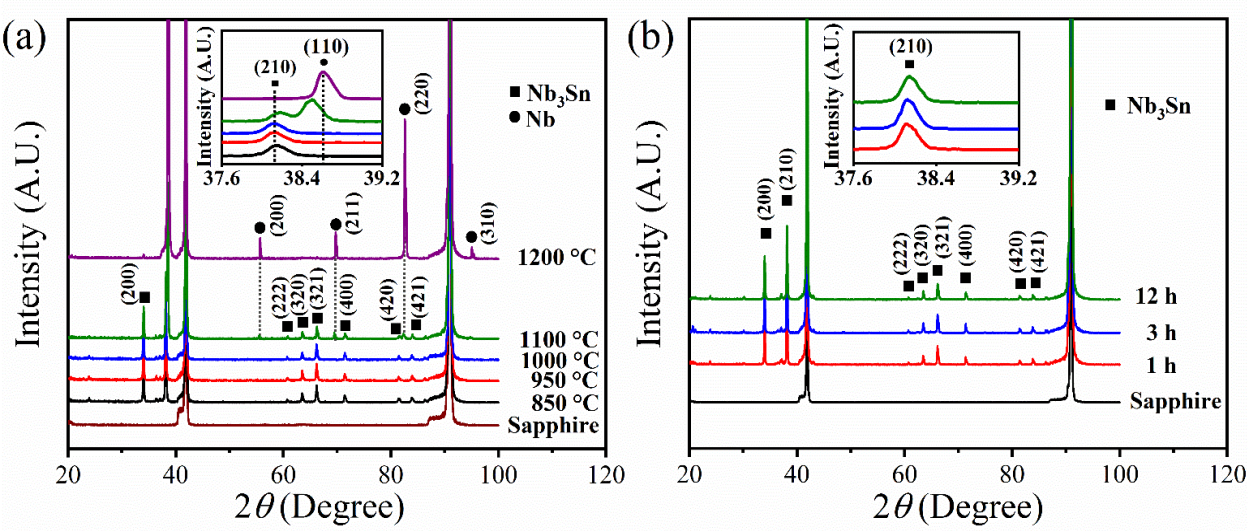

Fig. 4.8. XRD patterns of (a) films annealed for 3 h at different temperatures with inset image showing the XRD patterns for the films with 2θ between 37.6 and 39.2° The Nb_3Sn peaks disappeared completely for the film annealed at 1200 °C, and (b) films annealed at 950 °C for 1, 3, and 12 h with inset image showing the XRD patterns for the films with 2θ between 37.6 and 39.2° Only Nb_3Sn peaks are observed [102].

To study the effect of the annealing temperature on the structure of Nb_3Sn, XRD patterns of films annealed at 850, 950, 1000 and 1100 °C were considered. Films annealed at 1200 °C did not show XRD peaks corresponding to Nb_3Sn. The lattice parameter and the crystallite size of (210) diffraction order for different annealing temperature and annealing time are shown in Table 4.3 and 4.4, respectively. The error bars represent the standard deviation of measurement of two different films. As the annealing temperature increased, the Nb grains coalesced increasing in grain size. Meanwhile, Sn diffused through the grain boundaries of Nb and formed Nb_3Sn. Also, the crystallite size increased with increasing the annealing time because longer annealing times allow more grains to coalesce. The crystallite size increased from about 71.6 to 79.4 nm when the annealing time was increased from 1 to 3 h. A longer annealing time of 12 h resulted in crystallites with an average size of about 89 nm.

The measured lattice parameters from the Nb_3Sn (210) diffraction order were smaller than that of the bulk Nb_3Sn lattice parameter (5.290 Å). The lattice parameter of Nb_3Sn films decreases with decreasing Sn composition [114]. The Sn composition on the films after annealing were lower than the desired composition (25%), as found by EDS.

Table 4.3. The measured crystallite size and lattice parameter of the films annealed at different temperatures.

Annealing temperature (°C)	Annealing time (h)	Crystallite size (nm)	Lattice parameter (Å)
850	3	44.04	5.286
950	3	52.96	5.283
1000	3	53.25	5.285
1100	3	52.69	5.276

Table 4.4. The measured crystallite size and lattice parameter of the films annealed at 950 °C for different durations.

Annealing temperature (°C)	Annealing time (h)	Crystallite size (nm)	Lattice parameter (Å)
950	1	71.60	5.285
950	3	79.40	5.276
950	12	89.00	5.278

I studied film morphology by FESEM images. As shown in Fig. 4.9, annealing changed the grain size and shape. The annealed films had a crack-free surface with good adhesion of the

film with substrate. The grain size of the film annealed at 850 °C is smaller than that of films annealed at higher temperatures. For films annealed between 850 and 1000 °C, I observed dense grains linked together with some voids among the grain distribution. For films annealed above 950 °C, the grains are covered by a number of small particles of about 30 nm. Most of these particles are smaller in size than the spatial resolution of my EDS spot analysis. However, the EDS spectra obtained from spot analysis of the larger particles showed more Sn than the areas without particles, which indicates that these particles are Sn-rich. These Sn-rich particles adhere on the Nb_3Sn surface. The number of the Sn-rich particles is reduced with the increase in the annealing temperature. Segregation of Sn to the surface and its loss by evaporation resulted in the observed difference in the film crystal for films annealed at 1100 and 1200 °C, where the film annealed at 1200 °C was deficient in Sn.

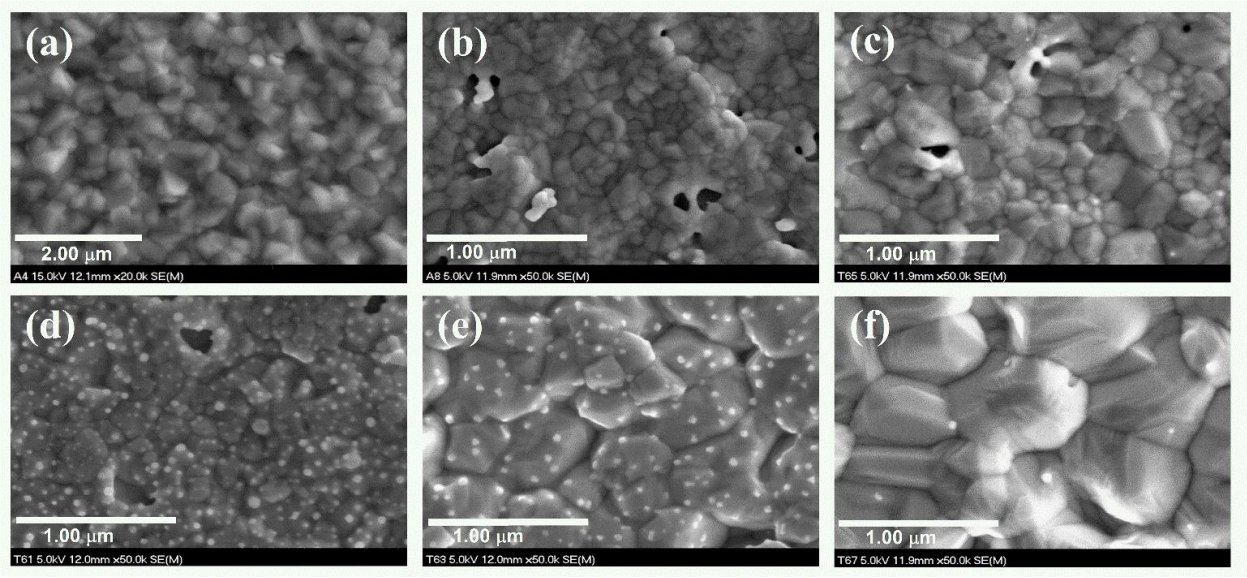

Fig. 4.9. FESEM micrographs of (a) as-deposited film and films annealed at (b) 850 °C, (c) 950 °C, (d) 1000 °C, (e) 1100 °C and (f) 1200 °C [102].

The atomic % of Sn for samples annealed at different temperatures is shown in Fig. 4.10. All films developed Sn deficiency after annealing. Sn deficiency was previously observed for multilayer sputtered films of Nb and Sn after annealing at 850 °C [115, 116]. Sn loss was also observed for Nb_3Sn films grown by evaporating Sn films on Nb followed by annealing [48]. In this process, the Sn layer grown on Nb undergoes solid-state diffusion into the bulk forming Nb_3Sn. Surface Sn loss occurs due to diffusion and evaporation. Sn loss due to diffusion on those films was less when annealed at 800–900 °C. For annealing at temperature above 980 °C, Sn loss was observed due to Nb_3Sn decomposition resulting in a Sn-deficient film [48, 49]. I observed small Sn loss for films annealed for 3 h at 850 and 950 °C and significant Sn loss for annealing at temperature above 1000 °C, also for 3 h. Both the films annealed at 850 and 950 °C had 21.6 At. % of Sn, whereas the as-deposited film had 23.2% Sn. As the annealing temperature was increased to 1000 °C, the Sn content detected by EDS decreased to 19.6%. Films annealed at 1100 °C had 6.1% Sn left after 3 h annealing although the XRD patterns of the films showed peaks from Nb_3Sn and Nb as EDS and XRD are sensitive to different depths in the film. At 1200 °C, almost all Sn evaporated leaving 0.8% Sn on the film and the XRD patterns showed peaks only due to Nb.

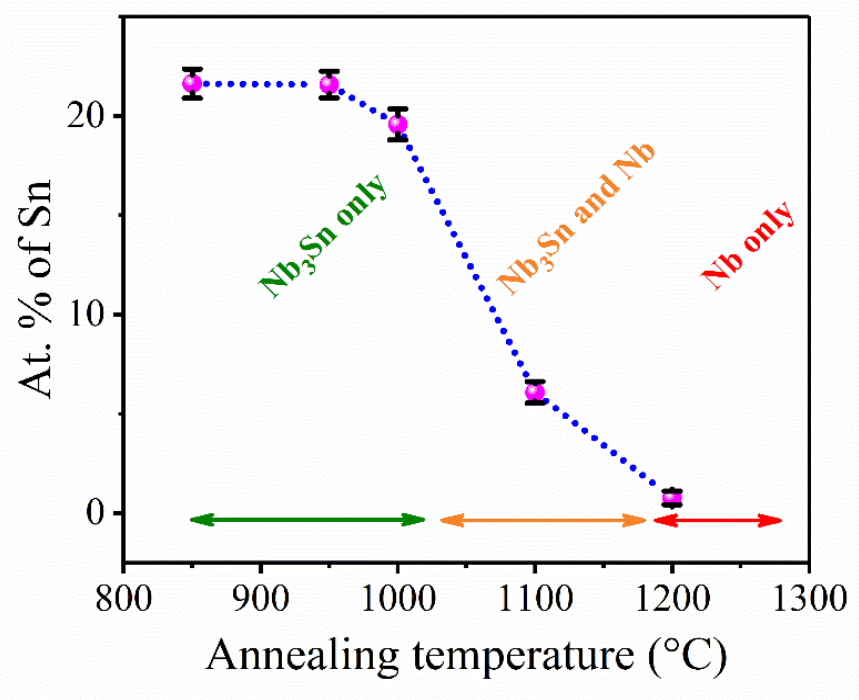

Fig. 4.10. Atomic composition of Sn after annealing for 3 h as a function of annealing temperature. The error bars represent standard deviation of measurements of 10 different regions of the films. The horizontal arrows identify the approximate annealing temperatures that results in different film compositions [102].

Fig. 4.11 shows AFM micrographs for films annealed at different temperatures, taken over an area of 2 μm × 2 μm. For the films annealed at 850 and 950 °C, the surface morphology indicated good substrate coverage. Annealing at 1000 °C resulted in grain agglomeration. Grain growth continued with an increase in the annealing temperature. For films annealed at 1000 and 1100 °C, the surface of the large grains was covered by small particles, which are best seen in FESEM image in Fig. 4.9(e) for films annealed at 1100 °C. These small particles on the surface were not present for the film annealed at 1200 °C, and smooth, large grains were observed.

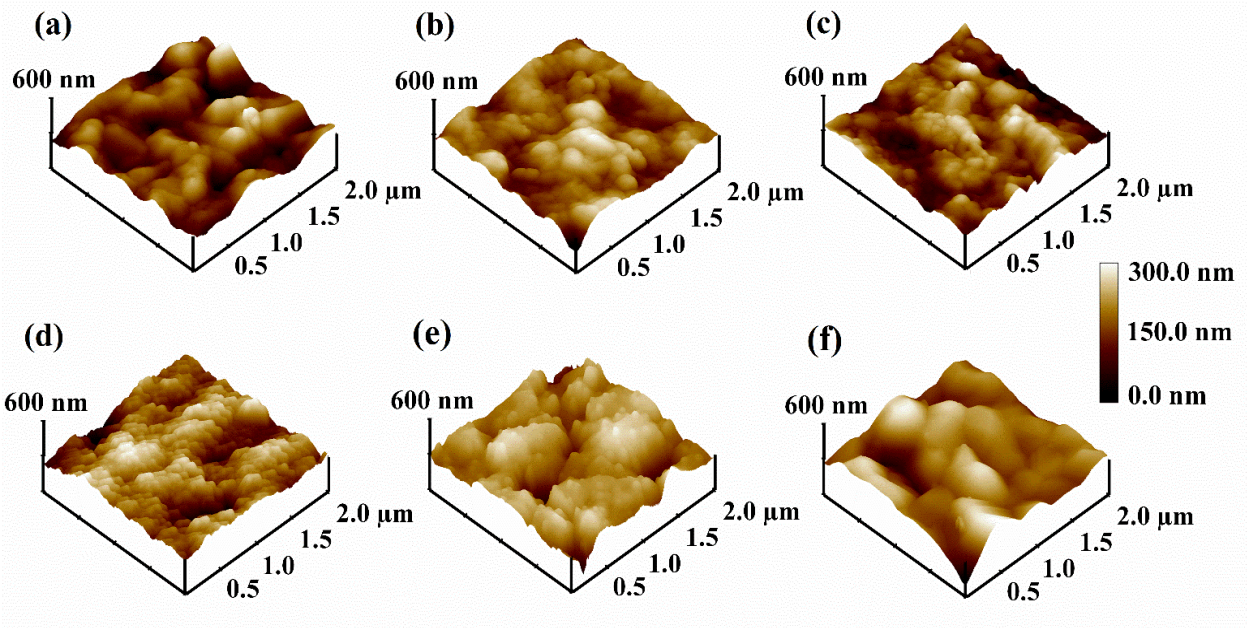

Fig. 4.11. (2 µm × 2 µm) AFM images of (a) as-deposited film, films annealed at (b) 850 °, (c) 950 °C, (d) 1000 °C, (e) 1100 °C, and (f) 1200 °C [102].

The RMS roughness (*Rq*) of the films for 5 µm × 5 µm scans are plotted in Fig. 4.12. The error bars in Fig. 4.12 represent the standard deviation of measurements of 3 regions of the films. The inset of Fig. 4.12 shows diagonal line scans of as-deposited and annealed films. The as-deposited film had an average RMS roughness of ~39 nm, which reduced to 36 nm when the film was annealed at 850 °C for 3 h. Further increase in the annealing temperature to 950 °C resulted in a smoother surface with a roughness of 34 nm. The surface roughness was reduced to 33 nm at an increased annealing temperature of 1000 °C. At this range, the crystallinity of the film improved with the increase in the annealing temperature and the surface became smoother. However, above 1000 °C, the surface becomes rough due to grain growth. The RMS surface roughness increased to 52 nm at 1100 °C. At 1200 °C, the small particles on the surface evaporated, which slightly smoothed the surface, reducing the surface roughness to 47 nm.

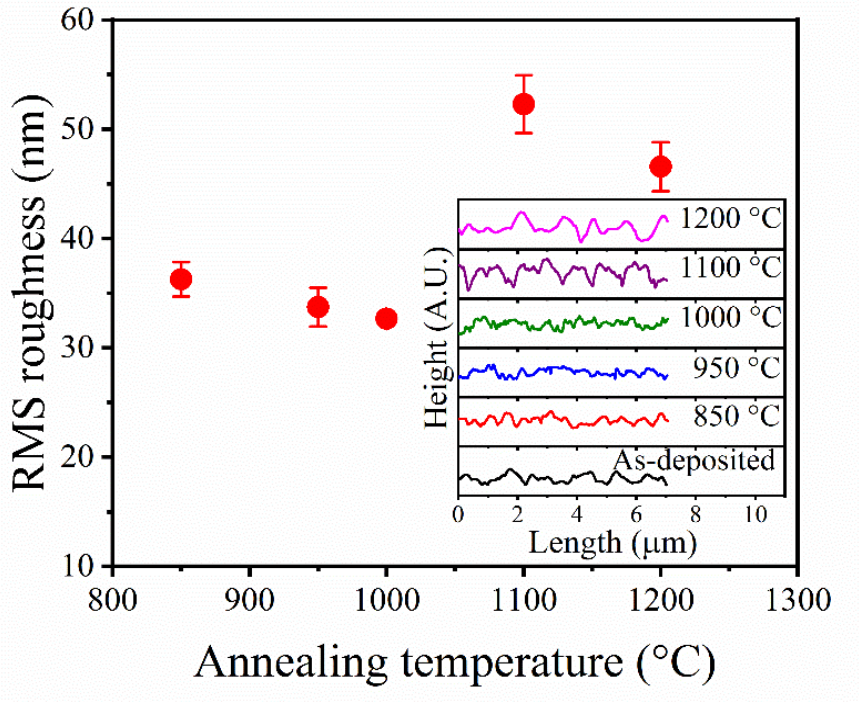

Fig. 4.12. RMS roughness of films as a function of annealing temperature. The inset image shows the diagonal line scans of (5 μm × 5 μm) AFM images of as-deposited and annealed films [102].

4.3.2.1.2. Superconducting Properties

The film resistivity as a function of annealing temperature and time is shown in Fig. 4.13(a) and 4.13(c), respectively. The transition regions of all films are shown in the inset of Fig. 4.13(a) and 4.13(c). The variation of T_c, ΔT_c and *RRR* as a function of annealing temperature and annealing time is shown in Fig. 4.13(b) and 4.13(d), respectively. All films except the one that annealed at 1200 °C had T_c values close to 18 K. The superconducting properties of the film did not follow the T_c dependence on the Sn composition previously reported [24]. All Nb_3Sn films had T_c in the range of 17.53-17.86 K, though Sn composition on the Nb_3Sn films varied from 6.1% to 21.6%, as detected by EDS. For the film annealed at 850 °C, T_c was approximately

17.61 K. Slightly increased T_c of 17.63 and 17.66 K was observed when the annealing temperature was increased to 950 and 1000 °C, respectively. The film transition widths, ΔT_c increased with the increasing annealing temperature up to 1100 °C and decreased afterward. The films annealed at 850, 950, 1000 and 1100 °C for 3 h had ΔT_c of 0.08, 0.09, 0.11 and 0.25 K, respectively. For films annealed at 1100 °C, the XRD pattern showed the presence of both Nb and Nb_3Sn. The lower T_c of Nb affects T_c of the films and as a result this film had a T_c ~ 17.53 K with wider ΔT_c than films annealed at lower temperatures. Such a relatively high T_c is due to the formation of Nb_3Sn although EDS analysis showed only 6.1% Sn within the sampled volume. No transition due to the presence of Nb in the film was observed near 9 K as the resistivity had already dropped to zero at 17.53 K. The film annealed at 1200 °C had T_c ~ 7.9 K and ΔT_c ~ 0.05 K, corresponding to that of Nb. *RRR* of the films decreased slowly from 3.92 to 3.71 with an increase in the annealing temperature from 850 to 950 °C. Further increase in the annealing temperature to 1000 °C caused the *RRR* to decrease to 3.33. The value of *RRR* decreased substantially from 3.33 to 2.01 at 1100 °C but increased to 2.58 at 1200 °C. A large reduction in the *RRR* value during annealing at 1100 °C may result due to the presence of Nb and Nb_3Sn mixed phase in the films. For films annealed at 950 °C for different annealing times of 1, 3 and 12 h, slight improvement in T_c and ΔT_c were observed when the annealing time was increased from 1 to 3 h; T_c increased from 17.85 K to 17.86 k and ΔT_c decreased from 0.05 to 0.04 K. Increasing the annealing time to 12 h degraded the superconducting performance due to Sn loss and T_c ~ 17.82 K was observed. The ΔT_c increased from 0.04 to 0.1 K when the annealing time was increased from 3 to 12 h. *RRR* of the films decreased with increasing annealing periods. *RRR* decreased slightly from 4.76 to 4.73 when annealing time was increased from 1 h to 3 h and decreased more to 4.55, when the annealing time was increased to 12 h.

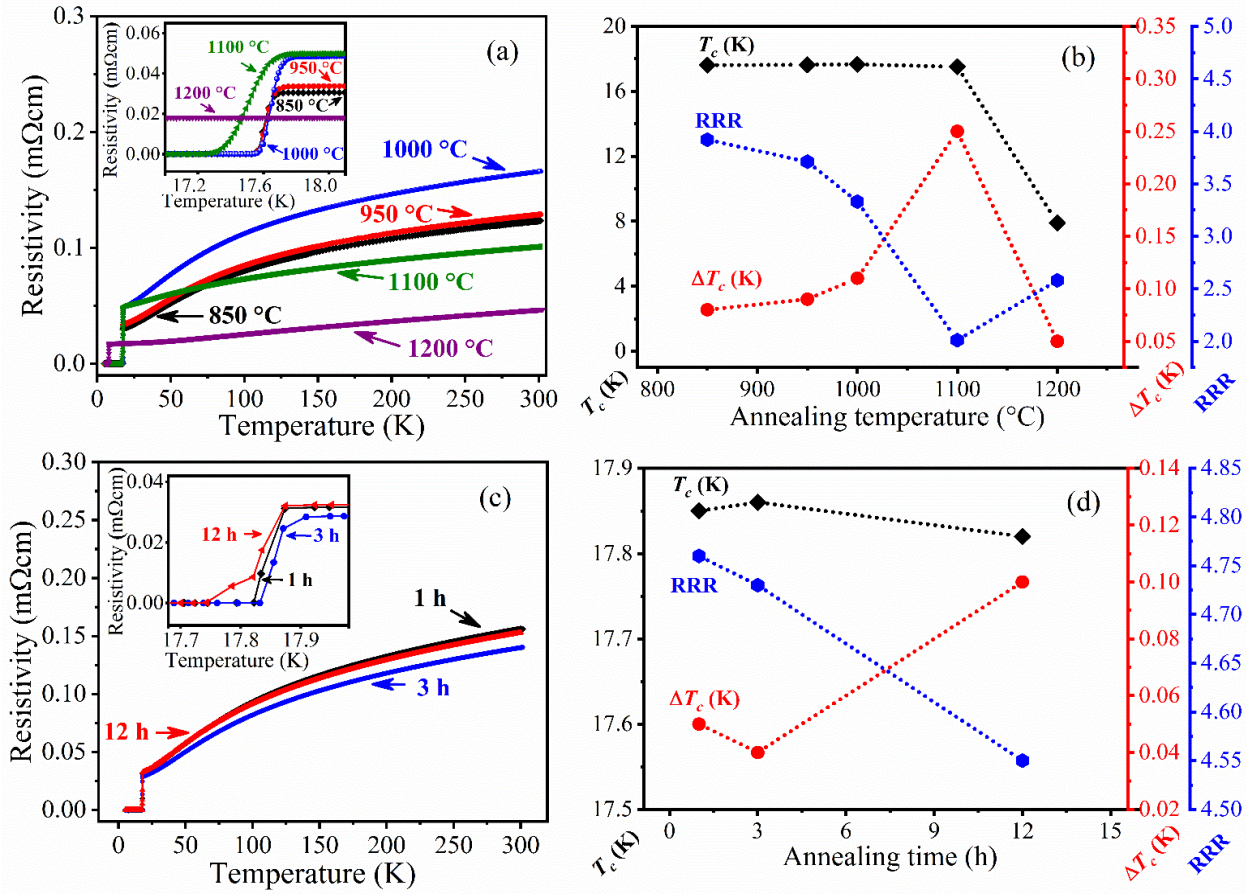

Fig. 4.13. (a) Film resistivity as a function of temperatures when the films are annealed at different temperatures for 3 h, (b) T_c, ΔT_c and *RRR* as a function of annealing temperature, (c) film resistivity as a function of temperatures when the films were annealed for different durations at 950 °C, (d) T_c, ΔT_c and *RRR* as a function of annealing time [102].

4.3.3. Effect of Substrate Temperatures

The goal of this study was to minimize the voids through the surface found in the earlier studies by optimizing the multilayer growth by depositing at heated substrates. The substrate temperature was varied using a resistive heater placed at the back of the substrate holder. The deposition of the multilayers was conducted at substrate temperatures of RT, 100, 150, and 250 °C. All multilayers were post-annealed inside a separate vacuum furnace at 950 °C for 3 h.

4.3.3.1. Results

4.3.3.1.1. Structural and Morphological Properties

Figs. 4.14 (a) and 4.14 (b) show the X-ray diffraction peaks of as-deposited and annealed films, respectively. The as-deposited films have diffraction peaks from Nb for all deposition conditions.

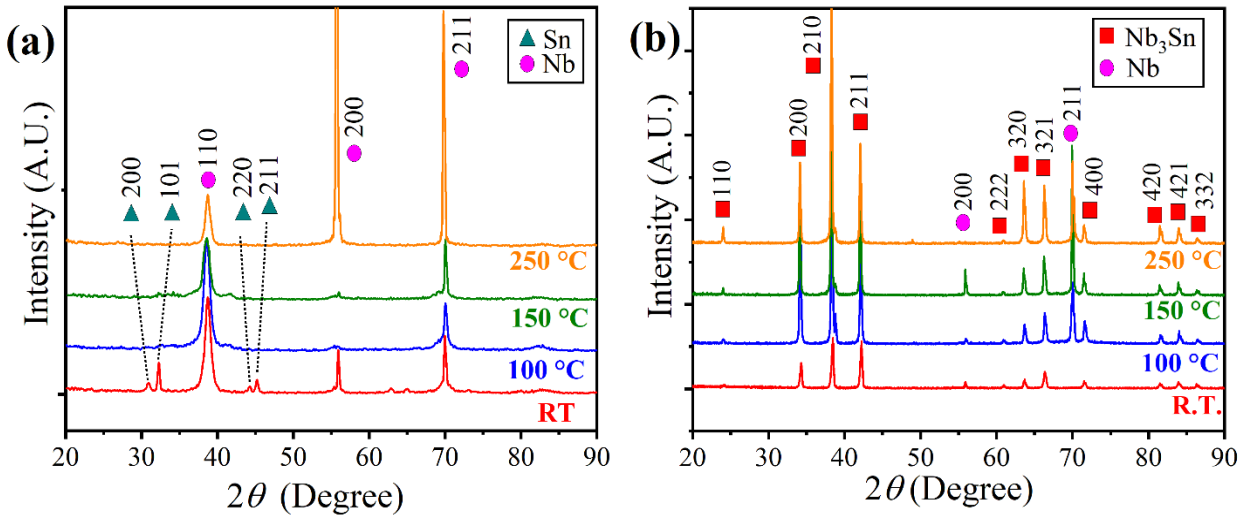

Fig. 4.14. X-ray diffraction peaks of (a) as-deposited, and (b) annealed films sputtered at a substrate temperature of RT, 100, 150, and 250 °C [117].

Figs. 4.14 (a) and 4.14 (b) show the X-ray diffraction peaks of as-deposited and annealed films, respectively. The as-deposited films have diffraction peaks from Nb for all deposition conditions. All the annealed films have polycrystalline Nb_3Sn with diffraction peaks identified as the (110), (200), (210), (211), (222), (320), (321), (400), (420), (421), and (332) orders. The

increased intensity of the Nb_3Sn diffraction orders with increased substrate temperature confirms the improved film crystallinity at the higher deposition temperatures.

The crystallite sizes for films deposited at different substrate temperatures are shown in Fig. 4.15. For all Nb_3Sn diffraction orders, the crystallite size increased with increasing substrate temperature. The crystallite size calculated from the Nb_3Sn (200) diffraction order changed from ~39 to ~80 nm when the substrate temperature was raised from RT to 250 °C.

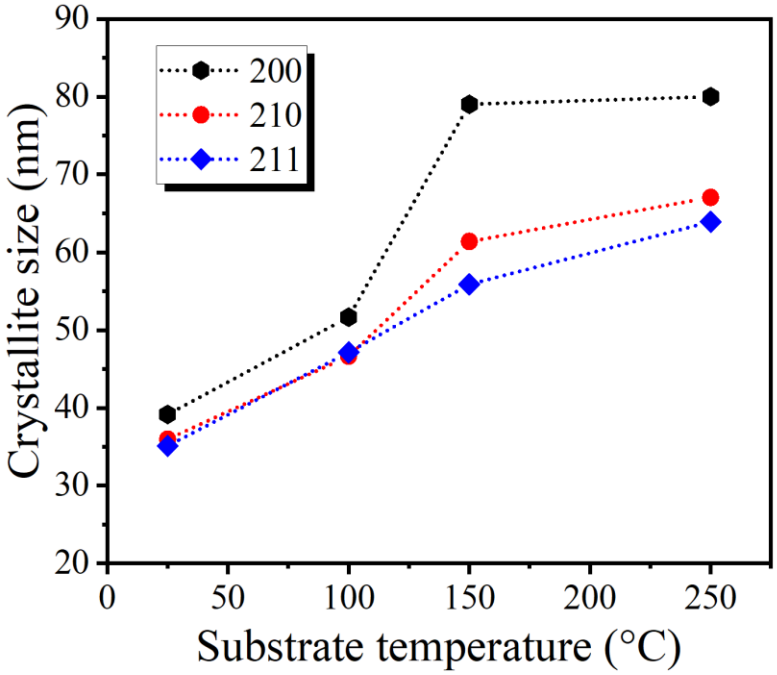

Fig. 4.15. Crystallite size of the Nb_3Sn calculated from the (200), (210), and (211) diffraction orders for different substrate temperatures [117].

The surface morphology was highly dependent on the substrate temperature during the deposition of the multilayers. Fig. 4.16 shows the SEM surface images of as-deposited films grown at different substrate temperatures. The film coated at RT has a fine grain structure. For

substrate temperature of 100 °C, some grains coalesced and created grain clusters. When the substrate temperature was further increased to 150 °C, the clustered regions separated from each other, leaving flat surface areas between the clusters. These flat areas increased, and the cluster size decreased when the substrate temperature was further increased to 250 °C. EDS scans show that random bright regions on the clusters, in Fig. 4.16(c) and 4.16(d), are Sn-rich regions.

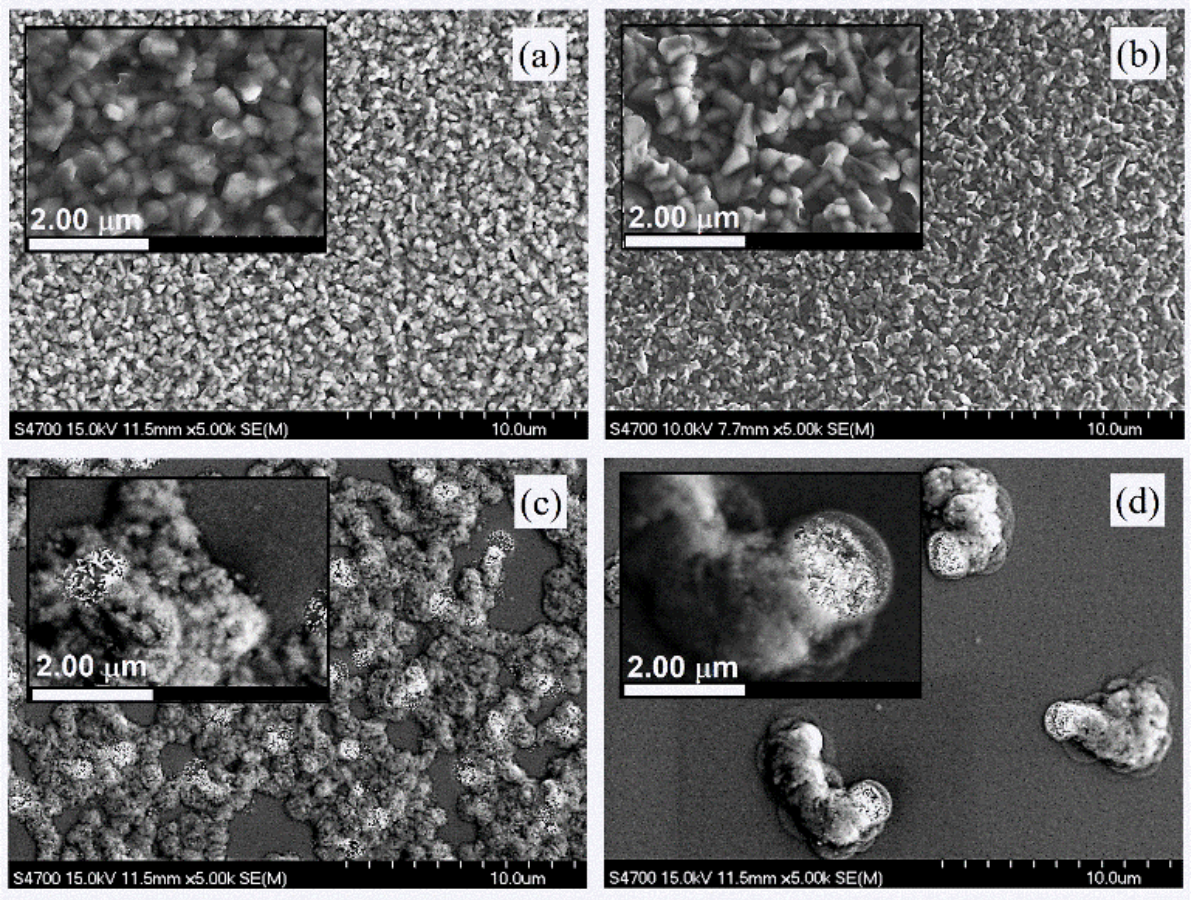

Fig. 4.16. SEM images of the as-deposited Nb-Sn films on Nb substrates for different temperatures: (a) RT, (b) 100 °C, (c) 150 °C, and (d) 250 °C [117].

Fig. 4.17(a) shows an SEM image of Nb-Sn multilayered films deposited at 250 °C. The arrow indicates the location of the EDS line-scan for the elemental mapping shown in Fig. 4.17(b). The EDS line-scan of the surface confirms the increased Sn-concentration across the clusters. The enhanced intensity near the clusters in Fig. 4.17(c) show the abundance of Sn on the clusters. Also, the EDS mapping of Nb shown in Fig. 4.17(d) confirms Nb deficiency in the same region.

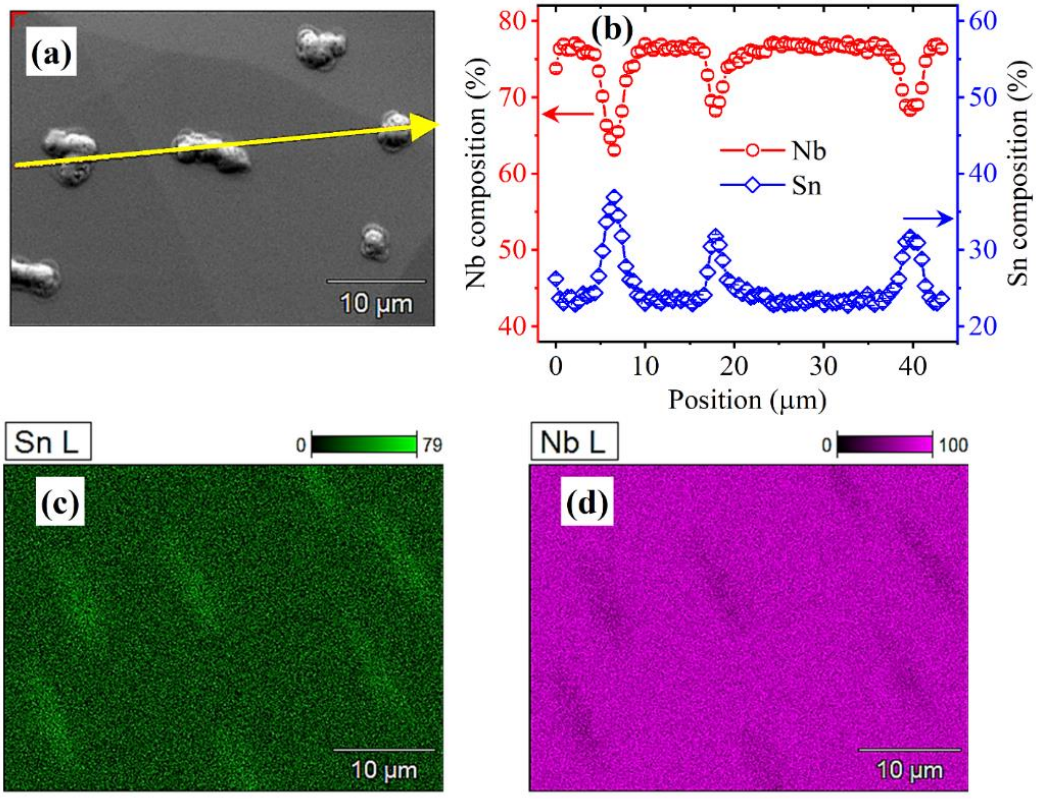

Fig. 4.17. (a) SEM image of Nb-Sn multilayered films deposited at 250 °C. The arrow shows the location of the EDS line scan. (b) Corresponding elemental composition from the EDS line-scan. (c) Elemental mapping of Sn. (d) Elemental mapping of Nb [117].

The SEM images of the annealed films are shown in Fig. 4.18. The inset of Fig. 4.18 shows the magnified images of the surface. The film coated at RT, shown in Fig. 4.18(a), had grains with an average size of ~200 nm with some voids distributed throughout the surface. The films coated at 100 °C, shown in Fig. 4.18(b), had fewer voids than those deposited at RT. The average size of the grains at clusters was smaller than the grains in the flat areas between the clusters. Similar morphology was also observed on the annealed films coated at 150 and 250 °C in Fig. 4.18(c) and 4.18 (d), respectively. Fig. 4.18(e) and 4.18(f) show the SEM images at location 1 (where the voids are found) and 2 (void-free location), respectively, obtained from Fig. 4.18(d).

The Sn composition of the films was measured by EDS over an area of 1.2 mm^2. The results are summarized in Table 4.5. The atomic compositions were derived by averaging the Sn compositions at five different locations on the films. The as-deposited film had ~25% Sn, which reduced to ~21% when annealed at 950 °C for 3 h.

Table 4.5. Sn composition of as-deposited and annealed films coated at different temperatures.

Deposition temperature (°C)	Sn % As-deposited	Sn % Annealed
RT	25.4 ± 0.7	21.1 ± 0.3
100	24.6 ± 0.8	20.7 ± 0.3
150	25.1 ± 0.4	21.2 ± 0.4
250	24.7 ± 0.8	21.2 ± 0.4

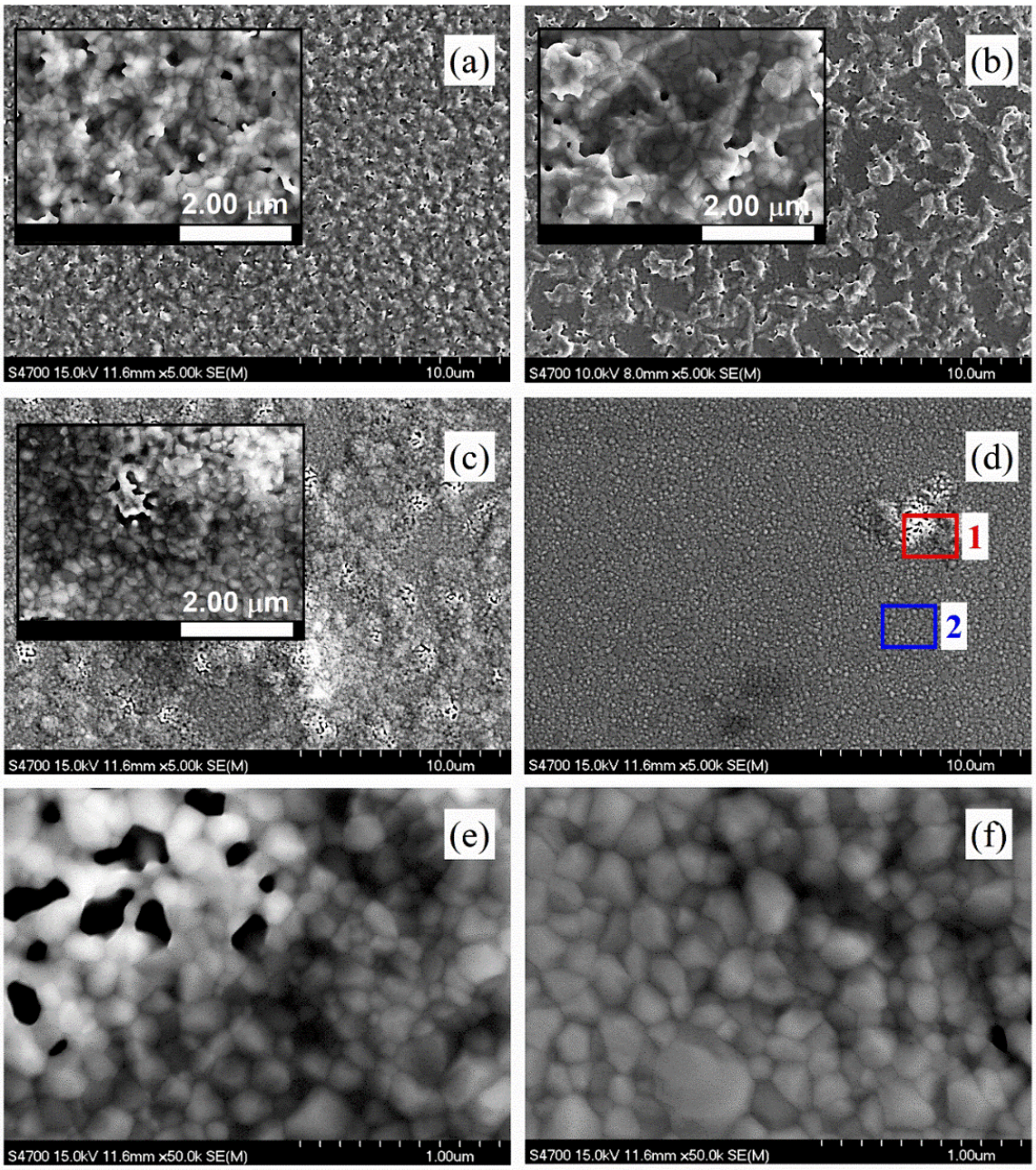

Fig. 4.18. SEM images of the annealed Nb_3Sn films on Nb substrates deposited at different temperatures: (a) RT, (b) 100 °C, (c) 150 °C, and (d) 250 °C. (e) Magnified image of area 1. (f) Magnified image of area 2 of (d) [117].

The AFM images recorded for a scan area of 20 µm × 20 µm are shown in Fig. 4.19(a-d).

The root-mean-square (RMS) surface roughness of the films is shown in Fig. 4.19(e). The error

bars in Fig. 4.19(e) represent the standard deviation of measurements of three different surface areas. The roughness of the films increased from 34 to 51 nm when the substrate temperature was increased from RT to 100 °C. Fig. 4.19(f) shows the line-scan of the films along the arrows indicated in Fig. 4.19(a-d). The maximum peak-to-valley height of the cluster in Fig. 4.19(b) was ~280 nm. At the substrate temperature of 150 °C, the surface had clusters of similar texture separated by small flat areas, as observed in the SEM image in Fig. 4.18(c). The RMS roughness was ~32 nm. Further increase in the substrate temperature increased the area of separated smooth flat regions, accompanied by a small increase in the surface roughness due to the topography difference between the smooth flat surface and the rough clusters. The clusters had a peak-to-valley height of 50 – 120 nm. Since the surface morphology shown in Fig. 4.19 is measured over an area of 20 μm × 20 μm, the measure of roughness should be considered in view of the limited surface area probed.

To better understand the development of the voids in the Nb_3Sn film, the cross-section of the as-deposited and annealed films deposited at RT and 250 °C were examined by TEM, as shown in Figs. 4.20(a) and 4.20(b), respectively. For the films deposited at RT, the as-deposited film showed columnar growth of the 200 nm thick Nb buffer layer, multilayers of Nb and Sn, and voids throughout the cross-section. The annealed films also had multiple voids throughout the cross-section. The film deposited at 250 °C had the columnar Nb buffer layer and stacks of multilayers. In contrast to the film deposited at RT, the film deposited at 250 °C did not show any voids between the multilayered stacks, as observed in Fig. 4.20(c). However, large grains with a height of ~500 nm were observed between the multilayer stacks. Annealing the Nb-Sn multilayers that were deposited at 250 °C resulted in a Nb_3Sn film without voids between the film grains. For the films deposited at RT and 250 °C, some voids were found at the interface of

the Nb substrate and the Nb buffer layer. These voids could have formed due to the Kirkendall effect, in which voids are formed near the intermetallic interface where the volume of one phase increases and the volume for the other phase decreases due to the difference in the diffusion rates of the two metals [118-120].

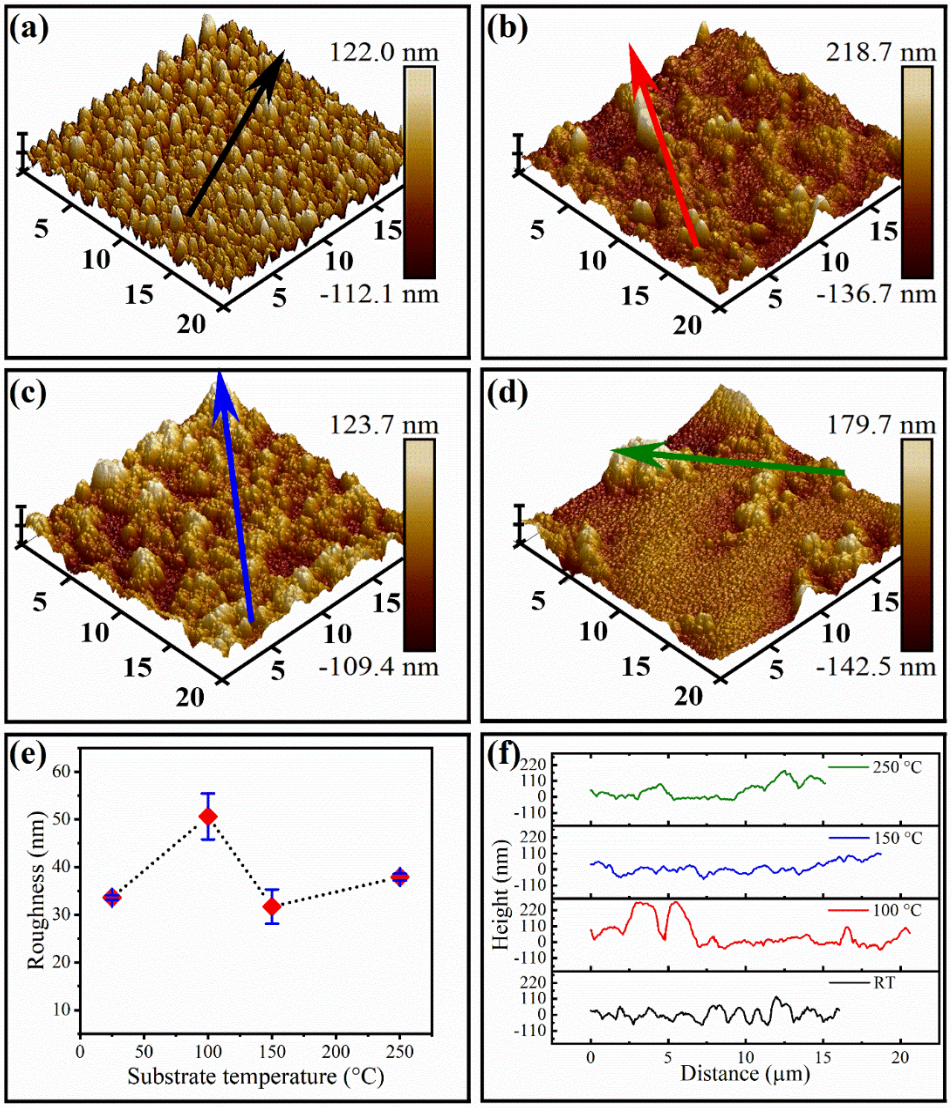

Fig. 4.19. (a-d) AFM images of Nb_3Sn films fabricated at a substrate temperature of (a) RT, (b) 100 °C, (c) 150 °C, (d) 250 °C. (e) Surface roughness of the films at different substrate temperatures. (f) Line-scans of the films obtained from the AFM images [117].

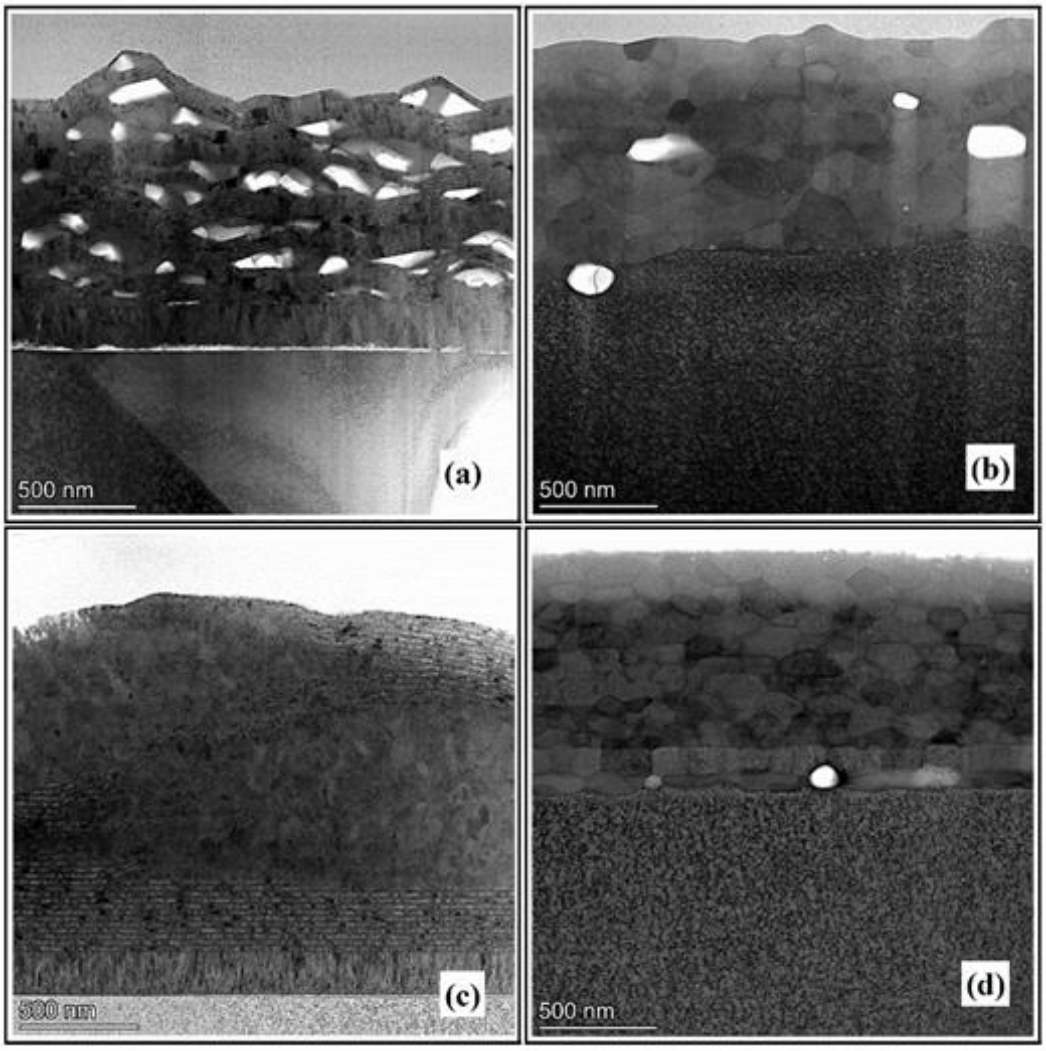

Fig. 4.20. TEM images of the cross-sections of the films: (a) As-deposited film sputtered at RT. (b) Annealed film deposited at RT. (c) As-deposited film sputtered at a substrate temperature of 250 °C. (d) Annealed film sputtered at a substrate temperature of 250 °C. The bright feature at the Nb_3Sn-Nb interface is void [117].

The EDS elemental mappings of the cross-sections of the films are shown in Fig. 4.21. The as-deposited film with the substrate at RT had Sn rich area near the voids, as observed in Fig. 4.21 (a). After annealing, Nb_3Sn forms by diffusion of Sn, and the voids remained throughout the cross-section of the film, as observed in Fig. 4.21(b). For the as-deposited film with the substrate at 250 °C, the EDS mapping showed Sn abundance at the large grains, but no

voids were observed, as shown in Fig. 4.21(c). Also, no voids were observed in the Nb_3Sn film after annealing, as shown in Fig. 4.21(d). Therefore, diffusion of Sn plays a major role in the formation of voids in Nb_3Sn growth by multilayer sputtering.

To better understand the development of Sn-rich clusters on the surface during the growth of the multilayers, I deposited different numbers of Nb-Sn multilayers at a substrate temperature of 250 ℃. Fig. 4.22 shows the SEM images of the surface of the films consisting of 1, 3, 10, and 34 layers (each layer is 20-nm Nb, 10-nm Sn). Fig. 4.22(a) shows several bright dotted circles on the surface of the Nb-Sn film of only 1 multilayer. The island growth starts from the first Sn layer as.

The inset of Fig. 4.22(a) shows bright elongated grains similar to the bright grains observed in Fig. 4.22(c-d). Increasing the number of multilayers enhance the density and size of the clusters. It appears that Sn clusters are formed at the early stages of the deposition due to the formation of liquid Sn droplets (melting point of Sn is 231 ^{o}C). With increased multilayer numbers, the size of the spherical-shaped grains increases. The spherical grains are probably formed by the condensation of liquid Sn droplets.

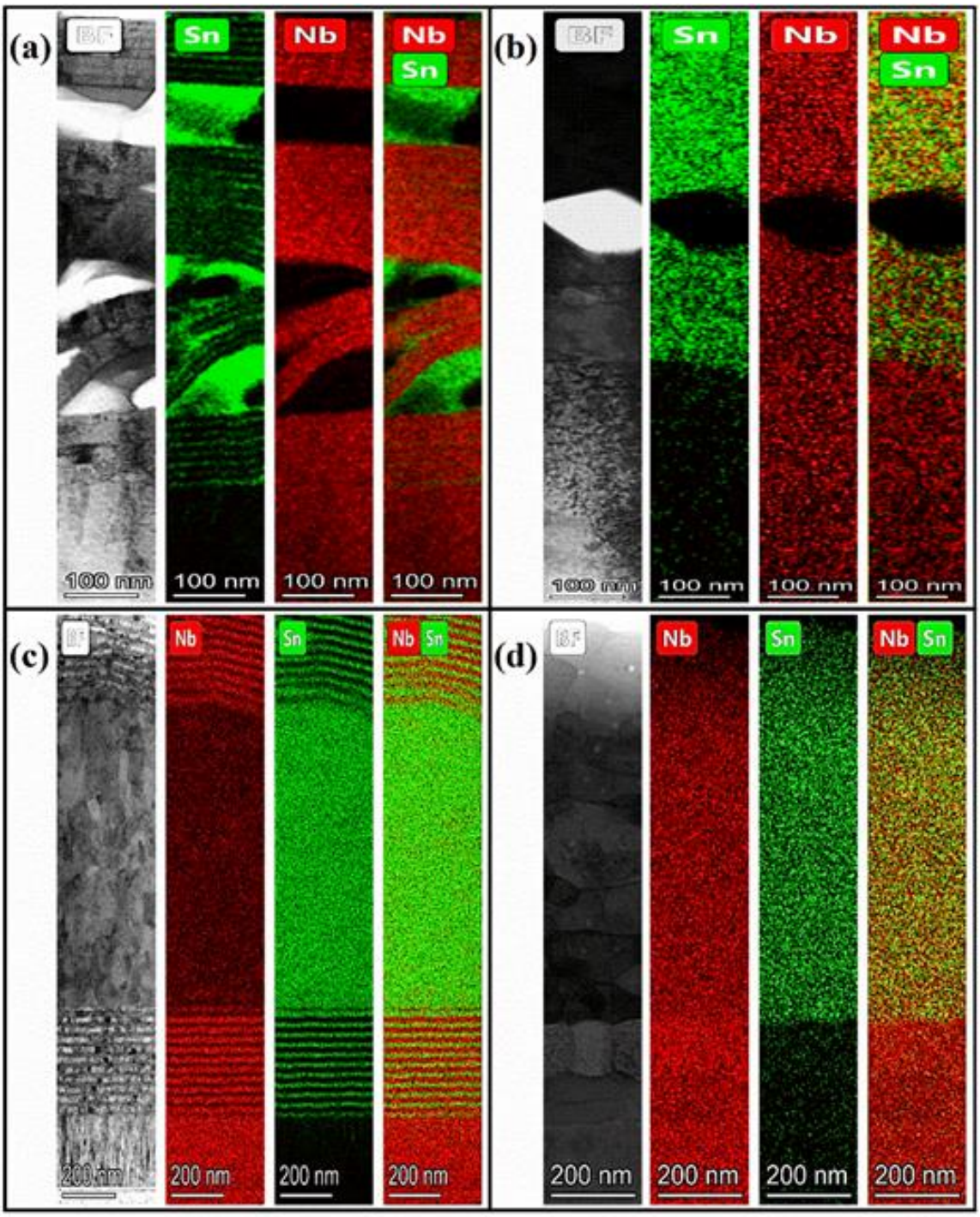

Fig. 4.21. TEM EDS mappings of the cross-sections of the films: (a) As-deposited film on substrate at RT. (b) Annealed film deposited with the substrate at RT. (c) As-deposited film sputtered at a substrate temperature of 250 °C. (d) Annealed film sputtered at a substrate temperature of 250 °C.

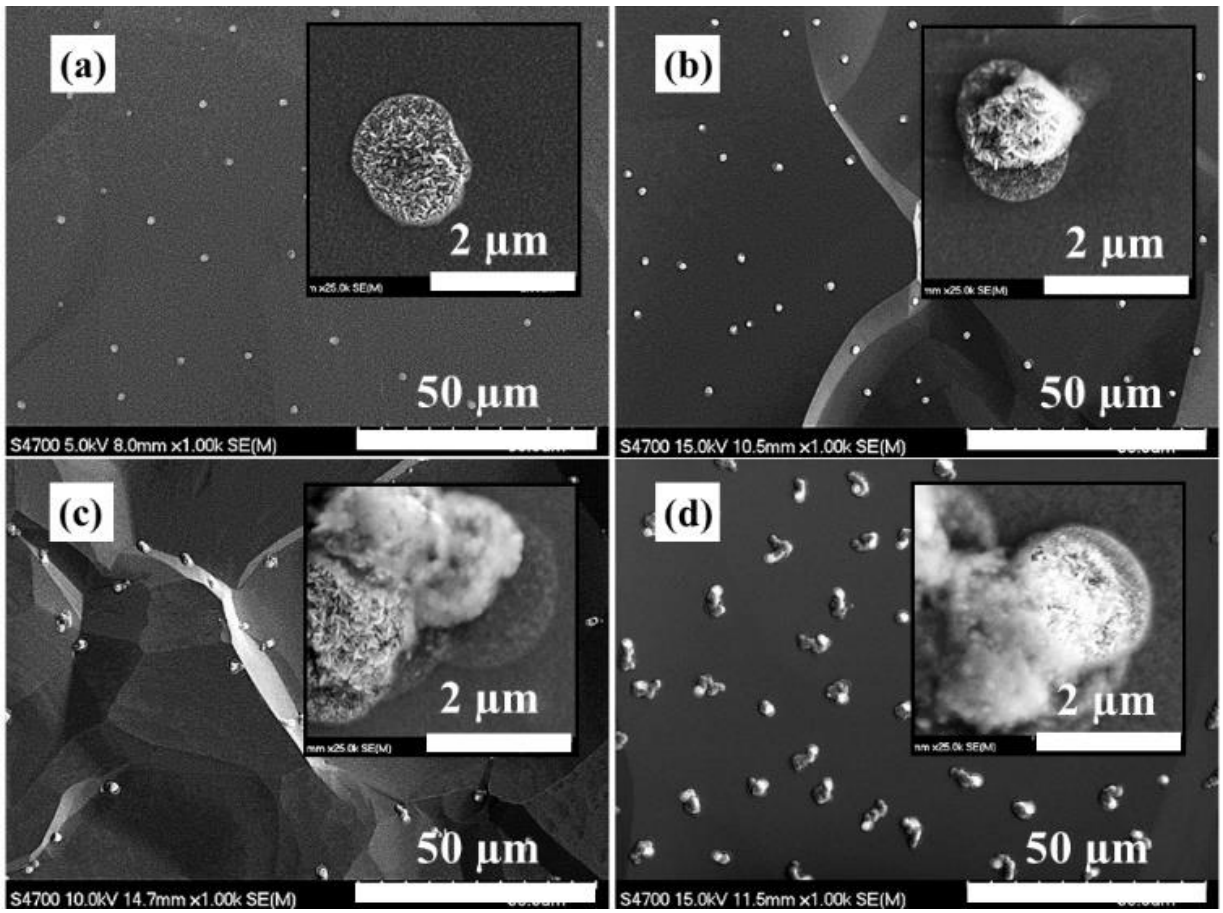

Fig. 4.22. SEM images of the Nb-Sn multilayers deposited at 250 °C with varied multilayer numbers: (a) 1 (b) 3, (c) 10, and (d) 34. The inset shows the magnified images of the surface.

4.3.3.1.2. Superconducting Properties

The temperature-dependent resistance of the annealed films measured by four-point probe over the range 4.5 to 300 K is shown in Fig. 4.23. The resistance decreased as the temperature is lowered, with a sharp resistance decrease observed below 18 K. The resultant superconducting T_c, ΔT_c, and *RRR* are summarized in Table 4.6. For all films, T_c varied in a narrow range of 17.58 – 17.76 K, which correspond to the T_c of Nb_3Sn. The transition width of the film was observed to increase with increasing the deposition substrate temperature. The film

coated at 250 °C had lower T_c and *RRR* and higher ΔT_c, though the surface of the film had fewer voids. Broader ΔT_c in Nb_3Sn thin films is often found because of non-uniform Sn composition or disorder in the crystalline lattice. Kampwirth et al. observed a broad ΔT_c of 5.8 K with three different transitions for Nb_3Sn films sputtered from a stoichiometric target on a sapphire substrate at a sputtering pressure of 5 mTorr and a substrate temperature of 800 °C [60]. Ilyina et al. reported an average ΔT_c of 1.7 ± 1.4 K for the Nb_3Sn films sputtered from a stoichiometric Nb_3Sn target [66]. The annealed film deposited at 250 °C showed two transitions at 17.4 and 17.8 K, which is due to the Sn composition variation throughout the film.

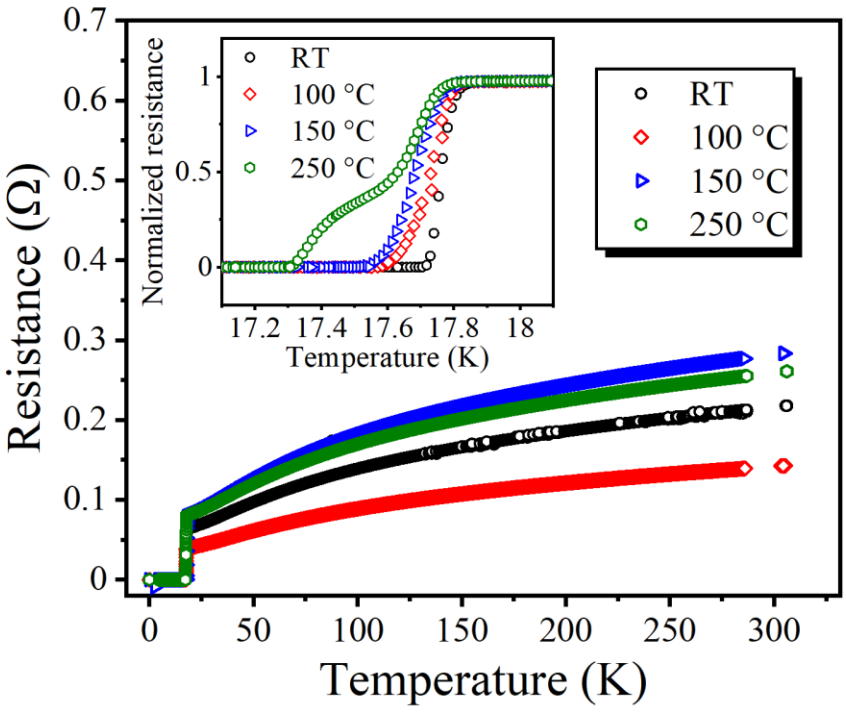

Fig. 4.23. Temperature dependence of the resistances of 1 µm thick Nb_3Sn films deposited at different substrate temperatures. The inset of the image shows the plot of normalized resistance (R/R_{20K}) with temperature close to T_c [117].

Table 4.6. Summary of the superconducting properties of the films.

Deposition temperature (°C)	T_c (K)	ΔT_c (K)	RRR
RT	17.76	0.06	3.42
100	17.72	0.13	3.53
150	17.67	0.15	3.49
250	17.58	0.37	3.18

4.4. RF Superconducting Properties

RF properties of the Nb_3Sn film were measured by the 7.4 GHz SIC system at Jefferson Lab and compared with a vapor diffused Nb_3Sn film [121]. The film was fabricated by annealing a Nb-Sn multilayer film that was deposited at room temperature. The T_c of the film was measured from the loaded quality factor of the cavity, as mentioned in Chapter 2. The resulting loaded quality factor as a function of sample temperature is shown in Fig. 4.24(a). The loaded Q_L value dropped gradually with increasing sample temperature until it reached the T_c of the film. The film exhibited a T_c of 17.2 K. Above this temperature, the Q_L value remained almost constant.

Fig. 4.24(b) shows the RF surface resistance of the sputtered film as a function of sample temperature. The surface resistance of a Nb_3Sn film fabricated by Sn vapor diffusion method in the same system is also plotted for reference. The measured surface resistance has temperature dependent BCS surface resistance and temperature independent residual resistance. At 12 K, the residual resistance of the sputtered Nb_3Sn film was ~5 mΩ, whereas the vapor diffuse sample exhibited residual resistance of ~60 μΩ. The sputtered sample had a superconducting transition

temperature lower than that of the vapor diffused sample. The inset of Fig. 4.24(b) shows the BCS portion of the surface resistance fitted by the SRIMP code by Jurgen Halbritter [122]. With constant fitting parameters coherence length ξ_0= 7 nm and mean free path = 3.10 nm, the residual resistance and the superconducting gap Δ obtained from the fit were 3.87 ± 0.28 mΩ and 2.52 ± 0.96 meV respectively.

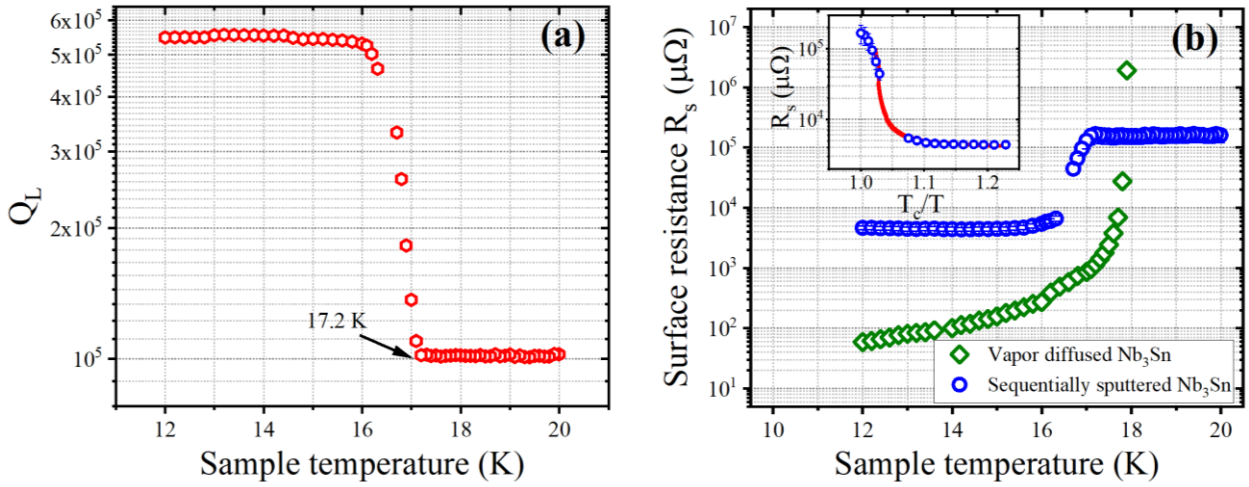

Fig. 4.24. (a) Loaded quality factor Q_L as a function of sample temperature of the film, (b) RF surface resistance as a function of sample temperature of the sputtered (blue circle) and vapor diffused (green diamond) Nb_3Sn films. The inset shows the BCS fit of the sputtered sample. The data for the vapor diffused sample was obtained from [121].

The superconducting T_c and gap of Nb_3Sn films depend on the atomic composition of Sn present on the films [24]. Sn composition on the sputtered film was less than standard composition of 25%. As a result, the RF superconducting T_c of the sputtered Nb_3Sn film was lower than that of the vapor diffused Nb_3Sn film. Based on the relationship between the superconducting T_c and gap with the Sn composition as reported by Godeke et al. [24], the Sn

composition of the film should be ~24% to achieve a T_c ~17 K and a superconducting gap ~2.50 meV. The Sn composition of the sputtered film was ~23% as obtained from EDS. Note that, the depth resolution of EDS is limited; for 15 keV electron, the X-ray transmission fraction for Nb-Lα and Sn-Lα lines are smaller than the thickness of the film. The residual resistance of the sputtered film was higher than the residual resistance of the vapor diffused Nb_3Sn film. The higher residual resistance of the sputtered film originated from the Nb of the uncoated regions of the substrate. RF surface resistance measurement at lower temperatures up to 2 K reported previously showed a second transition at ~8 K due to the uncoated region of the substrate [123]. Since the uncoated part of the substrate remains in the normal conducting state up to its critical temperature (9.23 K), the resistance measured is higher to 5 mΩ even though the film is in superconducting state below 17.2 K.

Another possible reason for the higher residual resistance of the sputtered Nb_3Sn film could be the voids observed on the surface. The residual resistance as well as the T_c of the films can be improved by improving the film surface and stoichiometry by optimizing the coating and annealing parameters.

4.5. Summary

Nb_3Sn films were fabricated by multilayer sputtering of Nb and Sn films and annealing the multilayer films. The effect of multilayer thickness on the structural and superconducting properties of the films were studied by varying the layer thickness ratio (Nb:Sn of 1:1, 2:1, 3:1 and 4:1) and varying both Nb and Sn thicknesses (Nb:Sn of 10:5, 20:10, 50:25 and 200:100) and annealing all films at 950 °C for 3 h. The highest Tc of 17.93 K was achieved on the film with a Nb:Sn thickness ratio of 1:1 but the surface of the film was very rough with large, cracked structure. Nb:Sn thickness ratio of 2:1 was used to study the effect of annealing temperature by

annealing at 850, 950, 1000, 1100, and 1200 °C. Annealing at temperatures higher than 1000 °C resulted to significant Sn loss due to evaporation. Film morphology was also optimized by varying the deposition temperature from room temperature to 250 °C. Depositing at high temperatures resulted to Sn rich island structures on the films. From these studies, the suitable deposition condition for fabricating Nb_3Sn film was determined and the RF superconducting properties of the film were measured and compared with the RF properties of a vapor diffused Nb_3Sn film using the 7.4 GHz SIC system. The film has a RF superconducting transition at 17.2 K. The residual resistance was higher than the vapor diffused Nb_3Sn film, partially, because of the uncoated Nb substrate region where the sample was held during the deposition. The results suggest that multilayer sputtering method can be a potential method to deposit Nb_3Sn inside SRF cavities.

CHAPTER 5

NB_3SN FABRICATION BY CO-SPUTTERING

5.1. Introduction

Co-sputtering has been used to deposit multi-elemental thin films because of the control on the stoichiometry. Since the elements are deposited from separate targets, the stoichiometry of the films can be adjusted by tuning each target power during the sputtering. The method has been successfully used to fabricate many types of thin films including superconducting YBCO [124], MgB_2 [125, 126], NbTiN [127], Nb_3Ge [128, 129], and Nb_3Sn [67, 68] thin films.

Tan et al. fabricated Nb_3Sn films on copper substrates by co-sputtering at a substrate temperature up to 500 °C, then annealed at a temperature up to 750 °C [67]. The maximum T_c achieved was 15 K [67]. Schafer et al. reported the properties of superconducting Nb_3Sn films fabricated by co-sputtering on glass substrates [68]. The films had crystalline Nb_3Sn structure with a maximum T_c of 16.31 K obtained for the films fabricated at a substrate temperature of 435 °C. Since most of the previously reported studies focused on the application of co-sputtering for coating Cu SRF cavities, the substrate temperature during the deposition and annealing was kept below 750 °C due to the thermal softening of Cu. I have fabricated Nb_3Sn films by co-sputtering of Nb and Sn on Nb substrates and studied the film properties at different power ratios, substrate temperatures, and annealing temperatures. A maximum annealing temperature of 950 °C was used to study the film properties for its application in Nb SRF cavities.

5.2. Design of Experiments

Fig. 5.1 shows the schematic of the sputter deposition chamber. The Nb target was connected to a DC power supply and the Sn target was connected to a RF power supply. Ar gas

was used as the sputtering gas during the process. A 200 nm thick Nb barrier layer was first deposited on the substrate. Then, Nb and Sn were sputtered simultaneously. The ratio of Nb and Sn in the film was varied while keeping the substrate at a constant substrate temperature of 400 °C.

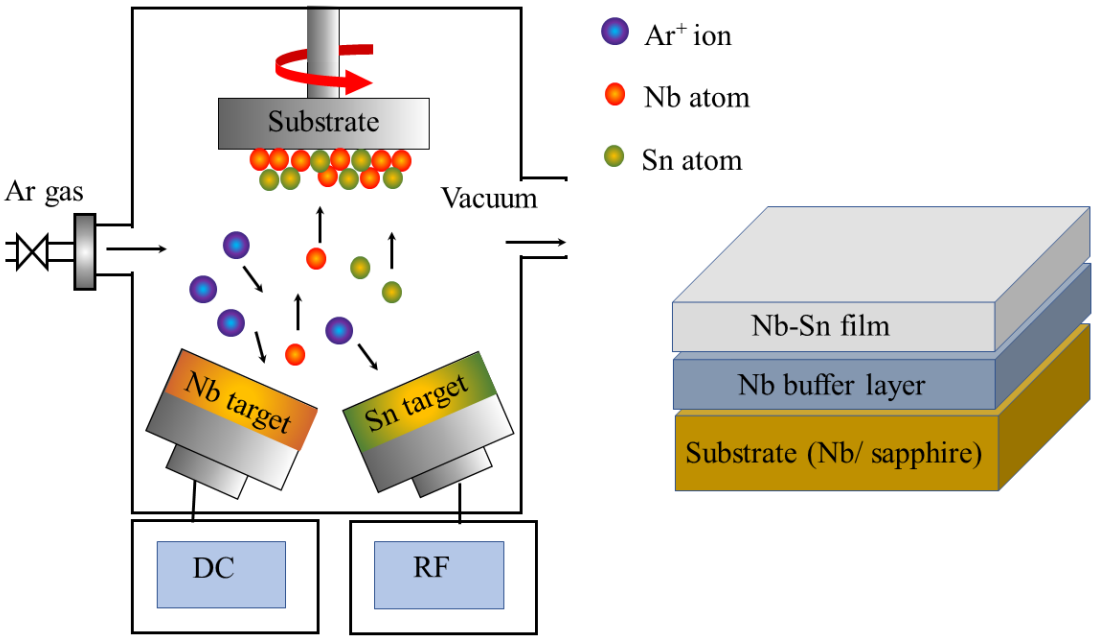

Fig.5.1. Schematic diagram of the co-sputtering process and the deposited films.

To vary the Sn deposition rate, the RF power applied to the Sn target was varied from 25 to 30 W, whereas the DC power applied to the Nb target was set at 190 W. The goal of this experiment was to obtain the appropriate power ratio to reach atomic Nb:Sn ratio close to 3:1. A magnetron power ratio of 190 W: 28 W was found to give the Nb:Sn ratio needed to form Nb_3Sn. That ratio was used to study the properties of the Nb_3Sn films fabricated at varied

substrate temperatures (room temperature, 200, 300, 400 and 500 °C). The effect of post-annealing on the structural, morphological, and superconducting properties of the films were also studied at annealing temperatures of 665 and 950 °C.

5.3. Results and Discussions

5.3.1. Effect of Varied Power Ratio

The XRD patterns of the films co-sputtered using varied Sn power is shown in Fig. 5.2. The diffraction peaks correspond to Nb_3Sn (200), (210), (211), (320), (321), (400), (420), and (421) diffraction orders. The observed Nb (200) and (210) diffraction orders arise from the Nb buffer layer and substrate. The peak intensities of Nb_3Sn ((320), (321), (420), (421)) diffraction peaks became visibly weak with increased Sn power to 30 W.

The atomic Sn composition of the films deposited at different Nb:Sn power ratios is shown in Table 5.1 and the Sn composition as a function of power ratio is shown Fig. 5.3. It is found that the Sn composition of the films vary significantly with a small change in the power applied to the Sn target for fixed power applied to the Nb target. Based on the XRD patterns and Sn composition, high quality Nb_3Sn films with correct stoichiometry can be obtained using DC power of 190 W for the Nb target and RF power of 28 W for the Sn target.

Table 5.1. Atomic composition of Sn at varied power ratio of Nb and Sn.

Nb target power (W)	Sn target power (W)	Sn composition (%)
190	25	21.96 ± 0.19
190	27	25.00 ± 0.50
190	28	25.47 ± 0.57
190	30	28.21 ± 0.30

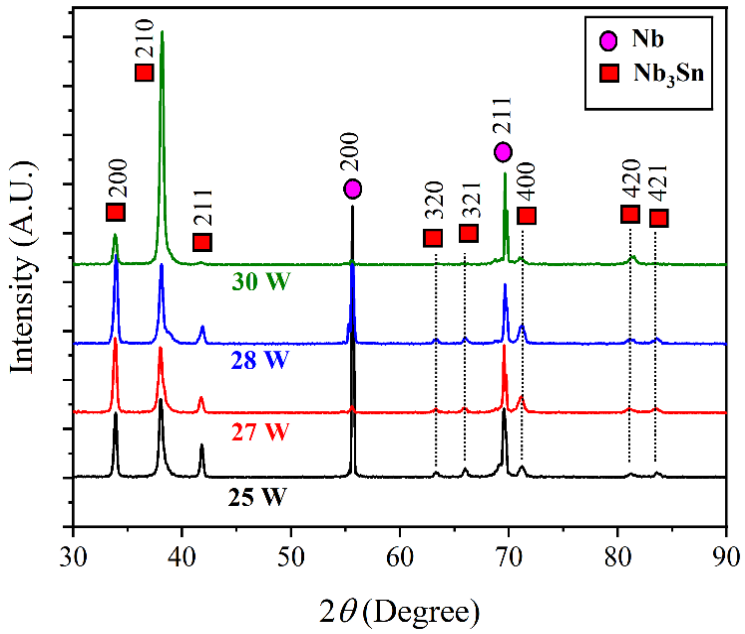

Fig. 5.2. X-ray diffraction patterns of the co-sputtered films at a substrate temperature of 400 °C. The power applied to the Nb target during sputtering was kept constant at 190 W, whereas the power applied to the Sn target was 25, 27, 28, and 30 W.

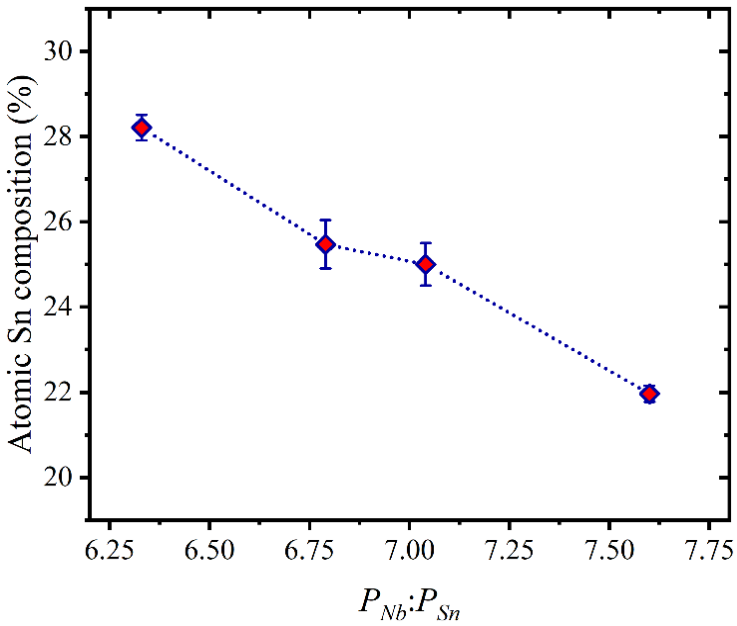

Fig. 5.3. Sn composition (At. %) obtained from EDS as a function of the ratio of power applied to the magnetrons with Nb and Sn targets (P_{Nb}:P_{Sn}). The error bar represents the standard deviation of the measurements at five different locations in a 1.5 μm^2 area.

5.3.2 Effect of Varied Substrate Temperature

5.3.2.1 Structural and Morphological Properties

Fig. 5.4 shows the XRD patterns of films coated by co-sputtering at different substrate temperatures. The film deposited at room temperature did not form Nb_3Sn and the XRD patterns did not show any diffraction peak due to Nb_3Sn. Films deposited at a substrate temperature of 200, 300, 400, and 500 °C show diffraction orders of Nb_3Sn. The improved crystalline structure of Nb_3Sn with increased substrate temperature was clearly visible from the XRD patterns. At substrate temperatures of 200 and 300 °C, diffraction peaks of Nb_3Sn 211, 320, 321, 400, 420, and 421 were either absent or the peak intensity was too weak. At 400 °C, almost all the expected diffraction peaks of Nb_3Sn were visible without any peaks corresponding to Nb_6Sn_5 and $NbSn_2$ phases. The Nb_3Sn diffraction peak intensities increased for substrate temperature of 500 °C. The FWHM of the diffraction peaks were reduced with increased substrate temperature indicating the increased crystallite size at higher coating temperatures. The crystallite sizes obtained from the FWHM of the (200) and (210) diffraction orders are reported in Table 5.2, along with the atomic Sn composition of the films obtained from EDS. The film deposited at room temperature had ~30% Sn whereas the other films had ~24-26% Sn and no significant trend in composition was observed with increasing the substrate temperatures.

Table 5.2. Properties of co-sputtered films at different substrate temperatures.

Substrate temperature (°C)	Crystallite size (200) diffraction (nm)	Crystallite size (210) diffraction (nm)	Sn composition (%)
RT	---	---	29.88 ± 1.05
200	19.79	14.58	25.78 ± 0.45
300	18.90	13.55	26.20 ± 1.48
400	22.33	18.70	25.47 ± 0.57
500	26.44	23.34	24.22 ± 0.36

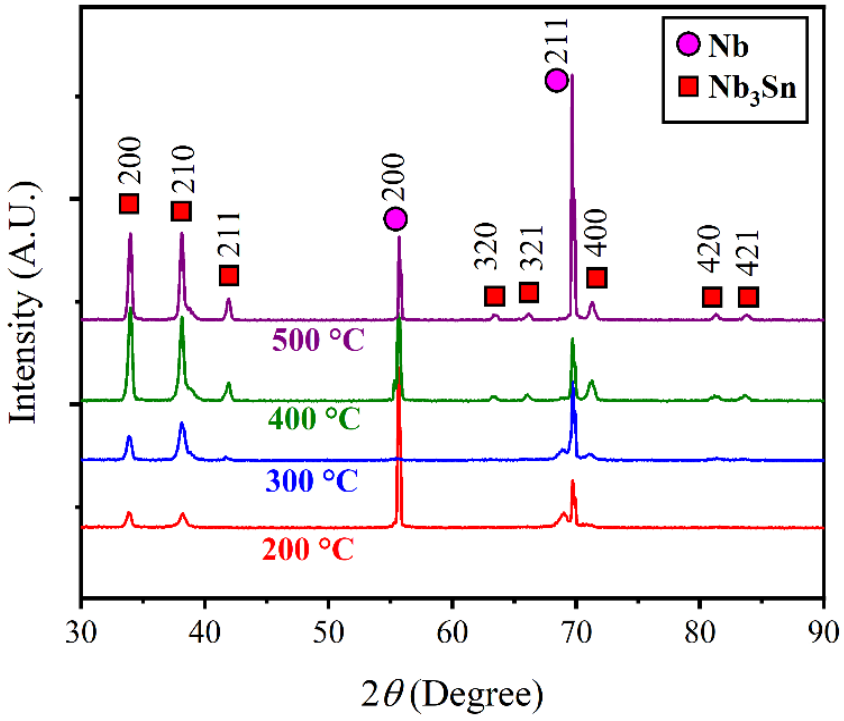

Fig. 5.4. XRD patterns of the Nb_3Sn films fabricated by co-sputtering of Nb and Sn at a power of 190 W and 28 W applied to the Nb and Sn targets, respectively. The substrate temperatures were 200, 300, 400, and 500 °C.

The SEM images of the co-sputtered Nb-Sn films at different substrate temperatures are shown in Fig. 5.5. For the film deposited at room temperature, elongated grain structures with random orientations are observed throughout the whole surface. Similar elongated structures were observed on sputtered Nb films on glass substrates [130, 131]. With increasing substrate temperatures, the size of the elongated grains increased. At the same time, some islands started to form. With increasing substrate temperatures, the density of the islands increased, and the density of the elongated grains was reduced.

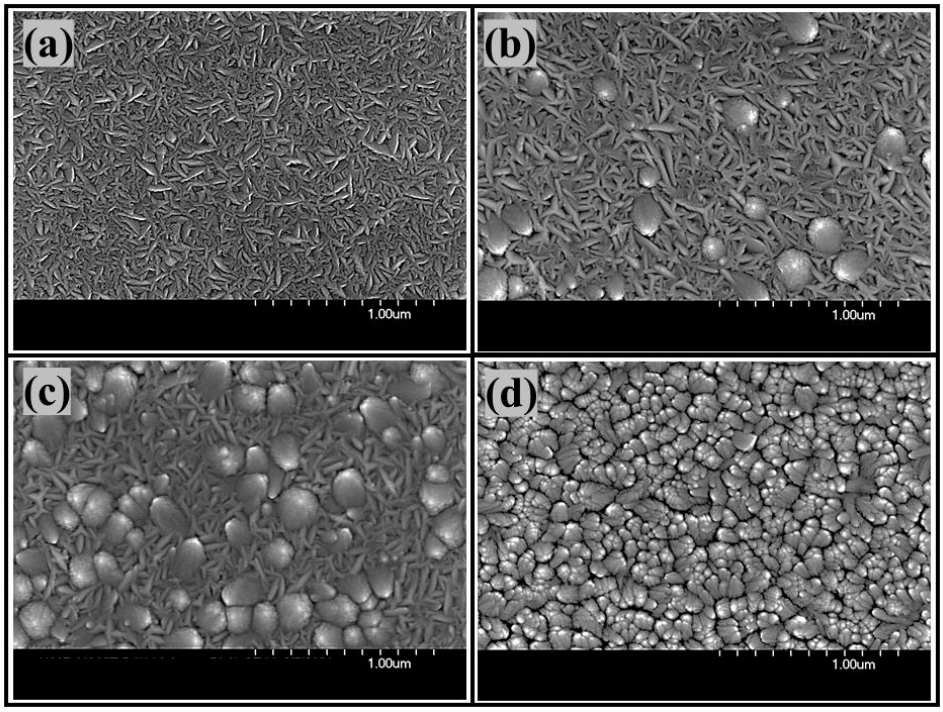

Fig. 5.5. Surface morphology of the as-deposited films deposited at different substrate temperatures: (a) room temperature, (b) 200 °C, (c) 300 °C, and (d) 400 °C.

At a substrate temperature of 400 °C, the whole surface is covered with the islands. At room temperature, co-sputtered Nb and Sn films do not form Nb_3Sn grains, and the film surface is dominated by the elongated Nb grains. At a substrate temperature of 200 °C, the atoms impinging on the surface gain enough energy to form Nb_3Sn. As a result, Nb_3Sn islands appeared randomly throughout the film and their density increased with temperature.

5.3.2.2 Superconducting Properties

The resistance of the films as a function of temperature is shown in Fig. 5.6. The inset of Fig. 5.6 shows the resistance of the films near the transition region. The film deposited at room temperature did not show any superconducting transition. All other films had superconducting transition due to Nb_3Sn. The measured T_c, ΔT_c, and *RRR* are shown in Table 5.3. The superconducting properties of the films improved with increased substrate temperature. The highest T_c =15.00 K was recorded for the film deposited at 500 °C.

Table 5.3. Superconducting properties of the films deposited at different substrate temperatures.

Substrate temperature (°C)	T_c (K)	ΔT_c (K)	*RRR*
RT	---	---	1.07
200	---	---	1.3
300	11.47	0.25	1.44
400	14.73	0.27	1.79
500	15.00	0.50	2.10

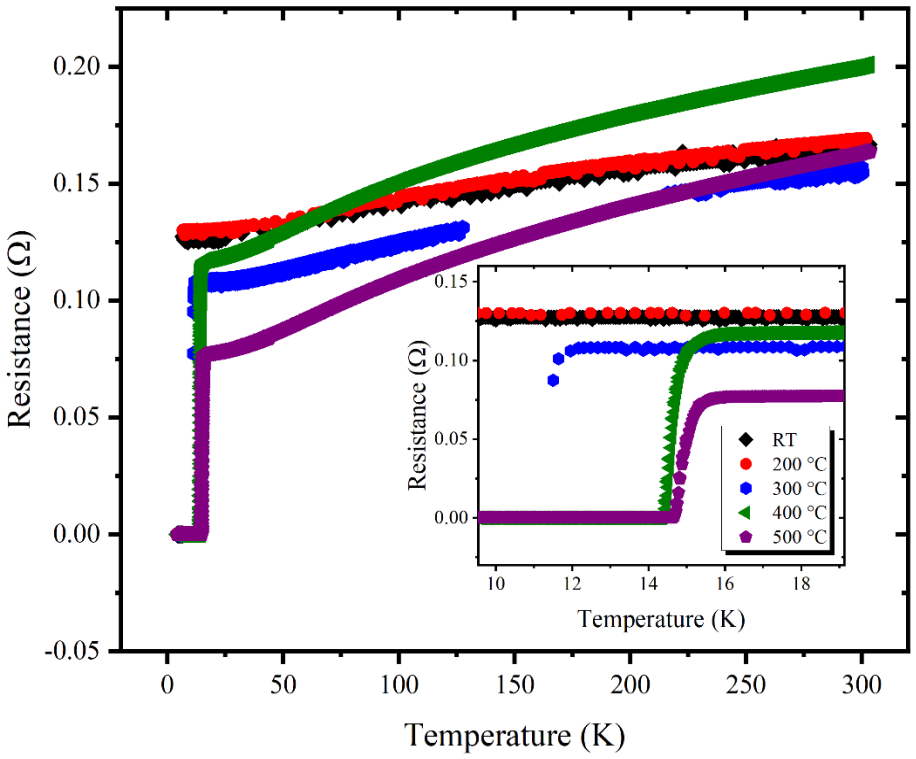

Fig. 5.6. Resistance versus temperature of the co-sputtered films deposited at different substrate temperatures. The inset shows the resistance near the transition.

5.3.3. Effect of Annealing

5.3.3.1. Structural and Morphological Properties

The XRD patterns of the films deposited at four different substrate temperatures (RT, 200, 300, and 400 °C) and then annealed at 665 and 950 °C for 3 h are shown in Fig. 5.7. The XRD peaks are from Nb_3Sn with some diffractions of Nb which are probably from the Nb buffer layer and substrate. The peak intensities of the films deposited at lower temperatures were stronger for the annealed films. The data suggests that high quality crystalline Nb_3Sn films can be fabricated by depositing films at room temperature and then annealing at 950 °C.

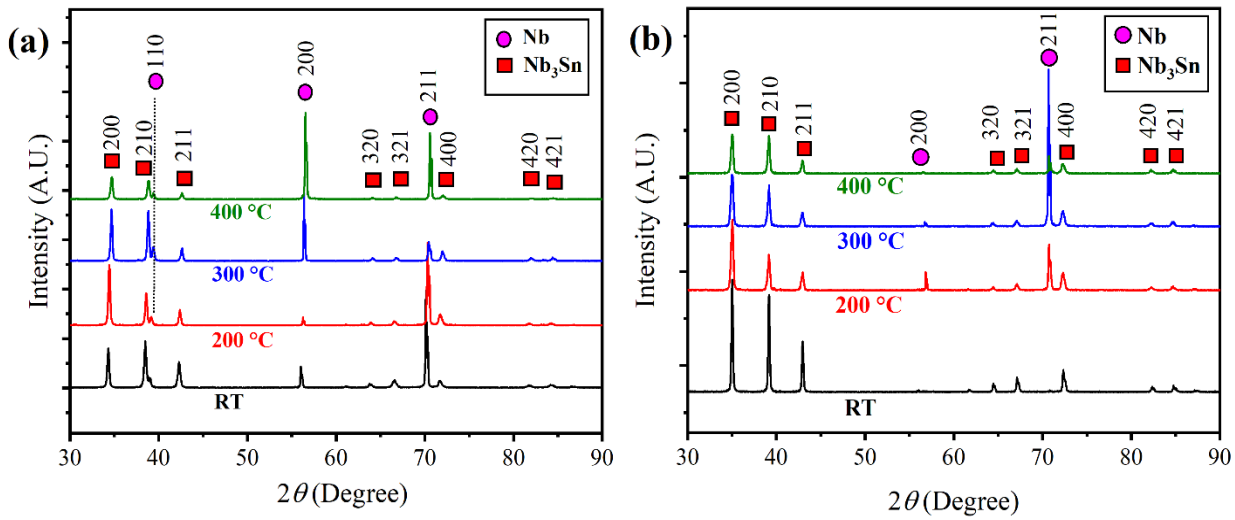

Fig. 5.7. X-ray diffraction pattern of the films deposited at different substrate temperatures and annealed afterwards at (a) 665 °C, and (b) 950 °C for 3 h.

The SEM images of the surface of the films annealed at 665 °C is shown in Fig. 5.8 and the AFM images obtained from the same film over a surface area of 5 µm × 5 µm are shown in Fig. 5.9. The RMS roughness of the films were estimated from the AFM images obtained over an area of 20 µm× 20 µm and the average roughness of two different locations of each film are shown in Table 5.4. The surface of the annealed films remained similar to the as-deposited films. The size of the elongated grains increased after annealing. The lowest roughness of 8.40 ± 1.12 nm is observed at this condition. The surface roughness increased to ~16-18 nm on the films deposited at 200-400 °C, which is due to the formation of islands with different heights.

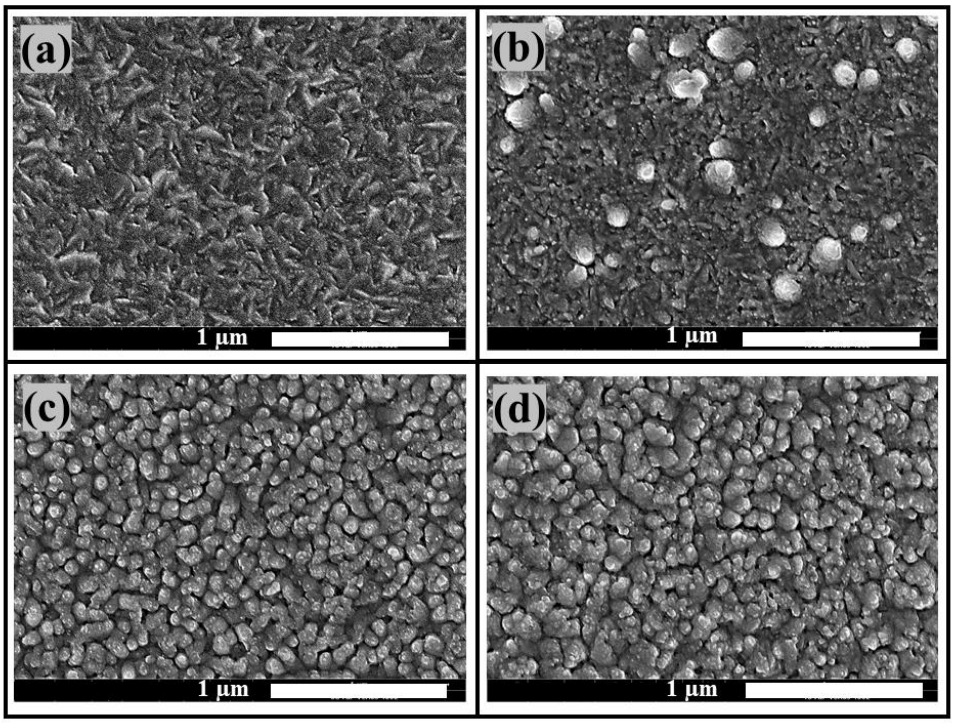

Fig. 5.8. SEM images of the films annealed at 665 °C for 3 h. The films were deposited at substrate temperatures of: (a) RT, (b) 200 °C, (c) 300 °C, and (d) 400 °C.

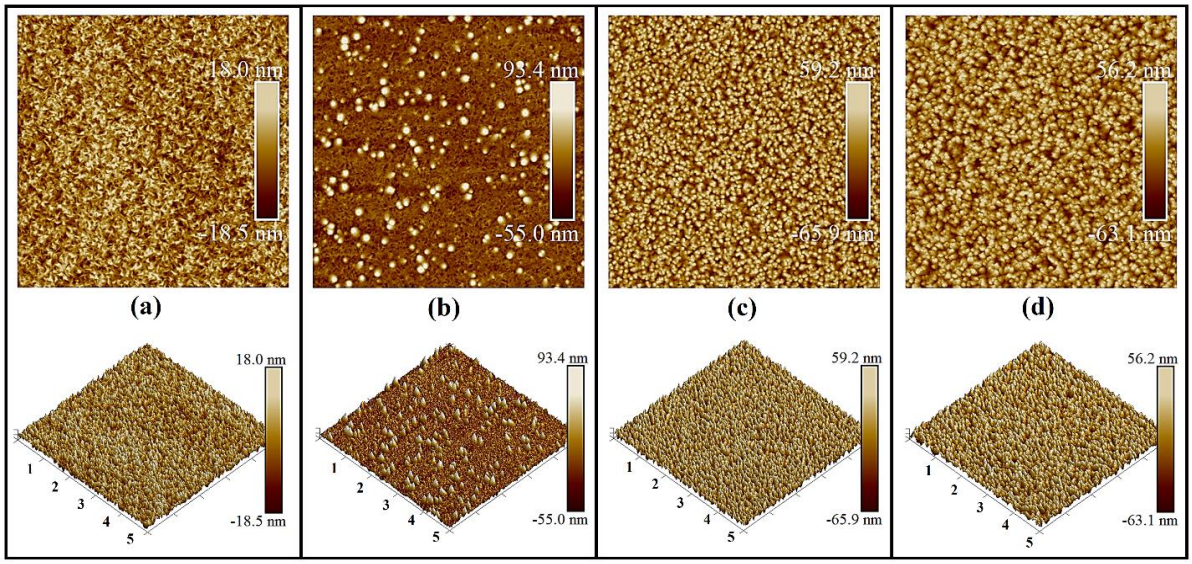

Fig. 5.9. AFM images of the films annealed at 665 °C for 3 h. The films were deposited at substrate temperatures of: (a) RT, (b) 200 °C, (c) 300 °C, and (d) 400 °C. AFM images were collected at an area of 5 µm × 5 µm by tapping mode. The SEM images of these films are shown in Fig. 5.8.

Fig. 5.10 and Fig. 5.11 show the SEM and AFM images of the films annealed at 950 °C respectively. The films had well-connected grains with grain boundaries without voids. The grain size of the annealed film deposited at room temperature had larger grains with an average grain size of 305 ± 120 nm. With increasing substrate temperatures, the grains became smaller, and the film deposited at 400 °C had the smallest average grain size of 140 ± 47 nm. The surface roughness of the films increased from 14.15 ± 3.04 to 18.70 ± 3.96 nm when the substrate temperature was increased from room temperature to 200 °C. The surface roughness remained in the same range to 18.30 ± 1.41 nm for the substrate temperature of 300 °C and was reduced to 11.20 ± 0.42 for the film deposited at 400 °C. It is observed from the SEM and AFM images that the films deposited at 200 and 300 °C had combination of large grains and smaller grains of different heights which resulted to a rougher surface. However, most of the grains on the films deposited at room temperature had large grains of similar heights. Similarly, the film deposited at 400 °C had mostly smaller grains with small height differences. Therefore, the surface was relatively smoother for these two deposition conditions.

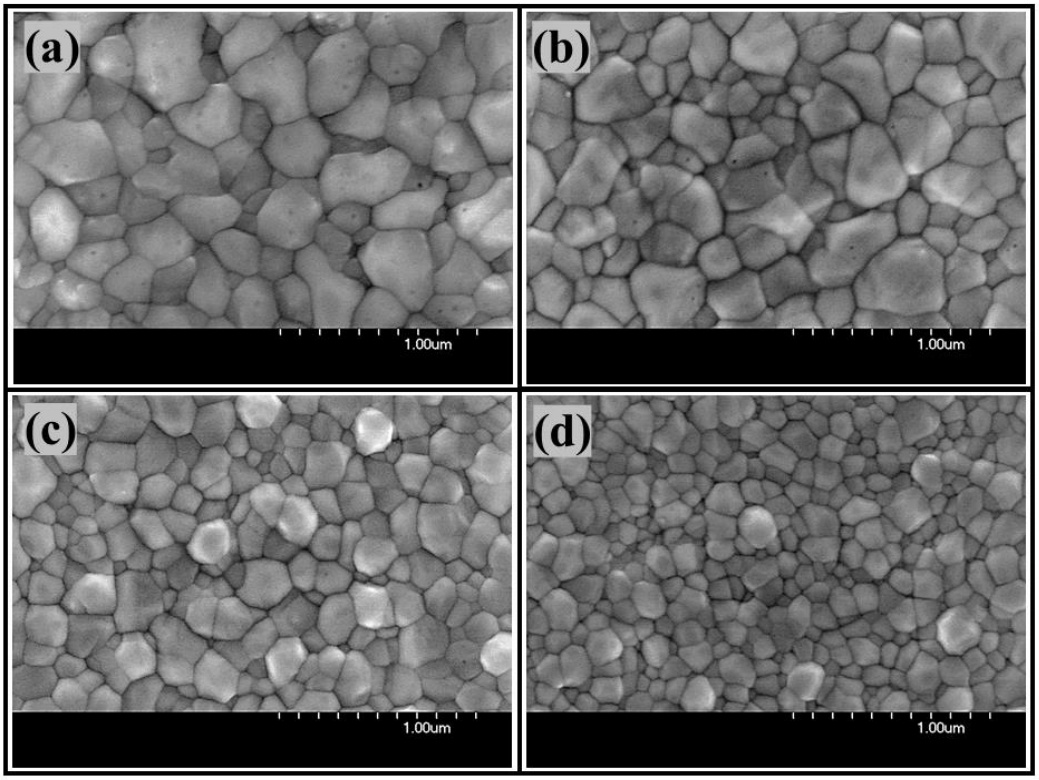

Fig.5.10. SEM images of the films annealed at 950 °C for 3 h. The films were deposited at substrate temperatures of: (a) RT, (b) 200 °C, (c) 300 °C, and (d) 400 °C.

The Sn composition of the films reduced after annealing and the Sn loss is higher at higher annealing temperature. For the films annealed at 665 °C for 3 h, the Sn composition reduced to ~23-27%. The highest Sn composition of ~27% was observed on the film deposited at room temperature. The as-deposited film for this condition also had the highest Sn composition on the surface. The films annealed at 950 °C had more reduced Sn composition of ~22-23% and no significant trend was observed on the Sn composition of the different films deposited at different substrate temperatures.

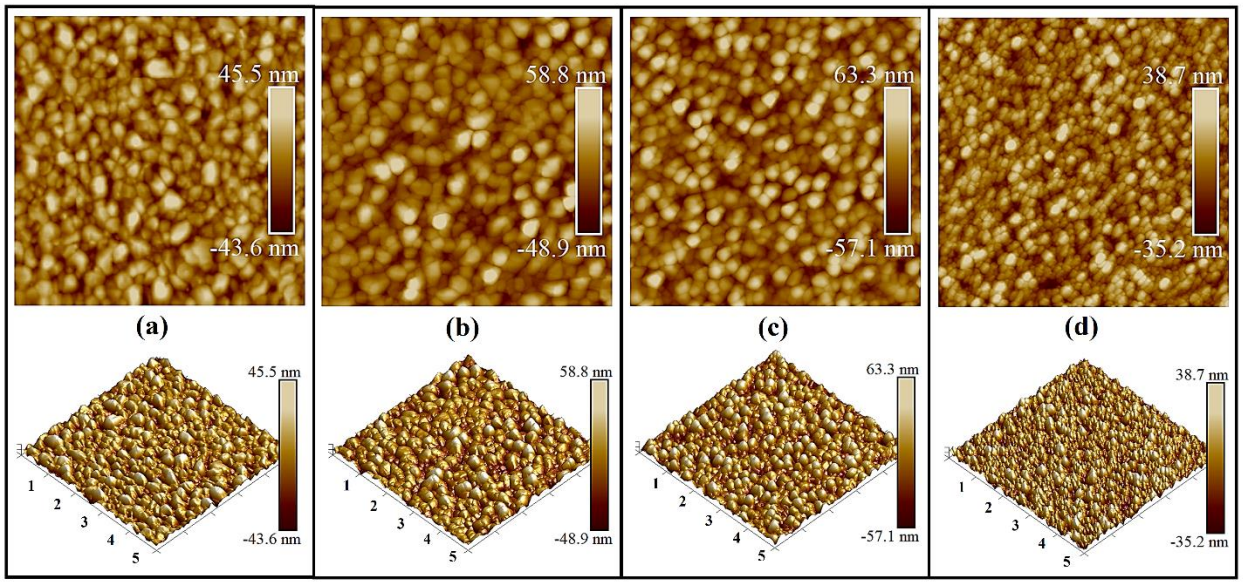

Fig. 5.11. AFM images of the films annealed at 950 °C for 3 h. The films were deposited at substrate temperatures of: (a) RT, (b) 200 °C, (c) 300 °C, and (d) 400 °C. AFM images were collected at an area of 5 µm × 5 µm by tapping mode. The SEM images of these films are shown in Fig. 5.10.

Table 5.4. Structural properties of the films after annealing at 665 and 950 °C for 3 h.

Annealing temperature (°C)	Substrate temperature (°C)	Crystallite size (200) diffraction (nm)	Crystallite size (210) diffraction (nm)	Sn composition (%)	Roughness (nm)
665	RT	32.34	25.92	26.96 ± 0.63	8.40 ± 1.12
665	200	29.00	25.11	24.83 ± 0.48	17.90 ± 0.99
665	300	31.83	27.84	23.03 ± 0.46	17.60 ± 0.28
665	400	26.69	24.43	23.34 ± 0.61	16.65 ± 0.49
950	RT	41.76	41.11	22.34 ± 0.41	14.15 ± 3.04
950	200	26.83	27.20	22.69 ± 0.68	18.70 ± 3.96
950	300	26.09	27.41	23.01 ± 0.27	18.30 ± 1.41
950	400	28.10	28.59	21.69 ± 0.31	11.20 ± 0.42

The cross-section of a film deposited at room temperature and that after annealing at 665 and 950 °C was studied by transmission electron microscope (TEM). Fig. 5.12 shows the TEM

images and EDS map of the cross-sections. The as-deposited film had a columnar growth and EDS mapping confirmed uniform distribution of Nb and Sn throughout the whole cross-section.

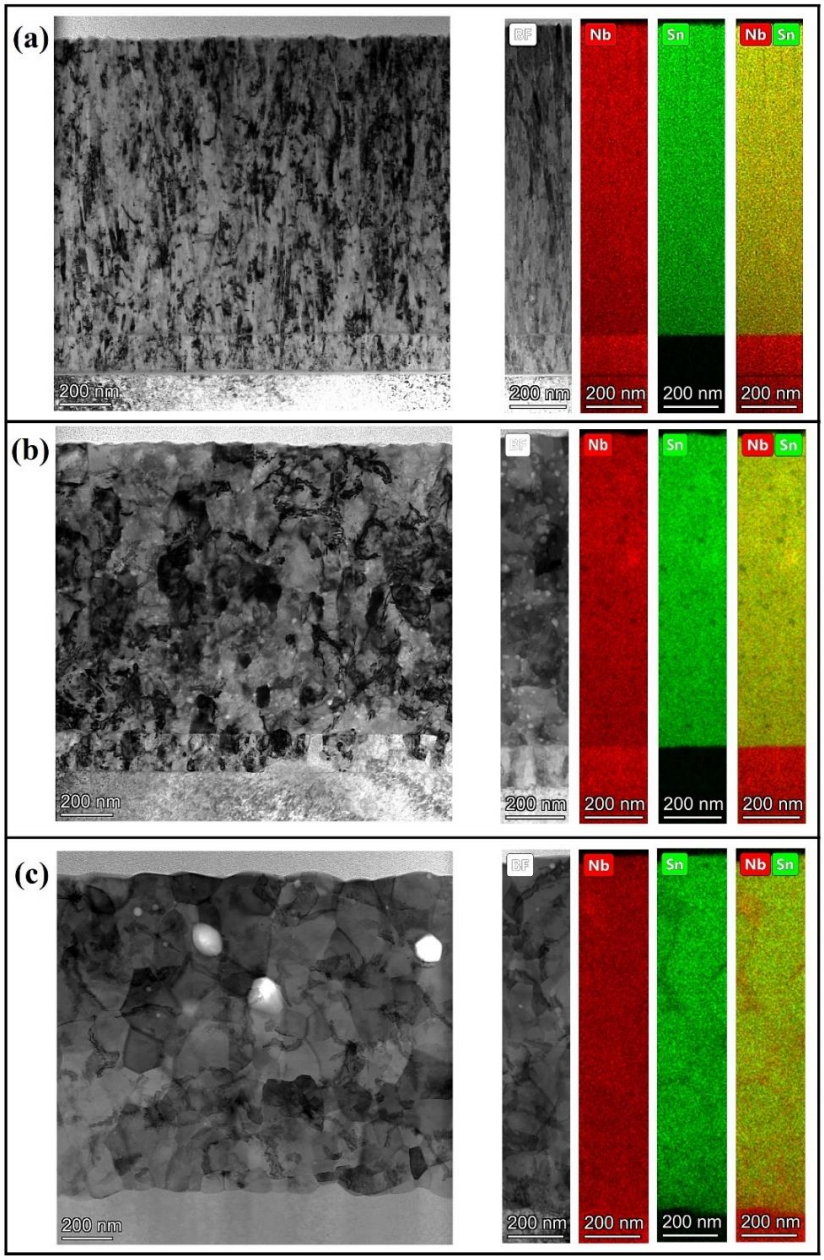

Fig. 5.12. Cross-sectional TEM images and corresponding EDS mapping of the films: (a) as-deposited co-sputtered Nb-Sn film at room temperature, (b) co-sputtered film at room temperature and then annealed at 665 °C for 3 h, and (c) co-sputtered film at room temperature and then annealed at 950 °C for 3 h.

The EDS map of the film annealed at 665 °C had some dark spots indicating deficiency of Nb and Sn at the same location which is possibly due some porous structure throughout the grains that are formed during the annealing. The film annealed at 950 °C had equiaxed grains of Nb_3Sn with some large voids between the grains. No Sn was found in the 200 nm Nb buffer layer of the as-deposited film and the film annealed at 665 °C. At this annealing temperature, Sn did not diffuse in the Nb buffer layer. However, the film annealed at 950 °C showed diffusion of Sn throughout the deposited film including the Nb buffer layer as seen from the EDS map in Fig. 5.12(c).

5.3.3.2. Superconducting Properties

The resistances of the annealed films are shown in Fig. 5.13. The measured T_c, ΔT_c, and *RRR* are reported in Table 5.5. All films had superconducting transition due to Nb_3Sn. The films annealed at 665 °C had relatively poor T_c and ΔT_c compared to the films annealed at 950 °C. The maximum T_c obtained for the films annealed at 665 °C was 15.88 K, whereas the film annealed at 950 °C had a T_c of 17.61 K. For both annealing conditions, the highest T_c was obtained on the film deposited at room temperature, which also agree with the crystalline structure obtained from the XRD data. The *RRR* value of the films were also related to the deposition temperature; *RRR* decreased with increasing substrate temperature.

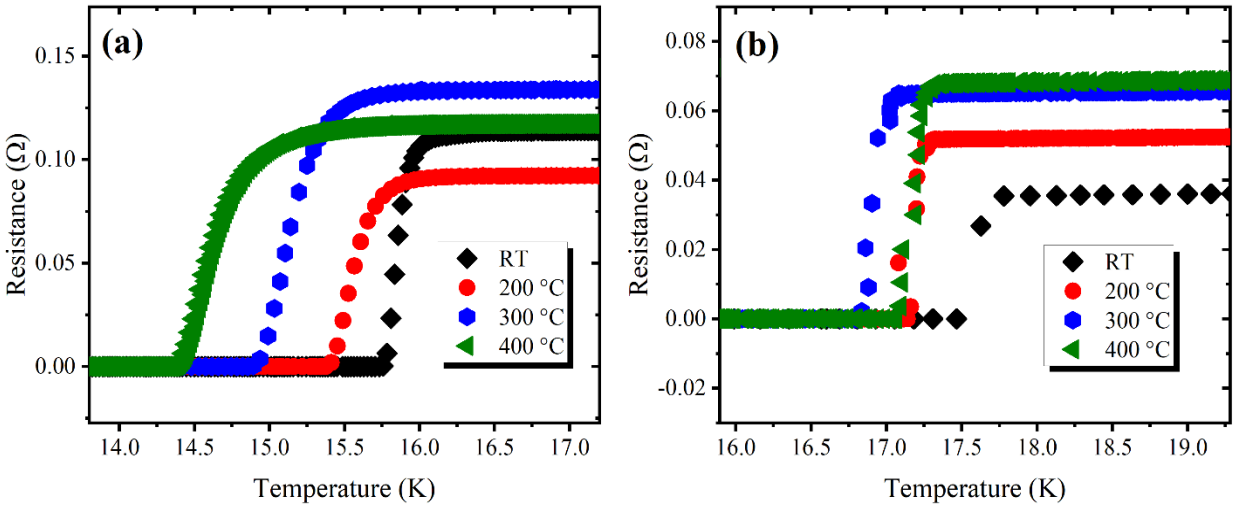

Fig. 5.13. Resistance versus temperature graph of the films annealed at (a) 665, and (b) 950 °C for 3 h. The black diamond, red circle, blue hexagon, and green triangle represent the substrate temperatures of room temperature, 200, 300, and 400 °C respectively.

Table 5.5. Superconducting properties of the films annealed at 665 and 950 °C for 3 h.

Annealing temperature (°C)	Substrate temperature (°C)	T_c (K)	ΔT_c (K)	*RRR*
665	RT	15.88	0.17	2.07
665	200	15.62	0.33	2.16
665	300	15.34	0.44	1.96
665	400	14.73	0.27	1.79
950	RT	17.61	0.19	3.63
950	200	17.21	0.14	3.27
950	300	16.94	0.13	2.82
950	400	17.17	0.23	2.68

5.4. Summary

The properties of Nb_3Sn films fabricated by co-sputtering method on Nb and sapphire substrates are described in this chapter. The Sn composition of the film was controlled by

varying the RF power applied to the Sn target and applying a constant DC power to the Nb target. The Sn composition of the films vary significantly with a small change in the power applied to the Sn target for fixed power applied to the Nb target and a power ratio P_{Nb}:P_{Sn} of 190:28 provided ~25% Sn on the films deposited for 1 h. The film deposited at room temperature was amorphous in structure and did not have any superconducting transition near 18 K. The crystallinity of the films was dependent on the substrate temperature during the deposition and the highest T_c of 15.00 K was observed on the film deposited at 500 °C. The films were annealed at two different annealing temperature of 665 and 950 °C for 3 h. The film surface changed from randomly oriented elongated grains to well-connected grains with grain boundaries when annealed at 950 °C. The superconducting properties also improved after annealing. The T_c of the films annealed at 665 °C were 14.73- 15.88 K. The films annealed at 950 °C had superconducting transition close to 18.3 K. The highest T_c of 17.61 K was recorded on the film that was deposited at room temperature and annealed at 950 °C for 3 h. Schafer et al. have reported the highest reported T_c of 16.31 K on Nb_3Sn films fabricated by co-sputtering of Nb and Sn [68]. Previously reported works were limited to the annealing temperature of 750 °C. This dissertation study of annealing at 950 °C showed that the T_c of the films can be improved by annealing the films at high temperature. These studies demonstrate the feasibility of applying the co-sputtering method and post-annealing at 950 °C to fabricate Nb_3Sn films inside Nb cavities.

CHAPTER 6

CYLINDRICAL MAGNETRON SPUTTERING SYSTEM FOR Nb_3Sn DEPOSITION INSIDE SRF CAVITIES

6.1. Introduction

To fabricate Nb_3Sn coating on the inside surface of SRF cavities, a magnetron sputtering system needs to be able to sputter Nb and Sn in radially symmetric geometry and the magnetron size must be small enough to fit inside the SRF cavity. Nb sputtering was conducted inside the Cu cavities of the Large Electron-Positron (LEP) collider in 1980 [73]. The facility used biased diode sputtering configuration initially on 3 GHz and 500 MHz cavities. The design was later upgraded to magnetron sputtering in 1985. The coated cavities at that time showed a higher Q_0 (~3.5×10^9) than the bulk Nb cavities (~2.5×10^9) at low field [74]. DC magnetron sputtering was also used to deposit 1-2 μm thick Nb layer inside 400 MHz RF cavities used in the LHC at CERN [75]. The HIE-ISOLDE at CERN used magnetron sputtering to deposit Nb inside 101.28 MHz Cu QWR cavities [76,132]. The magnetic field around the Nb cathode was generated by a solenoid placed around the vacuum chamber. The coated cavity surface had *RRR* up to 39 and Q_0 of ~2×10^9 [132]. The Acceleratore Lineare Per Ioni (ALPI) facility at INFN-LNL, Italy also applied sputtered Nb onto 160 MHz QWR resonators [77, 78]. The facility used DC biased Nb sputtering to deposit Nb inside Cu resonators by applying 1 kV cathode voltage and -120 V bias voltage. Other facilities that adapted sputtered Nb on Cu cavities include SOLEIL at Saclay Nuclear Research Centre, France [79], third harmonics superconducting passive cavities in Swiss Light Source (SLS) at Saclay [80], and at the IHEP and IMP in China [81, 82].

Deambrosis et al. reported on a cylindrical sputtering system with Nb-Sn composite cathode for depositing Nb_3Sn films inside 6 GHz SRF cavities [64]. The magnetic field was generated externally by using solenoids outside the deposition chamber. The cavity was moved up and down during the multilayer deposition for homogenous coating. The coated cavities had Q_{BCS} ~3×10^7 at 4.2 K.

I have worked with *PLASMIONIQUE Inc.*, Varennes, QC, Canada on designing and testing a cylindrical magnetron integrated to a home-designed chamber for cylindrical magnetron sputtering with two identical magnetrons to fabricate Nb_3Sn inside a 2.6 GHz cavity. This chapter discusses the design of the vacuum system and the magnetrons, and the initial results obtained from the system.

6.2. Design

6.2.1. Vacuum System

The vacuum chamber was custom-designed specifically for the cavity sputtering system. The drawing of the chamber is shown in Fig. 6.1. It has five 8-inch and two 4.5-inch conflate flange (CF) ports to connect the cathode and the vacuum components. Two 8-inch CF ports are placed at the top and bottom of the chamber for inserting the two magnetrons. The angular tolerance of these ports was within 0.01” to assure new axis placement of the magnetrons. Also, the vertical positioning of the magnetrons was chosen to eliminate the possibility of sagging if the magnetron placement was horizontal. The door was made from an aluminum QF400 flange with a centering ring for sealing. The chamber was connected to a TPS-flexy turbo pumping system from *Agilent Technologies*. The pumping system consists of a TwisTorr 305 FS turbo pump backed by a CFF6, IDP-10 dry scroll pump from *Agilent Technologies*. The pressure inside the chamber was measured by a cold cathode/Pirani combination gauge two sensor system

that can measure from atmosphere to 7.6 × 10^{-10} torr. A gas flow controller (GE50A013501RMV020 from *MKS*) was connected to the chamber to control the flow of Ar. The controller is calibrated to N_2 and has a full-scale flow range of 50 SCCM.

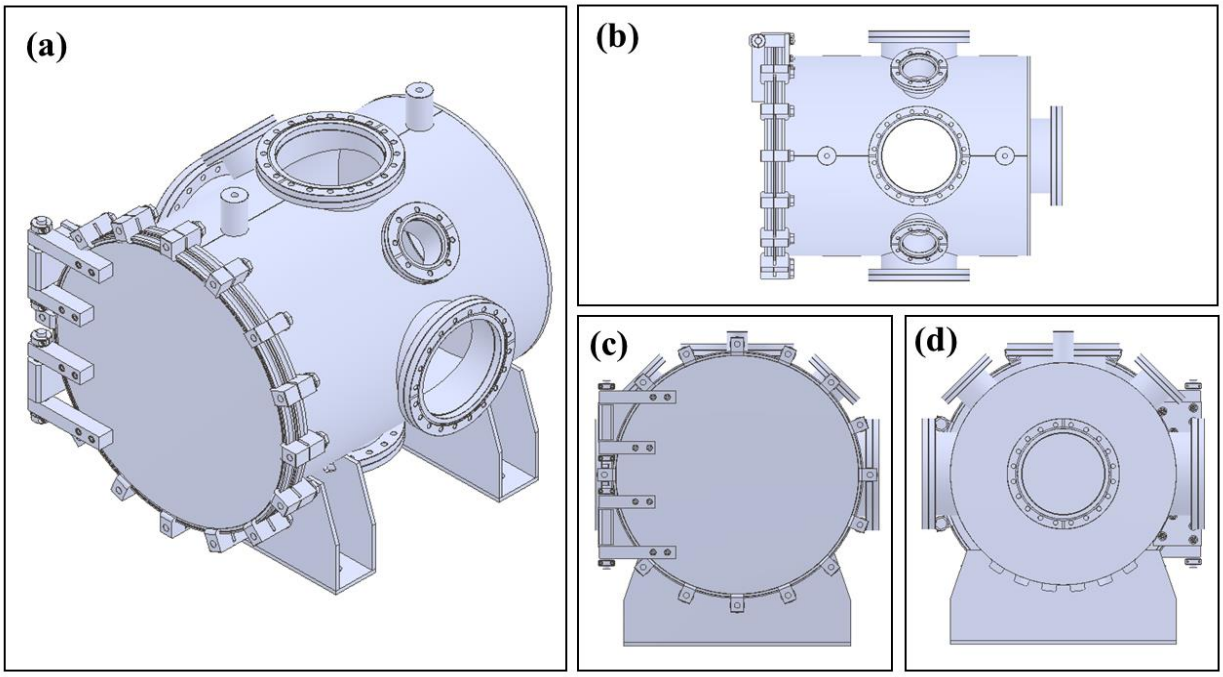

Fig. 6.1. Design of the vacuum chamber used for the cylindrical sputtering system: (a) isometric view, (b) top view, (c) front view, and (d) back view.

6.2.2. The Cavity

The cavity considered for the deposition is a 2.6 GHz Nb tesla shaped cavity. The design of the cavity is shown in Fig. 6.2. The cavity is made of two half-cells and two beam tubes. The two ends of the beam tubes are welded with mini-CF for sample holding support. The length of the whole cavity is ~198 mm. The beam tubes have inner diameter of ~39 mm.

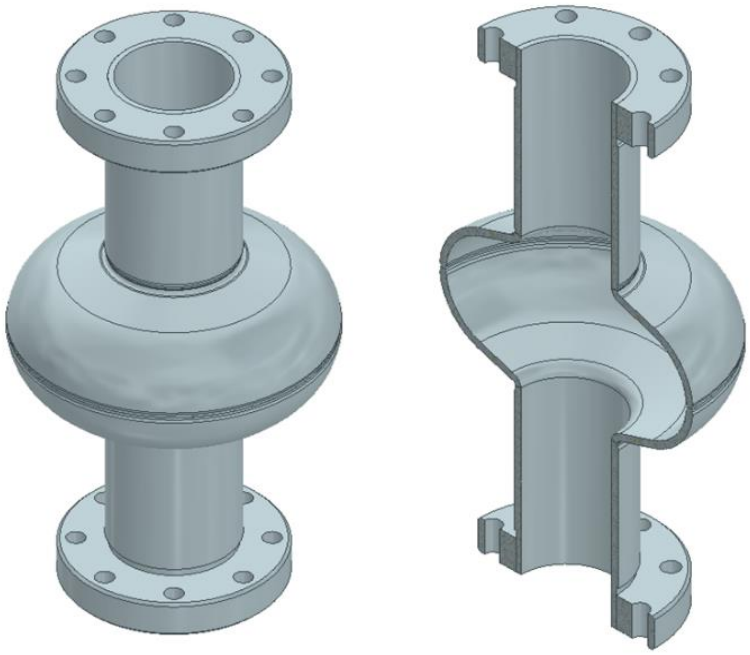

Fig. 6.2. Drawing of the 2.6 GHz single cell cavity used for the deposition. The cavity was designed and built in Fermilab.

6.2.3. The Magnetron

A cylindrical magnetron sputtering system for deposition of a multilayer Nb and Sn layers, with its associated computer control unit was designed and fabricated by *PLASMIONIQUE Inc.* [133]. The design of the magnetron is shown in Fig. 6.3 and the design, and picture of the assembled sputter coater are shown in Fig. 6.4 (a) and 6.4 (b), respectively. The goal of my current research is to fabricate a multilayer sputtering system to deposit Nb_3Sn films inside a single cell RF cavity. The system will be used to apply co-sputtering and sputtering from a stoichiometric target in future. The system consists of two identical cylindrical magnetrons placed on the axis of the SRF cavity (Fig. 6.4) in a vacuum chamber. The movement

of the magnetrons are controlled by a program that also controls the power applied to the magnetrons. The cathodes are water-cooled with the water flowing on the magnets.

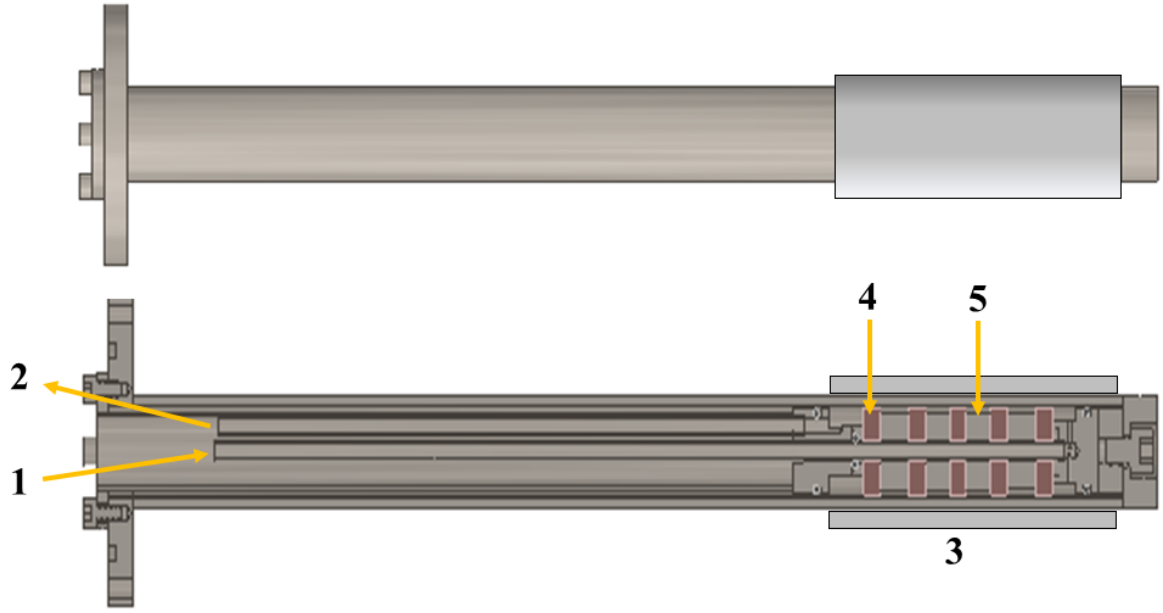

Fig. 6.3. Design of the cylindrical magnetron: (1) water input, (2) water output, (3) target (Nb/Sn), (4) magnet spacer, (5) magnets with an outer diameter of 16 mm.

Fig. 6.5(a) shows the control panel of the software during deposition and Fig. 6.5(b) shows the control panel of the motors for the magnetron motion. Selecting a specific magnetron to apply voltage to can be done manually by selecting 'Active Magnetron' from the control panel or can also be selected automatically from the program command. The movement of the magnetrons can be initiated by adjusting the 'Set Point' in the control panel. The set point is selected in a way so that the two magnetrons always maintain a safe distance to avoid collision.

For both magnetrons, the ‘Go Home’ button in the control panel brings back the magnetrons to their idle position. The movement of the magnetrons can be controlled by adjusting the ‘Motor Speed’, ‘Motor Acceleration’ and ‘Gain’ value from the settings.

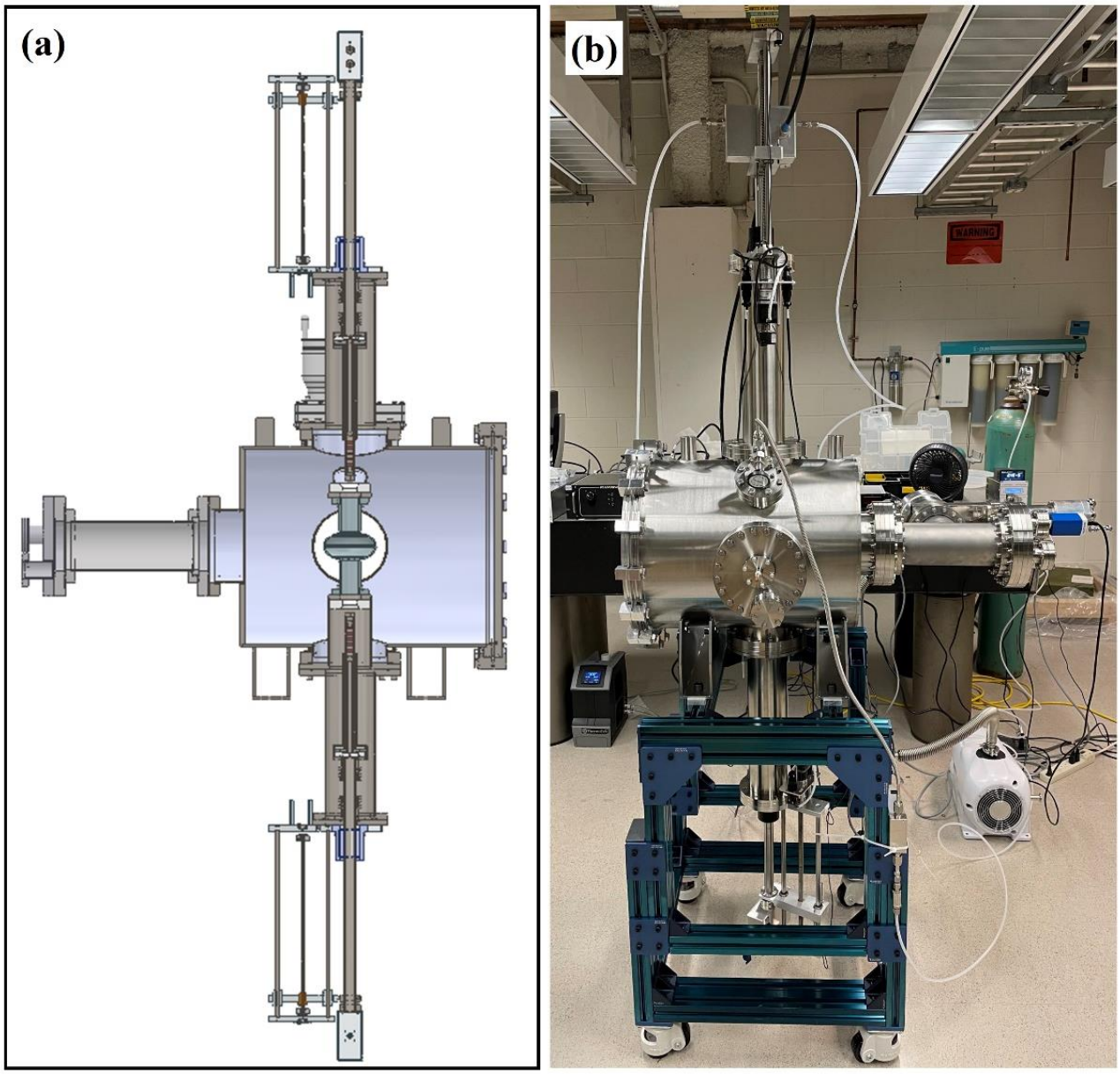

Fig. 6.4. (a) Design of the cylindrical sputtering system with two identical magnetrons. (b) Picture of the assembled system.

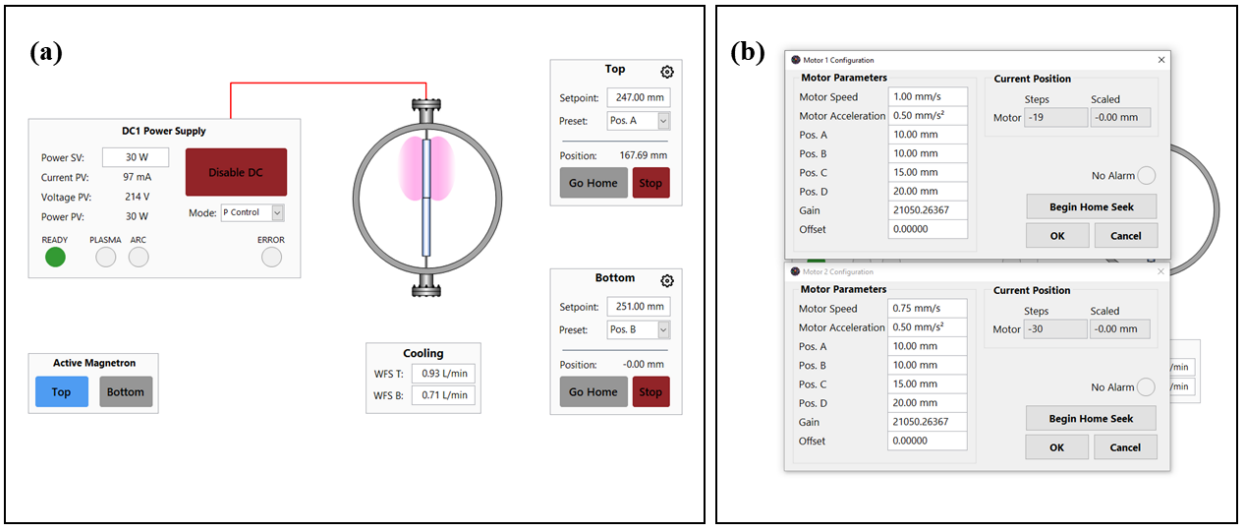

Fig. 6.5. (a) Control panel of the software during the deposition, the power applied to the top magnetron is 30 W. (b) Motor parameters adjustment before the multilayer deposition.

The magnetic field was generated by neodymium (NdFeB) N55 grade ring magnets placed inside the cathode separated by magnet spacers. A picture of the magnets is show in Fig. 6.6. The magnets are coated with Ni, Cu, and epoxy. Magnets of two different dimensions are used, the outer two magnets have outer diameter of 16 mm, inner diameter of 4 mm, and thickness of 7.74 mm. The inner two magnets have similar diameters with a thickness of 6.35 mm.

The magnetic field across the four plasma rings were measured on top of the magnetron surface and 0.1 and 0.45” away from the magnetron surface. Fig. 6.7 shows the magnetic field distribution for both magnetrons. The magnetic field distribution is similar for both magnetrons. Highest magnetic fields were observed near the thicker magnets. The magnetic field along the magnetron varied between 1750 and 2900 Gauss

Fig. 6.6. Picture of the magnets used in the magnetron. The white materials are washers used to separate the magnets from each other.

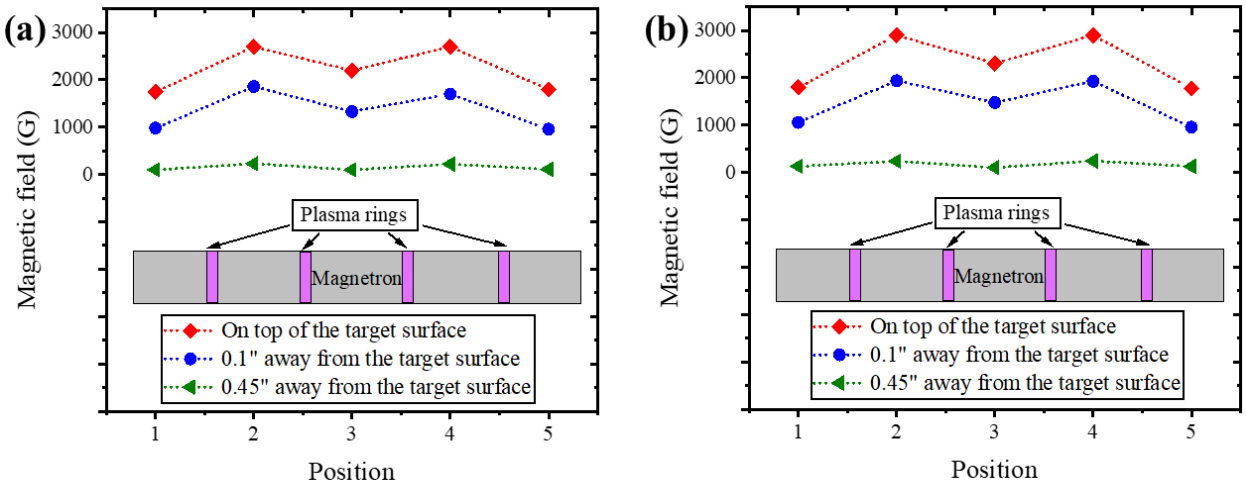

Fig. 6.7. Magnetic field distribution of two magnetrons near the plasma rings: (a) top magnetron, (b) bottom magnetron.

6.3. Deposition Process and Results

Fig. 6.8(a) shows the picture of the inside of the vacuum chamber with a loaded cavity. To calibrate the deposition rate of Nb and Sn, 1 cm × 1 cm Nb substrates were placed in three positions of the cavity; two substrates were placed at positions near the inner surface of the two beam tubes and one substrate was placed at a position near the equator of the cavity (Fig. 6.8(b)). The chamber was evacuated to low 10^{-7} Torr. Ar gas was inserted into the chamber at a flow rate of 50 SCCM. The sputtering was performed at 10 mTorr. The DC power used for Nb and Sn deposition was 30 and 8 W respectively. The temperatures of the targets were maintained by a continuous water flow of 1 L/min throughout the deposition.

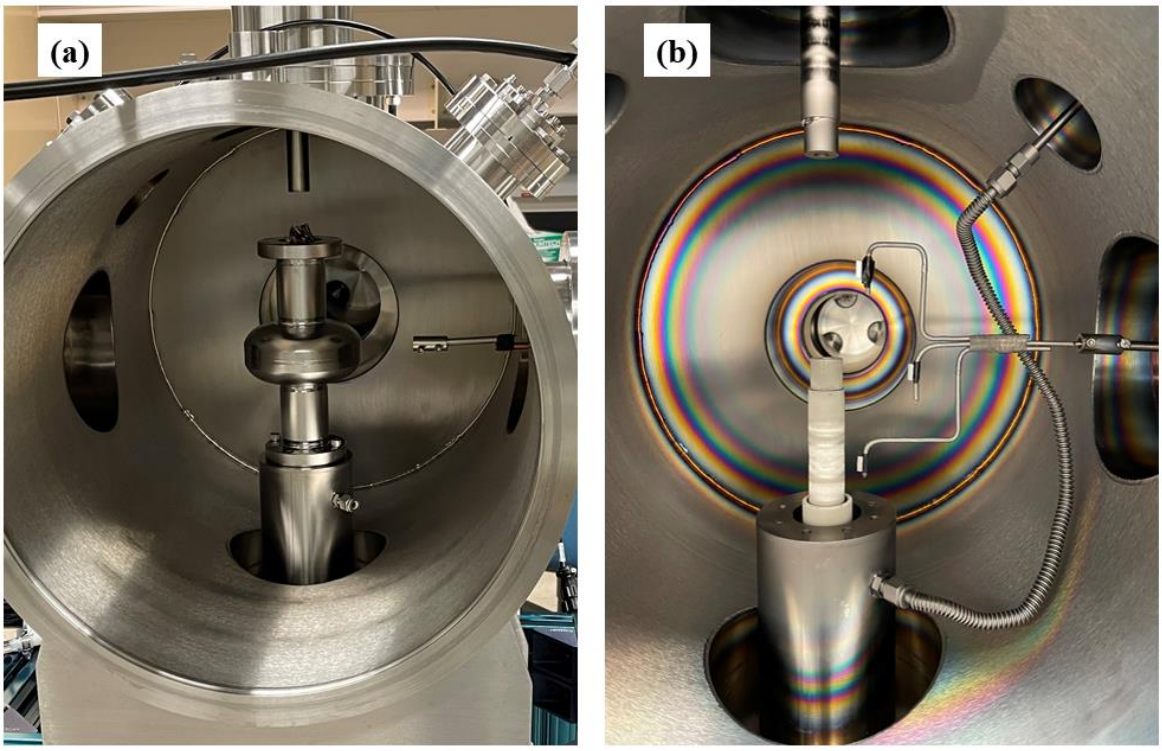

Fig. 6.8. Inside of the cylindrical sputtering system: (a) with loaded SRF cavity, (b) with the small substrates loaded on the sample holder.

6.3.1. Power Calibration for Nb Target

The Nb tube target was installed at bottom magnetron and used to find out the lowest DC power that can generate the glow discharge. The power calibration study was performed at 10 mTorr vacuum pressure and 20 SCCM Ar gas flow. At lower the power range of 2-8 W (3-23 mA), only one outer plasma ring glows with high intensity, the other three rings have very weak plasma intensity, as seen from Fig. 6.9. Figs. 6.9(a) and 6.9(b) show the plasma discharge for two different tests with the same calibration conditions. For the same applied power of 2 W, the strongest plasma ring was formed near two different magnets.

At applied powers of 9-16 W (25-45 mA discharge current), the glow discharge intensity of the weaker outer ring increased (Fig. 6.10(a)). After several test runs with different applied powers, the threshold power of 18 W was found. At this applied power, the glow discharges near the two outer magnets have visually similar intensities (Fig. 6.10(b)). Once the two strong plasma rings near the two outer magnets and two weaker plasma rings near the two inner magnets are formed at an applied power of 18 W or greater, the plasma rings maintain the same glow discharge even after reducing the applied power. During sputtering, the positively charged Ar^+ ions also eject secondary electrons. When the applied voltage reaches the breakdown voltage, the secondary electrons gain energy to collide with other Ar atoms, ionize them, and eject more secondary electrons. As a result, charge multiplication takes place, and the plasma remains self-sustaining even after the applied power is reduced. However, the plasma does not sustain if the applied power is reduced below 8 W because the applied voltage goes below the breakdown voltage.

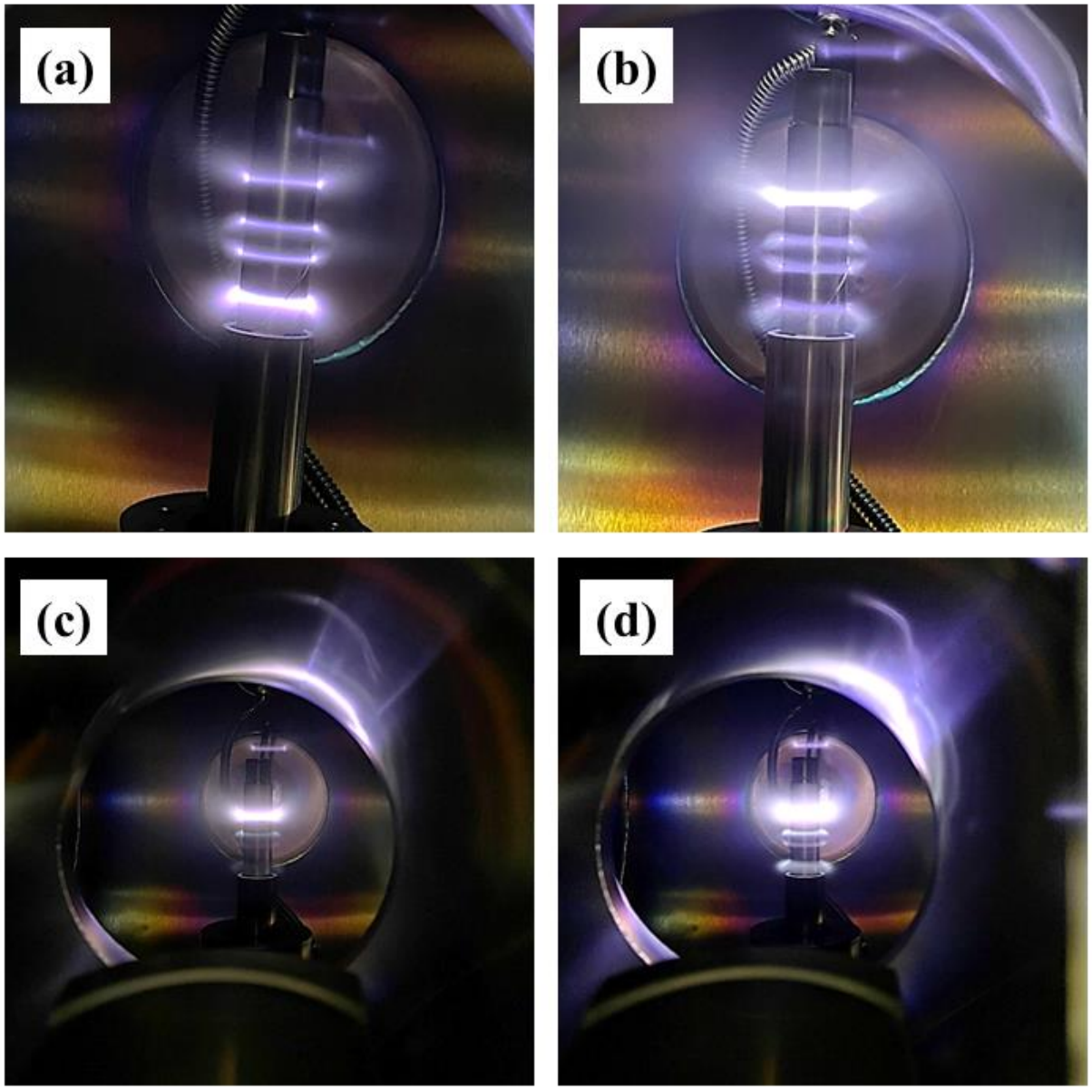

Fig. 6.9. Plasma discharge at different applied powers: (a) 2 W (3 mA), (b) 2 W (3 mA), (c) 4 W (10 mA), and (d) 8 W (23 mA).

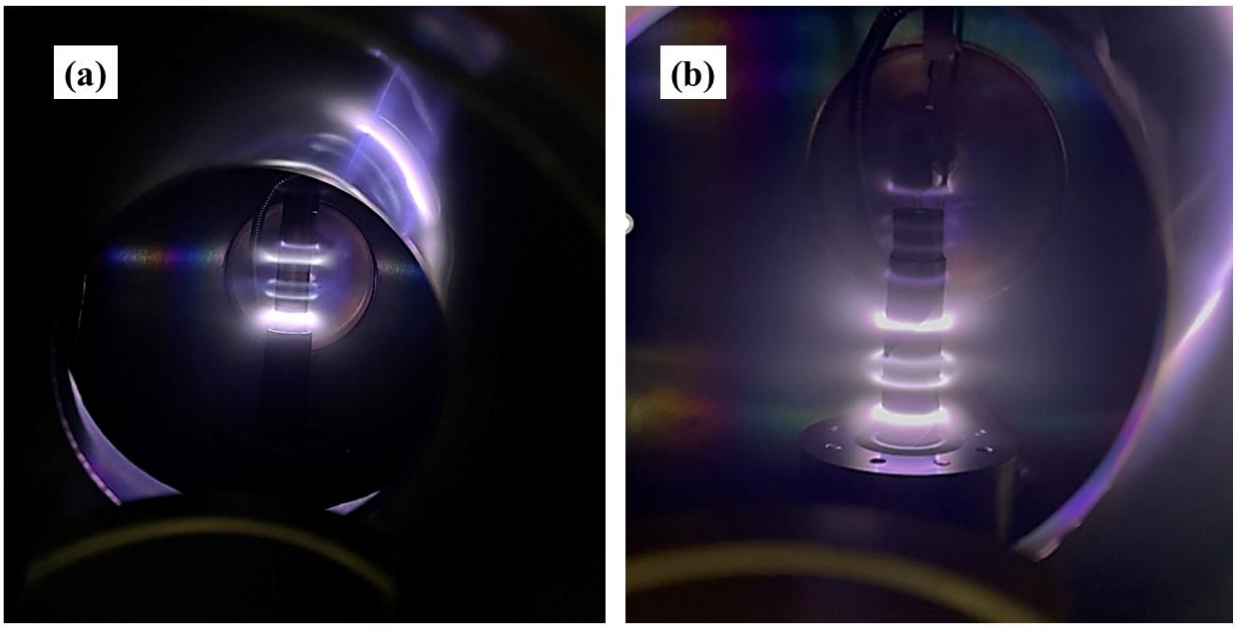

Fig. 6.10. Plasma discharge at an applied power of (a) 12 W, and (b) 18 W.

6.3.2. Power Calibration for Sn Target

Since Sn has a very low melting point compared to Nb, initially the target was made by wrapping Sn foil helically around Nb tube target (Fig. 6.11) to find out the optimum condition to produce 4 consistent plasma rings without melting the target. Then the discharge conditions were applied to a cylindrical target made of Sn.

To calibrate the Sn deposition, the DC power of 18 W was applied for 20s, then the power was reduced gradually to 15, 12, and 10 W for 20 s each. Finally, 8 W was applied for 20 minutes. The Sn foil starts melting within this 60 s of higher power applied. Fig. 6.12(a) shows the plasma discharge at an applied power of 12 W. The glow discharge near the outer two magnets was intense. Fig. 6.12(b) shows the Sn foil target after the experiment. The Sn foil near one of the plasma rings melted completely, whereas the location near the other intense ring has

signs of significant erosion. Further studies with reduced power revealed that Sn melting can be avoided if the applied power is reduced to 8 W.

Fig. 6.11. Sn target made of by wrapping Sn foil helically on Nb tube target.

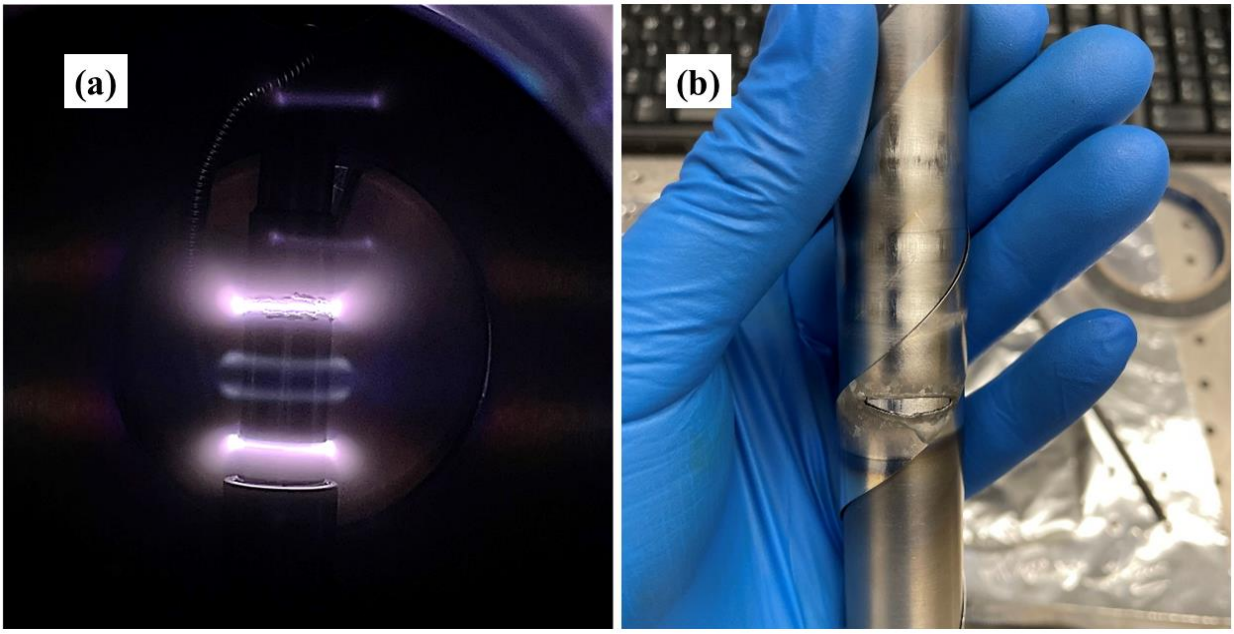

Fig. 6.12. (a) Plasma discharge at an applied DC power of 12 W, (b) the melted target at an applied power of 12 W.

The Sn foil target was replaced by the Sn target and 8 W was applied to check the reproducibility of the plasma. Fig. 6.13 shows the picture of the plasma discharge from the Sn tube target at an applied power of 8 W. At this applied power, the four plasma rings glow with almost equal intensity and the discharge was sustained over the experiment duration of 8 h.

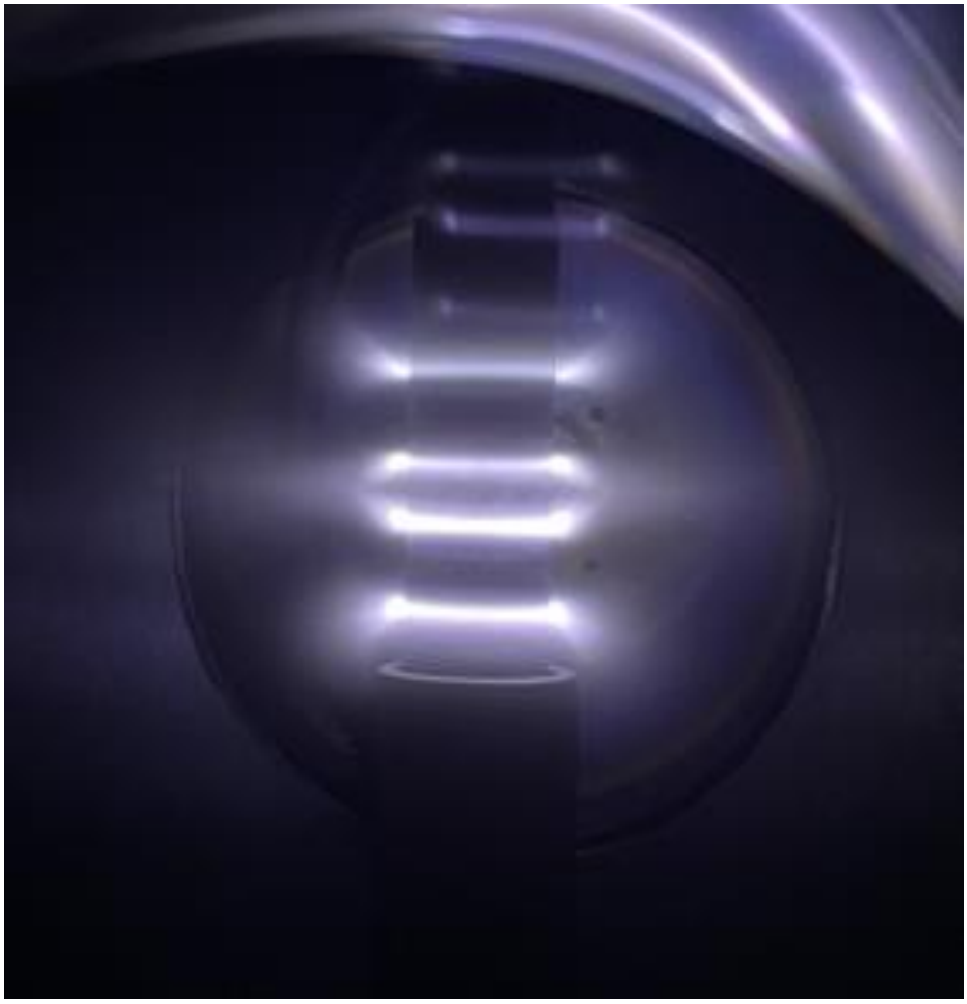

Fig. 6.13. Plasma discharge at Sn tube target with an applied DC power of 8 W.

6.3.3. Deposition Rate Calibration

For calibrating the deposition rate of Nb and Sn films, a sample holder was used to mount three sample substrates on three different positions. These three positions on the holder replicate three positions of the 2.6 GHz SRF cavity – the top sample position represents the middle point of the top beam tube (0.32” away from the target), the center sample position represents the middle point of the equator (1.575” away from the target), and the bottom sample position represents the middle point of the bottom beam tube of the cavity (0.32” away from the target).

A Si substrate was placed on each of these 3 positions and the deposition rate of the Nb and Sn targets were measured from the cross-sectional thickness of the deposited films for a deposition period of 46-93 minutes.

6.3.3.1. Nb Deposition Rate Calibration

For Nb deposition thickness rate measurement, a Nb tube target of the same dimension was installed with the top magnetron. The top magnetron was moved down to a starting position (133 mm from the home position) before applying the power to the magnetron. From this position, the magnetron travels to go up to a final position of 247 mm from the home position (travel distance ~114 mm). By traveling to the final position and then returning to the starting position, the magnetron completed one loop of travel. The DC power applied to the magnetron was 30 W (current 94-97 mA) and a total of 12 loops of travel between the initial and final position were completed with a magnetron speed of 1 mm/s and acceleration of 0.5 mm^2/s. The discharge stopped when the top magnetron finally reached its starting position after completing 12 loops of travel. The travel duration of deposition was 46 min 24 s. The deposited Nb films were very uniform throughout the surface and the measured thickness values had very low deviation (Fig. 6.14). The average thickness of the Nb film on the samples near the top beam tube, equator, and bottom beam tube position were 436, 600, and 395 nm respectively. The deposition rate estimated from these thicknesses rate on the top beam tube, equator, and bottom beam tube position of the cavity are 9.5, 13.1, and 8.6 nm/min respectively.

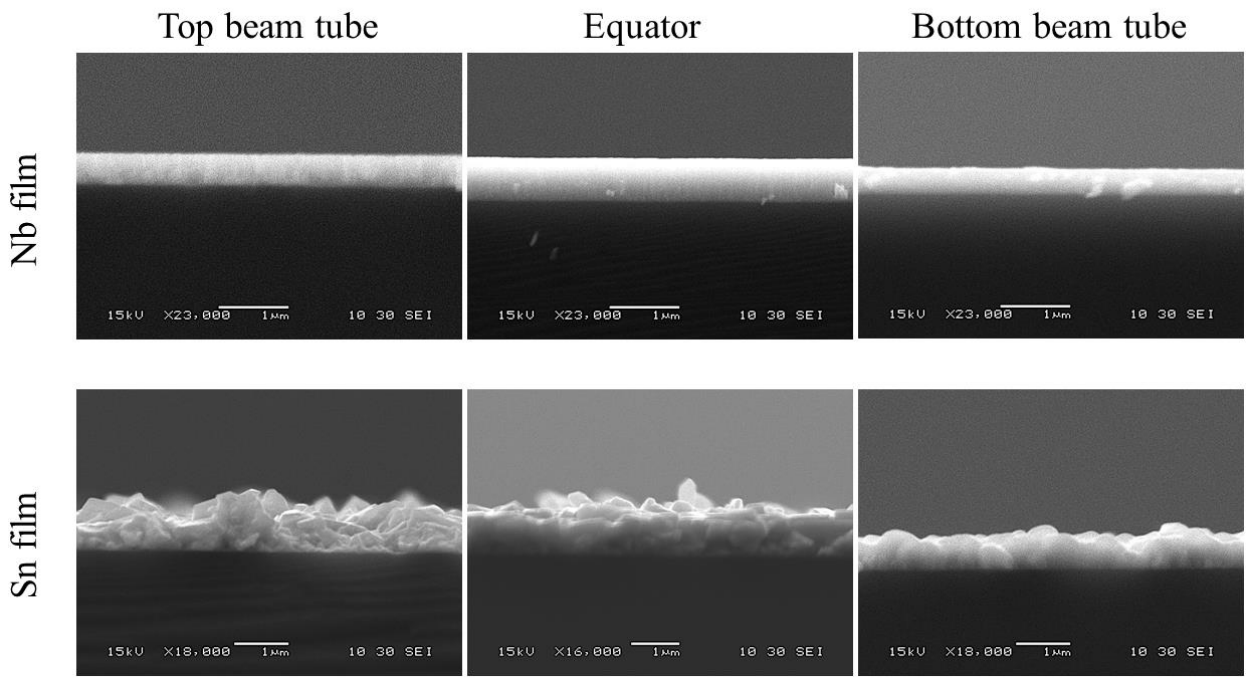

Fig. 6.14. SEM images of the cross-section of Nb and Sn films deposited on Si substrates placed near the top beam tube, equator, and the bottom beam tube position.

6.3.3.2. Sn Deposition Rate Calibration

For the Sn deposition rate calibration, the Sn tube target was placed on the bottom magnetron. The bottom magnetron was raised to a starting position (137 mm from the home position) before applying the power to the magnetron. From this position, the magnetron travels to go up to a final position of 251 mm from the home position (travel distance ~114 mm). By traveling to the final position and then returning to the starting position, the magnetron completed one loop of travel. A DC power of 8 W (current 22-23 mA) was applied to the target to generate the plasma and the magnetrons was moved to complete 24 loops of travel with a magnetron movement speed of 1 mm/s and acceleration of 0.5 mm^2/s. The total deposition time was 92 min 50 s. The magnetron came to the starting position after completing the deposition and the plasma discharge was stopped by turning off the applied power to the magnetron. The

cross-sections of the films were characterized by SEM and the thickness of the films were measured by averaging the thicknesses of the cross-section at 10 different locations of Fig. 6.14. While measuring the thickness of the films, some of the locations with higher thicknesses were excluded because those could be resulted from the residue coming from the Si wafer during the cross-sectional sample preparation. For the top beam tube, equator, and bottom beam tube position samples, the measured thicknesses of the Sn film were 675, 900, and 653 nm, respectively. The deposition rate estimated from these thicknesses rate on the top beam tube, equator, and bottom beam tube position of the cavity are 7.3, 9.7, and 7 nm/min respectively.

6.3.4. Multilayer Deposition

After the calibration of the sputter rate Nb and Sn targets, multilayered Nb-Sn films were deposited on the three substrates. For the multilayer deposition, 30 W DC power was used for depositing Nb layers, and 8 W DC power was used for depositing Sn layers. Fig. 6.15 shows the current reading from both magnetrons during the multilayer deposition.

Initially, a 200 nm Nb buffer layer was deposited, and then Nb-Sn layers were deposited sequentially. The thicknesses of Nb and Sn layers were 50 and 25 nm respectively and the sequential deposition was repeated 16 times to deposit ~1.5 μm thick film. The films were further annealed at 950 °C for 3 h at a separate furnace.

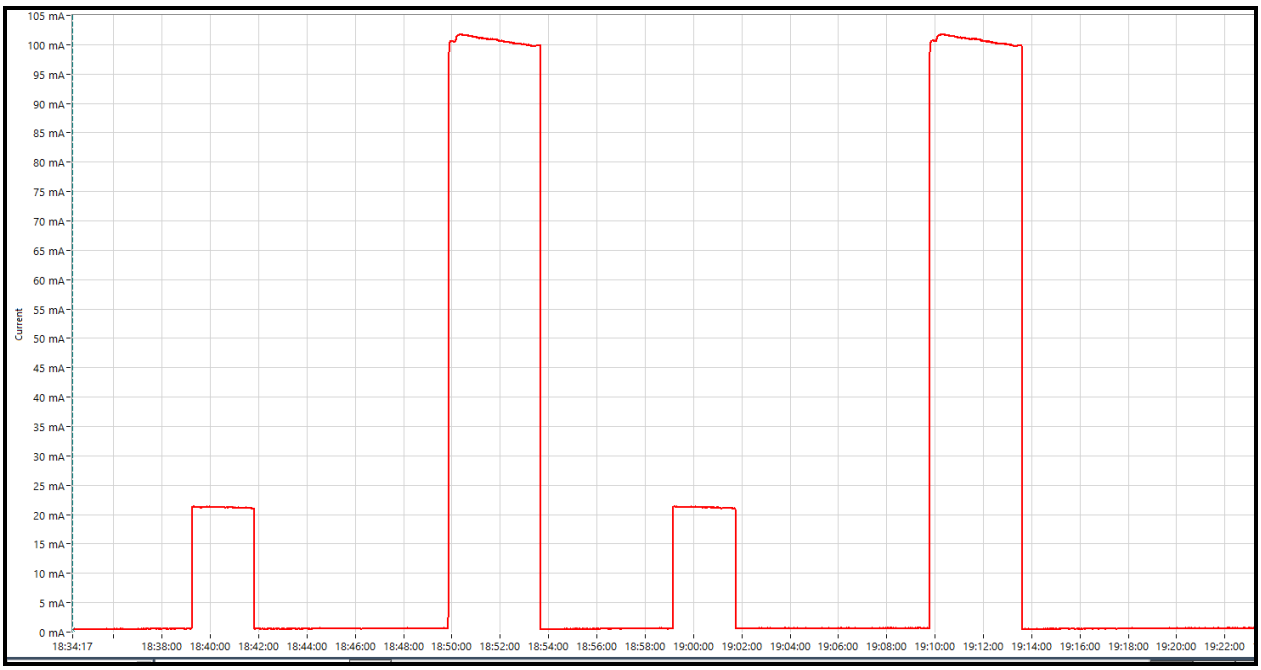

Fig. 6.15. Current reading during the multilayer deposition.

6.3.5. Results

The Sn composition of the as-deposited and annealed films deposited on three different substrates measured at three locations are shown in Table 6.1. The as-deposited films had Sn composition of 34-40%. Annealed films experienced Sn loss due to evaporation from the surface. The films near the beam tubes had Sn composition of 22-23%, whereas the film near the equator had ~18% Sn after annealing. Sn loss was also observed on the multilayered Nb_3Sn films discussed in Chapter 4. Previous experiments on different multilayer thicknesses showed that Sn loss occurred after annealing on the films with excessive Sn also and the composition of the annealed films were ~20-24% [89]. The film near the equator has Sn composition below this range. Since the equator location is far from the magnetron, the thickness of the film is less, and the electron beam penetrated through the thin film and some portion of the substrates and

extracted X-ray from the Nb substrate also. As a result, the overall atomic composition of Sn obtained from the EDS is less.

Table 6.1. The Sn composition obtained from EDS and the RMS roughness obtained from AFM of the as-deposited and annealed films. The samples were placed in three different locations near the two beam tubes and the equator of the SRF cavity.

Sample position	Sn composition as-deposited (%)	Sn composition annealed (%)	RMS roughness as-deposited (nm)	RMS roughness annealed (nm)
Top beam tube	34	22	68	50
Equator	40	18	26	28
Bottom beam tube	39	23	43	50

The XRD patterns of the as-deposited and annealed films are shown in Fig. 6.16. The formation of Nb_3Sn can be identified clearly by comparing the XRD patterns of as-deposited films and annealed films. The as-deposited films had multiple Nb diffraction peaks ((110), (200), (211), (310)) from the film and the substrate. The film near the top beam tube region had diffraction Sn peaks of ((200), (101), (220), (211), (112), and (400)). Samples in the other two locations did not have any diffraction peak of Sn. Several diffraction orders of the Nb_3Sn ((110), (200), (210), (211), (222), (320), (321), (400), (420), (421), (332)) were observed on all annealed samples. All samples showed no unreacted Sn phase and other intermetallic compounds of Nb and Sn (Nb_6Sn_5, $NbSn_2$). Some diffractions of Nb ((200), (211), (310)) were also observed which are probably from the substrate.

The crystallite size of (200), (210), and (211) diffraction orders were measured from the full width at half maximum (FWHM) of the diffraction peaks using Scherrer equation. The crystallite sizes of the films in three locations are shown in Fig. 6.17. The measured crystallite sizes were ~35-44 nm depending on the film location. The film near the equator had smallest crystallites of ~35-40 nm whereas the film near the top beam tube had crystalite size of ~39-44 nm and the film near the bottom beam tube had crystallite size of ~38-43 nm.

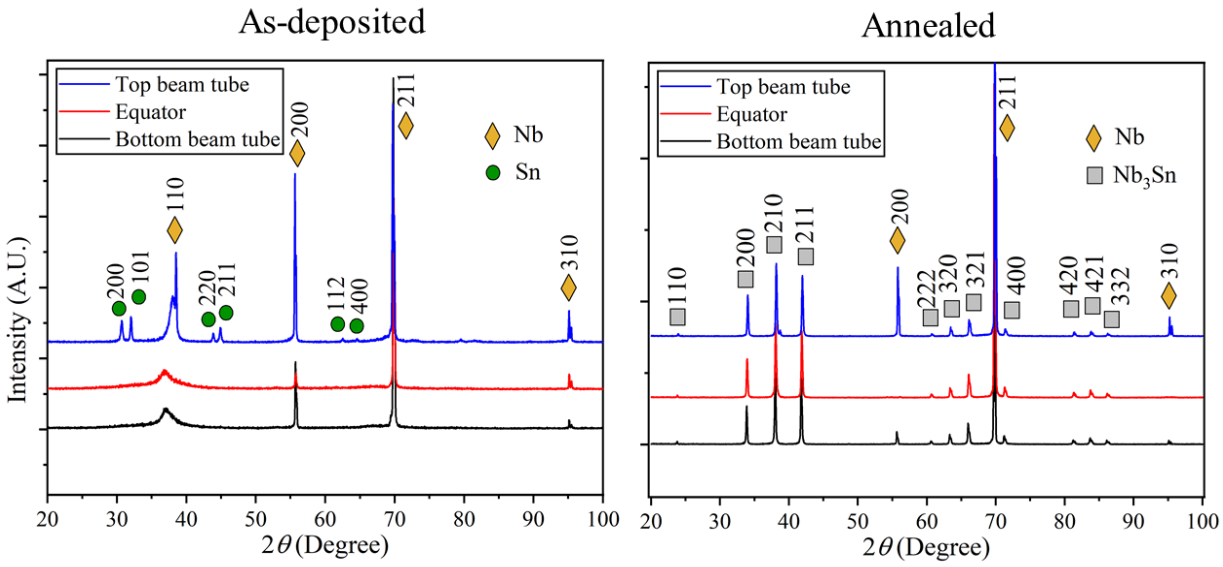

Fig. 6.16. X-ray diffraction patterns of the as-deposited and the annealed films. The substrates were placed in three different locations near the two beam tubes and the equator of the SRF cavity.

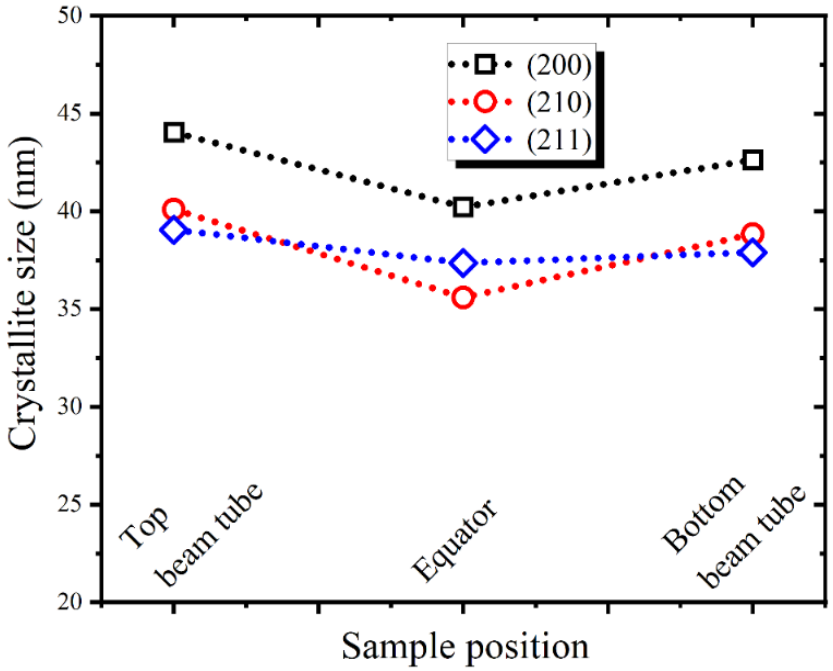

Fig. 6.17. Size of the crystallites across (200), (210), and (211) diffraction orders of the films deposited on substrates placed in different locations replicating the cavity locations.

The texture coefficients of the films were calculated from the diffraction peak intensity using Harris's formula [134]:

$$TC(hkl) = \frac{I\,(hkl)/I_0(hkl)}{\frac{1}{N}\sum_N I\,(hkl)/I_0(hkl)} \qquad (6.1)$$

Here, *TC(hkl)* is the texture coefficient of the (hkl) plane, *I(hkl)* is the measured intensity of the (hkl) plan and $I_0(hkl)$ is the standard intensity of the plane obtained from Nb_3Sn PDF card (PDF Card No.: 00-017-0909 Quality: I). The preferential orientation of the grains can be estimated from the measured TC. For a film with randomly oriented grains, the measured TC should be equal to 1. If the TC value for a certain diffraction order is greater than 1, then the preferential orientation exists across the film [135-137]. The measured TC of the diffraction planes are shown in Table 6.2. Films near all three locations had highest TC across (200)

direction. However, the TC of three other diffraction orders ((110), (210), (211)) are greater than 1, confirming the abundance of grains across these directions.

Table 6.2. The texture coefficient (TC) of different diffraction orders measured from the XRD peak intensity.

Texture Coefficient	Top beam tube	Equator	Bottom beam tube
TC (110)	1.38	1.21	1.18
TC (200)	1.55	1.26	1.33
TC (210)	1.35	1.20	1.25
TC (211)	1.26	1.19	1.29
TC (222)	0.82	1.04	1.03
TC (320)	0.85	0.81	0.86
TC (321)	0.69	0.86	0.83
TC (400)	0.87	0.99	0.90
TC (420)	0.84	0.84	0.77
TC (421)	0.65	0.86	0.81
TC (332)	0.75	0.73	0.74

The AFM images of the as-deposited and the annealed films are shown in Figs. 6.18 and 6.19 respectively. The surface of the films near the beam tubes were relatively rough with large grains. The beam tubes are very close to the magnetrons (0.32” away from the target) compared to the equator (1.575” away from the target). Therefore, the substrates are more exposed to the plasma and the kinetic energy of the incoming Nb and Sn atoms. The rough surface originated due to the significant bombardment of sputtered particles near these regions. The roughness of the film near the top equator region and the bottom equator region were 68 and 43 nm respectively whereas the film near the equator region had a surface roughness of 26 nm. The annealed film also had the similarities in the surface morphology and roughness. The grains near the equator region were finer compared to the grains of the films near the beam tube region. The

grain size observed in the AFM images follow the similar trend of the crystallite sizes obtained from the XRD diffraction peaks.

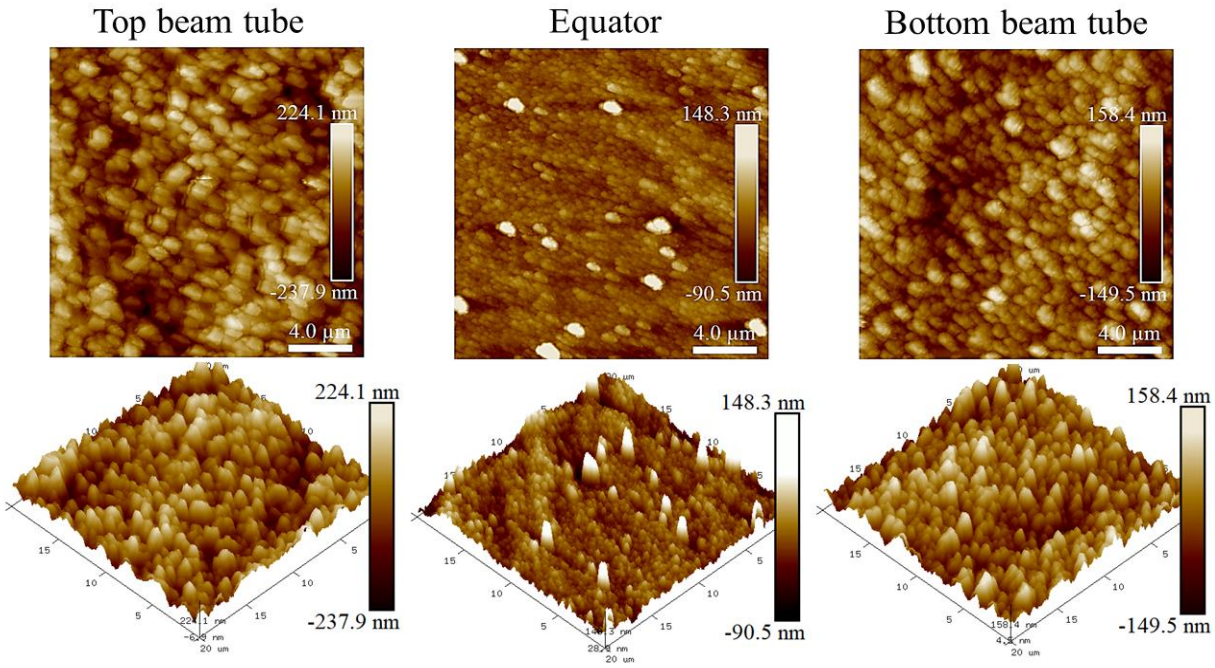

Fig. 6.18. AFM images of the as-deposited films. The substrates were placed in three different locations near the two beam tubes and the equator of the SRF cavity.

The line scan across the AFM images of the 20 µm × 20 µm is shown in Fig. 6.20. The film near the equator region had average height of ~62 nm with a maximum peak-to-valley height difference of ~164 nm whereas most of the grains of the films near the beam tubes had heights of ~120-240 nm. The smaller peak-to-valley height differences of the grains of the films near the equator region resulted to a smooth surface with an RMS surface roughness of ~28 nm.

Fig. 6.21 shows the resistance of the films as a function of temperature. For all three substrate locations, superconducting transition due to Nb_3Sn was observed. The superconducting T_c, ΔT_c, and *RRR* of the films measured from the resistance versus temperature data are shown in

Table 6.3. The highest T_c of 17.76 K and lowest ΔT_c of 0.06 K was obtained on the film near the equator region.

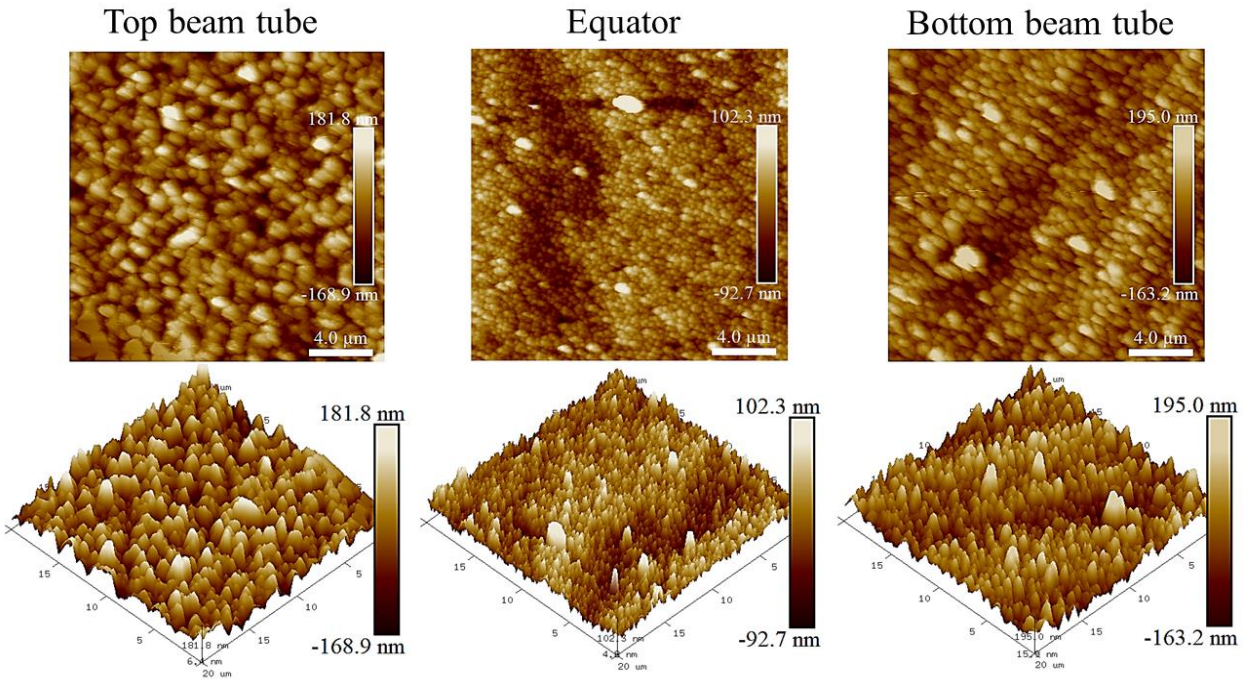

Fig. 6.19. AFM images of the annealed films. The substrates were placed in three different locations near the two beam tubes and the equator of the SRF cavity.

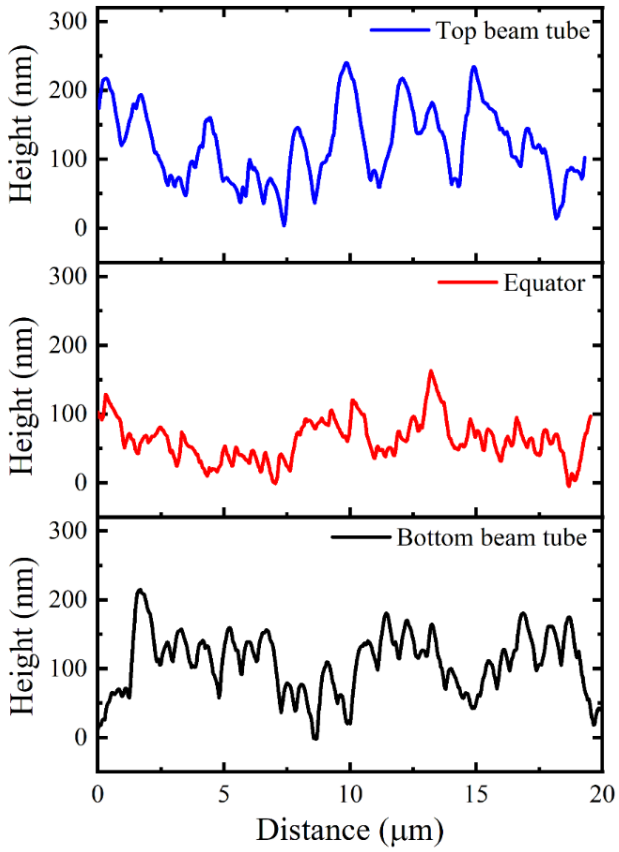

Fig. 6.20. Heights of the films deposited on substrates placed in different locations replicating the cavity locations. The heights are obtained from the line scan analysis of the AFM images.

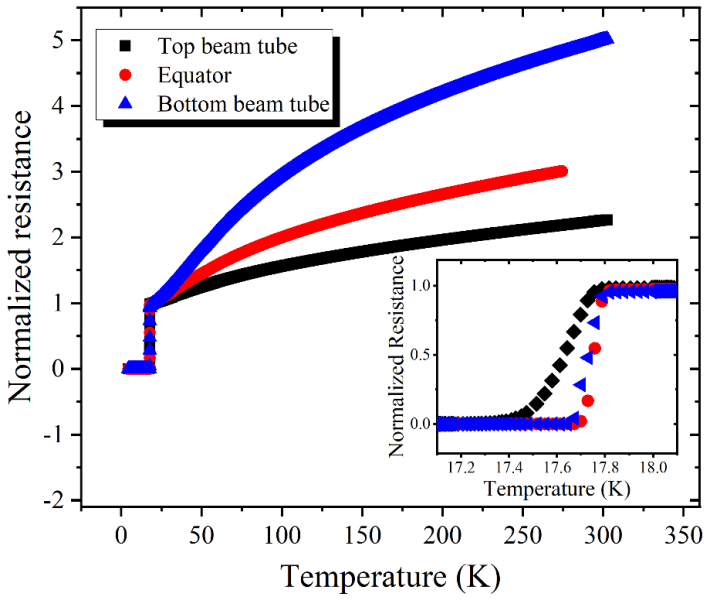

Fig. 6.21. Resistance versus temperature data of the films deposited near three different locations of SRF cavity.

Table 6.3. The superconducting T_c, ΔT_c, and *RRR* of the films measured from the resistance versus temperature data.

Sample position	T_c (K)	ΔT_c (K)	RRR
Top beam tube	17.61	0.24	2.26
Equator	17.76	0.06	3.00*
Bottom beam tube	17.73	0.1	5.01

* The *RRR* value for this sample was measured from the ratio of the resistance at 275 K to the resistance at 20 K. The other RRR value was measured from the ratio of resistance at 300 K to the resistance at 20 K.

6.4. Summary

Two identical cylindrical magnetrons were designed to deposit thin film inside the 2.6 GHz single cell cavity and assembled in a vacuum system for the cavity coating. The design of the vacuum chamber, SRF cavity, and the magnetrons are discussed. The magnetic fields generated by the four ring magnets were measured and a highest magnetic field of 2900 Gauss was observed across the thicker magnets. The deposition rate of the Nb and Sn was calibrated by varying the applied power to the magnetrons. A minimum DC power of the 8 W is required to achieve the breakdown condition for glow discharge. The two magnetrons were moved simultaneously to deposit multilayers of Nb and Sn films on 1 cm^2 Nb substrates replicating the beam tube and equator locations of the cavity applying DC power of 30 W for Nb deposition and 8 W for Sn deposition. Finally, Nb_3Sn films were formed by annealing the 1 cm × 1 cm samples at 950 °C for 3 h. The XRD of the as-deposited and annealed films confirmed the formation of Nb_3Sn after the annealing. The data corroborate the application of multilayer sequential sputtering method to fabricate Nb_3Sn film inside the 2.6 GHz single cell SRF cavity using the cylindrical magnetron sputtering system.

CHAPTER 7

CONCLUSION

Nb_3Sn is considered as a potential alternative of Nb for future SRF accelerator cavities to exceed the theoretical limit of Nb cavities. Magnetron sputtering is a simple and effective method that can be applied to fabricate Nb_3Sn films inside the SRF cavities. Magnetron sputtering was successful in fabricating Nb_3Sn films on Nb and sapphire by three different approaches: sputtering from a single Nb_3Sn target, multilayer sputtering of Nb and Sn and annealing the multilayered films, and co-sputtering of Nb and Sn. These approaches were previously studied on different substrates (copper, glass, sapphire, niobium) using different deposition systems. This dissertation presented the structural, morphological, and superconducting properties of Nb_3Sn films fabricated on Nb substrate using the three fabrication approaches in the same sputtering system and using the same background gas conditions and distance from sputter targets to substrate. Besides, the design and commissioning results of a cylindrical magnetron sputtering system to apply to fabricate Nb_3Sn inside the 2.6 GHz cavity is discussed. This chapter summarizes the work by comparing them with the properties of vapor diffused Nb_3Sn film.

7.1. Summary

The properties of Nb_3Sn films on sapphire and Nb substrates fabricated by DC magnetron sputtering from a stoichiometric target were discussed in Chapter 3. The films have scattered clusters of Sn rich islands on the surface. The distributions of these clusters depend on the grain orientation of the Nb substrate as obtained from SEM images. The films had polycrystalline

Nb_3Sn and developed improved crystallinity after annealing. The highest T_c of 17.83 K was observed for the film annealed at 800 °C for 24 h. The RF properties of films deposited on Nb substrates were measured by using the surface impedance characterization system at Jefferson Lab. The RF superconducting T_c of the as-deposited film increased from 16.02 to 17.44 K when annealed at 800 °C for 24 h. Annealing at 1000 °C reduced Sn content due to its decomposition and evaporation. This adversely affected the superconducting properties of the film. Raman study of the films show high sensitivity to the surface composition and show that the strength of the Nb_3Sn E_g phonon modes and absence of NbO_2 and Nb modes correlates well with obtaining the highest T_c for the film. The film quality degraded when annealed at 1000 °C for 12 and 24 h due to Sn evaporation from the surface.

Chapter 4 discussed the properties of Nb_3Sn films fabricated by multilayer sputtering of Nb and Sn films and annealing the multilayer films. The effect of multilayer thickness, annealing temperature and time, and substrate temperature were studied by varying the parameters during fabrication to understand the optimum fabrication condition. The Nb:Sn thickness ratio of 2:1 can provide the Sn composition close to 25% and an annealing temperature of 950 °C for 3 h is an optimum annealing condition to form Nb_3Sn films with minimum Sn loss. The annealed films have relatively less voids and well-structured grains when the films are deposited at 250 °C. However, the T_c of the film deposited at room temperature (T_c ~ 17.76 K) was slightly higher than the T_c of the film deposited at 250 °C (T_c ~ 17.58 K). The RF surface resistance of the films suggests that multilayer sputtering can be used to deposit Nb_3Sn inside SRF cavities.

The properties of Nb_3Sn films fabricated by co-sputtering on Nb and sapphire substrates are described in Chapter 5. The Sn composition of the film was controlled by varying the RF power applied to the Sn target and applying a constant DC power to the Nb target with a power

ratio P_{Nb}:P_{Sn} of 190:28 provided ~25% Sn on the films deposited for 1 h. The film deposited at room temperature on Nb substrate was amorphous and did not have any superconducting transition near 18.3 K. The crystallinity and the superconducting properties of the films depended on the substrate temperature during the deposition and the highest T_c of 15.00 K was observed on the film deposited at 500 °C. The films annealed at 665 °C for 3 h had T_c ~16 K, whereas the films annealed at 950 °C for 3 h had T_c ~18 K. The film morphology also changed after annealing at 950 °C. The film surface changed from randomly oriented elongated grains to well-connected grains with grain boundaries. While previous work on co-sputtering focused mainly on the application to copper cavities, the processing temperature was limited to 750 °C. I demonstrated the feasibility of applying the co-sputtering method and post-annealing at 950 °C to fabricate Nb_3Sn films inside Nb cavities where such high processing temperature is not a limiting factor.

The films grown from the three sputtering processes were compared with Nb_3Sn film grown from Sn vapor diffusion method at Jefferson Lab. Fig. 7.1 shows the SEM images of Nb_3Sn films fabricated from vapor diffusion and the three sputtering processes. The structural and superconducting properties of the films are given in Table 7.1. While the vapor-diffused film has large grains (average grain size ~ 2 μm), the sputtered Nb_3Sn films have average grain size of ~180-300 nm (note that the vapor diffused film was ~3-4 μm thicker compared to ~1 μm thick sputtered films). The sputtered Nb_3Sn film from a single target have some Sn-rich clusters which can result to a poor RF performance of a cavity. Since the lattice parameter of Nb_3Sn is strongly dependent on the Sn concentration of the film [114], the concentration gradient can introduce lattice imperfection which can limit the accelerating gradient and cause Q_0-slope (degradation of Q_0 with increasing accelerating field) at lower accelerating field [45]. The films from multilayer

sputtering have multiple voids on the surface. Though the voids could be reduced by setting the substrate temperature at 250 °C during the multilayer deposition, the voids could not be eliminated completely. The films fabricated by co-sputtering have void-free surface and the grains are well-connected without any Sn rich clusters.

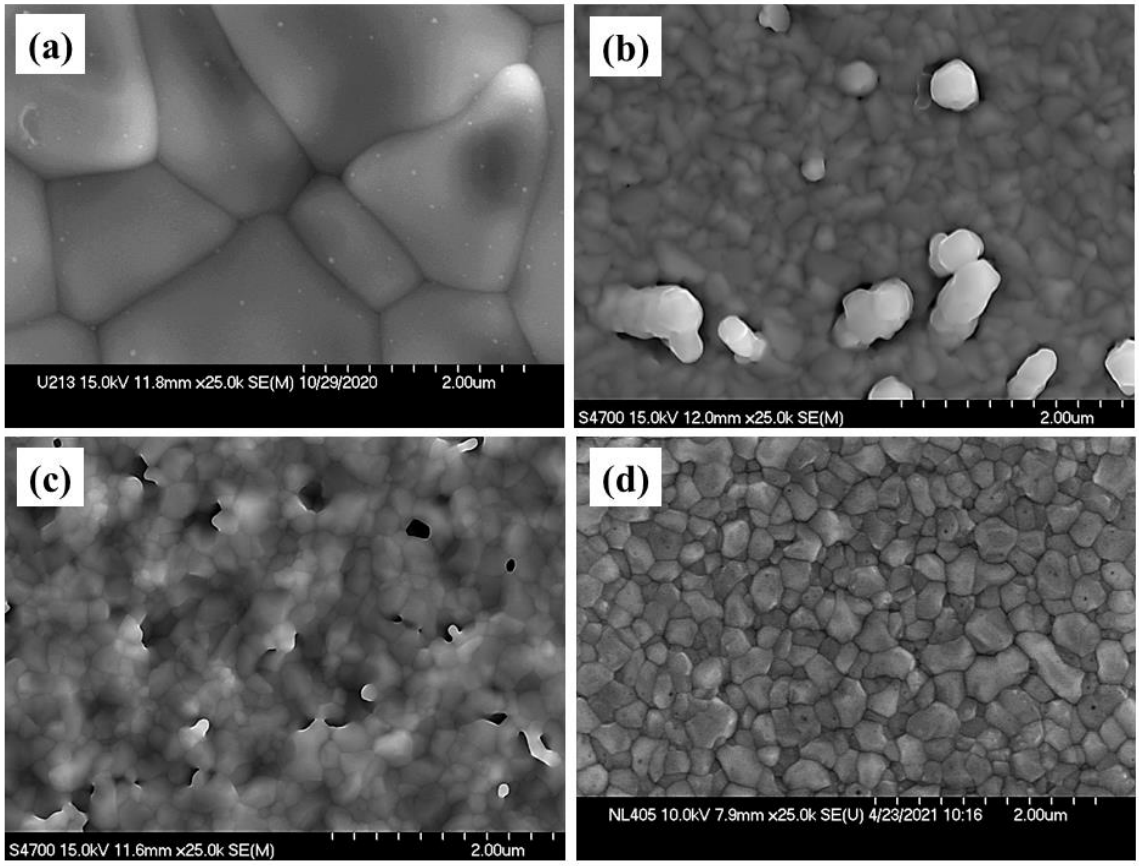

Fig. 7.1. SEM images of Nb_3Sn fabricated by different methods: (a) Sn vapor diffusion method, (b) sputtering from a single Nb_3Sn target, (b) multilayer sputtering of Nb and Sn, and (d) co-sputtering of Nb and Sn.

Surface roughness plays an important role in the performance of SRF cavities. In order to get a high Q_0, a relatively smooth surface is desired. The AFM images of 5 μm × 5 μm scan area

of the films are shown in Fig. 7.2 and the heights of the grains are shown in Fig. 7.3. The large grains of the vapor diffused Nb_3Sn resulted to a rough surface with an RMS surface roughness of 141 nm. The peak-to-valley height difference of the vapor diffused Nb_3Sn film was ~320 nm. The sputtered Nb_3Sn films have relatively smoother surface. Among the sputtered films, the film fabricated from the single target was relatively rougher due to the Sn rich clusters of ~230 nm height. The smoothest surface was observed on the Nb_3Sn films fabricated by co-sputtering method because of grains of similar heights (below 50 nm) throughout the whole surface.

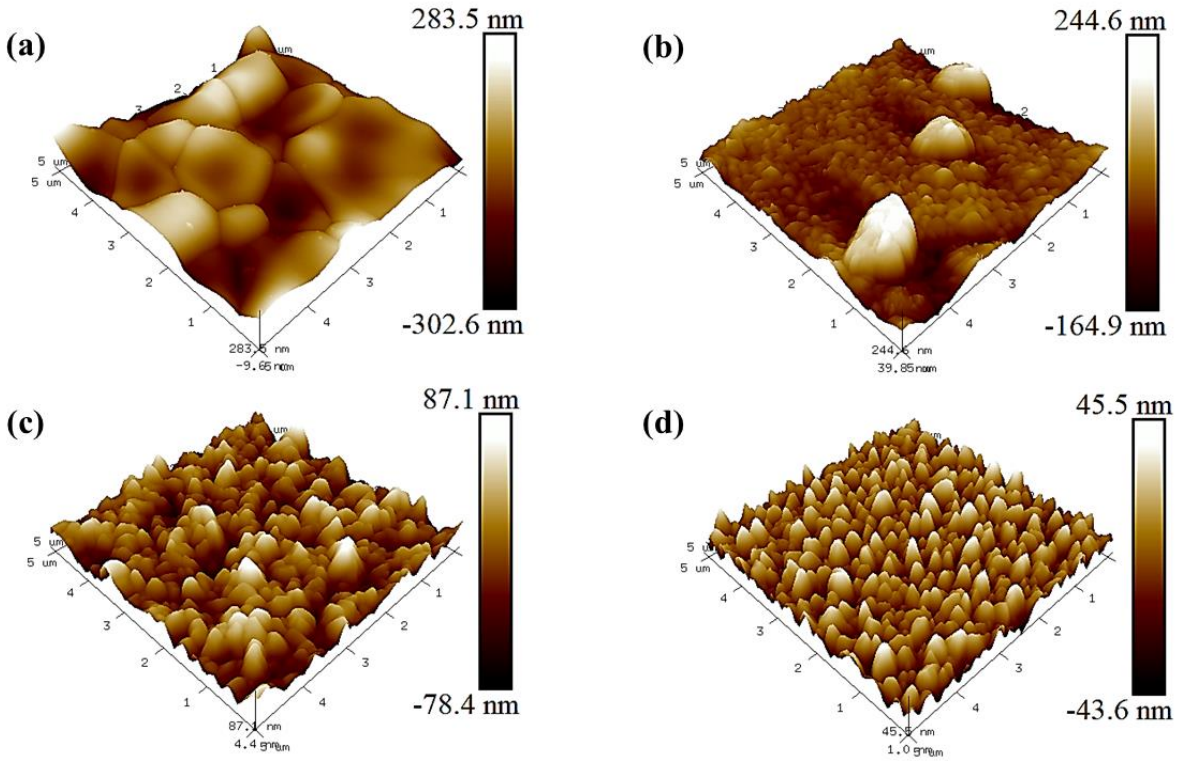

Fig. 7.2. AFM images of Nb_3Sn fabricated by different methods: (a) Sn vapor diffusion method, (b) sputtering from a single Nb_3Sn target, (b) multilayer sputtering of Nb and Sn, and (d) co-sputtering of Nb and Sn.

Table 7.1. Structural properties of Nb3Sn films fabricated by different methods.

Film processing method	Sn composition (%)	Grain size (nm)	RMS roughness (nm)
Vapor diffused	24.5	2000 ± 540	141
Single target sputtering	23.6	263 ± 108	30
Multilayer sputtering	23.0	187 ± 88	34
Co-sputtering	22.3	305 ± 120	14

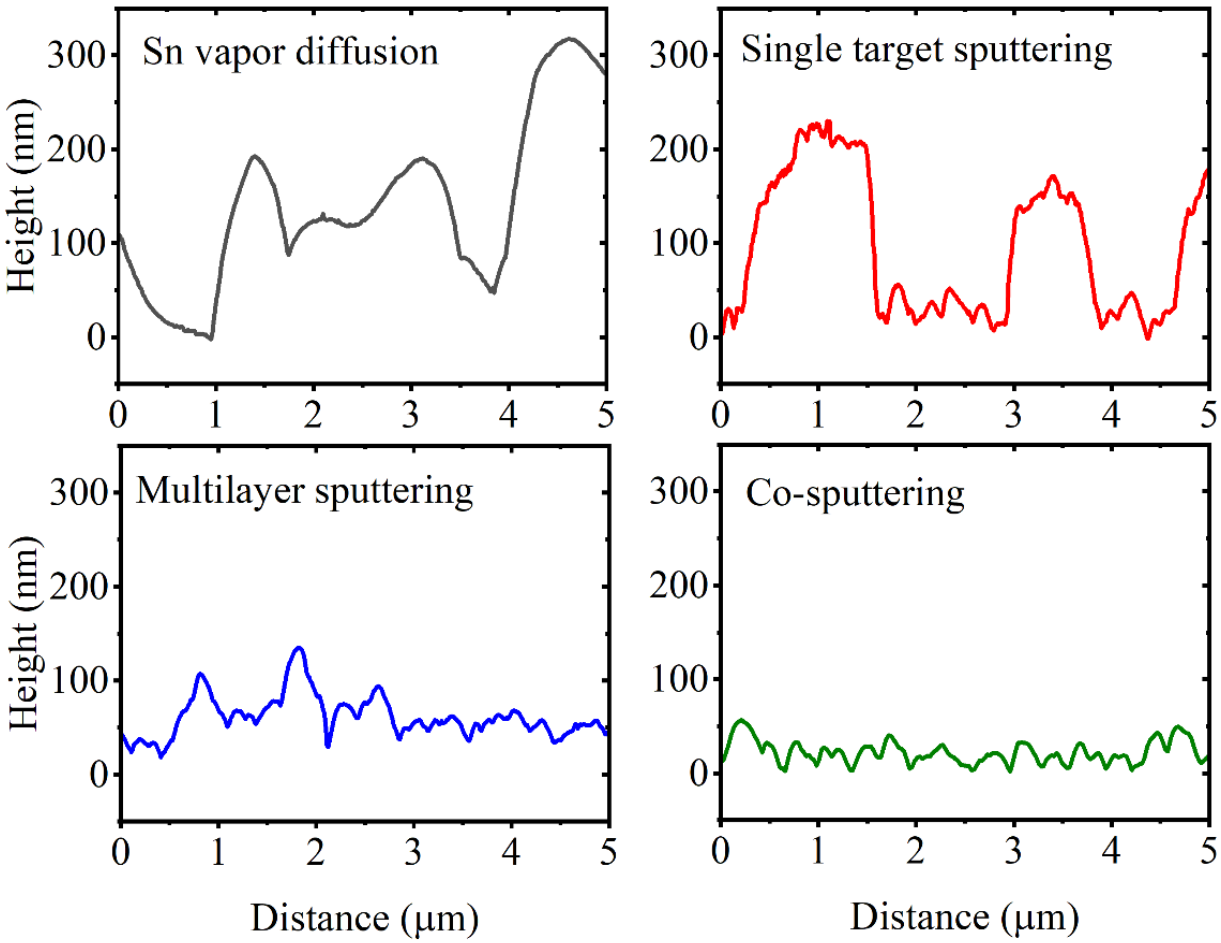

Fig. 7.3. Height data of Nb_3Sn films fabricated by different methods obtained from the AFM images.

Fig. 7.4 shows the XRD patterns of Nb_3Sn films fabricated from Sn vapor diffusion method and three sputtering methods. All XRD patterns confirmed multiple diffraction peaks of Nb_3Sn. The crystallite size of (200), (210), and (211) diffraction orders were calculated from Scherrer equation and the size of the crystallites across these diffraction orders for all processing methods are shown in Fig. 7.5. The vapor diffused Nb_3Sn films had largest crystallites of ~43-46 nm. The smallest crystallite sizes of ~29-31 nm were observed on the Nb_3Sn films fabricated by multilayer sputtering method. Among the films fabricated by magnetron sputtering, the co-sputtered films had the largest crystallite size of ~38-41 nm. The results agree with the grain sizes of the films as observed in Fig. 7.1.

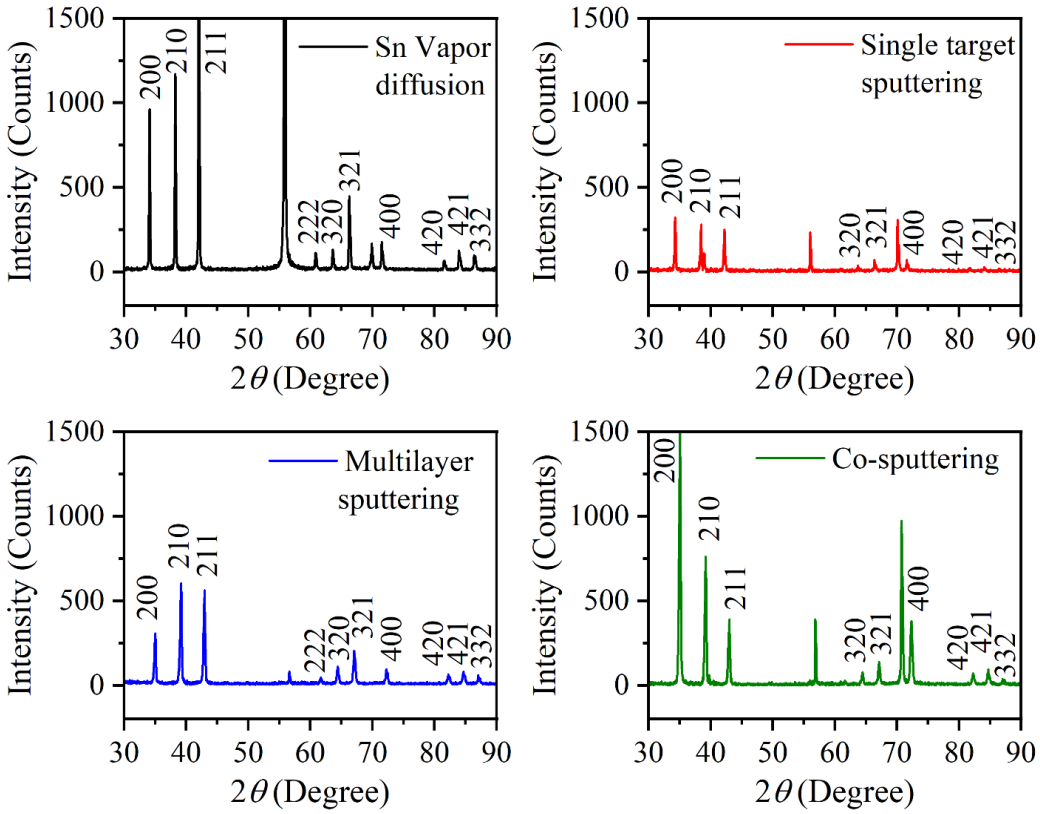

Fig. 7.4. XRD patterns of Nb_3Sn films fabricated by Sn vapor diffusion method and three sputtering methods. The diffraction peaks of only Nb_3Sn are labeled.

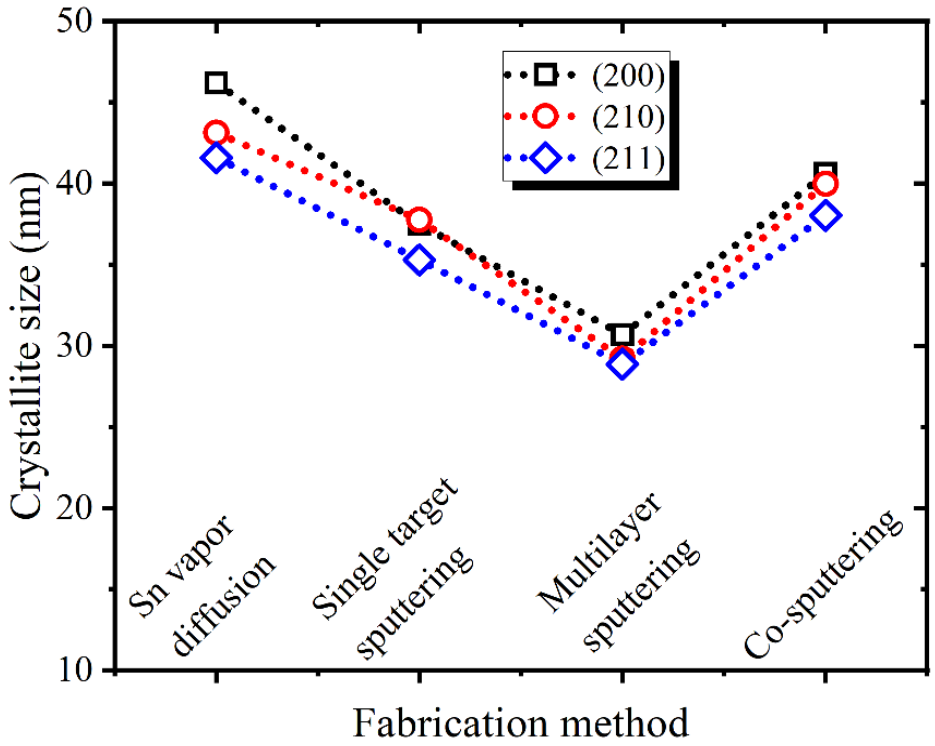

Fig. 7.5. Size of the crystallites along (200), (210), and (211) diffraction orders of the Nb_3Sn films fabricated by Sn vapor diffusion method and three sputtering methods.

The texture coefficients of different diffraction planes were also calculated from the XRD peak intensity, and the calculated TC are shown in Table 7.2. The vapor diffused and the multilayer sputtered Nb_3Sn films had TC value higher than unity along multiple (hkl) planes confirming no specific preferential growth of the films. The single target sputtered and the co-sputtered Nb_3Sn film had highest TC of 2.27 and 3.09 respectively along (200) orientation. The higher order (400) diffraction planes also have higher TC value of 1.38 and 2.16 which confirmed preferential growth along this direction.

Table 7.2. Texture coefficient (TC) of different diffraction orders measured from the XRD peak intensity.

Texture Coefficient	Sn vapor diffusion	Single target sputtering	Multilayer sputtering	Co-sputtering
TC (200)	1.53	2.27	1.08	3.09
TC (210)	1.00	1.01	1.06	0.78
TC (211)	1.85	0.98	1.10	0.47
TC (222)	1.37	---	1.31	---
TC (320)	0.59	0.65	0.57	0.41
TC (321)	0.83	0.55	0.79	0.32
TC (400)	0.82	1.38	0.92	2.16
TC (420)	0.60	0.87	1.19	0.75
TC (421)	0.70	0.59	0.89	0.61
TC (332)	0.72	0.70	1.10	0.42

The measured T_c, ΔT_c and *RRR* of the films are shown in Table 7.3 and RF surface resistances of the films as a function of temperature are shown in Fig. 7.6. The vapor diffused Nb_3Sn has the highest T_c of 17.89 K, which is thought to be due to the higher Sn composition on the film. Since the samples fabricated from magnetron sputtering experienced Sn loss after annealing, the T_c of the films were slightly lower than the vapor diffused Nb_3Sn film. In terms of the RF performance of the films, the films deposited from single target sputtering and multilayer sputtering have higher residual resistance than the vapor diffused Nb_3Sn film. However, the higher residual resistance could be originated from the uncoated Nb substrate that was covered by the sample holder clips during the deposition (Fig. 7.7).

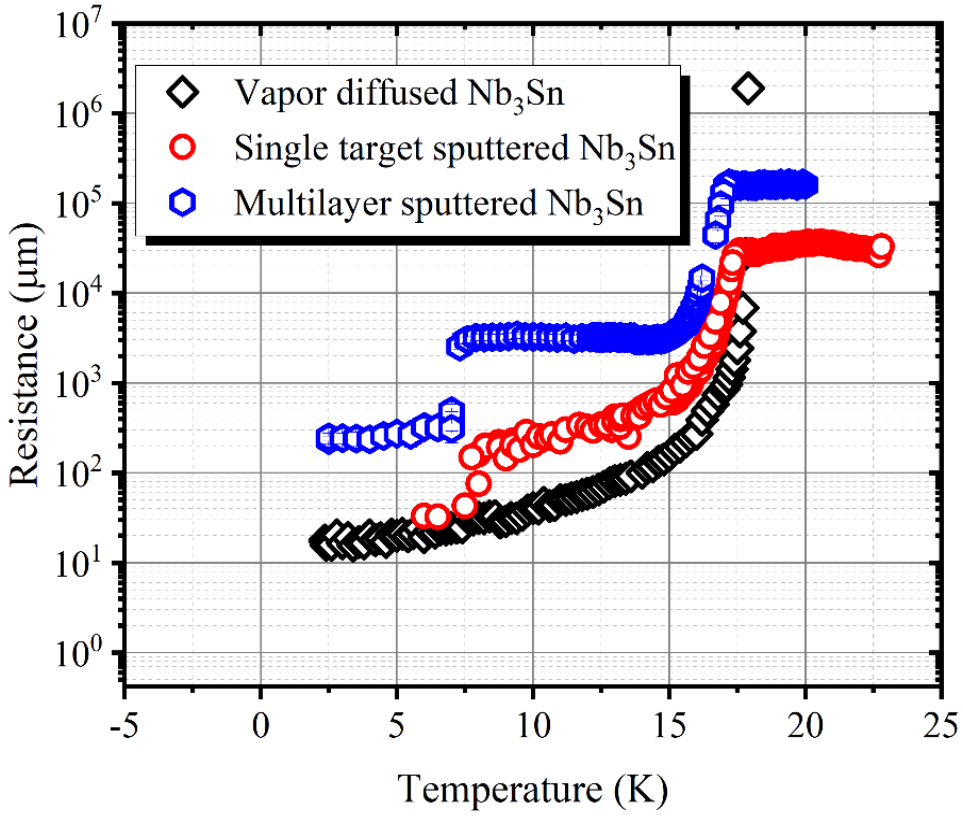

Fig. 7.6. RF surface resistance versus temperature of the vapor diffused Nb_3Sn film and Nb_3Sn films sputtered from single target and multilayer sputtering. The measurements were done using the 7.4 GHz SIC system at Jefferson Lab.

Table 7.3. Superconducting properties of Nb3Sn films fabricated by different methods.

Film processing method	T_c (K)	ΔT_c (K)	*RRR*	RF residual resistance at 12 K (mΩ)
Vapor diffused	17.89	0.14	3.47	0.06
Single target sputtering	17.83	0.03	5.41	0.32
Multilayer sputtering	17.84	0.03	4.40	5.00
Co-sputtering	17.61	0.19	3.63	---

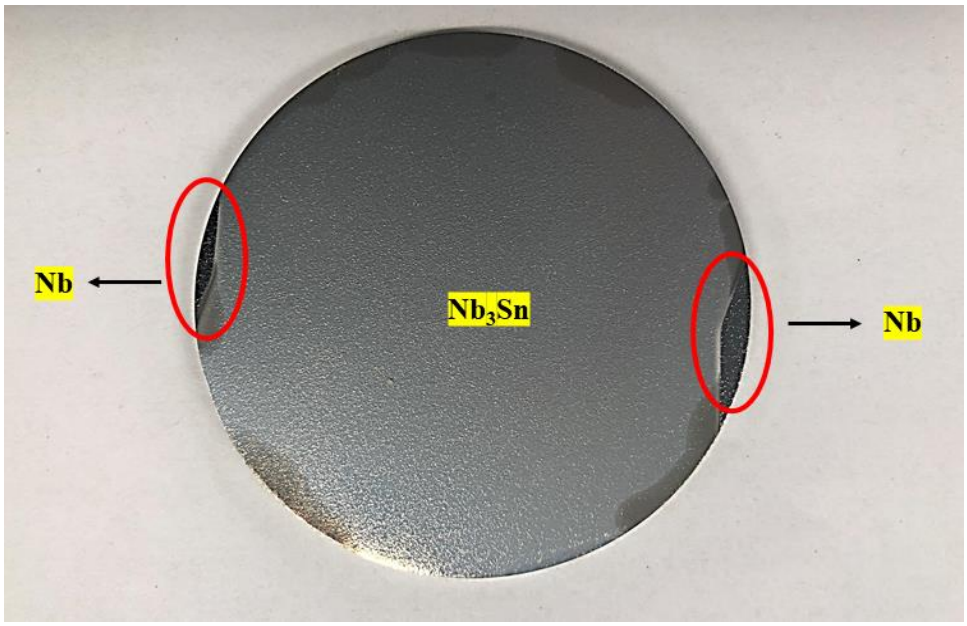

Fig. 7.7. Picture of the Nb_3Sn film coated for the RF surface impedance measurement. The exposed Nb substrate near the uncoated region is clearly seen from the picture.

From the comparison, films from all three processes can provide superconducting Nb_3Sn surface inside the cavities. To apply these methods inside a 2.6 GHz SRF cavity, a sputtering system with two identical cylindrical magnetrons was designed and commissioned. The design of the magnetron and the vacuum chamber and the preliminary data are discussed in Chapter 6. The deposition rate of Nb and Sn magnetrons were calibrated by varying the applied power to each magnetron. A minimum DC power of 8 W is required to sustain the plasma on each magnetron. Finally, three Nb substrates were placed near the two beam tubes and equator to deposit multilayer of Nb and Sn. The 1 μm thick multilayer films were annealed at 950 °C for 3 h and the XRD of the annealed films confirmed the formation of Nb_3Sn.

7.2. Future Work

The focus of this dissertation was to study the fabrication process of Nb_3Sn films by magnetron sputtering to apply the method to fabricate Nb_3Sn inside SRF cavities. Three different sputter fabrication methods (using single stoichiometric target, multilayers, and co-sputtering) were studied in the same deposition chamber. A cylindrical magnetron sputtering system was designed and commissioned for SRF cavity coating. Several points need further investigation.

For the films deposited from the single stoichiometric target, some clustered islands are found throughout the surface. The TEM-EDS confirmed abundance of Sn near those clusters. Since the superconducting properties of Nb_3Sn is strongly dependent on the Sn concentration, the concentration gradient through the films can result in poor RF performance. Therefore, further investigation is required to minimize the concentration gradient by optimizing the deposition conditions.

The films fabricated by multilayer sputtering had several voids on the surface. The TEM images of the cross-section of the films showed that the voids are formed due to the non-uniform Sn throughout the surface. Though, the void density reduced by depositing the films at high temperatures, the voids could not be eliminated completely. Studying the film growth of Nb substrates by optimizing the growth parameters can help to find uniform coating conditions which can be applied in future multilayer sputtered films.

Sn composition plays an important role on the superconducting properties of Nb_3Sn. In SRF cavities, Nb_3Sn films coated by conventional Sn vapor diffusion method resulted to Sn deficient patchy regions which degraded the performance of SRF cavities [10, 11]. Therefore, it is important to maintain the stoichiometry of the films after annealing. I have experienced Sn

loss on almost all condition after annealing. This Sn loss resulted from the Sn evaporation from surface. Further study is required to minimize the Sn loss to achieve the desired stoichiometry.

Results from the small samples coated by the cylindrical magnetron sputtering system demonstrated the feasibility of multilayer sputtering to fabricate Nb_3Sn inside the cavities. Future work on cavity coating with varied coating parameters and RF testing of the coated cavities to achieve high Q_0 and high E_{acc}. Besides, the cylindrical magnetrons need to be modified to apply co-sputtering method to fabricate Nb_3Sn. This can be done by applying small tube targets of Nb and Sn alternately in a single magnetron and modifying the magnetic field on each target to achieve the exact stoichiometry during the deposition.

REFERENCES

[1] Aad, G., Abajyan, T., Abbott, B., Abdallah, J., Khalek, S.A., Abdelalim, A.A., Aben, R., Abi, B., Abolins, M., AbouZeid, O.S. and Abramowicz, H., 2012. Observation of a new particle in the search for the Standard Model Higgs boson with the ATLAS detector at the LHC. *Physics Letters B*, *716*(1), pp.1-29.

[2] Chatrchyan, S., Khachatryan, V., Sirunyan, A.M., Tumasyan, A., Adam, W., Aguilo, E., Bergauer, T., Dragicevic, M., Erö, J., Fabjan, C. and Friedl, M., 2012. Observation of a new boson at a mass of 125 GeV with the CMS experiment at the LHC. *Physics Letters B*, *716*(1), pp.30-61.

[3] Barbalat, O. 1990, Applications of particle accelerators. *No. CERN-AC-90-04-DI-BLIT*. *CERN*.

[4] Abdel Rahman, M.M. and Helal, A.G., 2008. Developments and Applications of Particle Accelerators. International Conference for Nuclear Sciences and Applications, Sharm Al Sheikh (Egypt), TRN: EG0800258120273

[5] Sabharwal, S., 2013. Electron beam irradiation applications. In *Proc. 25th North Am Part Accel Conf* (pp. 745-748).

[6] Padamsee, H., 2017. 50 years of success for SRF accelerators—a review. *Superconductor science and technology*, *30*(5), p.053003.

[7] Evans, L., 2007. The large hadron collider. *New Journal of Physics*, *9*(9), p.335.

[8] Leemann, C.W., Douglas, D.R. and Krafft, G.A., 2001. The continuous electron beam accelerator facility: CEBAF at the Jefferson Laboratory. *Annual Review of Nuclear and Particle Science*, *51*(1), pp.413-450.

[9] Schwarz, A., 2004, August. The European X-Ray free electron laser project at DESY. In *26th International Free-Electron Laser Conference* (pp. 85-89).

[10] Bollen, G., 2010, April. FRIB—Facility for rare isotope beams. In *AIP Conference Proceedings* (Vol. 1224, No. 1, pp. 432-441). American Institute of Physics.

[11] Galayda, J., 2014, August. The new LCLS-II project: Status and challenges. In *LINAC* (pp. 404-408).

[12] Derwent, P.F., Carneiro, J.P., Edelen, J., Lebedev, V., Prost, L., Saini, A., Shemyakin, A. and Steimel, J., 2016. PIP-II Injector Test: challenges and status. *Proc. LINAC'16*, pp.641-645.

[13] Tigner, M., 1979. RF superconductivity for accelerators--Is it a hollow promise?. *IEEE Transactions on Magnetics*, *15*(1), pp.15-20.

[14] Padamsee, H., 2009. *RF superconductivity: science, technology, and applications*. John Wiley & Sons.

[15] Romanenko, A., Grassellino, A., Crawford, A.C., Sergatskov, D.A. and Melnychuk, O., 2014. Ultra-high quality factors in superconducting niobium cavities in ambient magnetic fields up to 190 mG. *Applied Physics Letters*, *105*(23), p.234103.

[16] Proch, D., 1998. Superconducting cavities for accelerators. *Reports on Progress in Physics*, *61*(5), p.431.

[17] Saito, K., 2001. Critical field limitation of the niobium superconducting RF cavity. In *The 10th Workshop on RF Superconductivity, Tsukuba, Japan* (pp. 583-587).

[18] Gurevich, A., 2006. Enhancement of rf breakdown field of superconductors by multilayer coating. Applied Physics Letters, 88(1), p.012511.

[19] Grassellino, A., Romanenko, A., Sergatskov, D., Melnychuk, O., Trenikhina, Y., Crawford, A., Rowe, A., Wong, M., Khabiboulline, T. and Barkov, F., 2013. Nitrogen and argon doping of niobium for superconducting radio frequency cavities: a pathway to highly efficient accelerating structures. *Superconductor Science and Technology*, *26*(10), p.102001.

[20] Dhakal, P., 2020. Nitrogen doping and infusion in SRF cavities: A review. *Physics Open*, *5*, p.100034.

[21] Calatroni, S., 2006. 20 Years of experience with the Nb/Cu technology for superconducting cavities and perspectives for future developments. *Physica C: Superconductivity*, *441*(1-2), pp.95-101.

[22] Valente-Feliciano, A.M., Eremeev, G., Phillips, H.L., Reece, C.E., Spradlin, J.K., Yang, Q., Batchelor, D. and Lukaszew, R.A., 2013. NbTiN Based SIS Multilayer Structures for SRF Applications. *TUP088 SRF*, pp.664-667.

[23] Valente-Feliciano, A.M., 2016. Superconducting RF materials other than bulk niobium: a review. *Superconductor Science and Technology*, *29*(11), p.113002.

[24] Godeke, A., 2006. A review of the properties of Nb3Sn and their variation with A15 composition, morphology and strain state. *Superconductor Science and Technology*, *19*(8), p.R68.

[25] Charlesworth, J.P., Macphail, I. and Madsen, P.E., 1970. Experimental work on the niobium-tin constitution diagram and related studies. *Journal of Materials Science*, *5*(7), pp.580-603.

[26] Eremeev, G., Clemens, B., Macha, K., Park, H. and Williams, R.S., 2013. Development of a Nb_3Sn cavity vapor diffusion deposition system. In *Proc. SRF* (Vol. 13, pp. 603-606).

[27] Posen, S. and Liepe, M., 2014. Advances in development of Nb_3Sn superconducting radio-frequency cavities. *Physical Review Special Topics-Accelerators and Beams*, *17*(11), p.112001.

[28] Saur, E. and Wurm, J., 1962. Präparation und Supraleitungseigenschaften von Niobdrahtproben mit Nb_3Sn-Überzug. *Naturwissenschaften*, *49*(6), pp.127-128.

[29] Hillenbrand, B., Martens, H., Pfister, H., Schnitzke, K. and Ziegler, G., 1975. Superconducting Nb_3Sn-cavities. *IEEE Transactions on Magnetics*, *11*(2), pp.420-422.

[30] Boccard, P., Kneisel, P., Muller, J., Pouryamout, J. and Piel, H., 1998. Results from some temperature mapping experiments on Nb_3Sn RF cavities. Jefferson Laboratory.

[31] Arnolds-Mayer, G. and Chiaveri, E., 1986. On a 500 MHz single cell cavity with Nb_3Sn surface Proc. 3rd Workshop on RF Superconductivity (Chicago).

[32] Allen, L., Beasley, M., Hammond, R. and Turneaure, J., 1983. RF surface resistance of high-T_c superconducting A15 thin films. *IEEE Transactions on Magnetics*, *19*(3), pp.1003-1006.

[33] Kneisel, P., Roeth, R., Piel, H., Mansen, D., Pouryamout, J. and Müller, G., 1996. Nb_3Sn Layers on High-Purity Nb Cavities with Very High Quality Factors and Accelerating Gradients.

[34] Posen, S. and Liepe, M., 2011. Stoichiometric Nb_3Sn in first samples coated at Cornell. *Proceedings of SRF 2011*.

[35] Eremeev, G.V., Kelley, M.J., Reece, C.E., Pudasaini, U. and Tuggle, J., 2015. Progress with multi-cell Nb_3Sn cavity development linked with sample materials characterization. (No. JLAB-ACC-15-2205; DOE/OR/23177-3641). Thomas Jefferson National Accelerator Facility (TJNAF), Newport News, VA (United States).

[36] Posen, S., Merio, M., Romanenko, A. and Trenikhina, Y., 2015. Fermilab Nb_3Sn R&D Program. *Proceedings of SRF 2015*.

[37] Pudasaini, U., Eremeev, G., Reece, C.E., Ciovati, G., Parajuli, I., Sayeed, N. and Kelley, M.J., 2019, June. Recent results from Nb_3Sn single cell cavities coated at Jefferson lab. In *Proc. 19th International Conference on RF Superconductivity,(SRF'19)*.

[38] Pudasaini, U., Kelley, M.J., Ciovati, G., Eremeev, G.V., Reece, C.E., Parajuli, I.P. and Sayeed, M.N., 2018. Nb_3Sn multicell cavity coating at JLAB. *Proc. IPAC 2018*.

[39] Eremeev, G., Clemens, W., Macha, K., Reece, C.E., Valente-Feliciano, A.M., Williams, S., Pudasaini, U. and Kelley, M., 2020. Nb_3Sn multicell cavity coating system at Jefferson Lab. *Review of Scientific Instruments*, *91*(7), p.073911.

[40] Posen, S., Lee, J., Seidman, D.N., Romanenko, A., Tennis, B., Melnychuk, O.S. and Sergatskov, D.A., 2021. Advances in Nb_3Sn superconducting radiofrequency cavities towards first practical accelerator applications. *Superconductor Science and Technology*, *34*(2), p.025007.

[41] Porter, R.D., Liepe, M. and Maniscalco, J.T., 2019. High frequency Nb_3Sn cavities. *MOP011, SRF2019, Dresden, Germany*.

[42] Pudasaini, U., Eremeev, G.V., Reece, C.E., Tuggle, J. and Kelley, M.J., 2019. Initial growth of tin on niobium for vapor diffusion coating of Nb_3Sn. *Superconductor Science and Technology*, *32*(4), p.045008.

[43] Pudasaini, U., Eremeev, G.V., Angle, J.W., Tuggle, J., Reece, C.E. and Kelley, M.J., 2019. Growth of Nb_3Sn coating in tin vapor-diffusion process. *Journal of Vacuum Science & Technology A: Vacuum, Surfaces, and Films*, *37*(5), p.051509.

[44] Lee, J., Posen, S., Mao, Z., Trenikhina, Y., He, K., Hall, D.L., Liepe, M. and Seidman, D.N., 2018. Atomic-scale analyses of Nb_3Sn on Nb prepared by vapor diffusion for superconducting radiofrequency cavity applications: a correlative study. *Superconductor Science and Technology*, *32*(2), p.024001.

[45] Lee, J., Mao, Z., He, K., Spina, T., Baik, S.I., Hall, D.L., Liepe, M., Seidman, D.N. and Posen, S., 2020. Grain-boundary structure and segregation in Nb_3Sn coatings on Nb for high-performance superconducting radiofrequency cavity applications. *Acta Materialia*, *188*, pp.155-165.

[46] Spina, T., Tennis, B.M., Lee, J., Seidman, D.N. and Posen, S., 2020. Development and Understanding of Nb_3Sn films for radiofrequency applications through a sample-host 9-cell cavity. *Superconductor Science and Technology*, *34*(1), p.015008.

[47] Neugebauer, C.A., 1964. Thin films of niobium tin by codeposition. *Journal of Applied Physics*, *35*(12), pp.3599-3603.

[48] Dickey, J.M., Strongin, M. and Kammerer, O.F., 1971. Studies of thin films of Nb_3Sn on Nb. *Journal of Applied Physics*, *42*(13), pp.5808-5820.

[49] Strozier, J.A., Miller, D.L., Kammerer, O.F. and Strongin, M., 1976. Alloys of Sn and Ge on Nb surfaces. *Journal of Applied Physics*, *47*(4), pp.1611-1615.

[50] Perpeet, M., Hein, M.A., Müller, G., Piel, H., Pouryamout, J. and Diete, W., 1997. High-quality Nb_3Sn thin films on sapphire prepared by tin vapor diffusion. *Journal of applied physics*, *82*(10), pp.5021-5023.

[51] Deambrosis, S.M., Keppel, G., Ramazzo, V., Roncolato, C., Sharma, R.G. and Palmieri, V., 2006. A15 superconductors: An alternative to niobium for RF cavities. *Physica C: Superconductivity*, *441*(1-2), pp.108-113.

[52] Koura, N., Umebayashi, T., Idemoto, Y. and Ling, G., 1999. Electrodeposition of Nb-Sn Alloy from $SnCl_2$–$NbCl_5$–EMIC Ambient Temperature Molten Salts. *Electrochemistry*, *67*(6), pp.684-689.

[53] Ui, K., Sakai, H., Takeuchi, K., Ling, G.P. and Koura, N., 2009. Electrodeposition of Nb_3Sn Alloy Film from Lewis Basic $NbCl_5$-$SnCl_2$-EMIC Melt. *Electrochemistry*, *77*(9), pp.798-800.

[54] Barzi, E., Bestetti, M., Reginato, F., Turrioni, D. and Franz, S., 2015. Synthesis of superconducting Nb_3Sn coatings on Nb substrates. *Superconductor Science and Technology*, *29*(1), p.015009.

[55] Franz, S., Barzi, E., Turrioni, D., Glionna, L. and Bestetti, M., 2015. Electrochemical synthesis of Nb_3Sn coatings on Cu substrates. *Materials Letters*, *161*, pp.613-615.

[56] Lu, M., Pan, F., Guo, H., Huang, S., Yang, Z., Chu, Q., Liu, F., Wu, A. and Tan, T., 2021. Electrochemical and thermal synthesis of Nb_3Sn coatings on Nb substrates. *Materials Letters*, *292*, p.129557.

[57] Withanage, W.K., Juliao, A. and Cooley, L.D., 2021. Rapid Nb_3Sn film growth by sputtering Nb on hot bronze. *Superconductor Science and Technology*, *34*(6), p.06LT01.

[58] Sun, Z., Liepe, M., Oseroff, T., Porter, R.D., Arias, T., Sitaraman, N., Connolly, A., Scholtz, J. and Thompson, M.O., 2020. Electroplating of Sn Film on Nb Substrate for Generating Nb_3Sn Thin Films and Post Laser Annealing. In *19th International Conference on RF Superconductivity (SRF'19), Dresden, Germany, 30 June-05 July 2019* (pp. 51-54).

[59] Wu, C.T., Kampwirth, R.T. and Hafstrom, J.W., 1977. High-rate magnetron sputtering of high T_c Nb_3Sn films. *Journal of Vacuum Science and Technology*, *14*(1), pp.134-137.

[60] Kampwirth, R., Hafstrom, J. and Wu, C., 1977. Application of high rate magnetron sputtering to the fabrication of A-15 compounds. *IEEE Transactions on Magnetics*, *13*(1), pp.315-318.

[61] Brimhall, J.L. and Wang, R., 1979. Effect of oxygen on microstructures of high-rate sputter-deposited Nb_3Sn superconductors. *Metallurgical Transactions A*, *10*(10), pp.1499-1503.

[62] Agatsuma, K., Tateishi, H., Arai, K., Saitoh, T. and Nakagawa, M., 1996. Nb_3Sn thin films made by RF magnetron sputtering process with a reacted Nb3Sn powder target. *IEEE Transactions on Magnetics*, *32*(4), pp.2925-2928.

[63] Vandenberg, J., Gurvitch, M., Hamm, R., Hong, M. and Rowell, J., 1985. New phase formation and superconductivity in reactively diffused Nb_3Sn multilayer films. *IEEE transactions on magnetics*, *21*(2), pp.819-822.

[64] Deambrosis, S.M., Keppel, G., Patron, N., Pretto, N., Rampazzo, V., Rossi, A.A., Sharma, R.G., Stivanello, F., Stark, S. and Plamieri, V., 2007. The progress on Nb_3Sn and V_3Si. In *Proceedings de "13th International Workshop on RF superconductivity", SRF* (pp. 393-399).

[65] Rossi, A.A., Deambrosis, S.M., Stark, S., Rampazzo, V., Rupp, V., Sharma, R.G., Stivanello, F. and Palmieri, V., 2009, September. Nb_3Sn films by multilayer sputtering. In *Proceedings of SRF* (pp. 149-154).

[66] Ilyina, E.A., Rosaz, G., Descarrega, J.B., Vollenberg, W., Lunt, A.J.G., Leaux, F., Calatroni, S., Venturini-Delsolaro, W. and Taborelli, M., 2019. Development of sputtered Nb_3Sn films on copper substrates for superconducting radiofrequency applications. *Superconductor Science and Technology*, *32*(3), p.035002.

[67] Tan, W., Ma, R., Pan, H., Zhao, H., He, X., Chen, X., Zhao, C. and Lu, X., 2020. The observation of tin islands in Nb_3Sn thin films deposited by magnetron sputtering. *Physica C: Superconductivity and its Applications*, *576*, p.1353667.

[68] Schäfer, N., Karabas, N., Palakkal, J.P., Petzold, S., Major, M., Pietralla, N. and Alff, L., 2020. Kinetically induced low-temperature synthesis of Nb_3Sn thin films. *Journal of Applied Physics*, *128*(13), p.133902.

[69] Valizadeh, R., Hannah, A.N., Aliasghari, S., Malyshev, O.B., Stenning, G.B.G., Turner, D., Dawson, K., Dahnak, V.R. and ISIS, S., 2019. PVD Depostion of Nb_3Sn thin film on copper substrate from an alloy Nb3Sn target. *Proc. IPAC'19*, pp.2818-2821.

[70] Xiao, L., Lu, X., Yang, Z., Tan, W., Yang, Y., Zhu, L. and Xie, D., 2021. Annealing study on the properties of Cu-based Nb_3Sn films under argon pressures for SRF applications. *Physica C: Superconductivity and its Applications*, *586*, p.1353894.

[71] Ito, R., Nagata, T., Hayano, H., Katayama, R., Kubo, T., Saeki, T., Iwashita, Y. and Ito, H., 2019. Nb_3Sn thin film coating method for superconducting multilayered structure. In *Proc. of SRF* (Vol. 19).

[72] Sundahl, C., Makita, J., Welander, P.B., Su, Y.F., Kametani, F., Xie, L., Zhang, H., Li, L., Gurevich, A. and Eom, C.B., 2021. Development and characterization of Nb_3Sn/Al_2O_3 superconducting multilayers for particle accelerators. *Scientific reports*, *11*(1), pp.1-9.

[73] Benvenuti, C., Circelli, N. and Hauer, M., 1984. Niobium films for superconducting accelerating cavities. *Applied Physics Letters*, *45*(5), pp.583-584.

[74] Calatroni, S., 2006. 20 Years of experience with the Nb/Cu technology for superconducting cavities and perspectives for future developments. *Physica C: Superconductivity*, *441*(1-2), pp.95-101.

[75] Bauer, S., Diete, W., Griep, B., Peiniger, M., Vogel, H., vom Stein, P., Calatroni, S., Chiaveri, E. and Losito, R., 1999. Production of Nb/Cu sputtered superconducting cavities for LHC. In *Proc. 9th Workshop on RF Superconductivity, Santa Fe, New Mexico, USA*.

[76] Sublet, A., Aviles Santillana, I., Bártová, B., Calatroni, S., Cantoni, M., Jecklin, N., Mondino, I., Therasse, M., Venturini Delsolaro, W. and Zhang, P., 2014, July. Nb Coated HIE-ISOLDE QWR Superconducting Accelerating Cavities: From Process Development to Series Production. In *5th Int. Particle Accelerator Conf. (IPAC'14), Dresden, Germany, June 15-20, 2014* (pp. 2571-2573).

[77] Porcellato, A.M., Palmieri, V., Bertazzo, L., Capuzzo, A., Giora, D., Stivanello, F., Stark, S.Y. and Kar, S., 2002. Production, installation and test of Nb-sputtered QWRs for ALPI. *Pramana*, *59*(5), pp.871-880.

[78] Bisoffi, G., Comunian, M., Facco, A., Galatà, A., Modanese, P., Pisent, A., Porcellato, A.M., Pengo, R., Stark, S. and Chalykh, B.B., 2012. A cost-effective energy upgrade of the ALPI Linac at INFN legnaro. *Proc. HIAT*, pp.107-111.

[79] Mosnier, A., Maurier, M., Hanus, X., Juillard, M., Chiaveri, E., Brédy, P., Chel, S., Bosland, P., Orsini, F., Boussard, D. and Périlhous, G., 1998. Genaral Layout of the SOLEIL SRF Unit. *In Proceedings of the 8th Workshop on RF Superconductivity*, pp. 510-517. 1997.

[80] Bosland, P., Brédy, P., Chel, S., Devanz, G., France, M.L.C.S., Craievich, P., Penco, G., Svandrlick, M., Pedrozzi, M., Gloor, W. and Chiaveri, E., 2003, September. Third harmonic superconducting passive cavities in ELETTRA and SLS. In *Proc. of 11th SRF workshop* (pp. 239-243).

[81] Dai, J., He, P., Li, Z., Ma, Y., Yang, F. and Zhang, P., 2019, August. The development of niobium sputtering on copper cavities at IHEP. In *19th International Conference on RF Superconductivity (SRF'19), Dresden, Germany, 30 June-05 July 2019*, pp. 613-615.

[82] Pan, F., Guo, H., He, Y., Jiang, T., Li, C., Lu, M. and Tan, T., 2019, August. New Progress for Nb Sputtered 325 MHz QWR Cavities in IMP. In *19th International Conference on RF Superconductivity (SRF'19), Dresden, Germany, 30 June-05 July 2019* pp. 621-623.

[83] Anders, A., Mendelsberg, R.J., Lim, S., Mentink, M., Slack, J.L., Wallig, J.G., Nollau, A.V. and Yushkov, G.Y. 2011, Deposition of niobium and other superconducting materials with high power impulse magnetron sputtering: Concept and first results.

[84] Terenziani, G., T. Junginger, I. A. Santillana, S. Calatroni, and A. P. Ehiasarian. 2013, Nb coating developments with HIPIMS for SRF applications. *in Proceedings of SRF'13*, pp 627-630.

[85] Burton, M.C., Palczewski, A.D., Phillips, H.L., Valente-Feliciano, A.M., Reece, C.E. and Lukaszew, R., 2019. RF Results of Nb Coated SRF Accelerator Cavities via HiPIMS. *in Proc. LINAC'18, Beijing, China*, pp. 427-430.

[86] Valente-Feliciano, A.M., 2013. HIPIMS: A new generation of film deposition techniques for SRF applications. *in Proceedings of SRF'13*, pp 754-760.

[87] Sigmund, P., 1969. Theory of sputtering. I. Sputtering yield of amorphous and polycrystalline targets. *Physical Review*, *184*(2), p.383.

[88] Cullity, B.D., 1956. *Elements of X-ray Diffraction*. Addison-Wesley Publishing.

[89] Sayeed, M.N., Pudasaini, U., Reece, C.E., Eremeev, G.V. and Elsayed-Ali, H.E., 2020, March. Effect of layer thickness on structural, morphological and superconducting properties of Nb_3Sn films fabricated by multilayer sequential sputtering. In *IOP Conference Series: Materials Science and Engineering* (Vol. 756, No. 1, p. 012014). IOP Publishing.

[90] Spradlin, J.K., Reece, C.E. and Valente-Feliciano, A.M., 2015, A multi-sample residual resistivity ratio system for high quality superconductor measurements. In *Proceedings, 17th International Conference on RF Superconductivity (SRF2015):* pp 726-730.

[91] Putti, M., Ferdeghini, C., Monni, M., Pallecchi, I., Tarantini, C., Manfrinetti, P., Palenzona, A., Daghero, D., Gonnelli, R.S. and Stepanov, V.A., 2005. Critical field of Al-doped MgB_2 samples: Correlation with the suppression of the σ-band gap. *Physical Review B*, *71*(14), p.144505.

[92] Xiao, B.P., Reece, C.E., Phillips, H.L., Geng, R.L., Wang, H., Marhauser, F. and Kelley, M.J., 2011. Note: Radio frequency surface impedance characterization system for superconducting samples at 7.5 GHz. *Review of Scientific Instruments*, *82*(5), p.056104.

[93] Sosa-Guitron, S., Gurevich, A., Delayen, J., Chang Beom, E., Sundahl, C. and Eremeev, G.V., 2015. Measurements of RF Properties of Thin Film Nb_3Sn Superconducting Multilayers Using a Calorimetric Technique. *in Proc. 17th Int. Conf. RF Superconductivity (SRF'15), Whistler, Canada*, Sep. 2015, pp. 720-722.

[94] Eremeev, G.V., Phillips, H.L., Valente-Feliciano, A.M., Reece, C.E. and Xiao, B.P. Characterization of Superconducting Samples with SIC System for Thin Film Developments: Status and Recent Results. *in Proc. 16th Int. Conf. RF Superconductivity (SRF'13)*, pp. 599-602.

[95] Sayeed, M.N., Pudasaini, U., Reece, C.E., Eremeev, G.V. and Elsayed-Ali, H.E., 2021. Properties of Nb_3Sn films fabricated by magnetron sputtering from a single target. *Applied Surface Science*, *541*, p.148528.

[96] Dierker, S.B., Klein, M.V., Webb, G.W. and Fisk, Z., 1983. Electronic raman scattering by superconducting-gap excitations in Nb_3Sn and V_3Si. *Physical Review Letters*, *50*(11), p.853.

[97] Schicktanz, S., Kaiser, R., Schneider, E. and Gläser, W., 1980. Raman studies of A15 compounds. *Physical Review B*, *22*(5), p.2386.

[98] Lee, S.H., Yoon, H.N., Yoon, I.S. and Kim, B.S., 2012. Single crystalline NbO_2 nanowire synthesis by chemical vapor transport method. *Bulletin of the Korean Chemical Society*, *33*(3), pp.839-842.

[99] Singh, N., Deo, M.N., Nand, M., Jha, S.N. and Roy, S.B., 2016. Raman and photoelectron spectroscopic investigation of high-purity niobium materials: Oxides, hydrides, and hydrocarbons. *Journal of Applied Physics*, *120*(11), p.114902.

[100] Raba, A.M., Bautista-Ruíz, J. and Joya, M.R., 2016. Synthesis and structural properties of niobium pentoxide powders: a comparative study of the growth process. *Materials Research*, *19*, pp.1381-1387.

[101] Zasadzinski, J., Albee, B., Bishnoi, S., Cao, C., Ciovati, G., Cooley, L.D., Ford, D.C. and Proslier, T., 2011. Raman Spectroscopy as a Probe of Surface Oxides and Hydrides on Niobium, *in Proc. SRF'11*, pp 912-916.

[102] Sayeed, M.N., Pudasaini, U., Reece, C.E., Eremeev, G. and Elsayed-Ali, H.E., 2019. Structural and superconducting properties of Nb_3Sn films grown by multilayer sequential magnetron sputtering. *Journal of Alloys and Compounds*, *800*, pp.272-278.

[103] Chen, Y., Jyoti, N., Hyun-U, K. and Kim, J., 2012. Effect of annealing temperature on the characteristics of ZnO thin films. *Journal of Physics and Chemistry of Solids*, *73*(11), pp.1259-1263.

[104] Sengupta, J., Sahoo, R.K., Bardhan, K.K. and Mukherjee, C.D., 2011. Influence of annealing temperature on the structural, topographical and optical properties of sol–gel derived ZnO thin films. *Materials Letters*, *65*(17-18), pp.2572-2574.

[105] G. Eremeev, Preliminary error analysis for surface impedance characterization (SIC) system, Technical Report JLAB-TN-12-048, TJNAF (2012).

[106] Schmidt, P.H., Vandenberg, J.M., Hamm, R. and Rowell, J.M., 1980. Characteristics of getter sputtered thin films of Nb_3Ge and multilayered films of Nb_3Ge/Nb_3Ir. In *Superconductivity in d-and f-band metals*. pp. 57-63.

[107] David, B., Mück, M. and Rogalla, H., 1986. A Multilayer Technology with High T c Nb_3Ge Films. In *Advances in Cryogenic Engineering Materials*, pp. 543-548.

[108] Vandenberg, J.M., Hong, M., Hamm, R.A. and Gurvitch, M., 1985. Reactive diffusion and superconductivity of Nb_3Al multilayer films. *Journal of Applied Physics*, *58*(1), pp.618-619.

[109] Im, Y., Johnson, P.E., McKnelly Jr, L.T. and Morris Jr, J.W., 1988. Nb3Al formation in sputter-deposited Nb/Al multilayer samples. *Journal of the Less Common Metals*, *139*(1), pp.87-95.

[110] Di Chiara, A., Scotti di Uccio, U., Senatore, M. and Maritato, L., 1986. Temperature dependence of resistivity for thermally diffused V_3Si multilayer films. *Journal of Low Temperature Physics*, *62*(5), pp.385-396.

[111] Ito, R., Nagata, T., Hayano, H., Katayama, R., Kubo, T., Saeki, T., Iwashita, Y. and Ito, H., 2019. Nb_3Sn thin film coating method for superconducting multilayered structure. In *Proc. of SRF* (Vol. 19).

[112] Xiao, L., Lu, X., Xie, D., Tan, W., Yang, Y. and Zhu, L., 2019. The technical study of Nb_3Sn film deposition on copper by HiPIMS. *Proc. SRF'19*, pp.846-847.

[113] Sayeed, M.N., Elsayed-Ali, H., Eremeev, G.V., Kelley, M.J., Pudasaini, U. and Reece, C.E., 2018, April. Magnetron Sputtering of Nb_3Sn for SRF Cavities. In *Proc. 9th Int. Particle Accelerator Conf. (IPAC'18)* (pp. 3946-3949).

[114] Devantay, H., Jorda, J.L., Decroux, M., Muller, J. and Flükiger, R., 1981. The physical and structural properties of superconducting A15-type Nb-Sn alloys. *Journal of Materials Science*, *16*(8), pp.2145-2153.

[115] Xiao, L., Lu, X., Tan, W., Xie, D., Yang, D.Y., Yang, Y., Yang, Z.Q. and Zhao, J., 2017, July. The study of deposition method of Nb_3Sn film on Cu substrate. In *Proc. of SRF* '17. pp 131-133.

[116] Tan, W., Lu, X., Xie, D., Xiao, L., Yang, Z., Zhao, J., Yang, D., Yang, Y. and Li, B., 2017. Nb_3Sn Thin Film Deposition on Copper by DC Magnetron Sputtering. *Proceedings SRF*, pp.512-515.

[117] Sayeed, M.N., Pudasaini, U., Reece, C.E., Eremeev, G.V. and Elsayed-Ali, H.E., 2021. Effect of substrate temperature on the growth of Nb_3Sn film on Nb by multilayer sputtering. *arXiv preprint arXiv:2109.07066*.

[118] Saud, N., Somidin, F., Ibrahim, N.S. and Mohd Salleh, M.A.A., 2015. Formation of Kirkendall voids at low and high aging temperature in the Sn-0.7 Cu-1.0 wt.% Si3N4/Cu solder joints. In *Advanced Materials Research*. Vol. 1107, pp. 577-581.

[119] Annuar, S., Mahmoodian, R., Hamdi, M. and Tu, K.N., 2017. Intermetallic compounds in 3D integrated circuits technology: a brief review. *Science and Technology of Advanced MaTerialS*, *18*(1), pp.693-703.

[120] Weinberg, K. and Bohme, T., 2009. Condensation and growth of Kirkendall voids in intermetallic compounds. *IEEE Transactions on Components and Packaging Technologies*, *32*(3), pp.684-692.

[121] Sayeed, M.N., Eremeev, G.V., Owen, P., Reece, C. and Elsayed-Ali, H.E., 2021. Microstructural and Superconducting Radiofrequency Properties of Multilayer Sequentially Sputtered Nb_3Sn films. *IEEE Transactions on Applied Superconductivity*, *31*(5), pp.1-4.

[122] Halbritter, J., 1970. Fortran-program for the computation of the surface impedance of superconductors. *Kernforschungszentrum, Karlsruhe (West Germany). Institut fuer Experimentelle Kernphysik.*

[123] Sayeed, M.N., Elsayed-Ali, H., Burton, M.C., Eremeev, G.V., Reece, C.E., Valente-Feliciano, A.M. and Pudasaini, U., 2019. Deposition of Nb_3Sn Films by Multilayer Sequential Sputtering for SRF Cavity Application", *in Proc. 19th Int. Conf. RF Superconductivity (SRF'19)*, pp. 637-641.

[124] Steinberg, R.N., McCambridge, J.D., Prober, D.E. and Guenin, B.M., 1992, April. $YBa_2Cu_3O_7$ films grown by metal cosputtering. In *AIP Conference Proceedings* (Vol. 251, No. 1, pp. 146-152). American Institute of Physics.

[125] Ahn, J.R., Lee, S.G., Hwang, Y., Sung, G.Y. and Kim, D.K., 2003. Fabrication of MgB_2 thin film by rf magnetron sputtering. *Physica C: Superconductivity*, *388*, pp.127-128.

[126] Fabretti, S., Thomas, P., Meinert, M., Imort, I.M. and Thomas, A., 2013. Fabrication of superconducting MgB_2 thin films by magnetron co-sputtering on (001) MgO substrates. *Journal of Superconductivity and Novel Magnetism*, *26*(5), pp.1879-1882.

[127] Del Giudice, L., Adjam, S., La Grange, D., Banakh, O., Karimi, A. and Sanjinés, R., 2016. NbTiN thin films deposited by hybrid HiPIMS/DC magnetron co-sputtering. *Surface and Coatings Technology*, *295*, pp.99-106.

[128] Braun, H.F. and Saur, E.J., 1978. Superconducting properties of Nb_3Ge thin films prepared by cosputtering. *Journal of Low Temperature Physics*, *33*(1), pp.87-104.

[129] Krevet, B., Schauer, W., Wuchner, F. and Jergel, M., 1981. Pinning behavior of Nb_3Ge thin film superconductors. *IEEE Transactions on Magnetics*, *17*(5), pp.1660-1663.

[130] Li, X., Cao, W.H., Tao, X.F., Ren, L.L., Zhou, L.Q. and Xu, G.F., 2016. Structural and nanomechanical characterization of niobium films deposited by DC magnetron sputtering. *Applied Physics A*, *122*(5), pp.1-6.

[131] Shimizu, Y., Tonooka, K., Yoshida, Y., Furuse, M. and Takashima, H., 2018. Room-temperature growth of thin films of niobium on strontium titanate (0 0 1) single-crystal substrates for superconducting joints. *Applied Surface Science*, *444*, pp.71-74.

[132] Sublet, A., Zhang, P., Aviles, I., Mondino, I., Prunet, S., Venturini Delsolaro, W., Calatroni, S., Therasse, M., D'Elia, A. and Jecklin, N., 2013. Preliminary results of Nb thin film coating for HIE-ISOLDE SRF cavities obtained by magnetron sputtering. *In Proceeding SRF'13*. pp 622-622.

[133] Sayeed, M.N., Elsayed-Ali, H.E., Côté, C., Farzad, M.A., Sarkissian, A., Eremeev, G.V. and Valente-Feliciano, A.M., 2021. Cylindrical Magnetron Development for Nb_3Sn Deposition via Magnetron Sputtering. *In Proceedings SRF'21*.

[134] Harris, G.B., 1952. X. Quantitative measurement of preferred orientation in rolled uranium bars. *The London, Edinburgh, and Dublin Philosophical Magazine and Journal of Science*, *43*(336), pp.113-123.

[135] Seetawan, U., Jugsujinda, S., Seetawan, T., Ratchasin, A., Euvananont, C., Junin, C., Thanachayanont, C. and Chainaronk, P., 2011. Effect of calcinations temperature on crystallography and nanoparticles in ZnO disk. *Mater Sci Appl*, *2*(09), p.1302.

[136] Hsu, H.C., Cheng, C.S., Chang, C.C., Yang, S., Chang, C.S. and Hsieh, W.F., 2005. Orientation-enhanced growth and optical properties of ZnO nanowires grown on porous silicon substrates. *Nanotechnology*, *16*(2), p.297.

[137] Navaladian, S., Viswanathan, B., Varadarajan, T.K. and Viswanath, R.P., 2008. Microwave-assisted rapid synthesis of anisotropic Ag nanoparticles by solid state transformation. *Nanotechnology*, *19*(4), p.045603.

APPENDIX A

DETAILS OF SAMPLES

Box #	Sample #	Sample description	Annealed?	Annealing temperature and time	Notes	Characterized data
1	A6	Nb-20 nm, Sn-10 nm 1.2 um, sapphire substrate	N		Temperature dependence study	Fig. 4.8-4.13
1	A7	Nb-20 nm, Sn-10 nm 1.2 um, sapphire substrate	Y	850 °C 3 h	Temperature dependence study	Fig. 4.8-4.13
1	A8	Nb-20 nm, Sn-10 nm 1.2 um, sapphire substrate	Y	850 °C 3 h	Temperature dependence study	Fig. 4.8-4.13
1	T60	Nb-20 nm, Sn-10 nm 1.2 um, sapphire substrate	Y	1000 °C 3 h	Temperature dependence study	Fig. 4.8-4.13
1	T61	Nb-20 nm, Sn-10 nm 1.2 um, sapphire substrate	Y	1000 °C 3 h	Temperature dependence study	Fig. 4.8-4.13
1	T62	Nb-20 nm, Sn-10 nm 1.2 um, sapphire substrate	Y	1100 °C 3 h	Temperature dependence study	Fig. 4.8-4.13
1	T63	Nb-20 nm, Sn-10 nm 1.2 um, sapphire substrate	Y	1100 °C 3 h	Temperature dependence study	Fig. 4.8-4.13
1	T64	Nb-20 nm, Sn-10 nm 1.2 um, sapphire substrate	Y	1200 °C 3 h	Temperature dependence study	Fig. 4.8-4.13
1	T65	Nb-20 nm, Sn-10 nm 1.2 um, sapphire substrate	Y	950 °C 3 h	Temperature dependence study	Fig. 4.8-4.13
1	T66	Nb-20 nm, Sn-10 nm 1.2 um, sapphire substrate	Y	950 °C 3 h	Temperature dependence study	Fig. 4.8-4.13
1	T67	Nb-20 nm, Sn-10 nm 1.2 um, sapphire substrate	Y	1200 °C 3 h	Temperature dependence study	Fig. 4.8-4.13
1	T164	Nb-20 nm, Sn-10 nm 1.2 um, sapphire substrate	Y	950 °C 3 h	Temperature dependence study	Fig. 4.8-4.13
1	T165	Nb-20 nm, Sn-10 nm 1.2 um, sapphire substrate	Y	950 °C 3 h	Temperature dependence	Fig. 4.8-4.13

					study	
1	T166	Nb-20 nm, Sn-10 nm 1.2 um, sapphire substrate	Y	950 °C 1 h	Temperature dependence study	Fig. 4.8-4.13
1	T169	Nb-20 nm, Sn-10 nm 1.2 um, sapphire substrate	Y	950 °C 12 h	Temperature dependence study	Fig. 4.8-4.13
1	M14	Nb-20 nm, Sn-10 nm 1.2 um, Nb substrate	Y	950 °C 1 h	Temperature dependence study	
1	N49	Nb-20 nm, Sn-10 nm 1.2 um, Nb substrate	Y	1100 °C 3 h	Temperature dependence study	
1	N82	Nb-20 nm, Sn-10 nm 1.2 um, Nb substrate	Y	1200 °C 3 h	Temperature dependence study	
1	N99	Nb-20 nm, Sn-10 nm 1.2 um, Nb substrate	Y	1000 °C 3 h	Temperature dependence study	
1	N30	Nb-20 nm, Sn-10 nm 1.2 um, Nb substrate	Y	950 °C 3 h	Temperature dependence study	
1	M32	Nb-20 nm, Sn-10 nm 1.2 um, Nb substrate	Y	950 °C 12 h	Temperature dependence study	
1	N46	Nb-20 nm, Sn-10 nm 1.2 um, Nb substrate	Y	850 °C 3 h	Temperature dependence study	
1	N46	Nb-20 nm, Sn-10 nm 1.2 um, Nb substrate	Y	850 °C 3 h	Temperature dependence study	
1	M11	Nb-20 nm, Sn-10 nm 1.5 um, no buffer layer um, Nb substrate	Y	950 °C 3 h	Buffer layer study	
1	M26	Nb-20 nm, Sn-10 nm 1.5 um, no buffer layer, Nb substrate	Y	950 °C 3 h	Buffer layer study	
1	M23	Nb-20 nm, Sn-10 nm 1.5 um, buffer layer 20 nm, Nb substrate	N		Buffer layer study	
1	T192	Nb-20 nm, Sn-10 nm 1.5 um, no buffer layer, sapphire substrate	Y	950 °C 3 h	Buffer layer study	
1	T188	Nb-20 nm, Sn-10 nm 1.5 um, buffer layer 20 nm, sapphire substrate	Y	950 °C 3 h	Buffer layer study	

1	T191	Nb-20 nm, Sn-10 nm 1.5 um, no buffer layer, sapphire substrate	Y	950 °C 3 h	Buffer layer study	
2	T187	Nb-20 nm, Sn-10 nm 1.5 um, buffer layer 20 nm, sapphire substrate	Y	950 °C 3 h		
2	T184	Nb-20 nm, Sn-10 nm 1.5 um, buffer layer 100 nm, sapphire substrate	Y	950 °C 3 h		
2	T158	Nb-50 nm, Sn-25 nm 1.2 um, sapphire substrate	Y	950 °C 3 h	Thickness dependence study	Fig. 4.4-4.7
2	T161	Nb-50 nm, Sn-25 nm 1.2 um, sapphire substrate	Y	950 °C 3 h	Thickness dependence study	Fig. 4.4-4.7
2	T160	Nb-50 nm, Sn-2 5nm 1.2 um, sapphire substrate	Y	950 °C 3 h	Thickness dependence study	Fig. 4.4-4.7
2	T159	Nb-50 nm, Sn-25 nm 1.2 um, sapphire substrate	N		Thickness dependence study	Fig. 4.4-4.7
2	T122	Nb-50 nm, Sn-25 nm 1.2 um, sapphire substrate	N		Thickness dependence study	Fig. 4.4-4.7
2	T154	Nb-10 nm, Sn-5 nm 1.2 um, sapphire substrate	N		Thickness dependence study	Fig. 4.4-4.7
2	T155	Nb-10 nm, Sn-5 nm 1.2 um, sapphire substrate	Y	950 °C 3 h	Thickness dependence study	Fig. 4.4-4.7
2	T156	Nb-10 nm, Sn-5 nm 1.2 um, sapphire substrate	Y	950 °C 3 h	Thickness dependence study	Fig. 4.4-4.7
2	T157	Nb-10 nm, Sn-5 nm 1.2 um, sapphire substrate	Y	950 °C 3 h	Thickness dependence study	Fig. 4.4-4.7
2	T150	Nb-200 nm, Sn-100 nm 1.2 um, sapphire substrate	Y	950 °C 3 h	Thickness dependence study	Fig. 4.4-4.7
2	T152	Nb-200 nm, Sn-100 nm 1.2 um, sapphire substrate	N		Thickness dependence study	Fig. 4.4-4.7
2	T112	Nb-100 nm, Sn-50 nm 1.2 um, sapphire substrate	N		Thickness dependence study	Fig. 4.4-4.7

2	T111	Nb-100 nm, Sn-50 nm 1.2 um, sapphire substrate	N		Thickness dependence study	Fig. 4.4-4.7
2	N68	Nb-100 nm, Sn-50 nm 1.2 um, Nb substrate	Y	950 °C 3 h	Thickness dependence study	
2	T162	Nb-20 nm, Sn-10 nm 1.2 um, sapphire substrate	Y	950 °C 3 h	Thickness dependence study	
2	T202	Nb-10 nm, Sn-10 nm 900 nm, sapphire substrate	Y	950 °C 3 h	Thickness dependence study	
2	T203	Nb-10 nm, Sn-10 nm 900 nm, sapphire substrate	Y	950 °C 3 h	Thickness dependence study	
2	T204, T205	Nb-10 nm, Sn-10 nm 900 nm, sapphire substrate	N		Thickness dependence study	
2	M16	Nb-10 nm, Sn-10 nm 900 nm, Nb substrate	N		Thickness dependence study	
2	M27	Nb-20 nm, Sn-10 nm 900 nm, Nb substrate	N		Thickness dependence study	
2	T206	Nb-20 nm, Sn-10 nm 900 nm, sapphire substrate	Y	950 °C 3 h	Thickness dependence study	
2	T207	Nb-20 nm, Sn-10 nm 900 nm, sapphire substrate	Y	950 °C 3 h	Thickness dependence study	
2	T210	Nb-20 nm, Sn-10 nm 900 nm, sapphire substrate	Y	950 °C 3 h	Thickness dependence study	
2	T211	Nb-30 nm, Sn-10 nm 900 nm, sapphire substrate	Y	950 °C 3 h	Thickness dependence study	
2	T212, T213	Nb-30 nm, Sn-10 nm 900 nm, sapphire substrate	N		Thickness dependence study	
2	M13	Nb-30 nm, Sn-10 nm 900 nm, Nb substrate			Thickness dependence study	
3	M10	Nb-30 nm, Sn-10 nm 900 nm, Nb substrate	N		Thickness dependence study	

3	M21	Nb-40 nm, Sn-10 nm 900 nm, Nb substrate	N		Thickness dependence study	
3	T216, T217	Nb-40 nm, Sn-10 nm 900 nm, sapphire substrate	N		Thickness dependence study	
3	T214	Nb-40 nm, Sn-10 nm 900 nm, sapphire substrate	Y	950 °C 3 h	Thickness dependence study	
3	T215	Nb-40 nm, Sn-10 nm 900 nm, sapphire substrate	Y	950 °C 3 h	Thickness dependence study	
3	M34	Nb-40 nm, Sn-10 nm 900 nm, Nb substrate	Y	950 °C 3 h	Thickness dependence study	
3	M37	Nb-10 nm, Sn-10 nm 900 nm, Nb substrate	Y	950 °C 3 h	Thickness dependence study	
3	M0	Nb-20 nm, Sn-10 nm 1.5 um, Nb substrate	Y	950 °C 3 h	Thickness dependence study	
3	N95	Nb-20 nm, Sn-10 nm 1.2 um, Nb substrate	Y	950 °C 3 h	Thickness dependence study	
3	T258	Nb-20 nm, Sn- 10 nm, 1 um, 10 rpm	Y	950 °C 3 h	Substrate rotation analysis	
3	T260	Nb-20 nm, Sn- 10 nm, 1 um, 10 rpm	Y	950 °C 3 h	Substrate rotation analysis	
3	T261	Nb-20 nm, Sn- 10 nm, 1 um, 20 rpm	Y	950 °C 3 h	Substrate rotation analysis	
3	T263	Nb-20 nm, Sn- 10 nm, 1 um, 20 rpm	Y	950 °C 3 h	Substrate rotation analysis	
3	T231	Nb-20 nm, Sn-10 nm, 1.5 um, 200 °C	Y	950 °C 3 h	Substrate temperature	
3	T239	Nb-20 nm, Sn-10 nm, 1.5 um, 100 °C	Y	950 °C 3 h	Substrate temperature	
3	T244	Nb-20 nm, Sn-10 nm, 1.5 um, 200 °C	Y	950 °C 3 h	Substrate temperature	
3	T247	Nb-20 nm, Sn-10 nm, 1 um, 100 °C	N		Substrate temperature	
3	T248	Nb-20 nm, Sn-10 nm, 1 um, 100 °C	Y	950 °C 3 h	Substrate temperature	

3	T250	Nb-20 nm, Sn-10 nm, 1 um, RT	Y	950 °C 3 h	Substrate temperature	
3	T255	Nb-20 nm, Sn-10 nm, 1 um, 65 °C	Y	950 °C 3 h	Substrate temperature	
3	T256	Nb-20 nm, Sn-10 nm, 1 um, 65 °C	N		Substrate temperature	
3	T264	Nb-20 nm, Sn-10 nm, 1 um, 150 °C	Y	950 °C 3 h	Substrate temperature	
3	T266	Nb-20 nm, Sn-10 nm, 1 um, 150 °C	Y	950 °C 3 h	Substrate temperature	
3	T267	Nb-20 nm, Sn-10 nm, 1 um, 250 °C	Y	950 °C 3 h	Substrate temperature	
3	T268	Nb-20 nm, Sn-10 nm, 1 um, 250 °C	N		Substrate temperature	
3	T273	Nb-20 nm, Sn-10 nm, 1 um, 600 °C	N		Substrate temperature	
3	T283	Nb-20 nm, Sn-10 nm, 1 um, 300 °C	N		Substrate temperature	
3	T269	Nb-20 nm, Sn-10 nm, 1 um, 250 °C	Y	950 °C 3 h	Substrate temperature	
4	T232	Nb-20 nm, Sn-10 nm, 1.5 um, 200 °C	N		Substrate temperature	
4	T245	Nb-20 nm, Sn-10 nm, 1 um, 200 °C	N		Substrate temperature	
4	T230	Nb-20 nm, Sn-10 nm, 1 um, 200 °C	Y	950 °C 3 h	Substrate temperature	
4	T242	Nb-20 nm, Sn-10 nm, 1 um, 200 °C	Y	950 °C 3 h	Substrate temperature	
4	T236 T237	Nb-20 nm, Sn-10 nm, 1.5 um, RT	N		Substrate temperature	
4	N22	Nb-20 nm, Sn-10 nm, 1 um, 200 °C	Y	950 °C 3 h	Substrate temperature	
4	N75	Nb-20 nm, Sn-10 nm, 1.5 um, 200 °C	N		Substrate temperature	
4	T233	Nb-20 nm, Sn-10 nm, 1 um, 200 °C	Y	950 °C 3 h	Substrate temperature	
4	N44	Nb-20 nm, Sn-10 nm, 1 um, 200 °C	Y	950 °C 3 h	Substrate temperature	
4	T238	Nb-20 nm, Sn-10 nm, 1.5 um, 100 °C	N		Substrate temperature	
4	N3	Nb-20 nm, Sn-10 nm, 1 um, 200 °C	N		Substrate temperature	
4	T243	Nb-20 nm, Sn-10 nm, 1 um, 200 °C	Y	950 °C 3 h	Substrate temperature	
4	T241	Nb-20 nm, Sn-10 nm,	Y	950 °C 3 h	Substrate	

		1.5 um, 100 °C			temperature	
4	T240	Nb-20 nm, Sn-10 nm, 1.5 um, 100 °C	Y	950 °C 3 h	Substrate temperature	
4	N8	Nb-20 nm, Sn-10 nm, 1 um, RT, 20 rpm	N		Substrate temperature	
4	N93	Nb-20 nm, Sn-10 nm, 500 nm, 100 °C	N		Substrate temperature	
4	T276	Nb-20 nm, Sn-10 nm, 500 nm, 100 °C	N		Substrate temperature	
4	T278	Nb-20 nm, Sn-10 nm, 500 nm, 100 °C	N		Substrate temperature	
4	N41	Nb-20 nm, Sn-10 nm, 500 nm, 100 °C	N		Substrate temperature	
4	T279	Nb-20 nm, Sn-10 nm, 500 nm, 100 °C	N		Substrate temperature	
4	T277	Nb-20 nm, Sn-10 nm, 500 nm, 100 °C	N		Substrate temperature	
4	T275	Nb-20 nm, Sn-10 nm, 500 nm, 100 °C	N		Substrate temperature	
4	T274	Nb-20 nm, Sn-10 nm, 500 nm, 100 °C	N		Substrate temperature	
4		Sn 500 nm, 250 °C	N		Substrate temperature	
4		Sn 300 nm, RT	N		Substrate temperature	
4		Sn 500 nm RT	N		Substrate temperature	
4	T124	Nb-18 nm, Sn-10 nm, RT	N		Substrate temperature	
4	T20	Nb-50 nm, Sn- 25 nm, RT	N		Substrate temperature	
5	T306	Nb 20 nm, Sn 10 nm, 3 cycles, 250 °C	N		Substrate temperature	
5	T300 T301	Nb 20 nm, Sn 10 nm, 1 cycle, RT	N		Substrate temperature	
5	T298 T299	Nb 20 nm, Sn 10 nm, 1 cycle, RT	N		Substrate temperature	
5	T297	Nb 20 nm, Sn 10 nm, 1 cycle, 250 °C	N		Substrate temperature	
5	GE94	Nb 20 nm, Sn 10 nm, 1 cycle, 250 °C	N		Substrate temperature	Fig. 4.22
5	T295	Nb 20 nm, Sn 10 nm, 1 cycle, 250 °C	N		Substrate temperature	
5	T310	Nb 20 nm, Sn 10 nm, 10 cycle, 250 °C	N		Substrate temperature	

5	T309	Nb 20 nm, Sn 10 nm, 10 cycle, RT	N		Substrate temperature	
5	T311	Nb 20 nm, Sn 10 nm, 10 cycle, 250 °C	N		Substrate temperature	
5	T308	Nb 20 nm, Sn 10 nm, 10 cycle, RT	N		Substrate temperature	
5	GE52	Nb 20 nm, Sn 10 nm, 1 cycle, RT	N		Substrate temperature	
5	T335 T336	Nb 200 nm buffer, Nb 20 nm, Sn 2.5 nm, 10 cycle, 250 °C	N		Substrate temperature	
5	GE49	Nb 20 nm, Sn 10 nm, 3 cycle, RT	N		Substrate temperature	Fig. 4.22
5	GE26	Nb 20 nm, Sn 10 nm, 10 cycle, 250 °C	N		Substrate temperature	Fig. 4.22
5	T306	Nb 20 nm, Sn 10 nm, 3 cycle, RT	N		Substrate temperature	
5	T303	Nb 20 nm, Sn 10 nm, 3 cycle, RT	N		Substrate temperature	
5	GE84	Nb 20 nm, Sn 10 nm, 3 cycle, 250 °C	N		Substrate temperature	Fig. 4.22
5	T307	Nb 20 nm, Sn 10 nm, 3 cycle, 250 °C	N		Substrate temperature	
5	T305	Nb 20 nm, Sn 10 nm, 3 cycle, 250 °C	N		Substrate temperature	
5	T317	Nb 20 nm, Sn 10 nm, 10 cycle, 250 °C	N		Substrate temperature	
5	T302	Nb 20 nm, Sn 10 nm, 3 cycle, RT	N		Substrate temperature	
5	T334	Nb 20 nm, Sn 5 nm, 10 cycle, 250 °C	N		Substrate temperature	
5	T332	Nb 800 C, Nb 20 nm, Sn 10 nm, 10 cycle, 250 °C	N		Substrate temperature	
5	T296	Nb 20 nm, Sn 10 nm, 1 cycle, 250 °C	N		Substrate temperature	
5	T331	Nb 800 C, Nb 20 nm, Sn 10 nm, 10 cycle, 250 °C	N		Substrate temperature	
5	N23	Nb 20 nm, Sn 10 nm, 1.5 um, RT	Y	950 °C 3 h	Substrate temperature	
5	C21, C22, C23	Nb 20 nm RF, Sn 10 nm DC, 1 um	N		Substrate temperature	
5	T347	Nb 4 nm, Sn 2 nm, 1 um, 250 °C	N		Substrate temperature	
6	X19	Nb 20 nm RF, Sn 10 nm	N		Substrate	

	X36	DC, 1 um			temperature	
6	T251	Nb 20 nm, Sn 10 nm, 1 um, RT	Y	950 °C 3 h	Substrate temperature	
6	T249	Nb 20 nm, Sn 10 nm, 1 um, RT	N		Substrate temperature	
6	GE17	Nb 20 nm, Sn 10 nm, 1 um, 40 °C	N		Substrate temperature	
6	GE15	Nb 20 nm, Sn 10 nm, 1 um, 40 °C	N		Substrate temperature	
6	T288	Nb 20 nm, Sn 10 nm, 1 um, 600 °C	N		Substrate temperature	
6	T292	Nb 20 nm, Sn 10 nm, 1 um, 40 °C	N		Substrate temperature	
6	T293	Nb 20 nm, Sn 10 nm, 1 um, 40 °C	N		Substrate temperature	
6	T287	Nb 20 nm, Sn 10 nm, 1 um, 600 °C	N		Substrate temperature	
6	T294	Nb 20 nm, Sn 10 nm, 1 um, 40 °C	N		Substrate temperature	
6	T286	Nb 20 nm, Sn 10 nm, 1 um, 600 °C	N		Substrate temperature	
6	T271	Nb 20 nm, Sn 10 nm, 1 um, 600 °C	N		Substrate temperature	
6	N4	Nb 20 nm, Sn 10 nm, 1 um, 65 °C	Y	950 °C 3 h	Substrate temperature	
6	GE98 GE93	Nb 20 nm, Sn 2.5 nm, 10 cycles um, 250 °C	Y	950 °C 3 h	Substrate temperature	
6	T349	Nb 100 nm, Sn 50 nm, 1 um, 250 °C	Y	950 °C 3 h	Substrate temperature	
6	T348	Nb 100 nm, Sn 50 nm, 1 um, 250 °C	Y	950 °C 3 h	Substrate temperature	
6	M6	Nb 100 nm, Sn 50 nm, 1 um, 250 °C	Y	950 °C 3 h	Substrate temperature	Fig. 4.14-4.20, Fig. 4.22
6	N92	Nb 20 nm, Sn 10 nm, 1 um, RT 10rpm	Y	950 °C 3 h	Substrate temperature	
6	T346	Nb 4 nm, Sn 2 nm, 1 um, 250 °C	Y	950 °C 3 h	Substrate temperature	
6	T286	Nb 20 nm, Sn 10 nm, 1 um, 0.5 A/s, 250 °C	Y	950 °C 3 h	Substrate temperature	
6	T287	Nb 20 nm, Sn 10 nm, 1 um, 0.5 A/s, 250 °C	Y	950 °C 3 h	Substrate temperature	
6	N38	Nb 20 nm, Sn 10 nm, 1 um, 250 °C 20 rpm	Y	950 °C 3 h	Substrate temperature	
6	GE5 GE11	Nb 20 nm, Sn 10 nm, 10 cycles, 250 °C	Y	950 °C 3 h	Substrate temperature	

6	N10	Nb 20 nm, Sn 10 nm, 1.5 um, 200 °C	Y	950 °C 3 h	Substrate temperature	
6	N8	Nb 20 nm, Sn 10 nm, 1 um, 250 °C	Y	950 °C 3 h	Substrate temperature	Fig. 4.14-4.20
6	N60	Nb 20 nm, Sn 10 nm, 1 um, 100 °C	Y	950 °C 3 h	Substrate temperature	Fig. 4.14-4.20
6	N72	Nb 20 nm, Sn 10 nm, 1 um, 150 °C	Y	950 °C 3 h	Substrate temperature	Fig. 4.14-4.20
6	N84	Nb 20 nm, Sn 10 nm, 1 um, RT	Y	950 °C 3 h	Substrate temperature	Fig. 4.14-4.20
7	T265	Nb 20 nm, Sn 10 nm, 1 um, 150 °C	N		Substrate temperature	
7	GE60	Nb 20 nm, Sn 10 nm, 1 um, 250 °C	N		Substrate temperature	Fig. 4.14-4.20
7	N54	Nb 20 nm, Sn 10 nm, 1 um, 150 °C	N		Substrate temperature	Fig. 4.14-4.20
7	T285	Nb 20 nm, Sn 10 nm, 1 um, 300 °C	N		Substrate temperature	
7	N6	Nb 200 nm, Sn 5 nm, RT	N		Substrate temperature	
7	N52	Nb 5 nm, Sn 2.5 nm, 1 um, 250 °C	N		Substrate temperature	
7	C10 C11	Nb 200 nm, Nb 2 nm Sn 0.5 nm, 200 layers	N		Substrate temperature	
7	C12	Nb 200 nm, Nb 2 nm Sn 0.5 nm, 200 layers	N		Substrate temperature	
7	T318	Nb 20 nm Sn 10 nm, 10 cycles	N		Substrate temperature	
7	N50	Nb 20 nm, Sn 10 nm, 1 um, 100 °C	N		Substrate temperature	
7	N51	Nb 20 nm, Sn 10 nm, 1 um, RT	N		Substrate temperature	
7	N88	Nb 200 nm, Sn 2 nm, 1 um, RT	N		Substrate temperature	
7	GE19 GE28	Nb 20 nm, Sn 5 nm, 10 cycles, 250 °C	N		Substrate temperature	
7	T342 T343	Nb 5 nm, Sn 2.5 nm, 10 cycles, 250 °C	N		Substrate temperature	
7	N25	Nb 5 nm, Sn 2.5 nm, 10 cycles, 250 °C	N		Substrate temperature	
7	T344	Nb 5 nm, Sn 2.5 nm, 1 um, 250 °C	N		Substrate temperature	
7	T341	Nb 20 nm Sn 2.5 nm × 5 Nb 20 nm Sn 5 nm × 5 Nb 20 nm Sn 7.5 nm × 5	N		Substrate temperature	

		Nb 20 nm Sn 10 nm × 7				
7	C9	Nb 2 nm, Sn 1 nm, 500 nm, 250 °C	N		Substrate temperature	
7	GE2 GE47	Nb 2 nm, Sn 1 nm, 500 nm, 250 °C	N		Substrate temperature	
7	T338	Nb 1 nm, Sn 0.5 nm, 500 nm, 250 °C	N		Substrate temperature	
7	N33	Nb 5 nm, Sn 2.5 nm, 1 um, 250 °C	N		Substrate temperature	
7	N67	Nb 20 nm Sn 2.5 nm × 5 Nb 20 nm Sn 5 nm × 5 Nb 20 nm Sn 7.5 nm × 5 Nb 20 nm Sn 10 nm × 7	N		Substrate temperature	
7	N2 N7	Nb 4 nm, Sn 2 nm, 1 um, 250 °C	N		Substrate temperature	
7	N13	Nb 20 nm, Sn 10 nm, 1 um, 300 °C	N		Substrate temperature	
7	T284	Nb 20 nm, Sn 10 nm, 1 um, 300 °C	N		Substrate temperature	
7	GE42	Nb 200 nm, RT	N		Substrate temperature	
7	GE78	Nb 20 nm, Sn 10 nm, 1 cycle, RT	N		Substrate temperature	
7	GE4	Nb 2 nm, Sn 1 nm, 500 nm, 200 °C	N		Substrate temperature	
8	M40, N42	Nb 200 nm, Sn 10 nm RT	N		Substrate temperature	
8	N5, N95	Nb 200 nm, Nb-Sn 2-0.5 nm	N		Substrate temperature	
8	C4, C5	Nb:Sn 2:1	N		Substrate temperature	
8	C3	Nb:Sn 2:1			Substrate temperature	
8	GE29, GE41	65 °C, Nb 1nm Sn 0.5 nm	N		Substrate temperature	
8	GE87, GE53	250 °C, Nb 4 nm Sn 2 nm	N		Substrate temperature	
8	N81, GE54	RT, Nb 2 Sn 1	N		Substrate temperature	
8	C1, C2	RT, Nb 2 nm Sn 1 nm	N		Substrate temperature	
8	C6	200 °C, Nb 2 nm Sn 1 nm	N		Substrate temperature	
8	N32, GE68	RT, Nb 2 nm, Sn 1 nm total 500 nm	N		Substrate temperature	

8	C7, C8	250 °C, Nb 2 nm Sn 1 nm	N		Substrate temperature	
8	T339	250 °C, Nb 1 nm Sn 0.5 nm	N		Substrate temperature	
8	N62, N86	250 °C, Nb 2 nm Sn 1 nm ×100	N		Substrate temperature	
8	T312	250 °C Nb 200 nm	N		Substrate temperature	
8	N90	65 °C Nb 20 nm Sn 10 nm	Y		Substrate temperature	Fig. 4.14-4.20
8	T314	RT Nb 200 nm	N		Substrate temperature	
8	N73	100 °C, Nb 20 nm Sn 10 nm	Y		Substrate temperature	Fig. 4.14-4.20
8	N26	100 °C, Nb 20 nm Sn 10 nm	N		Substrate temperature	Fig. 4.14-4.20
8	N74	150 °C, Nb 20 nm Sn 10 nm	Y		Substrate temperature	Fig. 4.14-4.20
8	GE97	40 °C, Nb 20 nm Sn 10 nm			Substrate temperature	
8	T291, T289	550 °C-250 °C Nb3Sn-Nb-Sn 1 um			Substrate temperature	
8	GE80, GE9	550 °C-250 °C Nb3Sn-Nb-Sn 1 um			Substrate temperature	
9	T329	RT Nb 20 nm Sn 10 nm	Y	780 °C 100 °C/min 5 min	Anneal rate	
9	T326	RT Nb 20 nm Sn 10 nm	Y	750 °C 100 °C/min 7 min	Anneal rate	
9	T360	RT Nb 20 nm Sn 10 nm	Y	800 °C 100 °C/min 3 h	Anneal rate	
9	T324	RT Nb 20 nm Sn 10 nm	Y	950 °C 100 °C/min 3 h	Anneal rate	
9	T328	RT Nb 20 nm Sn 10 nm	Y	850 °C 100 °C/min 5 min	Anneal rate	
9	T322	RT Nb 20 nm Sn 10 nm	Y	950 °C 100 °C/min 5 min	Anneal rate	
9	T329	RT Nb 20 nm Sn 10 nm	Y	780 °C 100 °C/min 5 min	Anneal rate	
9	T330	RT Nb 20 nm Sn 10 nm	Y	850 °C 100 °C/min 5	Anneal rate	

				min		
9	T361	RT Nb 20 nm Sn 10 nm	Y	800 °C 100 °C/min 5 min	Anneal rate	
9	T321	RT Nb 20 nm Sn 10 nm	Y	950 °C 100 °C/min 20 min	Anneal rate	
9	T353	RT Nb 20 nm Sn 10 nm	Y	775 °C 100 °C/min 7 min	Anneal rate	
9	T325	RT Nb 20 nm Sn 10 nm	Y	750 °C 100 °C/min 7 min	Anneal rate	
9	T323, M2, M35	RT Nb 20 nm Sn 10 nm	Y	950 °C 100 °C/min 3 h	Anneal rate	
9	N29, N39	RT Nb 20 nm Sn 10 nm	Y	950 °C 100 °C/min 5 min	Anneal rate	
9	GE69, GE82	RT Nb 20 nm Sn 10 nm	Y	800 °C 100 °C/min 3 h	Anneal rate	
9	N11, N64	RT Nb 20 nm Sn 10 nm	Y	850 °C 100 °C/min 5 min	Anneal rate	
9	N34, N17	RT Nb 20 nm Sn 10 nm	Y	750 °C 100 °C/min 7 min	Anneal rate	
9	N97, GE43, GE48	RT Nb 20 nm Sn 10 nm	Y	775 °C 100 °C/min 5 min	Anneal rate	
9	GE70, GE71	RT Nb 20 nm Sn 10 nm	Y	780 °C 100 °C/min 5 min	Anneal rate	
9	T345, N87	250 °C Nb 5 nm Sn 2.5 nm	Y	950 °C 3 h	Substrate temperature	
10	X24, X90	400 °C Nb:Sn 1000:625	N		Co-sputtering	Fig. 5.2, 5.3
10	X1	400 °C Nb:Sn 1000:560	Y	950 °C 3 h	Co-sputtering	
10	X10	400 °C Nb:Sn 1000:625	Y	950 °C 3 h	Co-sputtering	
10	N79	400 °C Nb:Sn 1000:500	Y	950 °C 3 h	Co-sputtering	
10	X90	400 °C Nb:Sn 1000:625	Y	950 °C 3 h	Co-sputtering	

10	X58	400 °C Nb:Sn 1000:750	Y	950 °C 3 h	Co-sputtering	
10	X50	400 °C Nb:Sn 1000:580	N		Co-sputtering	Fig. 5.2, 5.3
10	C17, C18, D31, D32	400 °C Nb:Sn 1000:625	N		Co-sputtering	
10	X3, D60, D59	200 °C Nb:Sn 1000:580	N		Co-sputtering	Fig 5.4-5.6
10	X39	400 °C Nb:Sn 1000:750	N		Co-sputtering	
10	X28	500 °C Nb:Sn 1000:580	N		Co-sputtering	Fig 5.4-5.6
10	X41, X46	Nb RF, Sn DC	Y	950 °C 3 h		
10	X20, X51, D37, D38	500 °C Nb:Sn 1000:580	N		Co-sputtering	Fig 5.4-5.6
10	X47	400 °C Nb:Sn 1000:625	N		Co-sputtering	Fig 5.2-5.3
10	X19	400 °C Nb:Sn 1000:560	N		Co-sputtering	Fig 5.2-5.3
10	X53	400 °C Nb:Sn 1000:560	Y	950 °C 3 h	Co-sputtering	
10	D69, D70	100 °C Nb:Sn 1000:580	N		Co-sputtering	Fig 5.4-5.6
10	D51, D52	RT Nb:Sn 1000:580	N		Co-sputtering	Fig 5.4-5.6
13	B114	Nb3Sn 6 h	Y	1000 °C 14h	Single target	Fig. 3.2-3.8
13	B127	Nb3Sn 6 h	N		Single target	Fig. 3.2-3.8
13	B122	Nb3Sn 6 h	N		Single target	Fig. 3.2-3.8
13	B115	Nb3Sn 6 h	Y	1000 °C 12h	Single target	Fig. 3.2-3.8
13	B83	Nb3Sn 3 h	Y	950 °C 3h	Single target	Fig. 3.2-3.8
13	B126	Nb3Sn 6 h	N		Single target	
13	B112	Nb3Sn 6 h	Y	1000 °C 12h	Single target	Fig. 3.2-3.8
13	B124	Nb3Sn 6 h	Y	900 °C 24	Single target	Fig. 3.2-

				h		3.8
13	B116	Nb3Sn 6 h	Y	800 °C 24 h	Single target	Fig. 3.2-3.8
13	B125	Nb3Sn 6 h	Y	900 °C 24 h	Single target	Fig. 3.2-3.8
13	B83	Nb3Sn 3 h	Y	950 °C 3 h	Single target	
13	B119	Nb3Sn 6 h	Y	800 °C 24 h	Single target	Fig. 3.2-3.8
13	B123	Nb3Sn 6 h	Y	1000 C 24 h	Single target	Fig. 3.2-3.8
13	N36	Nb3Sn 14 h	N		Single target	
14	D19	400 °C Nb:Sn 1000:560	Y	950 °C 3 h	Co-sputtering	
14	D12	400 °C Nb:Sn 1000:500	Y	950 °C 3 h	Co-sputtering	
14	D15	400 °C Nb:Sn 1000:750	Y	950 °C 3 h	Co-sputtering	
14	D20	400 °C Nb:Sn 1000:560	Y	950 °C 3 h	Co-sputtering	
14	D29, D30	400 °C Nb:Sn 1000:625	Y	950 °C 3 h	Co-sputtering	
14	D1	400 °C Nb:Sn 1000:580	Y	950 °C 3 h	Co-sputtering	
14	D16	400 °C Nb:Sn 1000:750	Y	950 °C 3 h	Co-sputtering	
14	D39	400 °C Nb:Sn 1000:580	Y	950 °C 3 h	Co-sputtering	
14	C16	400 °C Nb:Sn 1000:625	Y	950 °C 3 h	Co-sputtering	
11	D34	300 °C Nb:Sn 1000:580	Y	950 °C 3 h	Co-sputtering	
11	D71, D72	100 °C Nb:Sn 1000:580	Y	665 °C 3 h	Co-sputtering	Fig. 5.13
11	D63, D64	200 °C Nb:Sn 1000:580	Y	950 °C 3 h	Co-sputtering	Fig. 5.13
11	D27	200 °C Nb:Sn 1000:580		950 °C 3 h	Co-sputtering	
11	D36	300 °C Nb:Sn 1000:580	Y	665 °C 3 h	Co-sputtering	Fig. 5.13
11	D21, D22	400 °C Nb:Sn 1000:580	Y	950 °C 3 h	Co-sputtering	Fig. 5.13
11	D17	400 °C Nb:Sn 1000:560	Y	665 °C 3 h	Co-sputtering	Fig. 5.13

11	D53, D54	RT Nb:Sn 1000:580	Y	665 °C 3 h	Co-sputtering	Fig. 5.13
11	D28	200 °C Nb:Sn 1000:580	Y	950 °C 3 h	Co-sputtering	Fig. 5.13
11	D23, D24	400 °C Nb:Sn 1000:580	Y	665 °C 3 h	Co-sputtering	Fig. 5.13
11	D35	300 °C Nb:Sn 1000:580	Y	665 °C 3 h	Co-sputtering	Fig. 5.13
11	D61, D62	200 °C Nb:Sn 1000:580	Y	665 °C 3 h	Co-sputtering	Fig. 5.13
11	D10	400 °C Nb:Sn 1000:580	Y	665 °C 3 h	Co-sputtering	Fig. 5.13
11	D67, D68	100 °C Nb:Sn 1000:580	Y	950°C 3 h	Co-sputtering	Fig. 5.13
11	D33	300 °C Nb:Sn 1000:580	Y	950 °C 3 h	Co-sputtering	Fig. 5.13
12	X4	Nb:Sn 1000:580, 400 °C	Y	665 °C 3 h	Co-sputtering	Fig. 5.7-5.9, 5.12
12	N84	Nb:Sn 20:10, RT, 1 um	Y	950 °C 3 h	Substrate temperature	
12	N98	Nb:Sn 20:10 250 °C	Y	950 °C 3 h	Substrate temperature	
12	N60	Nb:Sn 20:10, 100 °C	Y	950 °C 3 h	Substate temperature	
12	X31	Nb:Sn 1000:580, 300 °C	Y	665 °C 3 h	Co-sputtering	Fig. 5.7-5.9, 5.12
12	X27	Nb:Sn 1000:580, 200 °C	Y	665 °C 3 h	Co-sputtering	Fig. 5.7-5.9, 5.12
12	X37	Nb:Sn 1000:580, 100 °C	Y	665 °C 3 h	Co-sputtering	Fig. 5.7-5.9, 5.12
12	N10	Nb:Sn 20:10 1.5 um, 200 °C	N		Substrate temperature	
12	N92	Nb:Sn 20:10, 1 um, RT, 10 RPM	Y	950 °C 3 h	Substrate rotation	
12	N4	Nb:Sn 20:10 1 um, 65 °C	Y	950 °C 3 h	Substrate temperature	
12	N72	Nb:Sn 20:10, 1 um, 150 °C	Y	950 °C 3 h	Substrate temperature	
12	N38	Nb:Sn 20:10 1 um, RT	Y	950 °C 3 h	Substrate rotation	
12	X8	Nb:Sn 1000:580, 300 °C	Y	950 °C 3 h	Co-sputtering	Fig. 5.7, 5.10, 5.11
12	X48	Nb:Sn 1000:580, 200 °C	Y	950 °C 3 h	Co-sputtering	Fig. 5.7, 5.10, 5.11
12	X7	Nb:Sn 1000:580, 400 °C	Y	950 °C 3 h	Co-	Fig. 5.7,

					sputtering	5.10, 5.11
12	X5	Nb:Sn 1000:580, RT	Y	950 °C 3 h	Co-sputtering	Fig. 5.7, 5.10, 5.11
15	X35, X58	Nb:Sn 1000:580, 200 °C	N		Co-sputtering	Fig 5.4-5.6
15	D25	Nb:Sn 1000:580, 200 °C	N		Co-sputtering	Fig 5.6
15	D13	Nb:Sn 1000:750, 400 °C	N		Co-sputtering	Fig 5.6
15	D26	Nb:Sn 1000:580, 200 °C	N		Co-sputtering	Fig 5.6
15	X15, X92	Nb:Sn 1000:580, 300 °C	N		Co-sputtering	Fig 5.4-5.6
15	D14	Nb:Sn 1000:750, 400 °C	N		Co-sputtering	
15	D18	Nb:Sn 1000:560, 400 °C	N		Co-sputtering	
15	D55, D56	Nb:Sn 1000:580, RT	N		Co-sputtering	
15	D49, D50	Nb:Sn 1000:580, RT	Y	950 °C 3 h	Co-sputtering	
15	X58	Nb:Sn 1000:580, 200 °C	Y	950 °C 3 h	Co-sputtering	Fig. 5.7, 5.10, 5.11
15	X22	Nb:Sn 1000:580, 100 °C	Y	950 °C 3 h	Co-sputtering	Fig. 5.7, 5.10, 5.11
15	T234, T235	Nb:Sn 20:101.5 um, RT	Y	950 °C 3 h	Multilayer	
16	C19, C20	Nb:Sn 20RF:10DC	Y	950 °C 3 h	Switched target	
16	C13, C14, C15, N1, N66	Nb:Sn 20RF:10DC, 250 °C	N		Switched target	
16	T200, T201	Nb:Sn 20:10, 0.5 Å/s	Y	950°C 3 h	Slow deposition	
16	M5	Nb:Sn 20:10 1.5 um, RT, 200 nm buffer	Y	950 °C 3 h	Buffer layer experiment	
16	N19	Nb_3Sn 14 h, 800C	N		Stoichiometric target	
16	T290	Nb-Sn 1 um, 550 °C-250 °C	N		Substrate temperature	
16	N28	Nb:Sn 20:10 RT	N		Multilayer	
16	GE18	Nb:Sn 100:50	Y	950 °C 3 h	Substrate	

					temperature	
16	GE19, M17	Nb 200 nm, Sn 10 nm	N			
16	T340, N56	Nb:Sn 20:10-7.5-5-2.5	Y	950 °C 3 h	Substrate temperature	
16	GE65	Nb:Sn 2:1	N		Co-sputtering	
16	M20	Nb_3Sn 6 h, 800 °C	Y	1000 °C 1 h	Stoichiometric target	
16	N63	Nb:Sn 20:10 1 um, 100 °C	Y	950 °C 3 h	Substrate temperature	
17	M15	Nb:Sn 20:10 RT, no buffer	N		Buffer layer	
17	ND4	Nb_3Sn 14 h, 800 °C	Y	1000 °C 1 h	Stoichiometric target	Fig. 3.9-3.13
18	ND1	Nb_3Sn 14 h, 800 °C	Y	800 °C 24 h	Stoichiometric target	Fig. 3.9-3.13
18	ND3	Nb_3Sn 14 h, 800 °C	N		Stoichiometric target	Fig. 3.9-3.13
18	D57, D58	Nb:Sn 1000:580, 200 °C	N		Co-sputtering	
18	D65, D66	Nb:Sn 1000:580, 100 °C	N		Co-sputtering	
18	WS07	Nb_3Sn			Vapor diffused	

APPENDIX B

MEASURED T_C, ΔT_C AND *RRR* OF THE FILMS

Sample name	T_c (K)	ΔT_c (K)	*RRR*	*Figure number*
S39	16.15	3.2	1.63	
S41	16.4	2.5	1.6	
T7	4.92	0.07	1.47	
T9	4.98	0.1	1.6	
T11	4.89	0.1	1.64	
T13	4.87	0.08	1.67	
T15	4.85	0.16	1.48	
T20	6.69	0.3	1.7	
T21	13.23	5.96	1.75	
T22	13.2	6	1.84	
T23	13.16	5.6	1.88	
T24	13.45	6.15	1.3	
A1	15.6	3.88	1.65	
A2	15.42	4.08	1.64	
A7	15.3	3.84	1.59	
T52	15.13	4.1	1.65	
T53	15.35	4.26	1.6	
T60	15.25	4.1	1.65	
T62	17.53	0.15	2	Fig. 4.13
T64	7.88	0.04	2.63	Fig. 4.13
T66	17.65	0.1	3.68	Fig. 4.13
T61	17.68	0.05	3.17	Fig. 4.13
T63	17.51	0.25	2.01	Fig. 4.13
T65	17.66	0.09	3.71	Fig. 4.13
T101	7.33	0.24	2.36	Fig. 4.13
T103	17.62	0.04	4.32	
T106	6.52	0.09	2.4	
T109	6.21	0.11	2.27	
T112	7.67	0.1	4.04	
T113	17.52	0.1	4.34	
T122	17.71	0.07	4.72	
T124	7.3	0.09	2.88	
T120	6.76	0.1	2.2	
B113	17.69	0.08	2.88	
B120	17.69	0.08	2.95	
D18	7.01	0.96	1.13	
D20	17.28	0.22	2.92	

D21	17.14	0.35	2.69	Fig. 5.13
D22	17.02	0.86	2.76	
D27	17.16	0.55	3.10	
D28	17.34	0.20	3.09	
D29	17.49	0.21	3.17	
D30	17.31	0.28	3.06	
D33	16.91	0.43	2.64	
D34	16.98	0.28	2.62	
D35	11.73	0.46	1.45	
D36	11.47	0.25	1.44	
D39	17.10	0.22	2.30	
D40	16.95	0.66	2.12	
NU10	17.90	0.28	3.42	
NU7	17.89	0.14	3.47	
D39	17.42	0.13	2.29	
D40	17.04	0.37	2.09	
D49	17.61	0.19	3.63	Fig. 5.13
D50	17.59	0.2	3.65	
D59	6.73	0.04	1.33	
D60	6.8	0.04	1.3	
D63	17.41	0.16	3.09	
D64	17.28	0.14	2.9	
D67	17.44	0.28		
D68	17.38	0.16	3.27	
T322	17.64	0.16	3.79	
T324	17.63	0.16	3.6	
T326	16.2	0.66	3	
T328	17.62	0.16	3.98	
T329	16.98	0.28	3.44	
T360	17.64	0.17	4.57	
D35	15.34	0.44	1.96	Fig. 5.13
D36	15.17	0.38	1.96	
D53	15.66	0.36	1.54	
D54	15.88	0.17	2.07	Fig. 5.13
D61	15.61	0.35	2.15	
D62	15.62	0.33	2.16	Fig. 5.13
D71	15.88	0.24	2.2	
D72	15.77	0.25	2.19	
D9	15.05	0.92	1.48	
D10	11.17	0.66	1.45	
D17	15	0.5	2.1	
D23	14.73	0.27	1.79	Fig. 5.13
D24	14.72	0.56	1.71	

D11	15.1	0.36	1.91	
D12	15.88	2.12	1.89	
D15	16.77	0.18	2.55	
D16	16.82	0.23	2.57	
D19	17.19	0.1	2.89	
D20	17.21	0.1	2.87	
D21	17.12	0.2	2.62	
D22	17.17	0.23	2.68	Fig. 5.13
D27	17.21	0.14	3.27	Fig. 5.13
D28	17.2	0.06	2.99	
D29	17.32	0.12	2.79	
D30	17.23	0.1	2.98	
D33	16.94	0.13	2.82	Fig. 5.13
D34	16.87	0.1	2.54	
D39	17.24	0.14	2.25	
D40	17.13	0.16	2.05	
D63	17.31	0.14	3	
D64	17.23	0.15	2.79	
T203	17.93	0.02	5.1	
T206	17.84	0.03	4.4	
T211	17.56	0.09	3.29	
T215	17.54	0.11	2.68	
T156	17.82	0.02	4.96	
T164	17.83	0.01	4.69	
T160	17.83	0.02	4.88	
T150	17.84	0.03	4.72	

APPENDIX C

UNPUBLISHED DATA

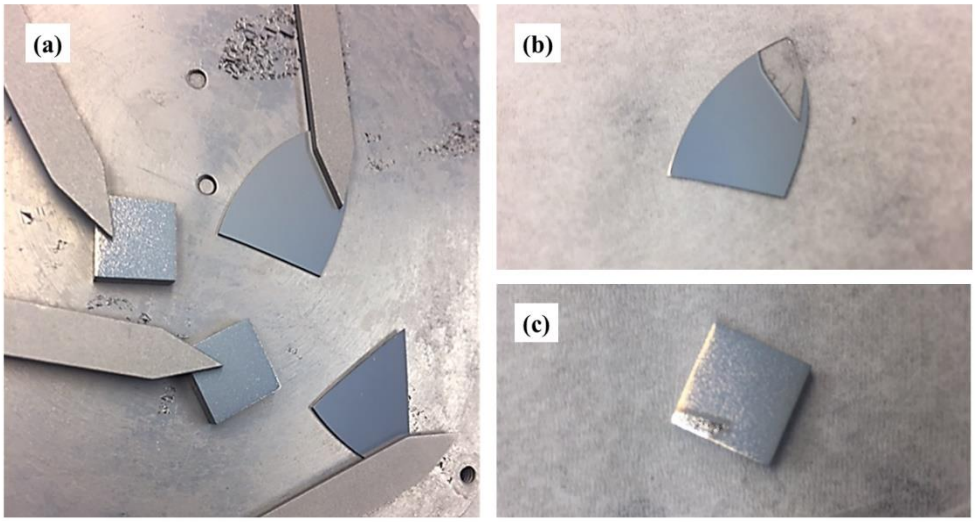

Fig. A.1. (a) The samples taken out from the sputter coater after deposition, (b) multilayered film coated on sapphire substrate, and (c) multilayered film coated on Nb substrate.

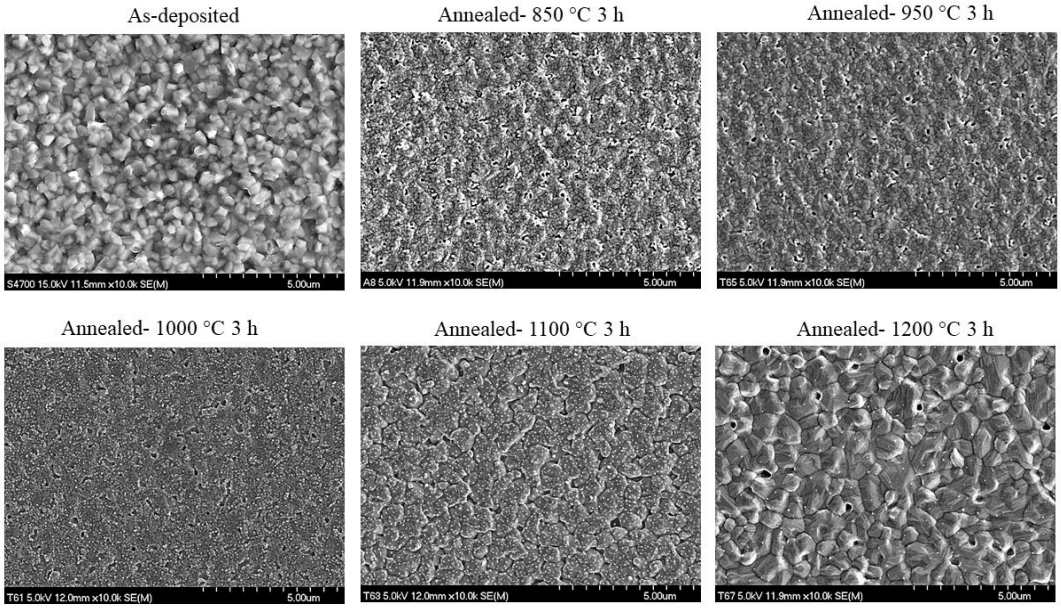

Fig. A.2. SEM images (low magnification) of Nb_3Sn films deposited by multilayer sputtering and annealed at different temperatures for 3 h.

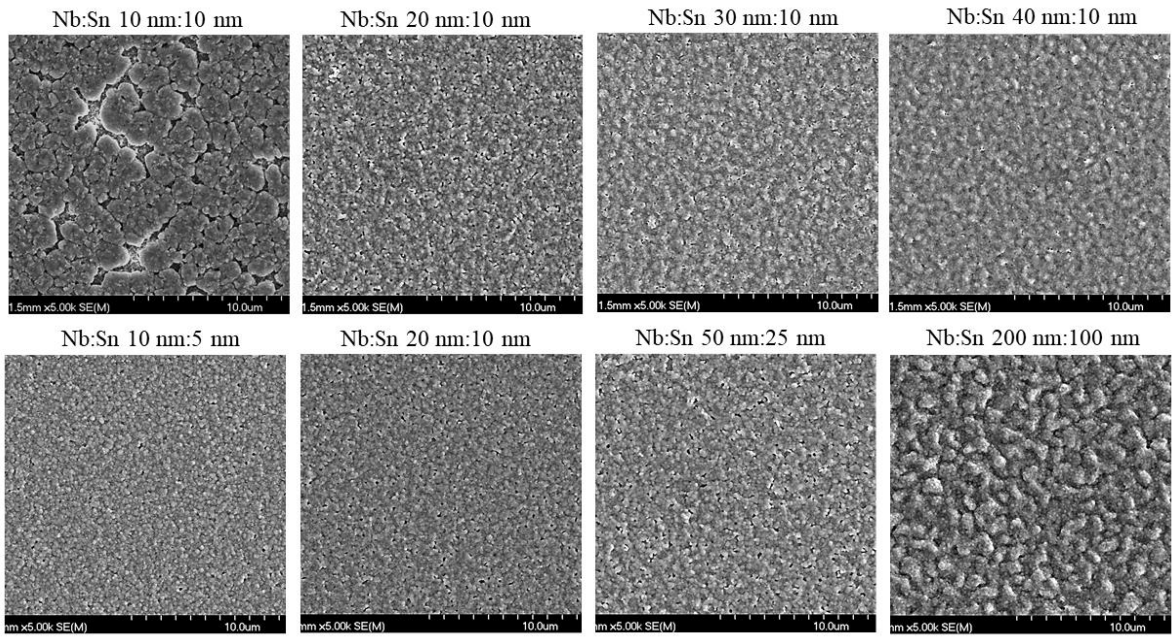

Fig. A.3. SEM images (low magnification) of Nb_3Sn films deposited by multilayer sputtering at different thickness ratio and annealed at 950 °C for 3 h.

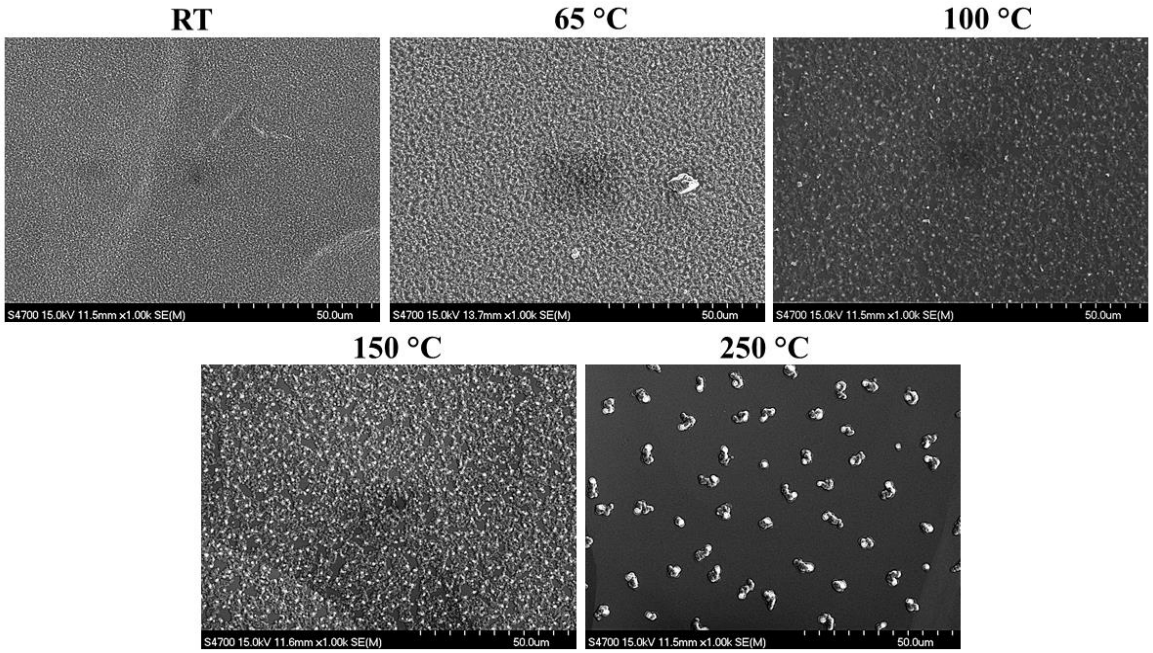

Fig. A.4. SEM images (low magnification) of Nb-Sn multilayered films deposited at different substrate temperatures.

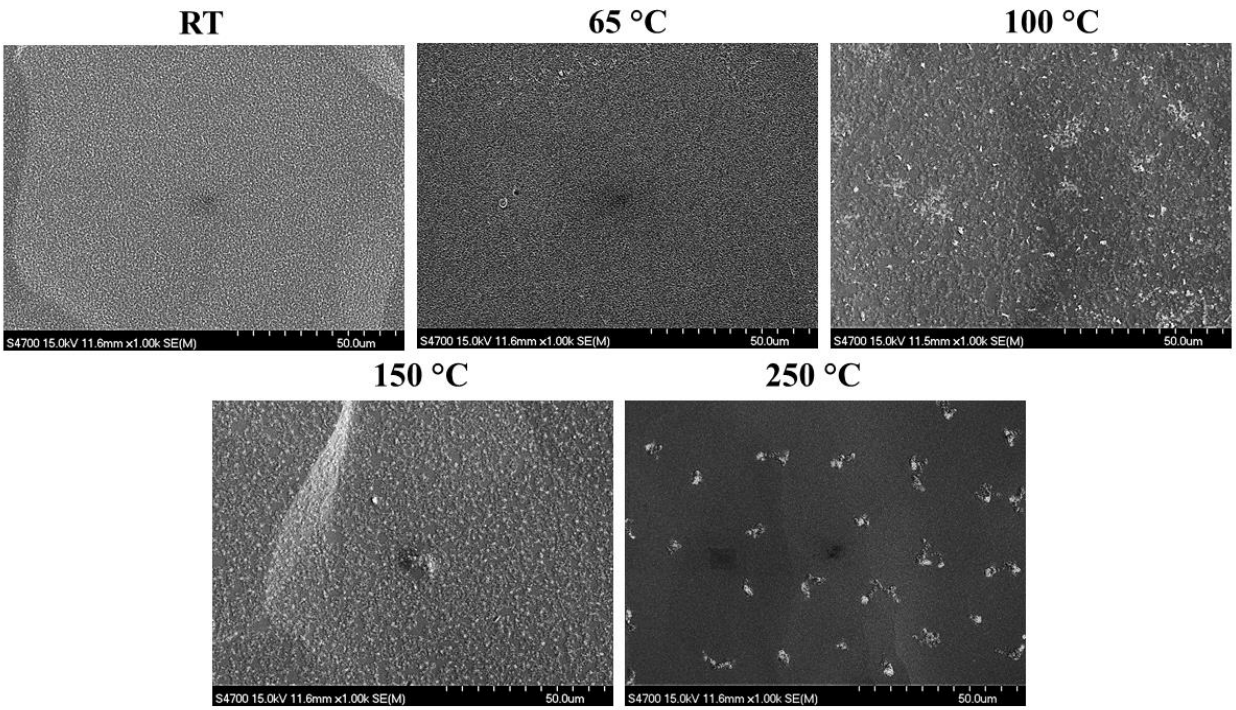

Fig. A.5. SEM images (low magnification) of Nb_3Sn films fabricated by multilayer sputtering at different substrate temperatures and annealing at 950 °C for 3 h.

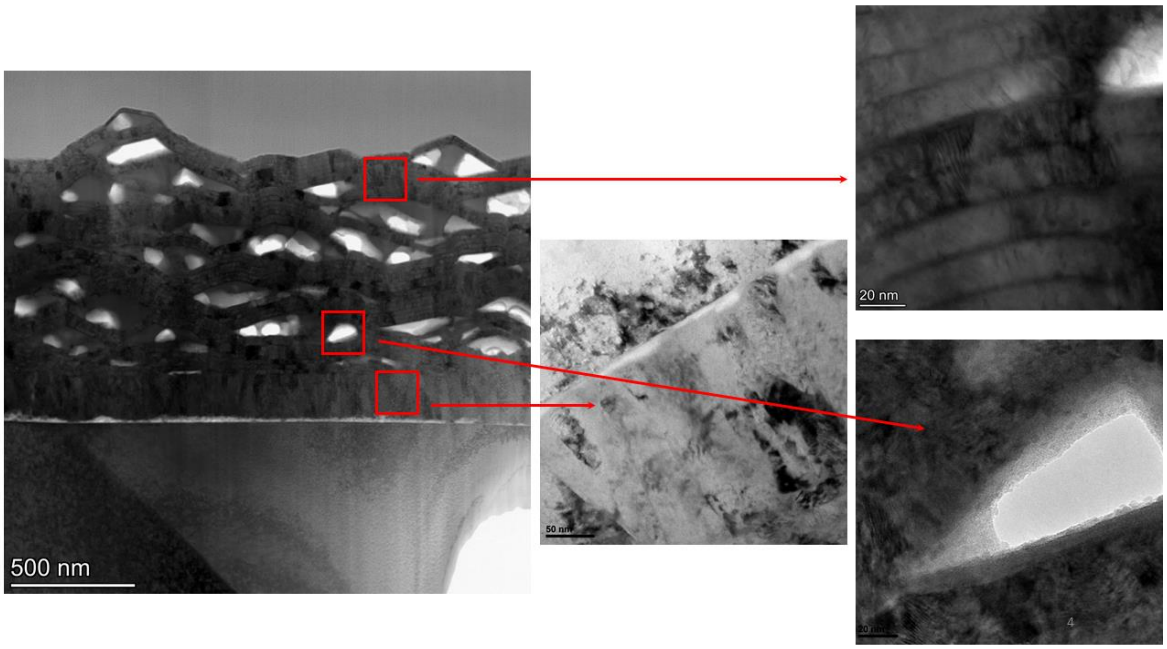

Fig. A.6. TEM images of as-deposited multilayered Nb-Sn film deposited at room temperature. Three different morphologies are observed: the columnar Nb buffer layer, voids between the multilayers and the stacks of multilayers.

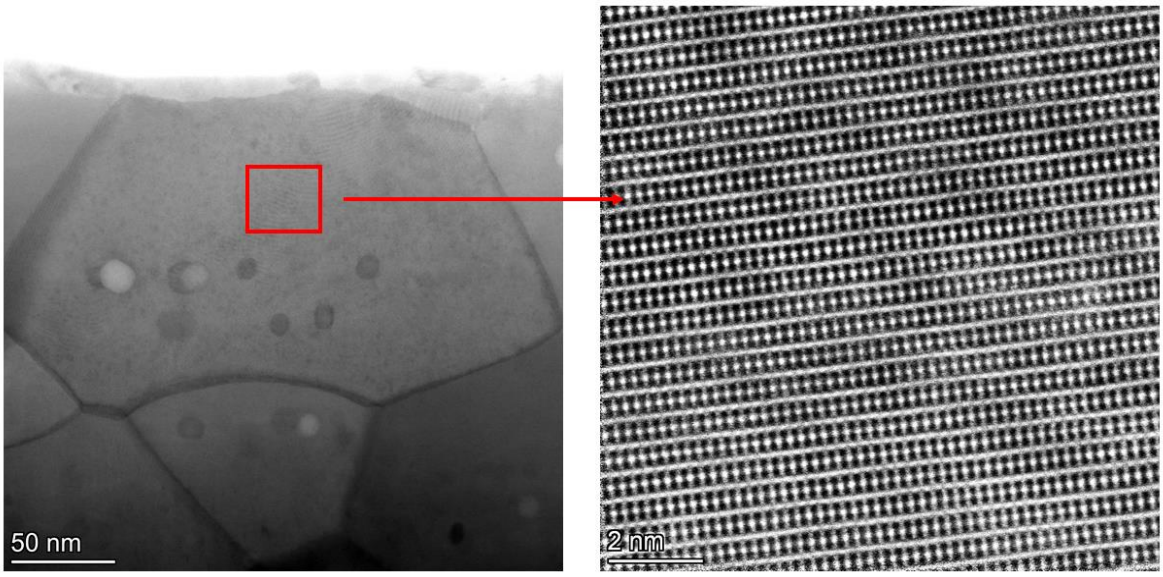

Fig. A.7. TEM image of the cross-section of Nb_3Sn film fabricated by multilayer sputtering and the atomic structure of the Nb_3Sn obtained from high magnification TEM image.

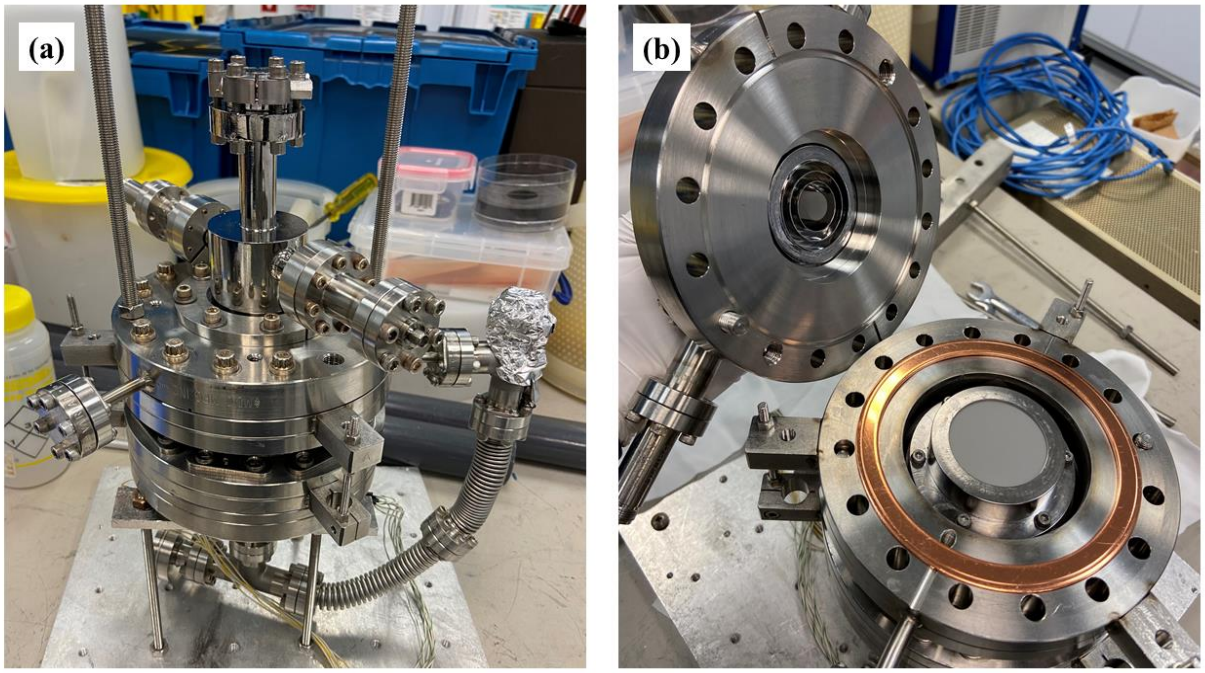

Fig. A.8. (a) Picture of the SIC system at Jefferson Lab used for the RF surface impedance measurement, (b) inside of the SIC cavity with a Nb_3Sn film coated on a 2-inch Nb disk substrate.

APPENDIX D

STEPS OF OPERATION OF AJA ATC ORION 5 SPUTTERING SYSTEM

Check outs

- Before preparing substrate, make sure that the pressure of the chamber is the atmospheric pressure which equal to 7.6×10^2 Torr. Check the Pressure at 937B Gauge Controller screen.
- If the chamber is under vacuum (the pressure is below atmospheric pressure), follow step 1A to vent the chamber, then follow step 1B.
- If the pressure is 7.6×10^2 Torr, follow step 1B.

Step 1A - Venting the Chamber

- Open the nitrogen cylinder (two valves: top and side).

- Open the vent valve.
- Turn off the vacuum pump switch.

- Once the pressure reaches atmospheric pressure, close the vent valve and nitrogen cylinder valve.

Step 1B - Preparation of Substrate

- Take out the substrate holder from the chamber.
- Clean the substrate holder with ethanol.
- Clean substrates before loading it on the substrate holder.
- Use the clips to hold the substrates.
- Proceed to Step 2.

Step 2 - Pump down the System

- Open the gate valve to open the deposition chamber to the pumps.
- Turn on the vacuum pump switch- the pressure on the screen of 937B gauge controller will start to decrease.
- When the pressure reaches to 10^{-4} Torr, turn on ion gauge because it works in the range of 10^{-3} to 10^{-10} Torr.
- Wait till the pressure reaches to approximately 10^{-8} Torr.
- Proceed to step 3.

Step 3 - Deposition Stage

Deposition can be done by manually controlling the chamber or automatically controlling from computer by giving certain command.

Follow Step 3A for manual deposition, Step 3B for automated deposition.

Step 3A - Manual Deposition

- Turn the control switch (located at right side below the heater controller) to HAND mode.

- Make sure to load the desired target before step 2.
- Turn on substrate rotation switch.

- Turn on the heater if substrate temperature is required.

- Connect DC/RF power cable to the target.
- Turn ion gauge sensor off because it doesn't work at deposition pressure range.
- Open the argon gas cylinder valves (top and side ones).

- Turn the Gas1 switch to OPEN.
- Once the Gas1 shutter is open, open the MFCX fully to control the flow rate of gas.

- N.B. The pressure will increase gradually.
- Close the gate valve till the pressure goes to 3×10^{-2} Torr.
- Turn on the desired power supply (RF/DC).
- Check the purple plasma through the window of the chamber.
- If the plasma is observed, open the gate valve till the pressure reaches to 3×10^{-3} Torr because it is the deposition pressure.
- Make sure the plasma exists at the deposition pressure.
- Set the power required for the deposition.
- Once the power reaches the set power, turn the shutter switch to OPEN (SH1 for target 1, SH2 for target 2, SH3 for target 3.

- Keep the shutter open till the desired deposition is done.
- Once the deposition is done, turn the shutter switch to CLOSE.
- Proceed to Step 4.

Step 3B - Automated Deposition

Follow this method if you need multilayer deposition with two different targets for longer time. For thin film deposition, Step 3A is recommended. Make sure you have the program written in text format. The program should start with opening the gas shutter and end with closing the gas shutter. See appendix for reference program.

- Turn the control switch (located at right side below the heater controller) to AUTO mode.
- Once the control is in AUTO mode, the power supplies, gas shutter, target shutters cannot be controlled manually.
- Make sure to load the desired target before step 2.
- Turn on substrate rotation switch.
- Turn on the heater if substrate temperature is required.
- Connect DC/RF power cable to the target and manually turn on the power supply switch.
- Change the power supply control; for DC power supply, change the control to ‘RS232’ from ‘local’ from menu, for RF power supply, change to ‘serial control’ from ‘panel control’.
- Turn ion gauge off because it doesn’t work at deposition pressure range.
- Open the argon gas cylinder valves (top and side ones).
- Go to Computer>Local Disk (C:)>grigory
- Open the LabView program named ‘sputter_systyem_ops_20nov2017’.
- Make a text file with any name to save the data.

- Load the file path on ‘Save Filename’ section.
- Write the program of the operation in text format that starts with opening the gas shutter.
- Load the program on ‘Run file’ section.
- Click the arrow bar at left corner of the LabView screen.
- Click the ‘Run button’ to execute the program.
- Quickly close the gate valve till the plasma is generated, once the plasma is generated, keep the Ar pressure 3 mTorr. The whole process should be done within the 120 s delay written in the program.
- Wait till the deposition is done.
- Proceed to Step 4.

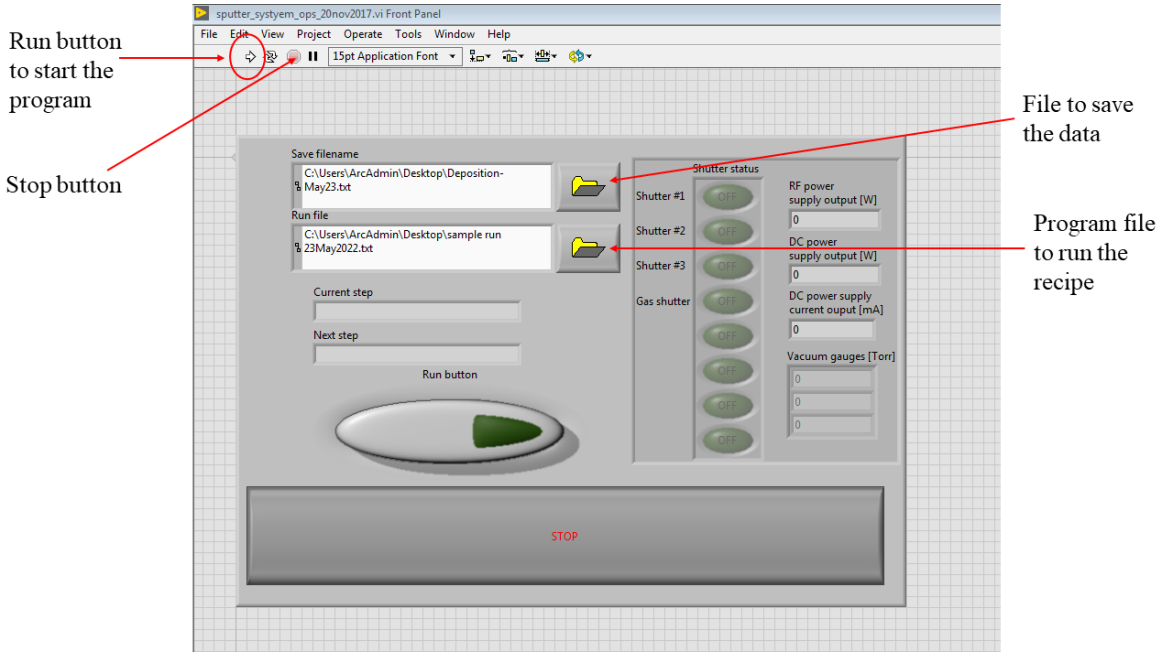

Step 4 - Turn off the system

- Turn off the heater if it was turned on.
- Stop rotation of the sample (substrate).
- Open the gate valve.
- Turn off the power supply.
- Wait till the temperature reaches to 25 ^{o}C – 50 ^{o}C.
- Follow Step 1A to vent the chamber and finally get your samples.

APPENDIX E

PROGRAM USED TO RUN THE SPUTTERING

Program 1: Program to deposit Nb_3Sn film from a single Nb_3Sn target applying a constant current of 150 mA.

START
Gas shutter, open;
RF power, on, 0 W;
DC power, on, 150 mA;
Delay, 10 s;
RF power, off;
DC power, off;
Delay, 5 s;
do, 1;
Shutter #2, open;
Delay, 5 s;
Shutter #2, close;
Delay, 5 s;
DC power, on, 150 mA;
Shutter #1, open;
Delay, 30 s;
Lock DC current,;
Delay, 21600 s;
Shutter #1, close;
Delay, 5 s;
DC power, off;
loop;
DC power, off;
Gas shutter, close;
END

Program 2: Program to deposit 200 nm Nb buffer layer and Nb-Sn multilayer with a Nb layer thickness of 20 nm and Sn layer thickness of 10 nm, total thickness of ~1 μm.

START
Gas shutter, open;
RF power, on, 45 W;
DC power, on, 200 W;
Delay, 120 s;
Shutter #1, open;
Delay, 2000 s;
Shutter #1, close;

do, 34;
Shutter #2, open;
Delay, 100 s;
Shutter #2, close;
Delay, 5 s;
Shutter #1, open;
Delay, 200 s;
Shutter #1, close;
Delay, 5 s;
loop;
RF power, off;
DC power, off;
Gas shutter, close;
END

Program 3: Program to deposit 200 nm Nb buffer layer and Nb-Sn co-sputtered film with a stoichiometry similar to Nb_3Sn.

START
Gas shutter, open;
RF power, on, 28 W;
DC power, on, 190 W;
Delay, 120 s;
Shutter #1, open;
Delay, 2500 s;
Shutter #1, close;
do, 1;
Shutter #2, open;
Shutter #1, open;
Delay, 12500 s;
Shutter #2, close;
Shutter #1, close;
Delay, 5 s;
loop;
RF power, off;
DC power, off;
Gas shutter, close;
END

APPENDIX F

LISTS OF ITEMS PURCHASED

Item	Part Number	Description	Company	Link
1	1251	Sapphire substrate	University wafers	https://order.universitywafer.com/default.aspx?cat=Sapphire&diam=50.8mm
2	EJTNBXX352A4	NIOBIUM TARGET, Nb, 99.95% PURE EX Ta, 2.00" DIAMETER X 0.250" THICK, +/- 0.010" ALL	Kurt J. Lesker	https://www.lesker.com/newweb/deposition_materials/depositionmaterials_sputtertargets_1.cfm?pgid=nb1
3	EJTSNXX502A4	TIN TARGET, Sn, 99.994%-99.999% PURE, 2.00" DIAMETER X 0.250" THICK, +/- 0.010" ALL	Kurt J. Lesker	https://www.lesker.com/newweb/deposition_materials/depositionmaterials_sputtertargets_1.cfm?pgid=sn1
4	EJTNBSN302A4	NIOBIUM TIN TARGET, Nb3Sn, 99.9% PURE, 2.00" DIAMETER X 0.25	Kurt J. Lesker	https://www.lesker.com/newweb/deposition_materials/depositionmaterials_sputtertargets_1.cfm?pgid=nb7
5	CCPG-L2-3	KJLC® Cold Cathode/Pirani Combination Gauge	Kurt J. Lesker	https://www.lesker.com/newweb/gauges/kjlc-cold-cathode-pirani-combo.cfm
6	KJL-SPARC-3.0	KJL-SPARC Power Supply & Display	Kurt J. Lesker	https://www.lesker.com/newweb/gauges/kjl-sparc-display-controller.cfm
7	F0800X000N	FLANGE, UHV, SS, BLANK, FXD, 8"OD	Kurt J. Lesker	https://www.lesker.com/flanges/flanges-cf-304ss/part/f0800x000n
8	GA-0800	Gasket, Copper, DN160CF (8.00" OD) Flange, 6.743" OD, 6.007" ID, (10)	Kurt J. Lesker	https://www.lesker.com/newweb/flanges/hardware_cf_gaskets.cfm?pgid=ofhc&highlight

		Per Package		=GA-0800
9	PNB-0800	Plate Nut, Bolt & Washer Set, Stainless Steel,	Kurt J. Lesker	https://www.lesker.com/newweb/search/sitesearch.cfm?stq=PNB-0800#stq=PNB-0800
10	HBS31224225	Hex Bolt, Nut & Washer Set, Stainless Steel, (25) 5/16-24 x 2.25" Hex Bolts, (25) Hex Nuts, & (50) Flat Washers	Kurt J. Lesker	https://www.lesker.com/newweb/flanges/hardware_cf_boltsets.cfm?pgid=6pt1&highlight=HBS31224225
11	SG0600MCCF	Manual SS Gate Valves (CF flanged; Copper bonnet)	Kurt J. Lesker	https://www.lesker.com/newweb/valves/gatevalves_standard_ss_man_copper.cfm?pgid=0
12	F0450X000N	FLANGE,UHV,SS, BLANK,FXD,4.50" OD	Kurt J. Lesker	https://www.lesker.com/flanges/flanges-cf-304ss/part/f0450x000n
13	GA-0450	Gasket, Copper, DN63CF (4.50" OD) Flange, 3.243" OD, 2.506" ID, (10) Per Package	Kurt J. Lesker	https://www.lesker.com/flanges/flanges-cf-304ss/part/f0450x000n
14	PNB-0450	Plate Nut, Bolt & Washer Set, Stainless Steel, DN63CF (4.50" OD) Flange, (32) 5/16-24 x 2.00" Hex Bolts, (16) 5/16-24 Plate Nuts, & (32) Flat Washers	Kurt J. Lesker	https://www.lesker.com/newweb/flanges/hardware_cf_boltsets.cfm?pgid=6pt2&highlight=PNB-0450
15	HBK31224125	Hex Bolt & Washer Kit, Stainless Steel, (25) 5/16-24 x 1.25" Long Hex Bolts & (25) Flat Washers	Kurt J. Lesker	https://www.lesker.com/newweb/flanges/hardware_cf_boltkits.cfm?pgid=6pt1&highlight=HBK31224125
16	CF0800S3	FLANGE, MULTIPORT, 8"UHV, (3)2.75"UHVS PORTS, STRAIGHT	Kurt J. Lesker	https://www.lesker.com/newweb/flanges/multiport-cluster-flanges.cfm

		TOLERANCES: KJLC STANDARD TOLERANCES APPLY MATERIAL: 304L SS FINISH: MACHINE FINISH OF 63 RA OR BETTER		
17	GA-0275	Gasket, Copper, DN35CF-DN40CF (2.75" OD) Flange, 1.895" OD, 1.451" ID, (10) Per Package	Kurt J. Lesker	https://www.lesker.com/newweb/flanges/hardware_cf_gaskets.cfm?pgid=ofhc&highlight=GA-0275S
18	F0275X000N	FLANGE,UHV,SS, BLANK,FXD,2.75" OD	Kurt J. Lesker	https://www.lesker.com/flanges/flanges-cf-304ss/part/f0275x000n
19	PNB-0275	Plate Nut, Bolt & Washer Set, Stainless Steel, DN35CF-DN40CF (2.75" OD) Flange, (24) 1/4-28 x 1.25" Long Hex Bolts, (12) 1/4-28 Plate Nuts, & (24) Flat Washers	Kurt J. Lesker	https://www.lesker.com/newweb/flanges/hardware_cf_boltsets.cfm?pgid=6pt2&highlight=PNB-0275
20	RF800X600	REDUCING FLANGE, 8" OD X 6" OD FLANGE	Kurt J. Lesker	https://www.lesker.com/flanges/flanges-cf-reducer/part/rf800x600
21	SURPLUS-2122	6.00" CF Manual UHV Gate Valve, Used	LDS Vacuum Products, Inc.	
22	GA-0600	OFHC Copper Gaskets for CF Flanges 6” CF	Kurt J. Lesker	https://www.lesker.com/newweb/flanges/hardware_cf_gaskets.cfm?pgid=ofhc
23	SS-4BG-V51	Stainless Steel Bellows Sealed Valve, Gasketed, Spherical Stem Tip, 1/4 in. Female Swagelok VCR Face Seal Fitting, SC-11 Cleaned	Swagelok	https://www.swagelok.com/en/catalog/Product/Detail?part=SS-4BG-V51

24	SS-4-VCR-2	316L Stainless Steel VCR Face Seal Fitting, 1/4 in. Silver Plated Gasket, Non-Retained Style	Swagelok	https://www.swagelok.com/en/catalog/Product/Detail?part=SS-4-VCR-2
25	SS-4F-7	Stainless Steel In-Line Particulate Filter, 1/4 in. Swagelok Tube Fitting, 7 Micron Pore Size	Swagelok	https://www.swagelok.com/en/catalog/Product/Detail?part=SS-4F-7
26	6LVV-DPS4-C	316L VIM-VAR UHP Diaphragm Sealed Valve, 1/4 in. Swagelok Tube Fitting, NC Actuator	Swagelok	https://www.swagelok.com/en/catalog/Product/Detail?part=6LVV-DPS4-C
27	TU0425BU2-20	SMC TU0425BU2-20 tubing, polyurethane, TU POLYURETHANE TUBING	SMC Pneumatics	https://www.smcpneumatics.com/TU0425BU2-20.html
28	F0275X4MVCR	ADAPTER,SS,2-3/4" UHV FLANGE TO 1/4" MALE VCR	Kurt J. Lesker	https://www.lesker.com/newweb/flanges/adapters_fittings_vcr.cfm?pgid=cf
29	36X084	5/32 in Plastic Male Elbow, 90 Degrees, White/Gray	Grainger	https://www.grainger.com/product/SMC-5-32-in-Plastic-Male-Elbow-36X084?internalSearchTerm=5%2F32+in+Plastic+Male+Elbow%2C+90+Degrees%2C+White%2FGray&suggestConfigId=8&searchBar=true
30	GA-0600	OFHC Copper Gaskets for CF Flanges 6” CF	Kurt J. Lesker	https://www.lesker.com/newweb/flanges/hardware_cf_gaskets.cfm?pgid=ofhc
31	RF800X600	REDUCING FLANGE, 8" OD X 6" OD FLANGE	Kurt J. Lesker	https://www.lesker.com/flanges/flanges-cf-reducer/part/rf800x600

32	T-0600	TEE, SS, 6.56"A, 6"OD, 8" FLANGE, UHV FITTING	Kurt J. Lesker	https://www.lesker.com/flanges/fittings-cf-tees/part/t-0600
33	GE50A013501RMV020	MFC, N2, 50 SCCM, 15 PIN ANALOG (TIED GROUNDS), N.C. VITON, LCEA51CR1MV20	MKS Instruments	https://www.mksinst.com/p/GE50A013501RMV020
34	CB259-5-10	CABLE,PR4000,627 TYPE	MKS Instruments	https://www.mksinst.com/p/CB259-5-10
35	X1699-64124	TPS-flexy 305 CFF6 IDP7 120-240V RemC/U	Agilent Technologies, Inc.	https://www.agilent.com/en/product/vacuum-technologies/turbo-pumping-systems-tps/modular-turbo-pumping-systems/tps-flexy-turbo-pumping-system

VITA

MD NIZAM SAYEED

msaye004@odu.edu, 757-785-8617

www.linkedin.com/in/mns

EDUCATION

Ph.D. in Electrical and Computer Engineering, Old Dominion University, Norfolk VA, 2022.

B.S. in Applied Physics, Electronics & Communication Engineering, University of Dhaka, Dhaka, Bangladesh, 2012

PROFESSIONAL EXPERIENCE

Graduate Research Assistant, Applied Research Center, Old Dominion University, Newport News, Virginia — **August 2014 – June 2021**

Graduate Technical Intern- Intel Corporation, Chandler, Arizona — **June 2021- March 2022**

KEY AWARDS

- PhD Researcher Award 2021-2022 awarded by the Department of Electrical and Computer Engineering of Old Dominion University.
- Finalist of the prestigious Nottingham Prize in the Physical Electronics Conference, 2021.
- Finalist of the PhD Tech and Career Symposium, 2020 organized by ASML.
- 1st place in the student poster presentation competition, 2018 organized by AVS Mid-Atlantic Chapter.
- Selected as Mid-Atlantic representative of AVS to attend 65th AVS International Symposium in Long Beach, California, 2018.
- 2nd place in the student poster presentation competition, 2019 organized by AVS Mid-Atlantic Chapter.
- Student grant in 19th International Conference on RF Superconductivity in Dresden, Germany, 2019.
- Student grant in the International Workshop on Nb_3Sn SRF Science, Technology and Applications Nb_3SnSRF'20, Cornell University, Ithaca, New York (changed to virtual workshop).

PUBLICATIONS

Published 5 journal articles and participated in 13 conference and poster presentations.

INVITED TALKS

1. **Sayeed, M. N.**, *et al.* "Nb_3Sn growth by sequential sputtering: film morphology and its RF properties", Virtual International Workshop on Nb_3Sn SRF Science, Technology, and Applications (Nb_3SnSRF'20).
2. **Sayeed, M. N.**, *et al.* "Development and Optimization of Sputtered Nb_3Sn Films", Virtual Cryogenic Engineering Conference & International Cryogenic Materials Conference, (CEC-ICMC 2021).